# Spectral analysis of atmospheric composition: Application to surface ozone

**Dene Bowdalo**

Doctor of Philosophy

University of York
Chemistry

September 2016

# Abstract

This thesis describes the undertaking of multiple studies designed to evaluate and reduce global modelled surface $O_3$ biases in CTMs/ESMs. Specific focus is placed on the evaluation of rural surface $O_3$ seasonal variability in a global CTM (GEOS-Chem). A major observational data collation is undertaken, processing 1,033,463,750 measurements of $O_3$ and some of its major precursors, from 16,996 sites, through a number of rigorous data quality checks, to ensure data is of a high enough quality for global model evaluation.

Through a model–measurement comparison, applying spectral analysis, substantial seasonal biases of surface $O_3$ in GEOS-Chem are found, with a general overestimation of the seasonal amplitudes in North America and Europe (by up to 16 ppbv), together with delayed phase maxima by 1–5 months. The main cause of these biases is found to be homogenous overestimates of summertime $O_3$ in all observed areas, by a minimum of 10 ppbv.

An extensive global sensitivity study is undertaken to evaluate the sensitivity of modelled surface $O_3$ biases to alterations of anthropogenic emissions, biogenic emissions, and the $O_3$ dry deposition flux. Constraining model biases jointly by $O_3$, NO and CO observations yields regional optimal monthly scaling factors. Driving GEOS-Chem with these derived factors results in the modelled summertime overestimates of surface $O_3$ being removed almost entirely, across all regions. The removal of this bias is dominantly controlled through increases to the summertime $O_3$ dry deposition flux (by factors of 2–4), with modifications to this term providing the only viable pathway for substantial reduction of modelled summertime biases, in all evaluated regions. Surface $O_3$ is found to be NOx sensitive in all regions, with scalings of VOC emissions generally not imparting significant change on $O_3$. General modelled winter underestimates of surface $O_3$ are able to be removed through reductions of NOx emissions.

# Table of contents

**Abstract** **3**

**Table of Contents** **5**

**List of figures** **9**

**List of tables** **17**

**Acknowledgements** **19**

**Declaration** **21**

**1 Introduction** **23**
1.1 Tropospheric ozone: an air pollutant and greenhouse gas . . . . . 23
1.2 Tropospheric ozone: sources and sinks . . . . . 24
1.2.1 Photochemistry . . . . . 24
1.2.2 Stratosphere–troposphere exchange . . . . . 39
1.2.3 Dry deposition . . . . . 40
1.2.4 Tropospheric ozone budget . . . . . 41
1.3 Evaluation of ozone in CTMs/ESMs . . . . . 42
1.4 Structure of the thesis . . . . . 43

**2 Gridded global metrics for surface ozone model evaluation** **45**
2.1 Introduction . . . . . 45
2.2 Contributing data sets . . . . . 46
2.3 Data processing . . . . . 47
2.3.1 Primary file parsing . . . . . 49
2.3.2 Metadata . . . . . 49
2.3.3 Concentrations and mixing ratios . . . . . 51
2.3.4 Date and time . . . . . 51
2.3.5 Correcting overlapping and removing duplicate data . . . . . 52
2.3.6 Coarse resolution / data plateaus . . . . . 52
2.3.7 Removing invalid measurement methods . . . . . 53
2.3.8 Removing duplicate sites . . . . . 62
2.3.9 Removing urban sites . . . . . 62

2.3.10 Removing high altitude sites . . . 63
2.3.11 Removing nighttime NO . . . 63
2.3.12 Removing data un-representative of the day . . . 64
2.3.13 Extreme / suspect data . . . 64
2.3.14 Removing data un-representative of year . . . 65
2.4 Final data sets . . . 68
2.5 Statistical overview of observations . . . 73
2.6 Gridding data for model evaluation . . . 76
2.7 Recommendations for data providers . . . 79

**3 Spectral analysis: a framework for application to atmospheric composition data 81**
3.1 Introduction . . . 81
3.2 DFT/FFT . . . 82
3.2.1 Founding . . . 82
3.2.2 Correlation . . . 84
3.2.3 Frequencies . . . 85
3.2.4 Limitations . . . 86
3.3 Lomb–Scargle periodogram . . . 90
3.4 Spectral leakage . . . 91
3.5 Validation of methods . . . 91

**4 Spectral analysis of surface ozone: a model–measurement evaluation 95**
4.1 Introduction . . . 95
4.2 Lomb–Scargle periodogram of surface $O_3$ . . . 95
4.2.1 Meteorological regimes . . . 99
4.2.2 Annual and daily cycles . . . 100
4.3 Application to observations . . . 101
4.3.1 Significance of seasonal and diurnal cycles . . . 104
4.3.2 Seasonal cycle . . . 106
4.3.3 Diurnal cycle . . . 109
4.4 Model perspective . . . 112
4.4.1 Modelled power spectrum . . . 112
4.4.2 Significance of seasonal and diurnal cycles . . . 113
4.4.3 Seasonal cycle . . . 115
4.4.4 Diurnal cycle . . . 115
4.5 Model – measurement comparisons . . . 115
4.5.1 Significance of seasonal and diurnal cycles . . . 116
4.5.2 Seasonal cycle . . . 118
4.5.3 Diurnal cycle . . . 120
4.5.4 Possible causes of biases . . . 123

**5 Summertime surface ozone bias: a problem with emissions? 125**
5.1 Introduction . . . 125
5.2 Measurements and model . . . 126
5.2.1 Observations . . . 126
5.2.2 GEOS-Chem model description . . . 129
5.3 Modelled seasonal ozone biases . . . 139
5.3.1 Spectral methodology . . . 139
5.3.2 GEOS-Chem biases by version . . . 139
5.3.3 GEOS-Chem biases by setup . . . 142
5.3.4 Day/night biases in GEOS-Chem . . . 144
5.3.5 ACCMIP biases . . . 148
5.4 Ozone sensitivity to emissions/dry deposition . . . 151
5.4.1 Sensitivity study setup . . . 151
5.4.2 Example output . . . 153
5.4.3 Sensitivity study results . . . 155
5.5 Nitric oxide/carbon monoxide sensitivity to emissions/dry deposition . . . 159
5.5.1 Nitric Oxide . . . 159
5.5.2 Carbon monoxide . . . 166
5.6 Integrated species sensitivity to emissions/dry deposition . . . 171
5.6.1 Composite sensitivity study results . . . 171
5.6.2 Optimal scalings . . . 174
5.7 Optimised simulation . . . 177
5.8 Discussion . . . 182

**6 Conclusions 185**

**Appendix A 189**

**Appendix B 191**

**Nomenclature 197**

**References 201**

# List of figures

1.1 Sensitivity of the rate of $O_3$ production ($P(O_3)$) to the OH production rate ($Q$), NOx concentration and VOC–OH reactivity ($VOC_R$). Given as a function of the fraction of OH removed by NOx ($L_N/Q$). Figure from Kleinman (2005). . . . . 38

2.1 Flow chart illustrating the data processing framework. . . . . 48
2.2 Time series of $NO_2$ measurements made by chemiluminescence instruments with molybdenum (black) and photolytic (red) converters at Rigi (upper panel), and the associated diurnal and seasonal cycles derived through spectral analysis (lower panels). . . . . 56
2.3 Maps of sites screened out in data processing through each data quality check, by species, coloured by the data network. . . . . 66
2.4 Maps of finalised valid site locations, by species, coloured by the data network. . . . . 69
2.5 Maps of finalised valid site locations, by species, coloured by the mode measurement methodology (acronyms defined in Tables 2.1–2.4). . . . . 70
2.6 The number of sites from each network reporting data for a given hour, from 1980 to 2015, by species. The colour represents the data network. The number of NO sites per hour fluctuates significantly because of the removal of nighttime NO. The number of WMO GAW CO sites per hour fluctuates due to the inclusion of the flask measurements, representing one hour a month. . . . . 71
2.7 PDF of all valid data between 2005 and 2010, by species, for observations (left panels, and in black) and GEOS-Chem (right panels, and in red). The sum of the bars equals 1. . . . . 72
2.8 Maps of observed statistical metrics (average, temporal standard deviation, skewness, kurtosis) for valid sites, by species, between 2005 and 2010. . . 74
2.9 Comparison of monthly gridded statistical metrics (average, temporal standard deviation, skewness, kurtosis) between observations (x axis) and GEOS-Chem (y axis) for the years 2005–2010, by species. Points are coloured by the spatial standard deviation between sites going into each gridded metric. The red best-fit line is the orthogonal least-squares regression. 78

3.1 Demonstration of the close relationship between the unit circle and the sine and cosine functions. **(a)** Unit circle in complex space illustrating the equality between the representation of periodic circular rotation by a complex exponential (polar notation) and in terms of sine and cosine (rectangular notation). **(b)** Illustration of the evolution of $\sin(x)$ with rotation of a point around the unit circle, representing the sine function. **(c)** Illustration of the evolution of $\cos(x)$ with rotation of a point around the unit circle, representing the cosine function. . . . . 87

3.2 Demonstration of the calculation of the complex number output of the DFT, at a single frequency ($\frac{1}{365}$ cycles per day). **(a)** Synthetic time series composed of annual and daily repeating sinusoids spanning 365 days. Annual sinusoid given a amplitude of 10 ppbv and phase of 2.4 radians. **(b)** Time series is multiplied by a pair of sine and cosine functions with a frequency of $\frac{1}{365}$ cycles per day. **(c)** The products of both multiplications are then summed, and after normalisation, the real and imaginary terms of the complex output are derived. **(d)** Through conversion to polar notation, it can be shown the DFT correctly derives the variability contained in the time series at a frequency of $\frac{1}{365}$ cycles per day. . . . . 88

3.3 Physical illustration of the output derived from the DFT at a specific frequency. **(a)** Representation of the output of the DFT at a specific frequency in complex space (the derivation of which is shown in Fig. 3.2). **(b)** Representation of the cosine and sine functions described by the rectangular output of the DFT, over one full oscillation in $x$. **(c)** Representation of the sinusoidal function described by the polar output of the DFT, over one full oscillation in $x$. . . . . 89

3.4 Evaluation of the amplitude and phase biases for multiple versions of the FFT and LSP methodologies, as a function of % data gaps. A 5 year synthetic time series consisting of daily and annual repeating sinusoids (amplitudes – 3 and 10 ppbv, phases both 0 radians) is incrementally filled with random gaps, and the amplitude and phase biases for both periods, associated with multiple FFT and LSP methods are iteratively calculated. FFT methods are the standard code (FFT Std.), with windowing (FFT Window), and with both zero padding and windowing (FFT Window, Over.). LSP methods are the standard code (LSP Std.), with windowing (LSP Window), and with both specific frequency estimation and windowing (LSP Window, Spec.). . . . . 93

3.5 Evaluation of the amplitude and phase biases for multiple versions of the LSP method, as a function of random noise (up to 25 $\sigma$). A 5 year synthetic time series consisting of daily and annual repeating sinusoids (amplitudes – 3 and 10 ppbv, phases both 0 radians) is incrementally added with random noise (up to 25 $\sigma$), and the amplitude and phase biases for both periods, associated with multiple versions of the LSP method are iteratively calculated. LSP methods are the standard code (LSP Std.), with windowing (LSP Window), and with both specific frequency estimation and windowing (LSP Window, Spec.). . . . . 94

4.1 Time series of surface $O_3$ at Cape Verde (16.51° N, 24.52° W) and Lompoc (34.73° N, 120.43° W) for the observations (black) and the GEOS-Chem model (red), between 2006 and 2012. . . . . 97

4.2 Lomb–Scargle periodogram spectra for surface $O_3$ at Cape Verde (16.51° N, 24.52° W) and Lompoc (34.73° N, 120.43° W), between 2006 and 2012. The upper panels shows the observed data spectra together with chi-squared false-alarm levels for significant periodicity based on linear piecewise fits to the spectra. The lower panels compare the spectra of the observations (black) and the GEOS-Chem model (red). . . . . 98

4.3 Example of spectral superposition of the average, fundamental frequency and the harmonics for a frequency of interest. . . . . 101

4.4 Map of valid surface sites reporting surface $O_3$ between 2005 and 2010 used in this work, coloured by the providing data network. . . . . 103

4.5 Observational fractional variance of time series by site from diurnal, seasonal and total periodicity, as well as the weather and macroweather (meteorological) regimes. NA is North America, EU is Europe, AS is Asia, and ROW is rest of world. . . . . 105

4.6 Seasonal amplitudes of observations (upper panels) and model (lower panel). NA is North America, EU is Europe, AS is Asia, and ROW is rest of world. . . . . 107

4.7 Seasonal phases of observations (upper panels) and model (lower panel). NA is North America, EU is Europe, AS is Asia, and ROW is rest of world. 108

4.8 Diurnal amplitudes of observations (upper panels) and model (lower panel). NA is North America, EU is Europe, AS is Asia, and ROW is rest of world. 110

4.9 Diurnal phases of observations (upper panels) and model (lower panel). NA is North America, EU is Europe, AS is Asia, and ROW is rest of world. 111

4.10 Modelled fractional variance of time series from diurnal, seasonal and total periodicity, as well as the weather and macroweather (meteorological) regimes. . . . . 114

4.11 Fractional variance differences of diurnal, seasonal and total periodicity, and weather and macroweather (meteorological) regimes, between observations and the GEOS-Chem model. NA is North America, EU is Europe, AS is Asia, and ROW is rest of world. . . . . 117
4.12 Seasonal amplitude (upper panel) and phase (lower panel) differences between observations and the GEOS-Chem model. NA is North America, EU is Europe, AS is Asia, and ROW is rest of world. . . . . 119
4.13 Diurnal amplitude (upper panel) and phase (lower panel) differences between observations and the GEOS-Chem model. NA is North America, EU is Europe, AS is Asia, and ROW is rest of world. . . . . 121
4.14 Polar plot of the diurnal and seasonal amplitudes and phases for observations and the GEOS-Chem model, and the differences between them. Circle colour indicates the location of the site. . . . . 122
4.15 **(a)** Seasonal amplitude bias vs. 2005–2010 Average GEOS-Chem model $NO_x$, **(b)** Seasonal phase bias vs. 2005–2010 Average GEOS-Chem model $NO_x$, **(c)** 2005–2010 Average GEOS-Chem model $NO_x$ by observational site. NA is North America, EU is Europe, AS is Asia, and ROW is rest of world. . . . . 124

5.1 Valid observational sites between 2009 and 2011 for $O_3$, NO and CO, coloured by the reporting monitoring network. . . . . 127
5.2 Set areas for averaging results regionally, predominantly defined by the spatial availability of observations. North America is split into 7 regions: south western (SW NA), north western (NW NA), central (C NA), north eastern (NE NA), central eastern (CE NA), south eastern (SE NA) and southern (S NA). Europe is split into 6 regions: south western (SW EU), north western (NW EU), northern (N EU), eastern (E EU), central (C EU) and southern (S EU). Japan is classed as a standalone area. . . . . 128
5.3 Comparison of average spectrally derived seasonal surface $O_3$ waveforms (for 2009–2011) between observations (black lines) and iterative versions of GEOS-Chem $4^\circ \times 5^\circ$ GEOS5 (v09.01.03. – blue lines; v09.02. – green lines; v10.01. – red lines), in multiple areas in North America, Europe and Japan. . . . . 141
5.4 Comparison of average spectrally derived seasonal surface $O_3$ waveforms (for 2009–2011) between observations (black lines) and multiple configurations of GEOS-Chem v10.01. (standard $4^\circ \times 5^\circ$ GEOS5 – red lines; $2^\circ \times 2.5^\circ$ horizontal resolution – blue lines; MERRA meteorology – green lines; interactive boundary layer height – orange lines; fully mixed boundary layer – purple lines), in multiple areas in North America, Europe and Japan. . . . . 143

5.5 Comparison of average spectrally derived seasonal surface $O_3$ waveforms (for 2009–2011) between observations (black lines) and GEOS-Chem v10.01. $4^\circ \times 5^\circ$ GEOS5 (red lines), in the day (solid lines) and at night (dashed lines), in multiple areas in North America, Europe and Japan. . . 146

5.6 Comparison of average spectrally derived diurnal surface $O_3$ waveforms (for 2009–2011) between observations (black lines) and GEOS-Chem v10.01. $4^\circ \times 5^\circ$ GEOS5 (red lines), in the summer (solid lines) and in the winter (dashed lines), in multiple areas in North America, Europe and Japan. 147

5.7 Comparison of average spectrally derived seasonal surface $O_3$ waveforms (for 2005–2010) between observations (black lines), GEOS-Chem v10.01. $4^\circ \times 5^\circ$ GEOS5 (red lines), median of the ACCMIP model spread (purple lines), and the range of the ACCMIP model spread (light blue), in multiple areas in North America, Europe and Japan. . . . . 150

5.8 Evolving representation of the output from a large-scale study using GEOS-Chem v10.01. $4^\circ \times 5^\circ$ GEOS5, designed to evaluate the sensitivity of regional spectrally determined monthly modelled surface $O_3$ biases to changes in emissions and the $O_3$ dry deposition flux (between 2009 and 2011). This figure shows output specifically for the defined C EU area. **(a)** Contour plot showing the January modelled surface $O_3$ biases resultant from multiple scalings of ANMVOC and ANOx emissions, in C EU. The plotted colour represents the spectrally derived monthly average absolute percentage difference from observations. The y-axis represents scalings of ANOx emissions, and the x-axis represents scalings of ANMVOC emissions. The centre of the box represents where no scalings have been applied. The scalings across both axes are 0.25, 0.5, 1, 2 and 4. **(b)** Expansion of (a), with multiple contour plots showing the modelled surface $O_3$ biases resultant from scalings of ANMVOC and ANOx emissions, across all months of the year, in C EU. **(c)** Expansion of (b), where each row represents output from scalings of different x-axis parameters, going top to bottom: A–ANMVOCs, B–BNMVOCs, C–ACO, D–$O_3$ dry deposition. The y-axis always represents scalings of ANOx. . . . . 154

5.9 Contour plots showing the sensitivity of regional spectrally derived monthly surface $O_3$ biases of GEOS-Chem v10.01. $4^\circ \times 5^\circ$ GEOS5, resultant from scalings of multiple emissions/deposition parameters (for 2009–2011). Each individual box represents the regional average monthly modelled biases from scalings of ANOx emissions (y-axis) and a changing x-axis parameter (ANMVOCs, BNMVOCs, ACO, $O_3$ dry deposition). Design of figure is explained in detail by Fig 5.8. The over-plotted white x marks represent the optimal monthly scalings for the minimisation of modelled biases, per region. . . . . 157

5.10 Comparison of regional spectrally derived seasonal surface $O_3$ monthly averages (for 2009–2011) between observations (black lines) and GEOS-Chem v10.01. $4^\circ \times 5^\circ$ GEOS5 (red lines), median of output from all 106 scaled simulations (purple lines), optimal model output of scaled simulations (green x marks), and the range of output from all scaled simulations (light blue), in multiple areas in North America, Europe and Japan. . . . . 158
5.11 Comparison of average spectrally derived seasonal surface NO waveforms (for 2009–2011) between observations (black lines) and GEOS-Chem v10.01. $4^\circ \times 5^\circ$ GEOS5 (red lines), in multiple areas in North America, Europe and Japan. . . . . 161
5.12 Contour plots showing the sensitivity of regional spectrally derived monthly surface NO biases of GEOS-Chem v10.01. $4^\circ \times 5^\circ$ GEOS5, resultant from scalings of multiple emissions/deposition parameters (for 2009–2011). Each individual box represents the regional average monthly modelled biases from scalings of ANOx emissions (y-axis) and a changing x-axis parameter (ANMVOCs, BNMVOCs, ACO, $O_3$ dry deposition). Design of figure is explained in detail by Fig 5.8. The over-plotted white x marks represent the optimal monthly scalings for the minimisation of modelled biases, per region. . . . . 164
5.13 Comparison of regional spectrally derived seasonal surface NO monthly averages (for 2009–2011) between observations (black lines) and GEOS-Chem v10.01. $4^\circ \times 5^\circ$ GEOS5 (red lines), median of output from all 106 scaled simulations (purple lines), optimal model output of scaled simulations (green x marks), and the range of output from all scaled simulations (light blue), in multiple areas in North America, Europe and Japan. . . . . 165
5.14 Comparison of average spectrally derived seasonal surface CO waveforms (for 2009–2011) between observations (black lines) and GEOS-Chem v10.01. $4^\circ \times 5^\circ$ GEOS5 (red lines), in multiple areas in North America, Europe and Japan. . . . . 167
5.15 Contour plots showing the sensitivity of regional spectrally derived monthly surface CO biases of GEOS-Chem v10.01. $4^\circ \times 5^\circ$ GEOS5, resultant from scalings of multiple emissions/deposition parameters (for 2009–2011). Each individual box represents the regional average monthly modelled biases from scalings of ANOx emissions (y-axis) and a changing x-axis parameter (ANMVOCs, BNMVOCs, ACO, $O_3$ dry deposition). Design of figure is explained in detail by Fig 5.8. The over-plotted white x marks represent the optimal monthly scalings for the minimisation of modelled biases, per region. . . . . 169

5.16 Comparison of regional spectrally derived seasonal surface CO monthly averages (for 2009–2011) between observations (black lines) and GEOS-Chem v10.01. $4^\circ \times 5^\circ$ GEOS5 (red lines), median of output from all 106 scaled simulations (purple lines), optimal model output of scaled simulations (green x marks), and the range of output from all scaled simulations (light blue), in multiple areas in North America, Europe and Japan. . . . . 170

5.17 Contour plots showing the sensitivity of regional spectrally derived monthly surface $O_3$+NO+CO biases of GEOS-Chem v10.01. $4^\circ \times 5^\circ$ GEOS5, resultant from scalings of multiple emissions/deposition parameters (for 2009–2011). Each individual box represents the regional average monthly modelled biases from scalings of ANOx emissions (y-axis) and a changing x-axis parameter (ANMVOCs, BNMVOCs, ACO, $O_3$ dry deposition). Design of figure is explained in detail by Fig 5.8. The over-plotted white x marks represent the optimal monthly scalings for the minimisation of modelled biases, per region. . . . . 173

5.18 Optimal monthly scalings of emissions/$O_3$ dry deposition parameters (between 2009 and 2011) in GEOS-Chem v10.01. $4^\circ \times 5^\circ$ GEOS5, for the minimisation of surface $O_3$+NO+CO biases. Plotted colour represents sign and intensity of scaling change. . . . . 176

5.19 Comparison of average spectrally derived seasonal surface $O_3$ waveforms (for 2009–2011) between observations (black lines), GEOS-Chem v10.01. $4^\circ \times 5^\circ$ GEOS5 (red lines), and an optimal regionally scaled version of the same model (using scalings shown in Fig 5.18) (blue lines), in multiple areas in North America, Europe and Japan. . . . . 179

5.20 Comparison of average spectrally derived seasonal surface NO waveforms (for 2009–2011) between observations (black lines), GEOS-Chem v10.01. $4^\circ \times 5^\circ$ GEOS5 (red lines), and an optimal regionally scaled version of the same model (using scalings shown in Fig 5.18) (blue lines), in multiple areas in North America, Europe and Japan. . . . . 180

5.21 Comparison of average spectrally derived seasonal surface CO waveforms (for 2009–2011) between observations (black lines), GEOS-Chem v10.01. $4^\circ \times 5^\circ$ GEOS5 (red lines), and an optimal regionally scaled version of the same model (using scalings shown in Fig 5.18) (blue lines), in multiple areas in North America, Europe and Japan. . . . . 181

B.1 Comparison of average spectrally derived seasonal surface NO waveforms (for 2009–2011) between observations (black lines) and multiple configurations of GEOS-Chem v10.01. (standard $4^\circ \times 5^\circ$ GEOS5 – red lines; $2^\circ \times 2.5^\circ$ horizontal resolution – blue lines; MERRA meteorology – green lines; interactive boundary layer height – orange lines; fully mixed boundary layer – purple lines), in multiple areas in North America, Europe and Japan. . . . . 192

B.2 Contour plots showing the sensitivity of regional spectrally derived monthly surface $O_3$+NO biases of GEOS-Chem v10.01. $4^\circ \times 5^\circ$ GEOS5, resultant from scalings of multiple emissions/deposition parameters (for 2009–2011). Each individual box represents the regional average monthly modelled biases from scalings of ANOx emissions (y-axis) and a changing x-axis parameter (ANMVOCs, BNMVOCs, ACO, $O_3$ dry deposition). Design of figure is explained in detail by Fig 5.8. The over-plotted white x marks represent the optimal monthly scalings for the minimisation of modelled biases, per region. . . . . 193

B.3 Contour plots showing the sensitivity of regional spectrally derived monthly surface $O_3$+CO biases of GEOS-Chem v10.01. $4^\circ \times 5^\circ$ GEOS5, resultant from scalings of multiple emissions/deposition parameters (for 2009–2011). Each individual box represents the regional average monthly modelled biases from scalings of ANOx emissions (y-axis) and a changing x-axis parameter (ANMVOCs, BNMVOCs, ACO, $O_3$ dry deposition). Design of figure is explained in detail by Fig 5.8. The over-plotted white x marks represent the optimal monthly scalings for the minimisation of modelled biases, per region. . . . . 194

B.4 Contour plots showing the sensitivity of regional spectrally derived monthly surface NO+CO biases of GEOS-Chem v10.01. $4^\circ \times 5^\circ$ GEOS5, resultant from scalings of multiple emissions/deposition parameters (for 2009–2011). Each individual box represents the regional average monthly modelled biases from scalings of ANOx emissions (y-axis) and a changing x-axis parameter (ANMVOCs, BNMVOCs, ACO, $O_3$ dry deposition). Design of figure is explained in detail by Fig 5.8. The over-plotted white x marks represent the optimal monthly scalings for the minimisation of modelled biases, per region. . . . . 195

# List of tables


1.1 Estimates of present day global annual tropospheric CO sources and sinks. 27
1.2 Estimates of present day global annual tropospheric $CH_4$ sources and sinks. 31
1.3 Estimates of present day global annual tropospheric NOx sources. . . . . 36
1.4 Mean and range of the multi-model estimates of the tropospheric $O_3$ budget from ACCENT and ACCMIP. Values summarised from Stevenson et al. (2006) and Young et al. (2013). . . . . 42

2.1 Accepted measurement methodologies for $O_3$. . . . . 59
2.2 Accepted measurement methodologies for $C_5H_8$. . . . . 59
2.3 Accepted measurement methodologies for NO and $NO_2$. . . . . 60
2.4 Accepted measurement methodologies for CO. . . . . 61
2.5 Counts of the number of observations and sites after each quality control step, by species. . . . . 67
2.6 Metrics prescribed for model evaluation via the BADC. . . . . 75
2.7 Spatial and temporal resolutions of metrics available for model evaluation via the BADC. . . . . 75

5.1 Summary of global and regional emissions inventories used in GEOS-Chem v10.01. Regional emissions overwrite global emissions of the same species. Emission grids are interpolated on the fly to the resolution of the model run by the HEMCO emissions component (Keller et al., 2014). . . 134
5.2 Description of simulations exploring the sensitivity of seasonal surface $O_3$ in GEOS-Chem to changes in model version, driven meteorology, horizontal resolution and boundary layer mixing. Each simulation is for 2 years between 2009 and 2011, spun up for 6 months prior. . . . . 138
5.3 Description of each of the parameter sets that are scaled in GEOS-Chem. ANMVOCs, BNMVOCs, ACO, ANOx, and the $O_3$ dry deposition flux are globally scaled by factors of: 0.25, 0.5, 2 and 4. Zonal $CH_4$ is scaled by factors of: 0.98, 0.99, 1.01 and 1.02. . . . . 152

A.1 Omitted measurement methodologies for all species. . . . . 190

# Acknowledgements

I would like to dedicate this thesis to my girlfriend and my loving family. Carmel, Paul, Lauren and Claudia, I love you all.

My everlasting thanks go to my supervisor Mathew Evans for his continued support, without who this work would not be possible.

# Declaration

I hereby declare that the work in this thesis, without specific reference, is original and has not been submitted in part or whole for any other award/degree in this or any other university.

This majority of work in this thesis is comprised from 3 first author (2 in prep.) and 1 second author publications. Chapter 2 is based on the work of Bowdalo et al. (2016b) and Sofen et al. (2016), Chapters 3 and 4 are both derived from Bowdalo et al. (2016a) and Chapter 5 is based on Bowdalo and Evans (2016).

Dene Bowdalo
September 2016

# Chapter 1

# Introduction

## 1.1 Tropospheric ozone: an air pollutant and greenhouse gas

Ozone ($O_3$) at the surface is a pollutant, harmful to both human and plant health (WHO, 2005; Fowler et al., 2009). It is the dominant source of the hydroxyl radical (OH) (Levy, 1971), which controls the concentration of key climate gases ($CH_4$, HCFCs etc.) and is an important climate gas in its own right (Myhre et al., 2013).

Large quantities of inhaled $O_3$ can bring about respiratory damage in humans, being strongly associated with premature mortality (Gryparis et al., 2004; Bell et al., 2006). $O_3$ is a strong oxidant, meaning that inhalation results in significant inflammation of the respiratory tract, shown in controlled human exposure studies even at background levels of $O_3$. The World Health Organisation (WHO) found $O_3$ imparts only short-term effects on mortality and morbidity (WHO, 2005). However, in recent years several new studies have shown associations between long term exposure to $O_3$ and mortality (Jerrett et al., 2009; Krewski et al., 2009). $O_3$ is estimated to be the cause of 5–20 % of deaths attributable to air pollution (Anenberg et al., 2009; Lim et al., 2012; Silva et al., 2013). The Organisation for Economic Co-operation and Development (OECD) suggest that without new air quality legislation, by 2050, air pollution will be the world‘s greatest environmental cause of premature mortality (OECD, 2012).

$O_3$ is also hugely damaging to ecosystems. $O_3$ primarily damages plants via stomatal uptake and subsequent reaction with plant tissues, significantly disrupting the plant's physiological processes (Fowler et al., 2009; Matyssek et al., 2008, 2010). $O_3$ also reacts with leaf cuticles and other external plant surfaces. The major effects of $O_3$ on plants are: stunted growth, lower functional leaf area and reduced seed production. Studies have shown that the most important global food crops (i.e. wheat, rice, maize) are “sensitive or moderately sensitive" to $O_3$ (Mills et al., 2007), and that the global crop production losses associated with $O_3$ total 79–121 million tonnes, worth 11–18 billion USD annually (Avnery et al., 2011). Reduced carbon sequestration by forests associated with damage by $O_3$ has been estimated to impart a significant indirect radiative forcing (RF) on climate (Sitch et al., 2007). In a warming climate, extreme weather events are set to increase (Fuhrer, 2009). There is also growing evidence that $O_3$ reduces the sensitivity of plants

to drought (Wilkinson and Davies, 2010), thus amplifying the impacts of these extreme weather events.

The Intergovernmental Panel on Climate Change (IPCC), in their fifth assessment report, found tropospheric $O_3$ produced a global average radiative forcing (RF) of $+0.40 \pm 0.2\,\mathrm{W\,m^{-2}}$ between 1750 and 2010 (Myhre et al., 2013). $O_3$'s RF impact is much more spatially variable than well-mixed greenhouse gases (GHGs) (e.g. carbon dioxide, $CO_2$), with industrialisation driving the major changes in $O_3$ spatially since 1750. Anthropogenic increases in the emissions of $O_3$'s main precursors: nitrogen oxides (NOx), carbon monoxide (CO), methane ($CH_4$), and volatile organic compounds (VOCs) have been suggested to be responsible for $44 \pm 12$ % of $O_3$'s 1850–2000 RF (Stevenson et al., 2013), with these precursors also indirectly affecting the lifetime of longer-lived GHGs through the production of the hydroxyl radical (OH). A major source of uncertainty in the estimation of $O_3$'s RF is primarily caused through a lack of confidence in the understanding of $O_3$ in the pre-industrial, with present-day models consistently overestimating surface $O_3$ measurements (thought to be unreliable) in the late 19th century (Cooper et al., 2014).

## 1.2 Tropospheric ozone: sources and sinks

Ozone is a secondary formed species, with numerous potential pathways existing for its production or loss, with a lifetime in the troposphere of approximately 22 days (Stevenson et al., 2006). The following subsections describe in detail the major processes that contribute to its tropospheric concentration. These are photochemistry (Sect. 1.2.1), stratosphere–troposphere exchange (Sect. 1.2.2) and dry deposition (Sect. 1.2.3). We conclude this section with present-day estimates of its global tropospheric budget (Sect. 1.2.4).

### 1.2.1 Photochemistry

The strong tropospheric photochemical production of $O_3$ was first realised in the 1970s upon the discovery of the role of the hydroxyl radical (OH) as the major tropospheric oxidant (Levy, 1971). OH is produced through the following reactions:

$$\mathrm{O_3} + h\nu\,(\lambda < 320\mathrm{nm}) \longrightarrow \mathrm{O_2} + \mathrm{O(^1D)} \tag{R1.1}$$

$$\mathrm{O(^1D)} + \mathrm{H_2O} \longrightarrow 2\,\mathrm{OH} \tag{R1.2}$$

After OH's tropospheric importance was found, it was initially thought the production of $\mathrm{O(^1D)}$ (the excited state of atomic oxygen) (R1.1) in the troposphere was negligible due to the absorption of ultraviolet (UV) radiation by stratospheric $O_3$. Therefore it was presumed the quantity of $O_3$ needed to generate tropospheric OH was mainly transported from the stratosphere, the source of which is far too insignificant to maintain tropospheric OH, in which case levels of CO, $CH_4$, etc. would rise to extremely damaging levels from a human health and climate perspective. In actuality, tropospheric production of $\mathrm{O(^1D)}$

(R1.1) takes place at wavelengths less than 320 nm. Despite the tropospheric production of $O(^1D)$ being slow relative to the stratosphere, production of OH (R1.2) is compensated by the much larger quantities of $H_2O$ in the troposphere. Production of OH is highest in the tropics, particularly in the lower to middle troposphere, where there are large abundances of water vapour, and higher incident UV radiation (Logan et al., 1981; Lelieveld et al., 2002).

Carbon monoxide (CO) and methane ($CH_4$) are the major sinks for OH in the troposphere, the reactions with which start chain mechanisms that can lead to significant photochemical production of $O_3$.

### Carbon monoxide

Carbon monoxide (CO) is predominately formed through the incomplete combustion of fossil fuels and biomass, and from the oxidation of $CH_4$ and other VOCs. It is the dominant sink for OH (Duncan et al., 2007) contributing indirectly to climate RF through the subsequent production of $O_3$, enhancing the lifetimes of $CH_4$ and other GHGs (Daniel and Solomon, 1998), and ultimately oxidising to $CO_2$ (Prather, 1996). Cumulatively these indirect forcings sum to a RF of $+0.23$ (0.18 to 0.29) $\mathrm{W\,m^{-2}}$ globally (Myhre et al., 2013). Surface measurements in the northern hemisphere (NH) mid-latitudes as well as by satellites suggest CO concentrations have been declining for the past decade or more (Angelbratt et al., 2011; Warner et al., 2013; Yoon and Pozzer, 2014). CO is relatively long lived ranging from 10 days in summer over continental regions to more than a year over polar regions in winter (Holloway et al., 2000), thus it can be used as a tracer of long-range anthropogenic pollution. Table 1.1 gives best estimates of the present day global tropospheric budget of CO.

Oxidation of CO by OH starts a chain mechanism that can result in catalytic production of $O_3$, dependent on the concentrations of NOx (Levy, 1971; Crutzen, 1973; Logan et al., 1981). CO oxidation by OH firstly rapidly forms the hydroperoxy radical ($HO_2$) (R1.3 and R1.4), with M being used to represent any third body, i.e. $N_2$:

$$\mathrm{CO + OH \longrightarrow CO_2 + H} \tag{R1.3}$$

$$\mathrm{H + O_2 + M \longrightarrow HO_2 + M} \tag{R1.4}$$

$HO_2$ can then follow 2 pathways. It can firstly self-react to produce hydrogen peroxide ($H_2O_2$) (R1.5), which is either quickly lost through wet deposition, oxidised by OH (R1.6), or photolysed (R1.7):

$$\mathrm{HO_2 + HO_2 \longrightarrow H_2O_2 + O_2} \tag{R1.5}$$

$$\mathrm{H_2O_2 + OH \longrightarrow HO_2 + H_2O} \tag{R1.6}$$

$$H_2O_2 + h\nu \longrightarrow 2\,OH \tag{R1.7}$$

Alternatively, $HO_2$ can react with nitric oxide (NO) (R1.8), regenerating OH and producing nitrogen dioxide ($NO_2$), which is rapidly photolysed in the daytime (R1.9), regenerating NO and going on to form $O_3$ (R1.10). Work has also shown other important routes for $HO_2$ loss in the marine boundary layer (MBL). $HO_2$ has been shown to be lost heterogeneously through reaction with aerosols (Sommariva et al., 2004; Whalley et al., 2010); and also through reaction with halogen oxides, leading to catalytic $O_3$ loss (Read et al., 2008; Mahajan et al., 2010; Sherwen et al., 2016).

$$HO_2 + NO \longrightarrow OH + NO_2 \tag{R1.8}$$

$$NO_2 + h\nu \longrightarrow NO + O \tag{R1.9}$$

$$O + O_2 + M \longrightarrow O_3 + M \tag{R1.10}$$

The concentrations of NOx (NO + $NO_2$) are thus critical in determining the chain length of this oxidation mechanism. In a high NOx environment $HO_2$ reacts dominantly with NO (R1.8), with the reactions R1.3 + R1.4 + R1.8 + R1.9 + R1.10 resulting in a molecule of $O_3$ being formed per CO molecule, the net reaction given by R1.11. R1.9 regenerates NO, meaning that no NOx is depleted through this pathway in the daytime. The generated $O_3$ molecule can then photolyse by R1.1 and R1.2 to produce 2 additional OH molecules, which can then go on to further oxidise CO, restarting the cycle, resulting in efficient $O_3$ production until either CO (and other VOCs), NOx or *hv* have been depleted. The production of OH through NOx recycling (R1.8 and R1.9) is particularly key at higher latitudes where OH production by R1.1 and R1.2 is smaller (due to smaller abundances of incoming solar radiation and water vapour), and NOx and $O_3$ concentrations are typically higher (Logan et al., 1981; Lelieveld et al., 2002).

$$net: CO + 2\,O_2 \xrightarrow{h\nu} CO_2 + O_3 \tag{R1.11}$$

In an atmosphere with little or no NOx, the reaction chain is terminated through the loss of HOx (H + OH + $HO_2$ + other peroxy radicals: $CH_3O_2$, $RO_2$), through the self-reaction of $HO_2$ (R1.5), resulting in no $O_3$ being formed. The reaction chain is limited to R1.3 + R1.4 + R1.5 + R1.6 + R1.7, the net reaction being:

$$net: CO + H_2O_2 \xrightarrow{h\nu} CO_2 + H_2O \tag{R1.12}$$

| | **Amount (Tg CO/yr)** | **References** |
|---|---|---|
| **Sources** | **1909–3362** | |
| $CH_4$ Oxidation | 578–999 | *Prather et al. (2001); Shindell et al. (2006)* |
| Other VOC Oxidation | 430–1198 | *Prather et al. (2001); Shindell et al. (2006); Duncan et al. (2007)* |
| Fossil Fuel Combustion | 494–611 | *Schultz et al. (2007); Lamarque et al. (2010); Janssens-Maenhout et al. (2010); Granier et al. (2011)* |
| Biomass Burning | 277–416 | *van der Werf et al. (2006, 2010); Kaiser et al. (2012)* |
| Biogenic | 76–84 | *Guenther et al. (2006); Sindelarova et al. (2014)* |
| Oceanic | 54 | *Aumont and Bopp (2006)* |
| **Sinks** | **1615–3340** | |
| Oxidation by OH | 1500–2700 | *Prather et al. (2001); Duncan et al. (2007)* |
| Dry Deposition | 115–640 | *Sanhueza et al. (1998); King (1999); Prather et al. (2001)* |

Table 1.1 Estimates of present day global annual tropospheric CO sources and sinks.

## Methane

Methane ($CH_4$) is a well-mixed GHG, the second most important GHG (after $CO_2$), with a RF of $+0.48 \pm 0.05\,W\,m^{-2}$, 28 times more efficient per mass as a GHG than $CO_2$ over a 100 year period (Myhre et al., 2013). $CH_4$ also imposes an indirect RF of $+0.49 \pm 0.12\,W\,m^{-2}$ through the production of $O_3$ and stratospheric water vapour and ultimate oxidation to $CO_2$. Atmospheric concentrations of $CH_4$ have increased significantly since the pre-industrial, from approximately $722 \pm 4$ ppbv in 1750 to $1803.2 \pm 0.7$ ppbv in 2011 (approximate 2.5 times increase) (Etheridge et al., 1998; Dlugokencky et al., 2005), with increases in anthropogenic emissions primarily driving this increase (Dlugokencky et al., 2011). Current concentrations are greater than at any time over the last 800,000 years (Loulergue et al., 2008). $CH_4$ is released predominately from natural wetland emissions, and from anthropogenic emissions associated with agriculture and waste. $CH_4$ is lost predominately through OH oxidation, this mechanism controlling its atmospheric lifetime (9–10 years) (Dlugokencky et al., 2003; Bruhwiler et al., 2014). $CH_4$ concentrations are sensitive to future climate change, as Arctic natural wetland emissions could potentially increase significantly with increasing temperatures thawing the large stores of soil carbon (Schuur and Abbott, 2011; Harden et al., 2012). Table 1.2 gives best estimates of the present day global tropospheric budget of $CH_4$.

$CH_4$ oxidation follows roughly the same blueprint as CO oxidation, also providing a mechanism for catalytic $O_3$ production, albeit with significantly more steps. The methylperoxy radical ($CH_3O_2$), homologous to $HO_2$, is quickly produced through oxidation by OH (R1.13 and R1.14):

$$CH_4 + OH \longrightarrow CH_3 + H_2O \tag{R1.13}$$

$$CH_3 + O_2 + M \longrightarrow CH_3O_2 + M \tag{R1.14}$$

$CH_3O_2$ can then follow 2 pathways. It can firstly react with $HO_2$ (R1.15), producing methylhydroperoxide ($CH_3OOH$). $CH_3OOH$ is then lost through photolysis (R1.18) or oxidised by OH (through two branches) (R1.16 and R1.17):

$$CH_3O_2 + HO_2 \longrightarrow CH_3OOH + O_2 \tag{R1.15}$$

$$CH_3OOH + OH \longrightarrow CH_2O + OH + H_2O \tag{R1.16}$$

$$CH_3OOH + OH \longrightarrow CH_3O_2 + H_2O \tag{R1.17}$$

$$CH_3OOH + h\nu \longrightarrow CH_3O + OH \tag{R1.18}$$

$CH_3O_2$ can otherwise react with NO, producing $CH_3O$ and $NO_2$ (R1.19):

$$CH_3O_2 + NO \longrightarrow CH_3O + NO_2 \quad \text{(R1.19)}$$

The methoxy radical ($CH_3O$), formed by R1.18 and R1.19, then rapidly reacts with $O_2$:

$$CH_3O + O_2 \longrightarrow CH_2O + HO_2 \quad \text{(R1.20)}$$

Formaldehyde ($CH_2O$), formed by R1.16 and R1.20, can be oxidised by OH (R1.21) or photolysed (two branches) (R1.22 and R1.23):

$$CH_2O + OH \longrightarrow CHO + H_2O \quad \text{(R1.21)}$$

$$CH_2O + h\nu \xrightarrow{O_2} CHO + HO_2 \quad \text{(R1.22)}$$

$$CH_2O + h\nu \longrightarrow CO + H_2 \quad \text{(R1.23)}$$

The CHO radical, formed by R1.21 and R1.22, then quickly reacts with $O_2$:

$$CHO + O_2 \longrightarrow CO + HO_2 \quad \text{(R1.24)}$$

The net result of the $CH_4$ oxidation mechanism is again dependent on the levels of NOx. In a high NOx environment, $CH_4$ oxidation provides a mechanism to drive greater $O_3$ production per molecule, than through CO oxidation, with the potential production of $HO_2$ (R1.20, R1.22, R1.24), $NO_2$ (R1.19) and CO (R1.23, R1.24), all of which can go on to form $O_3$. In an high NOx regime, $CH_3O_2$ reacts dominantly with NO (R1.19). Taking $CH_2O$ to react solely by R1.22 provides the optimal pathway for $O_3$ production, the chain being R1.13 + R1.14 + R1.19 + R1.20 + R1.22 + R1.24. The net direct $CH_4$ oxidation reaction being:

$$net: CH_4 + 4\,O_2 + NO + OH \xrightarrow{h\nu} CO + 3\,HO_2 + NO_2 + H_2O \quad \text{(R1.25)}$$

The resultant $3\,HO_2$, $NO_2$ and CO molecules can then each react additionally. Taking $HO_2$ to react solely with NO in a high NOx environment (R1.8) generates a net total of 5 $O_3$ molecules and 2 additional OH molecules per $CH_4$ molecule. The final net reaction given by:

$$net: CH_4 + 10\,O_2 \xrightarrow{h\nu} CO_2 + 5\,O_3 + 2\,OH + H_2O \quad \text{(R1.26)}$$

In an atmosphere with little NOx, $CH_3O_2$ would react dominantly with $HO_2$ (R1.15). Taking $CH_3OOH$ and $CH_2O$ to react by R1.16 and R1.21 respectively, gives the worst case mechanism for $O_3$ production, the chain being R1.13 + R1.14 + R1.15 + R1.16 + R1.21 + R1.24. The net direct $CH_4$ oxidation reaction being:

$$net : CH_4 + O_2 + 2\,OH \longrightarrow CO + 3\,H_2O \tag{R1.27}$$

The resultant CO molecule reacts again, resulting in the net products of $CO_2$ and $H_2O$ in a low NOx environment (R1.12). The total net reaction (R1.28) thus results in no $O_3$ production and 2 HOx molecules being lost per $CH_4$ molecule:

$$net : CH_4 + O_2 + H_2O_2 + 2\,OH \xrightarrow{h\nu} CO_2 + 4\,H_2O \tag{R1.28}$$

| | **Amount (Tg $CH_4$/yr)** | **Reference** |
|---|---|---|
| **Sources – Total** | **344–787** | |
| **Sources – Natural** | **123–285** | |
| Wetlands | 100–231 | *Bousquet et al. (2006); Forster et al. (2007); Melton et al. (2013)* |
| Termites | 19–29 | *Bousquet et al. (2006); Forster et al. (2007)* |
| Oceanic | 4–25 | *Lambert and Schmidt (1993); Houweling et al. (1999); Bousquet et al. (2006); Forster et al. (2007)* |
| **Sources – Anthropogenic** | **221–502** | |
| Natural Gas | 50–72 | *Bousquet et al. (2006); Crippa et al. (2016)* |
| Coal Deposits | 20–57 | *Bousquet et al. (2006); Crippa et al. (2016)* |
| Enteric fermentation | 76–104 | *Bousquet et al. (2006); Forster et al. (2007)* |
| Rice Agriculture | 26–112 | *Bousquet et al. (2006); Forster et al. (2007)* |
| Biomass Burning | 14–88 | *Bousquet et al. (2006); Forster et al. (2007); van der Werf et al. (2010)* |
| Waste | 35–69 | *Bousquet et al. (2006); Forster et al. (2007)* |
| **Sinks** | **476–596** | |
| Oxidation by OH | 428–511 | *Lelieveld et al. (1998); Bousquet et al. (2006); Forster et al. (2007)* |
| Transport to Stratosphere | 30–45 | *Bousquet et al. (2006); Forster et al. (2007)* |
| Soils | 18–40 | *Ridgwell et al. (1999); Bousquet et al. (2006); Forster et al. (2007)* |

Table 1.2 Estimates of present day global annual tropospheric $CH_4$ sources and sinks.

### Non–methane volatile organic compounds

Tens of thousands of non–methane volatile organic compounds (NMVOCs) in the atmosphere have been measured, with potentially hundreds of thousands more yet to be (Goldstein and Galbally, 2007). NMVOCs provide an indirect radiative forcing of +0.10 (0.06 to 0.14) $\mathrm{W\,m^{-2}}$ through the production of $O_3$, $CH_4$ and $CO_2$ (Myhre et al., 2013). An additional indirect RF comes from the formation of secondary organic aerosols (SOA) (Hoffmann et al., 1997; van Donkelaar et al., 2007), the net effect of which is currently not well restrained: $-0.03$ ($-0.27$ to $+0.20$) $\mathrm{W\,m^{-2}}$. NMVOCs also indirectly increase atmospheric acidity through oxidation to organic acids (Schultz et al., 2015). Biogenic VOC (BVOC) emissions contribute $\sim 90\,\%$ of total NMVOC emissions (Guenther et al., 1995), with a total global BVOC flux of approximately 1000 Tg C/yr (Guenther et al., 2012), in comparison with the 50–100 Tg C/yr from anthropogenic origin (Holzke et al., 2006), from sources such as combustion, oil and gas extraction, fuel evaporation etc. Emissions of BVOCs are dominantly from the tropics ($> 70\,\%$) (Karl et al., 2007), an area where measurements are extremely limited. The most abundant BVOCs are isoprene ($C_5H_8$) (53 %), monoterpenes (16 %) and methanol (10 %) (Guenther et al., 2012). $C_5H_8$ emissions increase strongly as a function of temperature and sunlight, with a summer peak in northern mid-latitudes (Guenther et al., 2006). BVOCs are generally highly reactive, but have a wide range of atmospheric lifetimes ranging from minutes to days ($\sim$ 1 hour for $C_5H_8$) (Atkinson and Arey, 2003).

NMVOC oxidation follows a similar chain mechanism as $CH_4$ and CO, providing another mechanism for significant $O_3$ production, however the existence of thousands of different NMVOCs provides significant chemical complexity. The organic peroxy radical ($RO_2$) is homologous to $HO_2$ and $CH_3O_2$, formed through oxidation of a NMVOC species (RH) by OH (R1.29 and R1.30) (with R representing an organic group, i.e. $CH_3$):

$$\mathrm{RH + OH \longrightarrow R + H_2O} \tag{R1.29}$$

$$\mathrm{R + O_2 + M \longrightarrow RO_2 + M} \tag{R1.30}$$

$RO_2$ can then broadly follow 2 different pathways, representing a significant branching point in the oxidation mechanism (Orlando and Tyndall, 2012), with the subsequent chemistry not currently well constrained (Fisher et al., 2016). In a low NOx atmosphere, $RO_2$ dominantly self-reacts or reacts with other peroxy radicals (mainly $HO_2$) producing a peroxide (R′OOH or ROOR′, with the prime indicating that the organic group R may differ from the previous reaction) (i.e. R1.31). $RO_2$ can also be transformed in low amounts through isomerisation (Peeters et al., 2009; Peeters and Müller, 2010). R′OOH/ROOR′ is rapidly lost through wet deposition, terminating HOx (Jacob and Wofsy, 1988). However, observations from numerous field campaigns do not show such a loss (Tan et al., 2001; Stone et al., 2010; Whalley et al., 2011). It has been suggested that this discrepancy can be explained by OH regeneration through the oxidation of epoxydiols (formed from the oxidation of ISOPOOH) (Paulot et al., 2009b), fast isomerisation of $ISOPO_2$ (Peeters et al.,

2009; Peeters and Müller, 2010; Wolfe et al., 2012), or measurement bias (Mao et al., 2012).

$$RO_2 + HO_2 \longrightarrow R'OOH + O_2 \quad \text{(R1.31)}$$

In a high NOx atmosphere, $RO_2$ reacts dominantly with NO, through 2 branches. The major pathway produces $NO_2$ and an organic oxy radical (RO) (R1.32), promoting $O_3$ formation (Paulot et al., 2009a), whereas the minor pathway leads to organic nitrate formation ($RONO_2$) (R1.33), typically thought to terminate both HOx and NOx chains (Ito et al., 2009; Paulot et al., 2012). However, $C_5H_8$ nitrates have been found to be partly recycled back to NOx upon further oxidation, leading to confusion over whether this reaction pathway acts as a sink or reservoir of NOx (Ito et al., 2009; Paulot et al., 2009a, 2012). Additionally, organic nitrates have been found to be significantly produced via nighttime oxidation of $C_5H_8$ by the nitrate radical ($NO_3$) (Rollins et al., 2009; Xie et al., 2013), degrading into stable forms over a few hours, also forming SOA (Rollins et al., 2009; Marais et al., 2016). These organic nitrates have also been found to provide a mechanism for significant long-range transport of NOx (Mao et al., 2013).

$$RO_2 + NO \longrightarrow RO + NO_2 \quad \text{(R1.32)}$$

$$RO_2 + NO \longrightarrow RONO_2 \quad \text{(R1.33)}$$

$RO_2$ can also react with $NO_2$, forming peroxynitrates ($RO_2NO_2$) (R1.34). These are typically thermally unstable, decomposing back to NOx in $\sim$ minutes, with the exception of peroxyacetylnitrates (PAN) (Singh and Hanst, 1981).

$$RO_2 + NO_2 + M \longleftrightarrow RO_2NO_2 + M \quad \text{(R1.34)}$$

RO (formed by R1.32) is quickly lost through reaction with $O_2$ (R1.35), regenerating HOx and forming a carbonyl compound ($R'CHO$). RO can also be quickly lost through isomerisation or thermal decomposition.

$$RO + O_2 \longrightarrow R'CHO + HO_2 \quad \text{(R1.35)}$$

As with the CO and $CH_4$ oxidation mechanisms, the concentrations of NOx are critical in determining the net products. However, the significant complexities that exist throughout the mechanism make it challenging to constrain. The yields of the multiple reactions in the mechanism branches all need to quantified, however the underlying chemistry is variable between the many thousands of NMVOCs, significantly complicating this task. Taking a simplistic approach, in an atmosphere with high NOx, it can be assumed $RO_2$ in the daytime will react dominantly with NOx. Assuming the mechanism follows the major pathway after $RO_2$ reacts with NO (R1.32), the reaction chain is as follows: R1.29 + R1.30 + R1.32 + R1.35, with the net direct reaction being:

$$net: \mathrm{RH} + 2\,\mathrm{O_2} + \mathrm{NO} + \mathrm{OH} \longrightarrow \mathrm{R'CHO} + \mathrm{NO_2} + \mathrm{HO_2} + \mathrm{H_2O} \quad \text{(R1.36)}$$

Then taking the resultant $HO_2$ and $NO_2$ to additionally react, again via high the NOx pathway (R1.8 and R1.9) generates a net total of 2 $O_3$ molecules per NMVOC molecule. The final net reaction being:

$$net: \mathrm{RH} + 4\,\mathrm{O_2} \xrightarrow{hv} \mathrm{R'CHO} + 2\,\mathrm{O_3} + \mathrm{H_2O} \quad \text{(R1.37)}$$

In an atmosphere devoid of NOx, $RO_2$ will be lost dominantly though self-reaction of reaction with other peroxy radicals (R1.31), limiting the reaction chain to R1.29 + R1.30 + R1.31, producing no $O_3$, (assuming no OH is regenerated from R′OOH/ROOR′):

$$net: \mathrm{RH} + \mathrm{HO_2} + \mathrm{OH} \longrightarrow \mathrm{R'OOH} + \mathrm{H_2O} \quad \text{(R1.38)}$$

### Nitrogen oxides

NOx (nitric oxide NO + nitrogen dioxide $NO_2$), as described previously, is often the key limiting species in controlling the rate of daytime $O_3$ formation, thus indirectly affecting the abundance of OH, via R1.1 and R1.2. From a climate perspective, NOx imposes a global indirect positive RF through $O_3$ production and an indirect negative RF through the reduction of the $CH_4$ lifetime (via enhanced OH production) and through nitrate aerosol formation, with an estimated net negative RF of $-0.15$ ($-0.34$ to $+0.02$) $\mathrm{W\,m^{-2}}$. Long-term $NO_2$ exposure has been associated with reduced respiratory function (Ackermann-Liebrich et al., 1997; Gauderman et al., 2000, 2002). NOx has both anthropogenic and natural sources. Anthropogenic sources come from the high temperature combustion of fossil fuels and biofuels from transport, industry and power plants, as well as biomass burning. Natural sources of NOx include soil and lightning emissions. It is predominantly lost through deposition (as nitric acid, $HNO_3$). Successful implementation of air quality legislation in Europe and North America has led to decreasing NOx emissions in these areas over the last few decades (Vestreng et al., 2009; Tørseth et al., 2012; Lamsal et al., 2015; Schneider et al., 2015), however NOx emissions are significantly increasing in rapidly developing regions (i.e. Asia) (Zhang et al., 2007; Tanimoto et al., 2009; Schneider et al., 2015). Table 1.3 gives best estimates of the present day global tropospheric sources of NOx.

NOx is referred to collectively due to the rapid interconversion between NO and $NO_2$ in the daytime, given by the reactions R1.39, R1.9 and R1.10:

$$\mathrm{NO} + \mathrm{O_3} \longrightarrow \mathrm{NO_2} + \mathrm{O_2} \quad \text{(R1.39)}$$

$$\mathrm{NO_2} + hv \longrightarrow \mathrm{NO} + \mathrm{O} \quad \text{(R1.9)}$$

$$\mathrm{O} + \mathrm{O_2} + \mathrm{M} \longrightarrow \mathrm{O_3} + \mathrm{M} \quad \text{(R1.10)}$$

NOx is present as $NO_2$ at night, as a result of R1.39. This reaction is also responsible for significant titration of $O_3$ in high NOx environments. Recent work has shown $NO_2$ may be converted to nitrous acid (HONO) by gas-phase or aerosol-phase mechanisms (R1.40), providing a potential new catalytic sink for $O_3$ when $NO_2$ is generated via R1.39, and also providing an additional source of HOx through photolysis of HONO (R1.41) (Li et al., 2014).

$$NO_2 \longrightarrow HONO\,(\text{via various reactions}) \tag{R1.40}$$

$$HONO + h\nu \longrightarrow NO + OH \tag{R1.41}$$

In the daytime, NOx is primarily lost through oxidation to nitric acid $HNO_3$ (R1.42). $HNO_3$ is extremely soluble, quickly lost through wet and dry deposition, often causing significant acidic damage to ecosystems in the process (Townsend and Howarth, 2010). NOx has a lifetime of hours to days in the troposphere (Lamsal et al., 2010).

$$NO_2 + OH + M \longrightarrow HNO_3 + M \tag{R1.42}$$

At night, the nitrate radical ($NO_3$) and its reservoir species, dinitrogen pentoxide ($N_2O_5$), become the abundant nitrogen species (by R1.43 and R1.44), ultimately also being lost through $HNO_3$ (R1.45).

$$NO_2 + O_3 \longrightarrow NO_3 + O_2 \tag{R1.43}$$

$$NO_3 + NO_2 + M \longrightarrow N_2O_5 + M \tag{R1.44}$$

$$N_2O_5 + H_2O \xrightarrow{\text{aerosol}} 2\,HNO_3 \tag{R1.45}$$

Organic nitrates and peroxyacetylnitrates (PAN), both formed through NMVOC oxidation (R1.33 and R1.34), provide reservoirs for the long-range transport of NOx. These species can therefore pose significant air quality issues, with NOx able to contribute to $O_3$ production in areas far from where it was emitted. PAN is an effective reservoir for NOx due to the strong dependence of its lifetime on temperature, therefore it is able to be transported over large distances at high altitudes, before thermal decomposition when it lowers in height. (Singh and Hanst, 1981; Fischer et al., 2014).

| | Amount (Tg N/yr) | Reference |
|---|---|---|
| **Sources – Total** | **46.2–60.12** | |
| **Sources – Anthropogenic** | **35.2–35.32** | |
| Industry and Surface Transport | 20.9 | *Lamsal et al. (2011)* |
| Biomass Burning | 9.43–9.53 | *van der Werf et al. (2010); Kaiser et al. (2012)* |
| Biofuels | 2.2 | *Yevich and Logan (2003)* |
| Aircraft | 2.67–2.69 | *Roof et al. (2007); Simone (2013)* |
| **Sources – Natural** | **11–24.8** | |
| Soils | 9–16.8 | *Hudman et al. (2012); Vinken et al. (2014)* |
| Lightning | 2–8 | *Schumann and Huntrieser (2007)* |

Table 1.3 Estimates of present day global annual tropospheric NOx sources.

### Summary of photochemistry

The plethora of pathways that exist for $O_3$ production and loss ensures we must turn to numerical models when trying to understand the full remit of the chemistry. Accurate representation of the range of chemical pathways and reaction yields is necessary, making the simulation of $O_3$ in chemical models an ongoing challenge, with NMVOC oxidation in particular an active area of research. Total global annual $O_3$ chemical production is estimated to be in the range of 3877–5989 Tg $O_3$/yr, and chemical loss in the range of 3638–5089 Tg $O_3$/yr (Young et al., 2013).

As a general summary, photochemical $O_3$ production in the troposphere is controlled by the availability of CO, $CH_4$, NMVOCs and NOx in the presence of appropriately energetic photons. $O_3$ production is initiated by the production of OH. This allows rapid oxidation of CO, $CH_4$, NMVOCs (grouped as VOC for simplicity), forming peroxy radicals ($HO_2$, $CH_3O_2$, $RO_2$), which allow NO to be converted to $NO_2$, which can then be photolysed, producing $O_3$.

The fate of the peroxy radicals is essentially hinged, dependent on the concentrations of NOx. In a high NOx environment, the peroxy radicals quickly react with NO. Critically, no NOx or HOx is lost through this route, meaning production of $O_3$ can continue catalytically until VOCs or appropriate photons are depleted. In a high NOx regime, for every $CH_4$ molecule, 5 $O_3$ molecules and 2 HOx molecules are formed, significantly increasing the oxidative capacity of the atmosphere. For every NMVOC molecule 2 $O_3$ molecules are formed and for every CO molecule 1 $O_3$ molecule is formed. In a low NOx environment,

the peroxy radicals are predominantly lost through self-reaction, forming no $O_3$ and also terminating HOx.

The concentrations of NOx in the atmosphere are not binary however, and subsequently the rate of $O_3$ production is not either. Kleinman (2005) derives a formula for the tropospheric rate of $O_3$ production ($P(O_3)$), as a power law function of the OH production rate ($Q$), NOx concentration, and a measure of VOC–OH reactivity ($VOC_R$), defined as $\sum k[\text{VOCs}]$, where $k$'s are the rate constants of the VOC–OH reactions. The sensitivity of $P(O_3)$ to each of these variables is assessed as a function of $L_N/Q$, where $L_N$ is the OH removal rate through reaction with NOx. $L_N/Q$ therefore represents the fraction of OH removed by reaction with NOx, providing a robust measure of the severity of a NOx regime. The sensitivity of $P(O_3)$ to each of these variables, as a function of $L_N/Q$, is given graphically by Fig. 1.1.

With increasing $L_N/Q$, $P(O_3)$ is increasingly positively dependent on the OH production rate ($Q$). The sensitivity of $P(O_3)$ to the NOx concentration decreases non-linearly as a function of $L_N/Q$, also changing in sign, going from a maximum positive sensitivity where $L_N/Q = 0\,\%$ (1), to a maximum negative sensitivity where $L_N/Q = 100\,\%$ (-1). The sensitivity of $P(O_3)$ to VOC–OH reactivity ($VOC_R$) is increasingly positively dependent, increasing non-linearly from a negligible effect where $L_N/Q = 0\,\%$ (0), to a maximum positive sensitivity where $L_N/Q = 100\,\%$ (1). There is a crossover between NOx and VOC limiting conditions for $O_3$ production where $L_N/Q = 50\,\%$. Above where $L_N/Q = 66.6\,\%$, the sensitivity of $P(O_3)$ to NOx flips in sign, i.e. enhanced NOx reduces $O_3$ production.

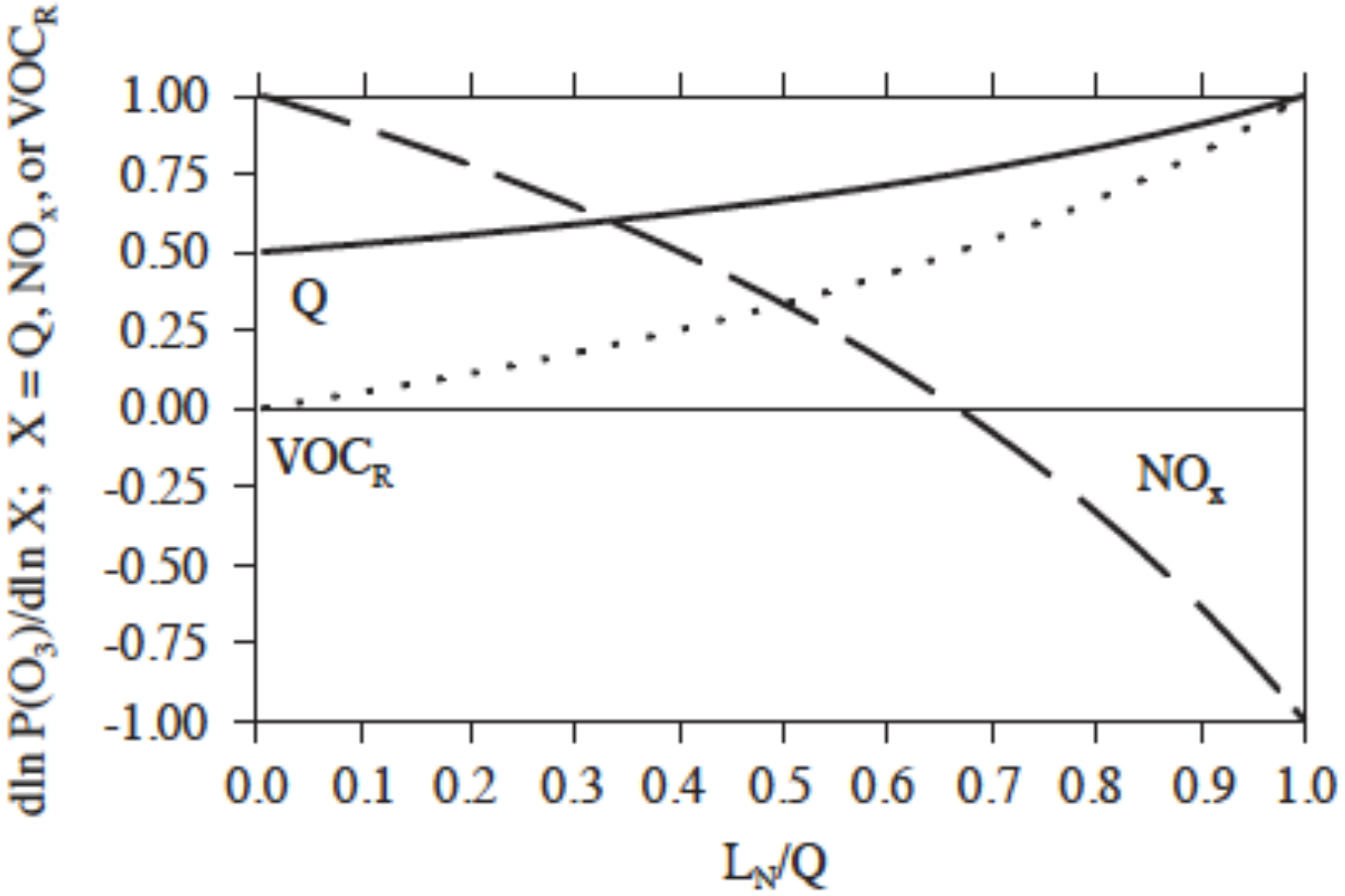


Fig. 1.1 Sensitivity of the rate of $O_3$ production ($P(O_3)$) to the OH production rate ($Q$), NOx concentration and VOC–OH reactivity ($VOC_R$). Given as a function of the fraction of OH removed by NOx ($L_N/Q$). Figure from Kleinman (2005).

### 1.2.2 Stratosphere–troposphere exchange

Stratospheric $O_3$ production far exceeds that of the troposphere, due to the availability of high energy photons. This is a result of chemistry termed the Chapman mechanism (derived in the 1920's), which also results in the stratospheric $O_3$ layer. $O_2$ is first photolysed by photons with wavelengths less than 242 nm (available in greater quantities with increasing altitude), yielding 2 O atoms (R1.46). O then rapidly reacts with $O_2$, forming $O_3$ (R1.47):

$$O_2 + h\nu\,(\lambda < 242\text{nm}) \longrightarrow O + O \tag{R1.46}$$

$$O_2 + O + M \longrightarrow O_3 + M \tag{R1.47}$$

$O_3$ is also lost through photolysis, just as it is in the troposphere, with lower energy photons needed to photo-disassociate $O_3$ than for $O_2$ ($< 320$ nm), forming $O_2$ and $O(^1D)$ (R1.1). $O(^1D)$ is then rapidly stabilised through collision with a third body (R1.48):

$$O_3 + h\nu\,(\lambda < 320\text{nm}) \longrightarrow O_2 + O(^1D) \tag{R1.1}$$

$$O(^1D) + M \longrightarrow O + M \tag{R1.48}$$

$O_3$ may also react with O, forming $2\,O_2$ (R1.49):

$$O_3 + O \longrightarrow 2\,O_2 \tag{R1.49}$$

The rates of the R1.47 and R1.1 reactions have been found to significantly exceed those of R1.46 and R1.49. Therefore, R1.47 and R1.1 rapidly cycle O and $O_3$, which can be thought of as a single species, termed odd oxygen ($Ox = O + O_3$). Under steady state, the rate of R1.46 can be shown to be equivalent to that of R1.49, thus the steady state Ox concentration can be represented as:

$$[Ox] = \sqrt{J_{O2}[O_2]/k_{49}}, \tag{1.1}$$

where $J_{O2}$ is the photolysis rate constant of R1.46, and $k_{49}$ the reaction rate constant of R1.49. More than 99 % of Ox is $O_3$, therefore local stratospheric $O_3$ concentrations are proportional to the square root of the $O_2$ photolysis rate. Stratospheric $O_3$ production is thus highest where the incoming solar radiation is greatest, over the equator, increasing with altitude. The highest $O_3$ concentrations in the stratosphere however do not coincide with the areas of greatest production. This is due to the global mass circulation of air polewards in the stratosphere, before descent in the mid-high latitudes, termed Brewer–Dobson circulation (Butchart, 2014). The highest $O_3$ concentrations are found in the NH mid-latitudes of the lower stratosphere.

Although the Chapman mechanism captures the general profile of the $O_3$ layer, the mechanism overestimates actual stratospheric $O_3$ concentrations by a factor of 2. Addi-

tional $O_3$ is lost catalytically through cycles involving NOx, HOx, ClOx and BrOx (Farman et al., 1985).

Stratosphere–troposphere exchange of $O_3$ (STE) provides a net source of $O_3$ into the troposphere. The processes driving this transport have been traditionally thought to be associated with the jet stream (Newell, 1963), tropopause folds (Danielsen, 1968) and Brewer–Dobson circulation (Holton et al., 1995; Butchart, 2014). Mid-latitude deep convection has recently been shown to significantly contribute also, with convection penetrating the lowermost stratosphere shown to increase the NH peak STE flux by 19 % (Hegglin et al., 2004; Tang et al., 2011). The total global annual flux is estimated to be in the range of 401–663 Tg $O_3$/yr (Young et al., 2013). This flux however significantly varies by year. Hsu and Prather (2009) find significant interannual variability in STE, of approximately 10 % between 2001 and 2005, suggested to be driven predominantly by meteorology (Voulgarakis et al., 2010; Hess and Zbinden, 2013). Hegglin and Shepherd (2009) suggest there has been a linear increase of the STE flux in the NH, by approximately 2 % per decade since 1970. STE also varies seasonally, with a NH peak flux in May and minimum in November, with seasonality most evident in the mid-latitudes (Hsu and Prather, 2009). This peak can be shifted to June through deep convection events (Tang et al., 2011).

Estimates of the contribution of STE to $O_3$ concentrations at the surface vary significantly by study, and also by the sites considered (i.e. different altitudes and regions). Hess and Zbinden (2013) find only 1–5 ppbv of $O_3$ for sites near sea-level is of stratospheric origin. Lamarque et al. (2005) finds the stratospheric monthly mean contribution to surface $O_3$ concentrations, over a range of sites in the mid-latitudes and tropics in both hemispheres, is always less than 5 ppbv, in all seasons. Whereas, Lin et al. (2012) find STE to elevate the median surface $O_3$ concentrations significantly in the USA springtime, by 10–22 ppbv in the high average altitude west, 8–13 ppbv in the north-east, and 3–8 ppbv in the south-east. Ordóñez et al. (2007) find very high correlations between concentrations of $O_3$ at high alpine sites over Europe and lower stratospheric ozone, particularly in the winter–spring.

### 1.2.3 Dry deposition

Aside from chemical loss, the only other significant loss mechanism for $O_3$ is deposition at the surface. $O_3$ is transported to the surface through atmospheric turbulence, where upon contact with the surface it can be deposited readily through various routes. The deposition flux of a species to the surface is assumed to be proportional to the concentration of the species near the surface, with the proportional constant termed the dry deposition velocity (Wesely and Hicks, 2000). The global annual dry deposition flux of $O_3$ is poorly constrained, estimated to provide a flux in the range of 687–1350 Tg $O_3$/yr (Young et al., 2013).

30–90 % of $O_3$ dry deposition is estimated to occur via the plant stomata (Fowler et al., 2001; Cieslik, 2004; Fowler et al., 2009). Plants open their stomata in the daytime to uptake $CO_2$ for photosynthesis, this process allowing other gases to be uptaken also (Farquhar et al., 1980). Non-stomatal uptake is the reaction of $O_3$ with external vegetation surfaces,

with this flux shown to increase with increasing surface temperature (Rondón et al., 1993; Fowler et al., 2001). $O_3$ can additionally be lost through in-canopy chemistry (Kurpius and Goldstein, 2003), and deposition over the oceans, which despite the low solubility of $O_3$ in water, is responsible for approximately 40 % of the global annual $O_3$ dry deposition flux (Hardacre et al., 2015).

### 1.2.4 Tropospheric ozone budget

The global annual tropospheric budget of $O_3$ thus comprises of 4 terms, sources from chemical production and stratosphere–troposphere exchange, and sinks from chemical destruction and dry deposition. The sizeable scale and complexity of $O_3$'s tropospheric influence makes it relatively impossible to constrain the magnitude of these terms using solely observations. The most appropriate tools for estimating the magnitude of the different terms are numerical models, either online – earth system models (ESMs), or offline – chemistry transport models (CTMs). A number of global collaborative projects have undertaken extensive evaulations of tropospheric $O_3$. These include: Atmospheric Composition Change: the European Network of excellence (ACCENT) (Dentener et al., 2006; Stevenson et al., 2006) and Atmospheric Chemistry and Climate Model Intercomparison Project (ACCMIP) (Lamarque et al., 2013; Young et al., 2013). Both projects use a number of global models (26 and 15 respectively), with a wide range of horizontal and vertical resolutions, chemical mechanisms and dynamics, to evaluate the state of current understanding for tropospheric $O_3$. The average and range of the multi-model estimates for each tropospheric $O_3$ budget term, by project, are summarised in Table 1.4.

Chemical production and loss dominates the budget in all models, with chemical production contributing 90 % and 91 % of the average total source across the ACCENT and ACCMIP models respectively, and chemical loss contributing 82 % and 80 % of the average total sink. In general, all budget terms are poorly constrained, with ranges of approximately 4000 Tg $O_3$/yr and 2000 Tg $O_3$/yr on both the total sources and sinks across the ACCENT and ACCMIP models respectively. Wu et al. (2007) find that 74 % of the variance in $O_3$ production across a range of models can be explained by linear dependences on NOx emissions, NMVOC emissions, and STE.

| | **ACCENT Mean (± range) Tg $O_3$/yr** | **ACCMIP Mean (± range) Tg $O_3$/yr** |
|---|---|---|
| **Sources** | **5662 (4073–7850)** | **5354 (4278–6465)** |
| Chemical Production | 5110 (3922–6920) | 4877 (3877–5989) |
| Stratosphere–Troposphere Exchange | 552 (151–930) | 477 (401–476) |
| **Sinks** | **5671 (4083–8124)** | **5354 (4503–6439)** |
| Chemical Loss | 4668 (3363–6617) | 4260 (3816–5089) |
| Dry Deposition | 1003 (720–1507) | 1094 (687–1350) |

Table 1.4 Mean and range of the multi-model estimates of the tropospheric $O_3$ budget from ACCENT and ACCMIP. Values summarised from Stevenson et al. (2006) and Young et al. (2013).

## 1.3 Evaluation of ozone in CTMs/ESMs

CTMs/ESMs are often used to develop air quality and climate mitigation policies, with tropospheric $O_3$ regularly in focus. The accuracy of the representation of tropospheric $O_3$ in these models can only be as good as the scientific understanding of the processes which control its spatial and temporal influence (i.e. chemistry, transport, emissions etc.). Comparison of these models with observations plays a key role in advancing this understanding. Assessment of model fidelity is essential to find errors in processes, to evaluate where model processes are inadequate, and to understand when models provide useful predictive capabilities.

A major barrier to such evaluations has typically been availability of observations. Measurements are regularly made by satellites, aircraft and weather balloons, however these measurement types all carry issues associated the temporal, horizontal or vertical resolution of measurements. Most model–measurement evaluations have made use of surface measurements; typically made by stable instruments measuring over long time periods, and of a high temporal resolution (i.e. hourly). Multiple public networks make surface observations of both $O_3$ and its precursors, however data is reported in a multitude of different formats, with a variety of different data quality issues associated. Most evaluations therefore typically incorporate data from a single network, limiting the spatial scope of the evaluation.

The inconsistent quality of atmospheric chemistry observations often ensures researchers must take long-term averages to be confident of data quality. These averages are typically on a monthly timescale, then compared to a similarly averaged model output. Such evaluations miss key processes that occur on the sub-monthly timescale (i.e. transport, emissions), which are key to the success of the model. Better quality observations would

allow evaluation of these processes, and also allow the application of more advanced data analysis methods, i.e. spectral analysis.

Across the universe there are numerous examples of periodic oscillations. The diurnal rotation of the Earth on its axis is one such example, with the incident solar light intensity on a fixed surface location oscillating with the rotation of the earth. Periodic oscillations of meteorological parameters impose variability on the chemical species of the atmosphere. $O_3$ in particular is extremely sensitive to the availability of high energy photons, and therefore has substantive diurnal variability. Likewise, the annual rotation of the Earth around the Sun encodes substantial seasonal variability on $O_3$. Typically, when evaluating the diurnal/annual cycles of $O_3$, simple averages are taken over fixed time steps (e.g. hourly/daily/monthly). These averages encode the variability not only resultant from periodic forcings, but also from highly variable weather associated processes. Spectral analysis provides a methodology for the precise mathematical separation of any time series into its dominant periodic components (i.e. diurnal, seasonal variability) and residual meteorological noise. Through application to model–measurement comparisons, model biases associated specifically with the magnitude and timing of periodic forcings can be quantified. Through this work, spectral analysis is used extensively for the quantitative assessment of the modelled periodicity of surface $O_3$.

## 1.4 Structure of the thesis

The work described in this thesis represents a number of studies undertaken to further understanding of surface $O_3$ chemistry, with particular regard to improving its representation in CTMs/ESMs. The following chapters are each framed around published and in prep. works, as outlined below:

Chapter 2 describes the substantive process of collating surface measurements for $O_3$ and 4 of its main precursors from all publicly available data networks through time, handling numerous data quality issues, creating globally gridded metrics for each species, for use by the atmospheric chemistry community. Work in this chapter is based on Bowdalo et al. (2016b) and an updated version of the surface $O_3$ collation framework outlined in Sofen et al. (2016).

Chapter 3 outlines the development of a novel spectral analysis methodology for the periodic evaluation of atmospheric species in CTMs/ESMs. This Chapter is partly based on Bowdalo et al. (2016a).

Chapter 4 demonstrates the validity of the spectral method, through the evaluation of a global CTM with collated hourly surface $O_3$ measurements. Significant biases are discovered, which are discussed. This Chapter is partly based on Bowdalo et al. (2016a).

Chapter 5 discusses potential reasons for surface $O_3$ biases in current CTMs/ESMs, and describes the undertaking of a large scale sensitivity study, scaling a multitude of emissions and deposition parameters of a global CTM, in an attempt to find valid pathways to better represent surface $O_3$. This Chapter is based on Bowdalo and Evans (2016).

The thesis is concluded by a summative chapter (Chapter 6).

# Chapter 2

# Gridded global metrics for surface ozone model evaluation

## 2.1 Introduction

A major limitation in the evaluation of $O_3$ in CTMs/ESMs is the availability and quality of observations. $O_3$ has been extensively measured around the world by long term balloon borne measurements, from suitably equipped commercial aircraft, from research aircraft, from ships, and satellites etc. However, each of these methods carry issues associated with the temporal, horizontal or vertical resolution of measurements. $O_3$ has also been extensively measured at the surface, by a range of regional and global networks.

Concurrent evaluation of both $O_3$ and its precursors gives greater confidence of our understanding of the chemistry, however, observations of these precursors are much sparser than for $O_3$. Measurements of these species are typically harder to make than for $O_3$, and scientific or air quality interest in many of these species is also often less than for $O_3$. Near global coverage by satellites exist for some of these precursors (i.e. CO, $NO_2$), these however require complex corrections and can not yet isolate concentrations at the surface (Lamsal et al., 2015; Strode et al., 2016), the air most relevant for humans and vegetation. Surface observations of a range of $O_3$ precursors are also collected by multiple public networks. Data from these networks is reported in a multitude of different formats, with a variety of different data quality issues associated. Most evaluations therefore typically incorporate data from a single network, limiting the spatial scope of the evaluation.

This chapter describes the synthesis of all publicly available surface data for several key species which play pivotal roles in the composition of the atmosphere, specifically, $O_3$, NO, $NO_2$, CO and $C_5H_8$. Extensive data quality screening is applied, providing high quality data appropriate for the detailed evaluation of modelled $O_3$ chemistry. The finalised data is made available to the atmospheric chemistry community through gridded statistical metrics, tailored specifically for robust global model comparison.

Section 2.2 outlines the data networks contributing to this work. Section 2.3 details the data quality checks applied to the raw data and Sect. 2.4 describes the temporal and spatial extent of the finalised data sets. Section 2.5 gives a statistical review of the processed data

and Sect. 2.6 details the production of gridded versions of the data. Finally, Sect. 2.7 gives recommendations for data providers and the modelling community based on experiences gleaned through this work.

## 2.2 Contributing data sets

There are multiple publicly available data sets that report $O_3$, NO, $NO_2$, CO and $C_5H_8$ observations. Due to the scarcity of $O_3$ precursor measurements relative to $O_3$, efforts are made to include data sets reporting hourly, daily and monthly mean resolution data as long as this data is representative in a daily context.

Data is taken from the following publicly available data sets:

**European Environment Agency AirBase**, http://www.eea.europa.eu/data-and-maps/data/airbase-the-european-air-quality-database-8 : European network made up of national air pollution monitoring networks from the European Union (EU), European Economic Area (EEA) member countries and some EEA potential candidate countries. The EU member states are required to report air quality data under the EU Council Decision 97/101/EC. Being designed to monitor air quality compliance, sites are typically urban (European Environment Agency, 2002; European Topic Centre on Air Pollution and Climate Change Mitigation, 2015).

**Air Quality System (AQS)**, http://www3.epa.gov/airdata/ad_data.html : USA (United States of America) network made up of air pollution data collected by the USA Environmental Protection Agency (EPA), state, local, and tribal air pollution control agencies from thousands of monitoring stations designed to monitor compliance with the Clean Air Act. As with AirBase, sites are typically urban.

**The Canadian Air and Precipitation Monitoring Network (CAPMoN)**, http://www.ec.gc.ca/rs-mn/default.asp?lang=En&n=752CE271-1 : Canadian network created in 1983, originally designed to aid understanding of the sources and impacts of acid rain, with a present day remit to study regional patterns and trends for a range of atmospheric pollutants. As of 2010 there are 33 active sites across Canada, predominantly in the central and eastern regions.

**Clean Air Status and Trends Network (CASTNET)**, http://www.epa.gov/castnet : Long term environmental background monitoring network consisting of sites located in the USA and Canada. CASTNET is managed and operated by the EPA. The network was established under the 1991 Clean Air Act Amendments to assess the trends in acidic deposition due to emission reduction programs (AMEC Environment and Infrastructure Inc., 2014).

**Acid Deposition Monitoring Network in East Asia (EANET)**, http://www.eanet.asia : Asian intergovernmental monitoring network, primarily focused on acid deposition that was set up to promote efforts towards environmental sustainability and protection of human health in the east Asian region.

**European Monitoring and Evaluation Programme (EMEP)**, http://ebas.nilu.no/default.aspx : European scientific and policy driven program based under the Convention on

Long Range Transboundary Air Pollution (CLRTAP) for international co-operation to solve transboundary air pollution problems. EMEP sites are intended to provide representative regional observations to monitor long range transport in Europe (Tørseth et al., 2012).

**Canadian National Air Pollution Survey Program (NAPS)**, http://maps-cartes.ec.gc.ca/rnspa-naps/data.aspx : Canadian network operated by Environment Canada, established in 1969 as a joint program of the federal and provincial governments to monitor and assess the quality of ambient air in urban areas.

**South Eastern Aerosol Research and Characterisation (SEARCH)**, http://www.atmospheric-research.com/studies/SEARCH : South eastern USA multi-pollutant network designed to address policy and scientific driven questions related to: $O_3$ and its precursors, particulate matter composition, mercury and acid deposition. Originally setup in the early 1990s, when 3 rural ozone sites were deployed as part of the Southern Oxidants Study (SCION) network to understand regional transport of ozone and its precursors in the southern USA.

**World Data Center for Greenhouse Gases (WDCGG) from the World Meteorological Organisation (WMO) Global Atmospheric Watch (GAW)**, http://ds.data.jma.go.jp/gmd/wdcgg/ : The GAW network was established by the WMO in the 1960's with the major aim to understand and control the increasing influence of human activity on the global atmosphere. GAW sites are classified into global, regional, and contributing stations. Global stations are sites that provide data to study global scale environmental issues. Regional stations provide data related to regional aspects of global environmental issues and environmental problems of regional scale and importance. Contributing stations are sites owned by external data groups and share data through mutual agreements with GAW (Müller et al., 2007).

These data sets do not represent all of the observations of these compounds made globally. However other data sets are not readily available (e.g. not available online), unlikely to conform to the quality assurance standards followed by the above networks, or are reported individually in a plethora of different data formats. Data from the networks used was last downloaded on August 15th 2015. In total, combined for all species the data collection comprises of 24,334 sites, and 1,640,864,217 measurements, beginning in 1971 ($O_3$ measurements from the WMO GAW network) going through to January 1st 2015.

## 2.3 Data processing

The data processing framework used is now outlined, shown visually in Fig. 2.1. The file parsing involved in processing a range of data formats is first described (Sect. 2.3.1 – Sect. 2.3.4) followed by descriptions in turn of each the multiple data quality steps implemented on the raw data, outlining any unresolved uncertainties (Sect. 2.3.5 – Sect. 2.3.14). Figure 2.3 shows all sites, by species, that are omitted from processing following each data quality check. Table 2.5 outlines the number of sites and measurements remaining after each quality check, by species.

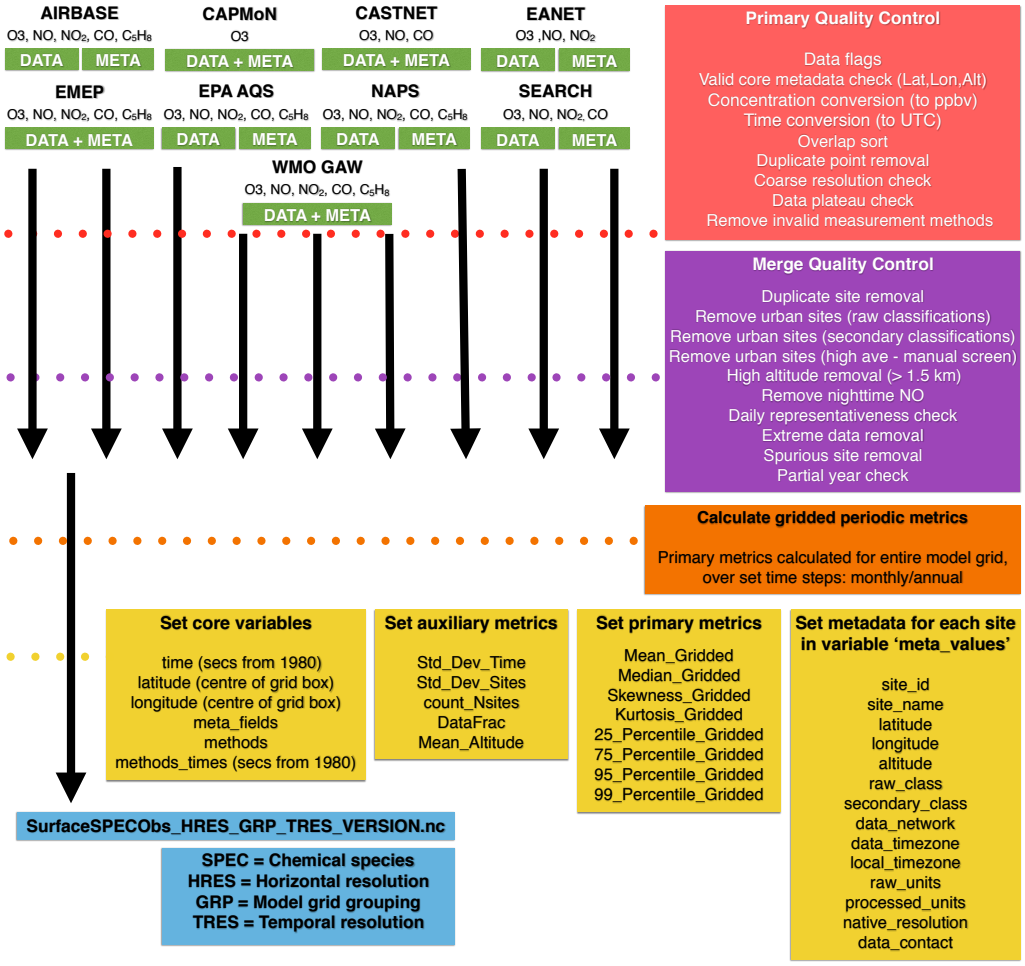


Fig. 2.1 Flow chart illustrating the data processing framework.

### 2.3.1 Primary file parsing

A range of file formats are processed, with no real consistency between any of the networks: AirBase (fixed format text), CAPMoN (CSV), EANET (CSV), EMEP (NASA Ames), SEARCH (CSV and XLS) and WMO GAW (fixed format text) all provide an annual file for each site. AQS (CSV), CASTNET (CSV) and NAPS (CSV and XLS) provide annual data files, containing data for all sites. Some of these networks provide different species data in the same files (EANET, SEARCH), the rest (AirBase, AQS, CAPMoN, CASTNET, EMEP, NAPS, WMO GAW) separate different species data out into separate files. SEARCH data prior to 1997 is reported as XLS files and after as CSV files. Inconsistency in file formats is also inherent between different species for some networks. This is the case for AQS ($C_5H_8$ and other species), and NAPS ($C_5H_8$ and other species). Daily and monthly average data (and data with resolution in between) is incorporated in the processing along with hourly data. The networks that provide data on these longer timescales ($>$ hourly) are: AirBase, AQS (for $C_5H_8$), EMEP, NAPS (for $C_5H_8$) and WMO GAW. It is sometimes the case that there are duplicate data files reported for the same site at different temporal resolutions. In all instances the highest temporal resolution data is preferentially kept. All data is processed onto an hourly data grid between January 1st 1970 and January 1st 2015. For all valid data with a temporal resolution lower than 1 hour, each measurement is repeated for the day or month, or over the range of specified sampled hours, if given. Most of the data networks provide data quality flags to highlight bad quality data. These flags are used wherever provided converting the bad data to NaN (Not a Number) values. AirBase, CAPMoN, CASTNET, NAPS and SEARCH networks provide data flags for all observational points. EMEP and WMO GAW data files have flags for the majority of site data, but not all. AQS and EANET do not provide data flags. Flag definitions are generally determined through analysing network reports, but their application is often inconsistent, particular for the EMEP and WMO GAW networks owing to the large number of flag options. A strict filter is imposed, removing observations flagged as having any concerns with the quality of measurement. Additionally, missing or bad quality observations are often set as filler values (i.e. -99999), with these values set as NaNs also. Filler values however are often set inconsistently in-network (i.e. 999,9999, -99999 etc.), with no additional meta data providing definitions for differences.

### 2.3.2 Metadata

Each of the data networks provide metadata supplementing the data measured. For each site a consistent dictionary containing the following metadata is built: site reference code, site name, latitude, longitude, altitude, raw land use classification, secondary land use classification, data network, data timezone, local timezone, raw measurement unit, processed measurement unit (ppbv), coarsest data resolution (lowest resolution of data going into site averages, i.e. monthly) and site contact. Additionally collected are the valid measurement methodologies applied at each site, along with the timespan of their usage.

AirBase metadata is split between 2 country specific CSV files reporting primary metadata and measurement configurations respectively as well as single country specific XML files which report country wide metadata (i.e. time zone). AQS metadata is split between the data files per line (i.e. measurement methods) and a standalone metadata file (CSV) giving constant site metadata (latitude, longitude etc.). CASTNET and NAPS provide standalone metadata files (CSV) providing metadata for all sites (NAPS measurement units and methods are homogenous per species and obtained online from separate documentation). CAPMoN, EMEP and WMO GAW metadata is given in the header of each data file. SEARCH metadata is manually taken from the SEARCH website. EANET metadata is stripped from a PDF document describing each site and manually cleaned up.

Site reference codes are used to track site data throughout the processing. The type of codes used are unique for each data network, as these codes are mostly provided by the networks, often used to link site data to external metadata. Only the AQS and EANET networks do not give site reference codes. For the AQS data set, reference codes are manually created for each site, concatenating "aqs" + state code + county code + state specific site number. For the EANET data set the codes are created by concatenating "ea" + first two letters of the site name + a three-digit integer (from 0, the alphabetical sorted position of the site name).

The metadata describing the measurement and sampling methodologies vary significantly in detail by measurement network and also, at many sites, change over time. The accurate attribution of measurement and sampling methodologies is essential to ensuring the accuracy of any one measurement. WMO GAW is particularly inconsistent in the reporting of methodologies, particularly for older time periods, with methodologies often left blank. Site specific methodologies are reported in much greater detail on the GAWSIS web platform (http://ds.data.jma.go.jp/gmd/wdcgg/), therefore this resource is used to manually fill in the majority of missing methodologies.

There are occasions where metadata is reported per year (CAPMoN, EMEP and WMO GAW), where the physical location (latitude, longitude or altitude) changes once or multiple times through the time record. This is typically due to typographical errors or varying numbers of digits being used to represent the latitude, longitude or altitude information, but there are examples where the change is due to an actual physical change in monitoring location. These changes in location are all small enough that they do not significantly alter the composition at the sites. In these instances, the mode value found in the metadata is taken to be the set metadata value for the site.

Much of the data reported is given in a local time, this is corrected for (described in Sect. 2.3.4) but in order to do this the local timezone is needed. This is reported for almost all sites, however not for AQS $C_5H_8$ data. A Python timezone package (tzwhere) is thus used to provide a site's local timezone based on its latitude and longitude coordinates.

If any metadata field is not reported, the value is set to be NaN. A data quality step is included that checks if any of the key metadata (latitude, longitude, altitude) is not a NaN or arbitrary string. If so, the site is excluded from processing.

### 2.3.3 Concentrations and mixing ratios

The concentrations reported for all species are either volumetric mixing ratios (e.g. ppbv = nmol mol$^{-1}$ = $1 \times 10^{-9}$ mol$^{-1}$) or mass densities (e.g. µg m$^{-3}$), in a range of different units. For consistency, all concentrations are converted to ppbv. Some measurement methodologies fundamentally measure in the units of molecules cm$^{-3}$ or as a mass density, not as a volumetric mixing ratio. The conversion from molecules cm$^{-3}$ to a mass density, i.e µg m$^{-3}$, is a simple constant: $M_S/N_A \times 10^6$, where $M_S$ is the molar mass of the species and $N_A$ is Avogadro's number ($6.0221 \times 10^{23}$ mol$^{-1}$). The conversion from µg m$^{-3}$ to a mixing ratio (ppbv) however carries uncertainty as it depends on both temperature and pressure:

$$X_S = C_S \cdot \frac{RT}{M_S P}, \tag{2.1}$$

where $X_S$ refers to the species mixing ratio in ppbv, $C_S$ the species concentration in µg m$^{-3}$, $R$ is the gas constant (8.3144 J mol$^{-1}$ K$^{-1}$), $M_S$ is the molar mass of the species in g mol$^{-1}$, $P$ is pressure in mPa, and $T$ is temperature in K. The temperature and pressure referenced refers the internal temperature and pressure of the instrument, not ambient conditions. However, the concentrations actually reported are standardised to a fixed temperature and pressure. This is done to ensure measurements are comparable across all sites. This standardisation differs between the USA and the EU. The EU standard (used by AirBase, EANET, EMEP) sets the temperature and pressure as 293 K and 1013 hPa (European Environment Agency, 2002). The USA standard (used by AQS, CAPMoN, CASTNET, NAPS and SEARCH) is 25°C (298.15 K) and 1013.25 hPa (U.S. Environmental Protection Agency, 2016). WMO GAW standards differ by site, all using a fixed pressure of 1013.25 hPa but differing temperatures (293.15 K or 298.15 K). The difference between these standards will bias results slightly high in North America compared to the rest of the world. Taking CO to be 150 µg m$^{-3}$ for example adds 2.2 ppbv at 25°C (131.02 ppbv) compared to 20°C (128.82 ppbv). For measurement methodologies that directly measure as a volumetric mixing ratio it is not known if the standardisation is applied retrospectively to the measurements, which adds additional uncertainty.

Some $C_5H_8$ AQS measurements are reported in a mixing ratio per carbon (i.e. ppbv per carbon). This is converted to a standard mixing ratio (ppbv) by:

$$X_S = \frac{XC_S}{N_C}, \tag{2.2}$$

where $XC_S$ is the mixing ratio per carbon and $N_C$ is the number of carbon atoms in the species (i.e. 5 for $C_5H_8$).

### 2.3.4 Date and time

The time zones that data are reported in vary by site thus all observational times are needed to be adjusted to a consistent timeframe. All times are shifted to Coordinated Universal Time (UTC). AirBase, CASTNET, EANET, AQS (only $C_5H_8$), NAPS and SEARCH data

sets are reported in local time and provide integer time zone offsets from UTC. For the WMO GAW data set some sites report data in UTC and others in local times, reported in a range of non-standardised strings (i.e. "Local time UTC+1" vs "Local time+1"), and in many instances report no time zone information at all (which are filled in manually using data found on the GAWSIS web platform). AQS (all but $C_5H_8$), CAPMoN and EMEP data is reported in UTC time.

A small number of sites have consistent daily gaps on the 29th February during leap years. It is assumed that this a missing day of data, caused by the data processing, and that data labeled for the 1st of March is indeed for the 1st of March. The WMO GAW network reports times either as 00:00–23:00 or 01:00–24:00. In all these instances, 24:00 is converted to be 00:00 of the next day. Coupled with this difference in notation is the uncertainty regarding whether any time reported relates to the beginning, middle or end of an average time window and whether this varies by data network. For example, a data point reported at 07:00 could reasonably relate to the average between 06:00–07:00, 07:00–08:00 or 06:30–07:30. This is impossible to resolve given the number of sites analysed and thus adds uncertainty on the time of day measurements relate to.

The number of data quality checks implemented during the processing procedure are now described. Counts are maintained of the number of sites and number of observations removed by each step, for each species. Each data point that is of raw daily or monthly temporal resolution is treated simply as 1 count, rather than counting their duplicated values in the final output. The number of sites and observations remaining after each processing step are shown for each species by Table 2.5. The sites removed by each check are shown spatially by network, for each species, by Fig. 2.3.

There are sites which have no valid measurements through the time record, these sites are removed by the first data quality check.

### 2.3.5 Correcting overlapping and removing duplicate data

Some sites have overlapping or duplicate data for a single time point with no explanation in any case given. A two step process is implemented for dealing with these instances. Firstly, data is sorted in ascending order in time. Secondly, if any data is reported more than once for any hour, the first value is kept and all subsequent values are removed. This second step thus removes instances where data values are simply duplicated for a single time point, and the more problematic instances where there are different values reported for a single time point, which is seen as the fairest way of treating this data.

### 2.3.6 Coarse resolution / data plateaus

The measured data resolution for all species has improved over time as measurement methodologies have improved. Some species, particularly NOx and CO, are often only measured for air quality indexing purposes, with the resolution of the data being often very coarse (i.e. in 100 ppbv intervals for CO in many cases for AQS sites) and thus not very suitable for model evaluation purposes. Coarse data is filtered out by implementing an

algorithm to look, year by year, at the minimum differences between all of the measurement points (excluding zeros). Annual site data which has a minimum difference of greater than 1 ppbv for $O_3$ and $NO_2$, 0.3 ppbv for NO, 10 ppbv for CO and 0.2 ppbv for $C_5H_8$, is set as NaNs for the entire year. A whole site is removed from processing if all years of data are removed. This approach allows for the keeping of site data where the data resolution improves over time.

Additionally, there are instances where the limit of detection of the instruments leads to a plateau of measurements concentrated on this limit, with the true concentration being lower. This is more apparent for older data when instruments had poorer limit of detections. Including insufficiently resolved data would impose a high average bias, thus a semi-automatic method is implemented for removing data. A minimum concentration is imposed for each species: $O_3$ – 4.9 ppbv, NO – 0.099 ppbv, $NO_2$ – 1.9 ppbv, CO – 49 ppbv, $C_5H_8$ – 0.09 ppbv. If one year of data for a site is all above the set minimum level the site is manually screened. If there is clear evidence of a data plateau above this minimum level then each year of data, for each site, when this is the case is removed. A site is removed from processing if all years are invalid.

Additional uncertainty arises from inconsistencies regarding the inclusion of zero and negative concentrations. In many cases zeros and negative concentrations are included by the reporting site, however this is not the case for all stations. The most consistent approach for dealing with this issue would be to remove all instances of zeros and negative concentrations in the processing. However, for species such as $C_5H_8$, concentrations of zero represent a significant fraction of the total concentrations, therefore the removal of these values would result in the measured distribution not being fully representative. Thus zeros are retained in the processing. There exists significant confusion throughout the measurement community regarding the proper protocol for dealing with negative concentrations. Negative concentrations are reported in much fewer instances than zeros, thus it is not deemed their their removal biases the measured distribution, and therefore are removed.

### 2.3.7 Removing invalid measurement methods

A range of measurement methodologies exist for each of the different species. The accuracy of any measurement can only be as as good as the methodology employed for its taking. Therefore, it is essential to correctly attribute each measurement with the methodology used. This is made an extremely problematic task due to the metadata reported regarding measurement methodologies being generally sparse or non-existent. Many sites are found which report no methodology information at all in the metadata, which in all cases is set following manual investigation. This is the case for many WMO GAW site files, where additional information was found using the GAWSIS system. Some networks do not give any methodology information at all (i.e. NAPS), either in the raw data files or a separate metadata file, rather it is buried in network reports.

After setting a methodology for every measurement, the number of differing methodologies (by describing string) goes into the 1000s. In a small number of cases the methodolo-

gies reported are meaningless (e.g. “NANADE03L_NA”, “NANAAT01L_CO”, “NANA”) and all data associated with these sites is therefore screened out. A large amount of work has been devoted towards standardising the remaining methodologies, resulting in 24 unique methodologies across all species. Some of these methodologies carry very large uncertainties or are not typically associated with measuring the species stated. All data associated with these invalid methods is screened out , outlined in Table A.1 in Appendix A, by species. Following all quality checks (including removal of invalid measurement methods) 11 unique methodologies are found across all species. Tables 2.1–2.4 give a small description and the advantages and disadvantages associated with each accepted methodology. Table 2.1 focuses on $O_3$ methodologies, Table 2.2 reports $C_5H_8$ methodologies, Table 2.3 focuses on NOx methodologies and Table 2.4 reports CO methodologies. Figure 2.5 shows the mode measurement methodologies spatially at all valid sites, by species.

Some notable methodological issues encountered that require consideration are now detailed.

### $NO_2$ measurement bias

The vast majority of $NO_2$ measurements are made using the chemiluminescence methodology. Chemiluminescence measures $NO_2$ indirectly, requiring conversion of $NO_2$ to NO (which can be measured directly). The converter used is either a heated metal surface, almost always molybdenum, or a photolytic converter. The heated metal surface converters convert not only $NO_2$ to NO but other oxidised nitrogen compounds such as $N_2O_5$, $HNO_3$, PAN and other organic nitrates, with the efficiencies of these conversions being dynamic by location (Steinbacher et al., 2007). This leads to measurements that are essentially a fraction of the sum of oxidised nitrogen species (NOy) as opposed to $NO_2$. Thus $NO_2$ measurements by this methodology are typically overestimated, particularly in cleaner environments (Winer et al., 1974; Steinbacher et al., 2007). Despite this, many regulatory networks still mandate the use of this technique. Photolytic conversion of $NO_2$ to NO is achieved through photolysis of $NO_2$ at wavelengths less than 420 nm by either Xenon lamps or UV emitting diodes (blue light converters) (Ryerson et al., 2000; Sadanaga et al., 2010). Small interferences caused by photolysis of HONO by Xenon lamps and in the presence of hydrocarbons have been reported (Rohrer et al., 2005; Bejan et al., 2006; Villena et al., 2011), however the biases imposed are significantly less than associated with molybdenum converters and is the recommended methodology for measuring $NO_2$ (Penkett et al., 2011). The vast majority of $NO_2$ measurements made to date however have used chemiluminescence instruments with molybdenum converters, thus significantly biasing the majority of global $NO_2$ measurements.

Rigi (47.056°N, 8.485°E) is a rural Swiss WMO GAW site, that makes in situ $NO_2$ measurements using both types of chemiluminescence instruments. This gives an opportunity to directly analyse the bias imposed by the molybdenum converter referenced directly with relatively unbiased data. Figure 2.2 shows the time series of $NO_2$ for both methodologies at Rigi between 2002 and 2015. Inspection of the time series reveals the highest $NO_2$ to be consistently reported by the molybdenum instrument, however the

significant amount of noise makes any systematic seasonal or diurnal trend difficult to derive. Using spectral analysis (described in detail in Chapter 3) the periodic signals (seasonal and diurnal) contained in the data are isolated from the meteorological noise. The molybdenum converted measurements are found to be higher than the photolysis converted measurements in all months and all hours of the day. No systematic biases associated with any specific time of day are found, with the molybdenum data consistently biased 1.5 ppbv high across the day. Seasonally, larger high biases are found January to April of 2.5 ppbv, with a 1.5 ppbv high bias across the rest of the year. These findings are consistent with previous studies at this site (Steinbacher et al., 2007).

Therefore it is decided to separate the $NO_2$ measurements into two different groups: $NO_2$–M ($NO_2$–Molybdenum) and $NO_2$–O ($NO_2$–Other). The $NO_2$–O grouping includes both Differential Optical Absorption Spectroscopy (DOAS) and photolytic measurements. The $NO_2$–M measurements are retained primarily due to the large number of valid measurements that are made in this way (883 sites and 58,706,945 measurements), with these measurements potentially being useful for long term trends etc. Work has also been done attempting to correct these observations using a global CTM (Lamsal et al., 2008), showing a potential use.

There is often little detail reported in the metadata regarding the type of converter used for chemiluminescence $NO_2$ measurements. The only method of determining this information was manually looking through instrumental handbooks, when a instrument name is given. In cases where the instrument name is not given, no determination is possible, and these measurements are grouped by default as using molybdenum converters. This therefore imposes more uncertainty on the $NO_2$–M grouping.

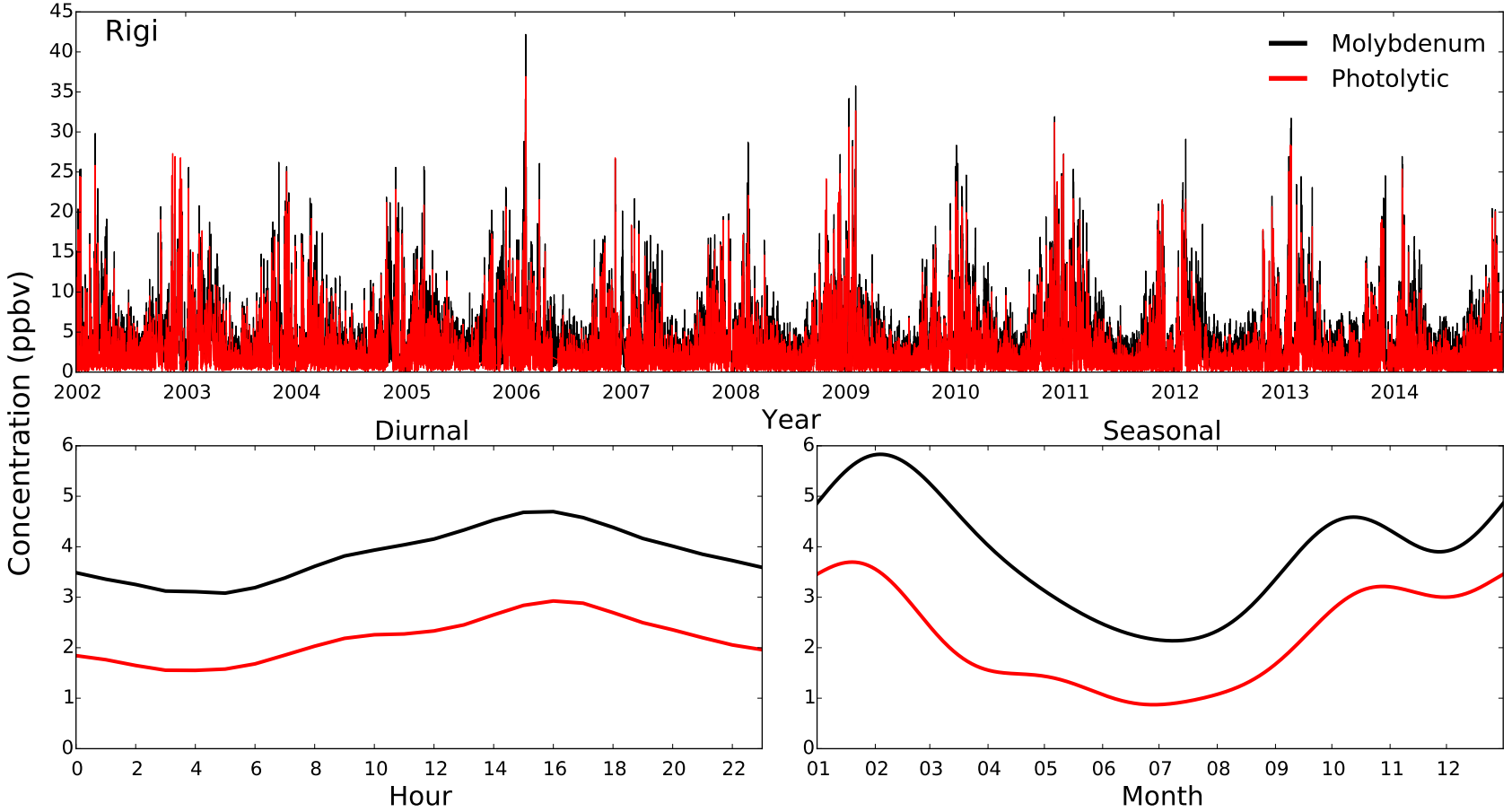


Fig. 2.2 Time series of $NO_2$ measurements made by chemiluminescence instruments with molybdenum (black) and photolytic (red) converters at Rigi (upper panel), and the associated diurnal and seasonal cycles derived through spectral analysis (lower panels).

### WMO GAW flask network – CO

The WMO GAW flask network exists to provide an economical way of determining seasonal/multi-annual variations for multiple carbon gases, CO included, in a global context. It involves the air filling of flasks (with approximately 10 minute sampling time) across a large range of locations, for later analysis at a central laboratory using gas chromatography – mercury oxide reduction (GCHgO). They are reported in the raw data as a single monthly average value with no details of sample times included. The reported monthly average could potentially therefore be the average of multiple flask samples or only one. As this network of measurements exhibits such excellent global coverage, these measurements are kept in the data set. These values are set as single hourly measurements the first hour of each month. This approach is taken as the representativeness of the measurements over timescales longer than an hour cannot be trusted, and it is not wished to bias areas which contain more representative continuous measurements in the averaging process. However, these flask measurements represent the only CO measurements in many areas and in these cases some measurements are preferable to none.

### CO calibration scale uncertainty

Calibration is necessary for all CO instruments using gas standards. Every calibration requires setting new calibration factors for methods with a linear response (NDIR, GCFID etc.), or a new calibration curve for methods with a non-linear response (GCHgO).

Typically when calibrating the measurements of a specific species via a gas standard, a defined calibration scale is referred to, directly linked to a single set of stable primary standards that are used over a long period of time, maintaining consistency of calibration (Novelli et al., 1991). Each scale is directly associated with a specific set of primary standards, named according to the year they were created. Thus the creation and use of new primary standards for a particular compound results in a new calibration scale.

However, concentrations of CO standards in high pressure cylinders have been shown to drift over relatively short time periods (1–2 years) which has led to the CO scale being redefined by new sets of gravimetric standards made every few years. Secondary (in-house) standards are calibrated by the gravimetric standards before they become invalid. This makes the CO scale relatable across multiple gravimetric sets over multiple years and allows quantification of the drift in the secondary standards. Uncertainties arise however as there has not been consistency in the definition of primary and secondary standards with time. Additionally not all secondary standards have been measured against all gravimetric sets, thus it is uncertain how well different sets of gravimetric standards agree.

More uncertainty arises when comparing the CO calibration scales associated with the standards of CO provided by the multiple different national and commercial laboratories. Measurements of CO made by different laboratories have been known to differ in the past by up to 40 %, a significant fraction of which is attributed to differences in calibration scales (Novelli et al., 1998). Zellweger et al. (2009) found that the major limiting factor

for accurate CO measurements, when comparing 4 different co-located measurement methodologies, was the uncertainty of the calibration standards.

The most referenced scale is the NOAA/WMO scale, applied by the WMO GAW network, the only network which gives any detail in the metadata regarding calibration. It is therefore possible a range of different CO scales have been applied by the different data networks. It is impossible to place a number on the uncertainty imposed because of this. However, all data networks from which data is drawn in this work have comprehensive quality control procedures and as such the assumption is made that this uncertainty is not significant.

The calibration procedures for the other species carry less uncertainties. No standards of $O_3$ can currently be stably stored, due its reactivity. $O_3$ is thus calibrated dynamically, typically using a standard reference photometer (SRP). The SRP generates a synthetic stream of $O_3$ in dry air, which is measured, and flows a fraction of the $O_3$ through the instrument wanted to be calibrated, with the linear regression between the different measurements providing calibration factors (Galbally and Schultz, 2013). Many national and commercial laboratories provide NO and $NO_2$ standards. NO standards are prepared through the dilution of pure NO in pure nitrogen ($N_2$), in concentrations of 10 mmol $mol^{-1}$ or less, to protect against reaction to $NO_2$, $N_2O$ and $N_2$. These standards have been shown to be stable over many years (Wielgosz et al., 2008; Penkett et al., 2011). $NO_2$ standards are generally prepared through gravimetric dilution of NO in pure $N_2$. NO is then converted to $NO_2$ through addition of excess $O_2$. Water vapour can cause problematic interference, converting $NO_2$ to $HNO_3$. The most experienced laboratories are are able to reproduce independent standards of $NO_2$ that agree within 0.5 % (Flores et al., 2012). There currently exist only two sets of traceable pure calibration standards for VOCs in the sub-ppbv range, provided by Apel-Riemer (Environmental Inc. Denver, Colorado, USA). The first of these standards is designed for the calibration of 75 non-oxygenated species (i.e. $C_5H_8$) in the range of 0.2–10 ppbv, and the other for oxygenated species. These standards are certified with an accuracy of $\pm$ 3–5 %, stable on time scales greater than a year (WMO/GAW, 2007).

| Measurement Method | Outline | Advantages | Disadvantages |
|---|---|---|---|
| **$O_3$** | | | |
| UV Absorption Spectrophotometry (UV–A) (Galbally and Schultz, 2013) | Sample is irradiated in measurement cell (at wavelengths less than 254 nm), by a low pressure, cold cathode mercury vapour lamp. The absorption at 253.65 nm (principally by $O_3$) is measured by a photodetector, with the concentration of specific molecules of $O_3$ then derived using the Beer–Lambert Law. | • Well established method<br>• Low cost<br>• Direct measurement | • Interferences by aromatic hydrocarbons<br>• Water vapour interferences<br>• Interferences by mercury |
| Differential Optical Absorption Spectroscopy (DOAS) (Platt et al., 1979; Edner et al., 1993; Galbally and Schultz, 2013) | Optical method that analyses spectrum of light (either from a continuous source–typically UV, or direct or scattered sun light) that is beamed through a fixed optical path (from hundreds of metres to many kilometres), with concentrations of specific species' molecules in optical path, over set wavelength ranges, determined using the Beer–Lambert Law. | • Low detection limit ($\sim$ 1 ppbv)<br>• High precision | • Interferences by NO, $NO_2$ and $SO_2$ in wavelength ranges<br>• Complex corrections for variable optical conditions<br>• Measures average concentration along the path length, not any single molecule |

Table 2.1 Accepted measurement methodologies for $O_3$.

| Measurement Method | Outline | Advantages | Disadvantages |
|---|---|---|---|
| **$C_5H_8$** | | | |
| Gas Chromatography – Flame Ionisation Detection (GCFID) (WMO/GAW, 2007) | Chromatographic separated $C_5H_8$ is measured through oxidation in a hydrogen flame, generating electrically charged ions (FID). | • Well established method<br>• Very linear response<br>• Low cost | • Potentially unsensitive for VOCs<br>• Labour intensive |
| Gas Chromatography – Mass Spectrometry (GCMS) (WMO/GAW, 2007) | Chromatographic separated $C_5H_8$ is ionised, fragmenting the sample into charged ions with a certain mass, resulting in a spectrum where compounds can be separated based on their mass to charge ratio. | • Well established method<br>• Very sensitive | • Careful calibration necessary<br>• Expensive |

Table 2.2 Accepted measurement methodologies for $C_5H_8$.

| Measurement Method | Outline | Advantages | Disadvantages |
|---|---|---|---|
| **NO** | | | |
| Chemiluminescence (CL) (Fontijn et al., 1970; Ridley and Howlett, 1974; Penkett et al., 2011) | $O_3$ created by a generator produces $NO_2$, a fraction of which is exited. This decays releasing light, the intensity of which is directly proportional to the NO mixing ratio. | • Well established method<br>• Low cost<br>• Direct measurement | • Interference at low mixing ratios due to reaction of $O_3$ with other gases<br>• Water vapour interferences |
| **$NO_2$** | | | |
| Chemiluminescence – molybdenum converter (CL–M) (Winer et al., 1974; Steinbacher et al., 2007; Penkett et al., 2011) | NO is measured by chemiluminescence (NO cell). In another cell, $NO_2$ is converted to NO by a molybdenum converter and then measured (NOx cell). The difference between the NO mixing ratios in the different cells gives the $NO_2$ concentration. | • Well established method<br>• Low cost | • Indirect measurement<br>• Overestimates $NO_2$ due to conversion of $NO_2$ to other oxidised nitrogen compounds than NO |
| Chemiluminescence – photolytic converter (CL–P) (Ryerson et al., 2000; Rohrer et al., 2005; Bejan et al., 2006; Sadanaga et al., 2010; Villena et al., 2011) | Same as above, but instead uses photolytic conversion (Xenon lamps or UV emitting diodes – blue light converters) of $NO_2$ to NO at wavelengths less than 420 nm. | • Well established method<br>• Good precision | • Indirect measurement<br>• Small interferences caused by photolysis of HONO by Xenon lamps and in the presence of hydrocarbons |
| Differential Optical Absorption Spectroscopy (DOAS) (Platt et al., 1979; Edner et al., 1993; Thornton et al., 2003) | Optical method that analyses spectrum of light (either from a continuous source–typically UV, or direct or scattered sun light) that is beamed through a fixed optical path (from hundreds of metres to many kilometres), with concentrations of specific species' molecules in optical path, over set wavelength ranges, determined using the Beer–Lambert Law. | • Low detection limit ($\sim$ 1 ppbv)<br>• High precision | • Interferences by $O_3$, NO or $NO_2$ and $SO_2$ in wavelength ranges<br>• Complex corrections for variable optical conditions<br>• Measures average concentration along the path length, not any single molecule |

Table 2.3 Accepted measurement methodologies for NO and $NO_2$.

| Measurement Method | Outline | Advantages | Disadvantages |
|---|---|---|---|
| **CO** | | | |
| Non-Dispersive Infrared Radiometry (NDIR) (Parrish et al., 1994; WMO/GAW, 2010) | Near infrared spectral absorption by CO at 4.67 µm in an optical cell with the attenuated energy proportional to the CO concentration. NDIR instruments are usually continuously calibrated using the gas filter correlation technique (GFC). | • Well established method<br>• Low cost<br>• Little maintenance | • Water vapour interferences<br>• Significant differences in NDIR instrument detection limits possible (10 to 40 ppbv) |
| Gas Chromatography – Mercury Oxide Reduction (GCHgO) (Novelli et al., 1992; Novelli, 1999; WMO/GAW, 2010) | Following separation by gas chromatography, CO reacts with mercury oxide (HgO) to produce mercury vapour detected by UV absorption at 254 nm. | • Well established method<br>• Low detection limit (2 ppbv)<br>• High precision | • Non-linear response (up to 8 %): frequent determination of the calibration curve is necessary |
| Gas Chromatography – Flame Ionisation Detection (GC-FID) (Rasmussen and Khalil, 1981; Novelli, 1999; WMO/GAW, 2010) | Chromatographic separated CO is converted to $CH_4$ using a heated nickel catalyst and measured through oxidation in a hydrogen flame, generating electrically charged ions (FID). | • Well established method<br>• Very linear response<br>• Low cost | • Indirect measurement<br>• Heated nickel catalyst may need regular replacement<br>• Labour intensive |
| Vacuum Ultraviolet Resonance Fluorescence (VURF) (Gerbig et al., 1999; Holloway et al., 2000; WMO/GAW, 2010) | Pulsed fluorescence of CO in the vacuum ultraviolet, using a photomultiplier tube to measure the emitted photons. | • Very low detection limits ($< 1$ ppbv)<br>• Extremely linear response<br>• High frequency measurments | • Water vapour interferences<br>• Frequent cleaning of the optical parts is essential<br>• Expensive |
| Cavity Ring Down Spectroscopy (CRDS) (WMO/GAW, 2010; Richardson et al., 2012) | Sample is introduced into a high-finesse optical cavity illuminated by a laser and the optical absorbance of the sample, and in turn concentration, is determined. | • Very low detection limits ($< 1$ ppbv)<br>• Very linear response<br>• Requires very little maintenance | • Expensive |

Table 2.4 Accepted measurement methodologies for CO.

### 2.3.8 Removing duplicate sites

Duplicate site records are in some cases reported by different observing networks. For example, many of WMO GAW sites also appear in the AirBase and EMEP networks. The WMO GAW sites at Cape Point (cpt), Niwot Ridge (nwr) and Ushuia (ush) report two versions of data, one unfiltered and one filtered for local influences. Only unfiltered forms are used in this work. Sites are determined as duplicate if they have latitudes/longitudes that are equivalent to 2 decimal places, altitudes within 50 m and have the same measurement methodology. The amount of duplicates found for one location is as many as 4 sites in some cases. A 4 step process is implemented for the resolving of these duplicates. It is primarily tested if the temporal range of the data sets are distinctly different, which is defined as being if the start and end times are both significantly different ($> 5$ years) with the data overlap between them $< 50\,\%$. Any sites that are distinctly different are removed from the test and kept. If duplicates still exist, sites with the highest temporal resolution are kept preferentially. Next, the site which has the greatest number of valid data points is kept. Lastly, if there are still duplicates, the first indexed site is simply taken, discarding the others.

### 2.3.9 Removing urban sites

The majority of data for $O_3$ and its precursors is reported for air quality purposes, therefore a significant fraction of sites are located in urban areas. The major motivation for this work is the evaluation of global models for which the grid boxes have horizontal resolutions of 10s of kilometres or coarser. It is not expected that these models are able to resolve point source urban chemistry, therefore it is decided to exclude urban sites.

The definition of a "urban" site is rather subjective, with no global unified method of determination. In this work, urban sites are defined in a 3 step process. Firstly, most networks provide a raw land use classification (AirBase, AQS, CAPMoN, CASTNET, EANET, NAPS and SEARCH). These are defined in most cases by the site operators, who are best placed to define the classification their sites fall under. Any sites with classifications associated with urban influence are excluded ("urban", "suburban", "traffic", "industrial" etc.). Secondly, in order to screen sites from databases that do not provide their own classification scheme (EMEP and WMO GAW), land use data from the Anthropogenic Biomes of the World v2 data set is used (Ellis and Ramankutty, 2008; Ellis et al., 2010) at $\sim$5 km resolution. This data set allows the splitting of sites into 7 different anthropogenic land use classifications (dense settlements, villages, croplands, rangelands, forested, wildlands and oceans) achieved through a methodology that uses cluster analysis to group multiple metrics of anthropogenic influence (i.e. population density, land cover, biodiversity etc.). If more than 50 % of the grid boxes in a $4 \times 4$ cell area around any one site are classified as urban (dense settlements or villages), a site is excluded. In this way sites are kept that may be located on the very edge of an urban area.

Finally, maximum and minimum extreme average limits are applied for each species (except $C_5H_8$), set empirically looking at the average site probability distribution function

(PDF) of each species. This check is not applied for $C_5H_8$ as its emissions are overwhelmingly biogenic. The minimum and maximum limits for each species are: $O_3$ – 20 ppbv and 50 ppbv, NO – 2 ppbv and 10 ppbv, $NO_2$ – 2 ppbv and 10 ppbv, CO – 100 ppbv and 200 ppbv. If any year of data for a site has an average not within the set extreme average limits, the site location is explored manually via satellite imagery and it is determined if the site is significantly urban influenced. If so, the secondary land use classification metadata is changed to "urban" and the site is removed from processing.

### 2.3.10 Removing high altitude sites

Just as it cannot be expected that global models are able to capture urban point source chemistry, it equally cannot expected that global models are able to capture the chemistry of high altitude mountain sites, with the average nature of the model grid boxes resulting in much lower average surface grid box heights than the peak altitudes of the mountaintop sites. This impact is therefore limited by removing any stations above 1500 m from sea level. Taking this simple approach means that many sites in regions with a high average altitude (i.e. eastern and central USA) are lost from processing. More complex approaches were considered (i.e. determining mountain sites by peak elevation roll off, with data drawn from orthographic maps), but were deemed too uncertain for global application.

### 2.3.11 Removing nighttime NO

Through this evaluation significant issues associated with nighttime NO have been observed. NOx is efficiently recycled in the daytime between NO and $NO_2$ by the previously outlined reactions:

$$NO_2 + h\nu \longrightarrow NO + O \tag{R1.9}$$

$$NO + O_3 \longrightarrow NO_2 + O_2 \tag{R1.39}$$

At night (away from direct emission and urban areas), with no light for R1.9 to proceed, NOx should exist solely as $NO_2$ due to R1.39, with concentrations of NO essentially negligible. However, several sites are found with concentrations of nighttime NO significantly above zero. This is most probably associated with sites not wanting to report negative or zero concentrations (as discussed in Sect. 2.3.6) and leads to minimum values being set that are above zero. Including nighttime NO would impose a high average bias over the day, thus it is decided to remove all nighttime NO values from the data set. This is done by applying an algorithm that determines the number of daylight and nighttime hours (rounded to nearest hour) for each different day of the year, for each site. An astronomical python package (PyEphem) is used to achieve this, which applies the United States Naval Observatory (USNO) definition of distinguishing between day and night (based on the angle of the centre of the sun to the horizon). Any measurements at hours which are

deemed nighttime, by site, are then removed. Sites at higher latitudes (i.e. Svalbard) thus lose whole days of NO data in the winter, when there is total darkness.

### 2.3.12 Removing data un-representative of the day

A key concern when averaging observations of very reactive species such as $C_5H_8$, for multiple sites over an area, is whether all of these observations are truly a representative average in a daily context.

The first step in ensuring a good temporal representation of averaged data is to ensure the raw data going into the average is actually representative of the time period over which it is reported. In most cases the data reported is simply a continuous average over a 1 hour period. However, measurements which are stated to be of a daily or monthly resolution are also incorporated. It is not always clear if these measurements are truly representative over the whole time period reported, therefore it is important to have accurate information regarding the sampling times. Both EMEP and WMO GAW provide data files which state the temporal resolution in the metadata as well as the sample start and end times. This is consistently used in EMEP but not so by WMO GAW, with sample times often left blank, however additional metadata provided on the GAWSIS network is used to determine sample lengths. AQS and NAPS measurements of $C_5H_8$ are reported as the average over a stated number of sampled hours. AirBase report different temporal resolution data files but do not give any information regarding the sample time, thus it cannot be determined if the data provided is representative over the entire time span it is reported. They do however have a metadata flag that shows if the measurement method is continuous or not. Thus daily and monthly AirBase data is only kept if it is flagged as continuous. The hourly grid of measurements is therefore filled for each time series based on the sample times derived, not over the stated raw time period.

Once happy that the measurements ingested into the data set are representative of the hours actually sampled, the next step is to determine if the observations are truly representative in a daily context. An algorithm is applied that looks at data for each time series day to day. A set of observations is defined as being representative over a day if there is a minimum of 6 hours represented with a maximum spacing between all the points of 4 hours (for NO the minimum number of hours changes to 3 – due to removal of nighttime values). Data on days which do not meet this requirement are set as NaNs. This quality check is not applied for CO flask measurements, with these measurements chosen to be retained in the data set due to the long lifetime of CO and the flask networks' excellent spatial coverage.

### 2.3.13 Extreme / suspect data

Extreme data is checked for by site for each species through a semi-automatic process. First an extreme limit is defined for each species, set empirically by looking at the probability distribution function (PDF) of each species' data combined: $O_3$ – 200 ppbv, NO – 200 ppbv, $NO_2$ – 150 ppbv, CO – 500 ppbv, $C_5H_8$ – 10 ppbv and manually screen sites with any data

exceeding this limit. In most cases any deemed "extreme" data is consistent with the rest of the site data, however some instances of very extreme data are removed.

There are some sites which are removed outright from processing as they have time series that show baseline shifts or very spiky data that appear to be from the result of instrumental or methodology failures.

### 2.3.14 Removing data un-representative of year

Many $O_3$ sites only operate for some months a year, as dictated by the USA EPA "$O_3$ season", typically April through October, when violations of air quality standards are highest. Additionally, AQS $C_5H_8$ measurements are in some cases limited to the summer months, when $C_5H_8$ emissions are strongest. A check is therefore included to ensure data is representative in an annual context. For example, the annual mean value would be biased if only summer time values were reported. For each site, the largest continuous data gap in each year is identified. Any year with a data gap of greater than 2 months (60 days) is deemed invalid. The first year of a time series is only flagged as being invalid if the subsequent year is also flagged as being invalid. The check of the subsequent year is intended to avoid removing the start of a many-year time series simply because the time series starts at a time other than January. A whole site is removed from the data set if all years of data are removed.

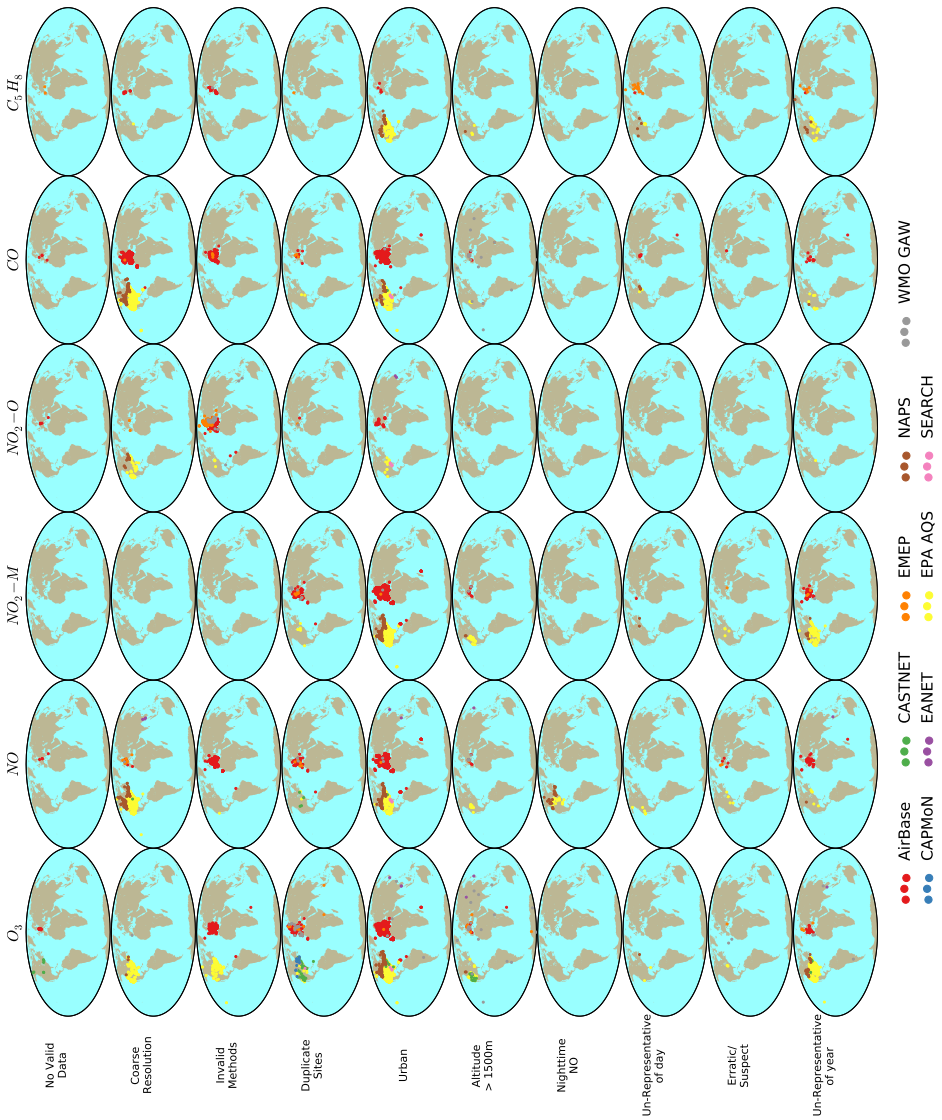


Fig. 2.3 Maps of sites screened out in data processing through each data quality check, by species, coloured by the data network.

| | $O_3$ | | NO | | $NO_2$-M | |
|---|---|---|---|---|---|---|
| Quality control step | Sites | Obs. | Sites | Obs. | Sites | Obs. |
| Original data | 7338 | 607 400 467 | 5359 | 303 392 066 | 6037 | 449 615 668 |
| No key meta | 7316 | 607 008 634 | 5330 | 302 948 752 | 6037 | 449 615 668 |
| Data flags | 7316 | 585 032 792 | 5330 | 288 305 789 | 6037 | 430 176 830 |
| Duplicate points | 7316 | 585 032 689 | 5330 | 288 305 689 | 6037 | 430 176 907 |
| No valid data | 7290 | 585 032 689 | 5326 | 288 305 689 | 6037 | 430 176 907 |
| Coarse resolution / Data plateau | 7077 | 559 097 300 | 4452 | 188 298 174 | 6037 | 405 407 024 |
| Invalid methodology | 6586 | 529 788 346 | 4157 | 177 497 769 | 6037 | 405 407 024 |
| Duplicate sites | 6395 | 511 630 738 | 4100 | 175 413 206 | 5942 | 400 434 296 |
| Urban sites | 2183 | 173 884 289 | 676 | 30 938 189 | 1131 | 68 017 801 |
| High altitude sites | 1995 | 159 539 741 | 631 | 29 565 812 | 1063 | 64 769 465 |
| Nighttime NO | 1995 | 159 539 741 | 584 | 15 521 939 | 1063 | 64 769 465 |
| Un-representative of day | 1992 | 159 460 005 | 577 | 15 272 330 | 1060 | 64 717 010 |
| Extreme / Suspect data | 1986 | 159 217 171 | 567 | 14 903 798 | 1055 | 64 266 677 |
| Un-representative of year | 1466 | 127 429 986 | 526 | 13 999 243 | 883 | 58 706 945 |
| | $NO_2$-O | | CO | | $C_5H_8$ | |
| Quality control step | Sites | Obs. | Sites | Obs. | Sites | Obs. |
| Original data | 1082 | 32 210 187 | 3983 | 243 512 708 | 535 | 4 733 121 |
| No key meta | 1041 | 31 743 016 | 3961 | 243 300 849 | 531 | 4 727 465 |
| Data flags | 1041 | 29 330 215 | 3961 | 234 659 324 | 531 | 3 768 592 |
| Duplicate points | 1041 | 29 330 212 | 3961 | 234 659 312 | 531 | 2 832 630 |
| No valid data | 1036 | 29 330 212 | 3957 | 234 659 312 | 529 | 2 832 630 |
| Coarse resolution / Data plateau | 919 | 26 145 010 | 2045 | 60 159 199 | 516 | 2 523 097 |
| Invalid methodology | 81 | 3 660 579 | 1805 | 56 257 239 | 471 | 2 500 035 |
| Duplicate sites | 78 | 3 481 944 | 1792 | 55 702 981 | 470 | 2 491 206 |
| Urban sites | 18 | 939 025 | 251 | 7 495 843 | 111 | 447 489 |
| High altitude sites | 15 | 778 629 | 222 | 6 715 753 | 106 | 446 962 |
| Nighttime NO | 15 | 778 629 | 222 | 6 715 753 | 106 | 446 962 |
| Un-representative of day | 15 | 777 416 | 210 | 6 706 440 | 79 | 397 505 |
| Extreme / Suspect data | 15 | 777 404 | 209 | 6 624 057 | 79 | 394 419 |
| Un-representative of year | 14 | 742 001 | 184 | 5 969 083 | 39 | 82 964 |

Table 2.5 Counts of the number of observations and sites after each quality control step, by species.

## 2.4 Final data sets

After this final check the data totals 3112 sites and 206,930,222 valid observations across all species, of high enough quality appropriate for global model evaluation. Figure 2.4 shows the location of the valid sites for each species set, coloured by the data network, and Fig. 2.5 shows the same sites but coloured by the mode measurement methodology. The vast majority of sites are located in the NH mid-latitudes, particularly in North America and Europe. The WMO GAW network tends to have the greatest spatial coverage (particularly for CO – due to the flask network) but does not have global coverage. The $O_3$ data set dwarfs all other data sets in terms of numbers of measurements, with 127,429,986 measurements over 1466 sites. Regarding solely $O_3$ precursor measurements, the NO and $NO_2$–M species sets have the largest number number of measurements, with 13,999,243 and 58,706,945 measurements over 526 and 883 sites respectively. There is evidently very little spatial coverage for the $NO_2$–O set relative to the $NO_2$–M set, with 742,001 total hourly observations made over 14 sites, showing how few $NO_2$ measurements have been made without the potential interference from the molybdenum converters. Additionally, there are only a small number of $C_5H_8$ measurements of sufficient representative quality for model evaluation, in total, 82,964 hourly measurements over 39 sites.

The number of valid sites that report data at each hour is shown for each species set by Fig. 2.6, coloured by the data network. The majority of observations initially stem from the USA AQS network, but over time the AirBase network in Europe comes to represent the largest number of contributing sites. $O_3$ measurements begin in 1971 at the WMO GAW site Hohenpeissenberg, but measurements only truly take off in significant numbers in 1980, with the AQS network providing $O_3$, NO and $NO_2$–M measurements. The large vertical width variability for the NO networks is due to the nighttime NO being removed every day, making the number of valid sites by hour vary significantly. There is also large vertical width variability for the WMO GAW curve for CO, this represents the number of sites jumping up on the 1st hour of each month due to the incorporation of the flask measurements. Figure 2.7 shows the PDF of all valid data between 2005 and 2010, by species set, for the observations and equivalently sampled model data from a global CTM, GEOS-Chem version v9.01.03 at $2^\circ \times 2.5^\circ$ resolution. The observed distributions of all species are log-normal to varying extents, with $O_3$ and CO being the most normally distributed. The model overestimates the magnitude of the log-normal distributions for both NO and $NO_2$–M, overestimating the fractional amount of low concentrations. This is the opposite for $NO_2$–O, underestimating the fraction of low concentrations. The model does a reasonable job of capturing the observed distributions of $O_3$, CO and $C_5H_8$.

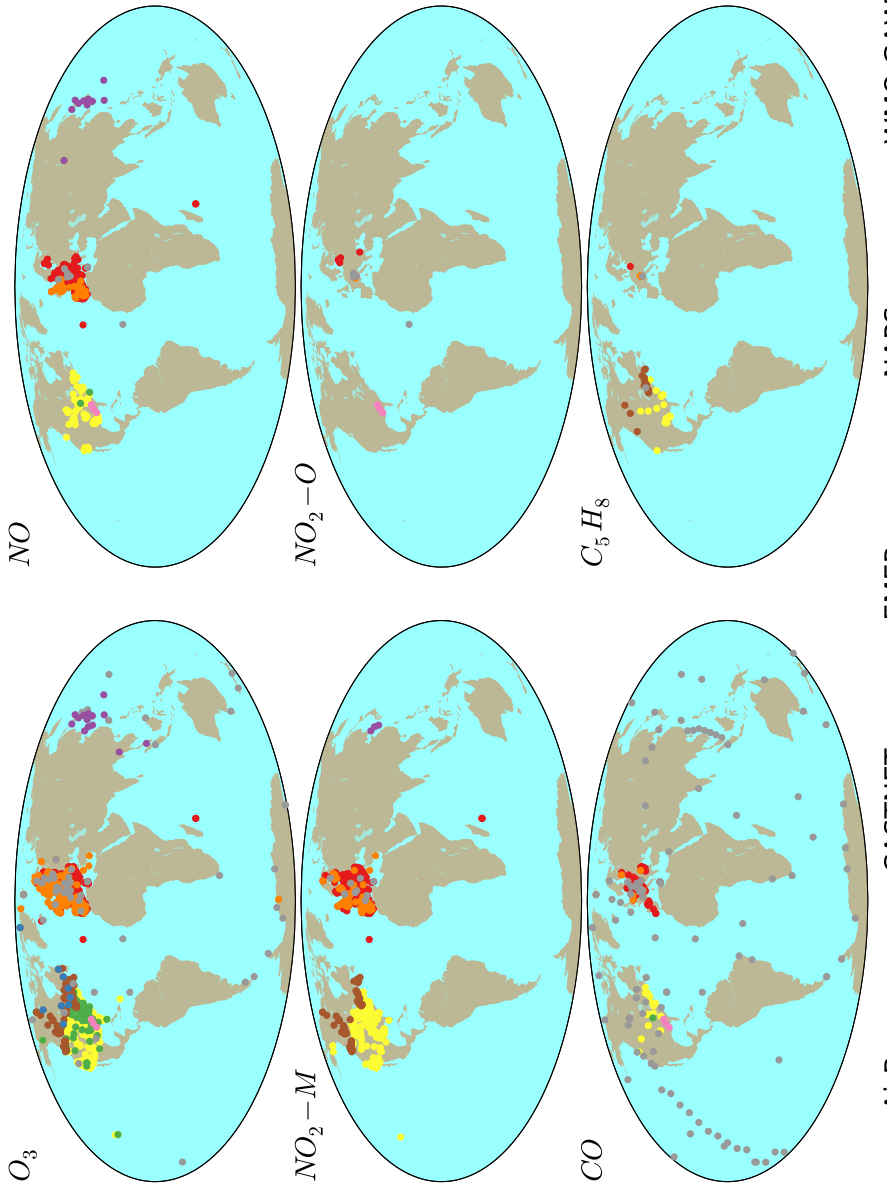


Fig. 2.4 Maps of finalised valid site locations, by species, coloured by the data network.

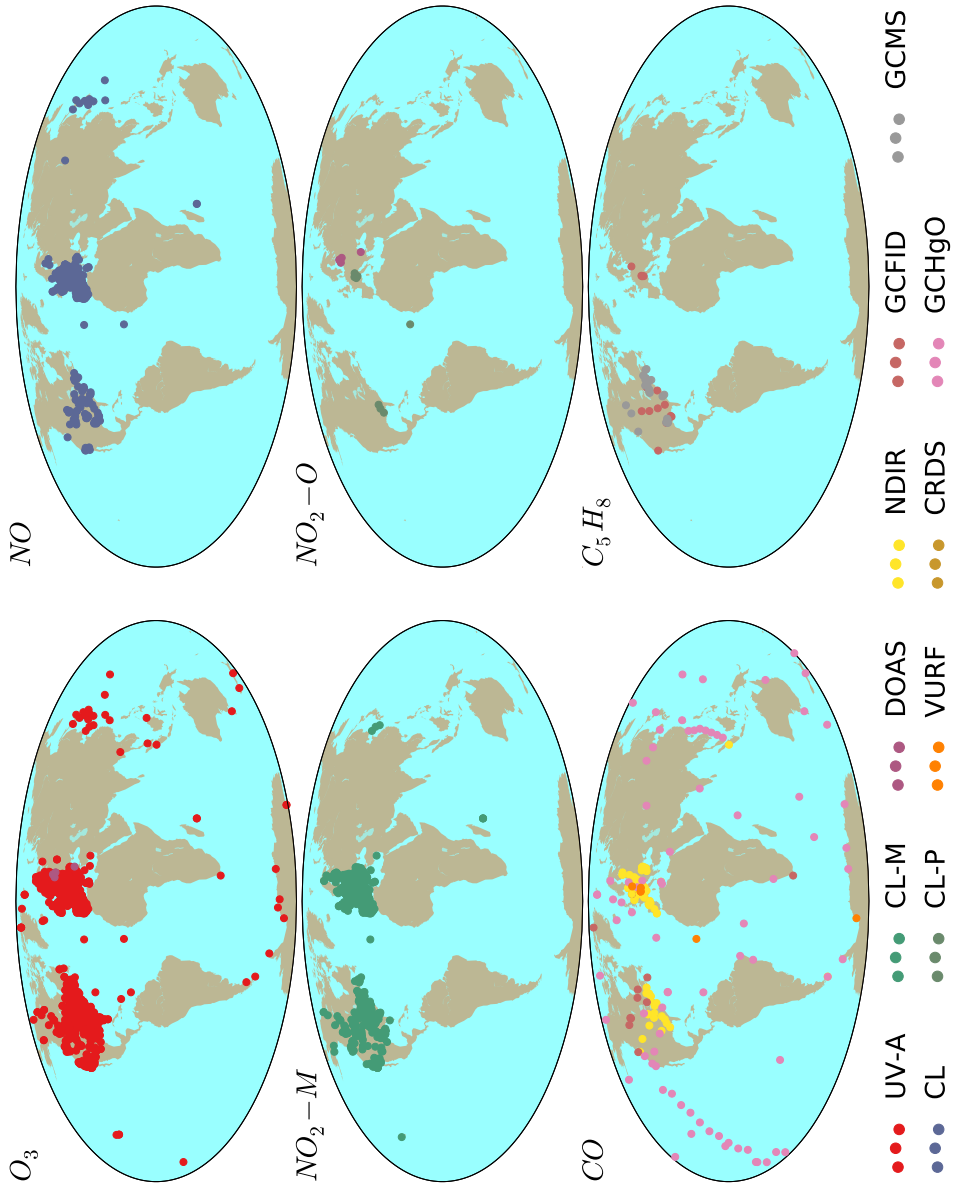


Fig. 2.5 Maps of finalised valid site locations, by species, coloured by the mode measurement methodology (acronyms defined in Tables 2.1–2.4).

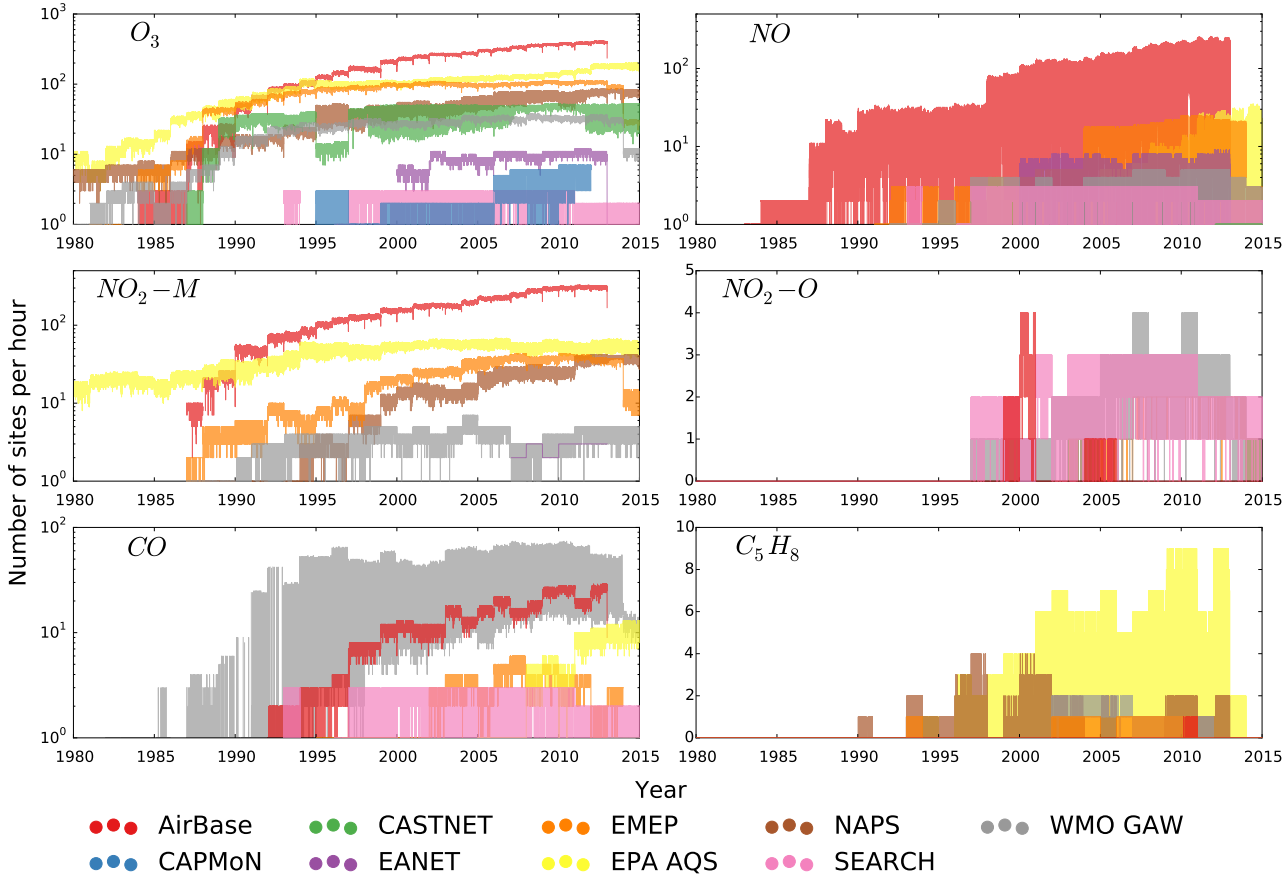


Fig. 2.6 The number of sites from each network reporting data for a given hour, from 1980 to 2015, by species. The colour represents the data network. The number of NO sites per hour fluctuates significantly because of the removal of nighttime NO. The number of WMO GAW CO sites per hour fluctuates due to the inclusion of the flask measurements, representing one hour a month.

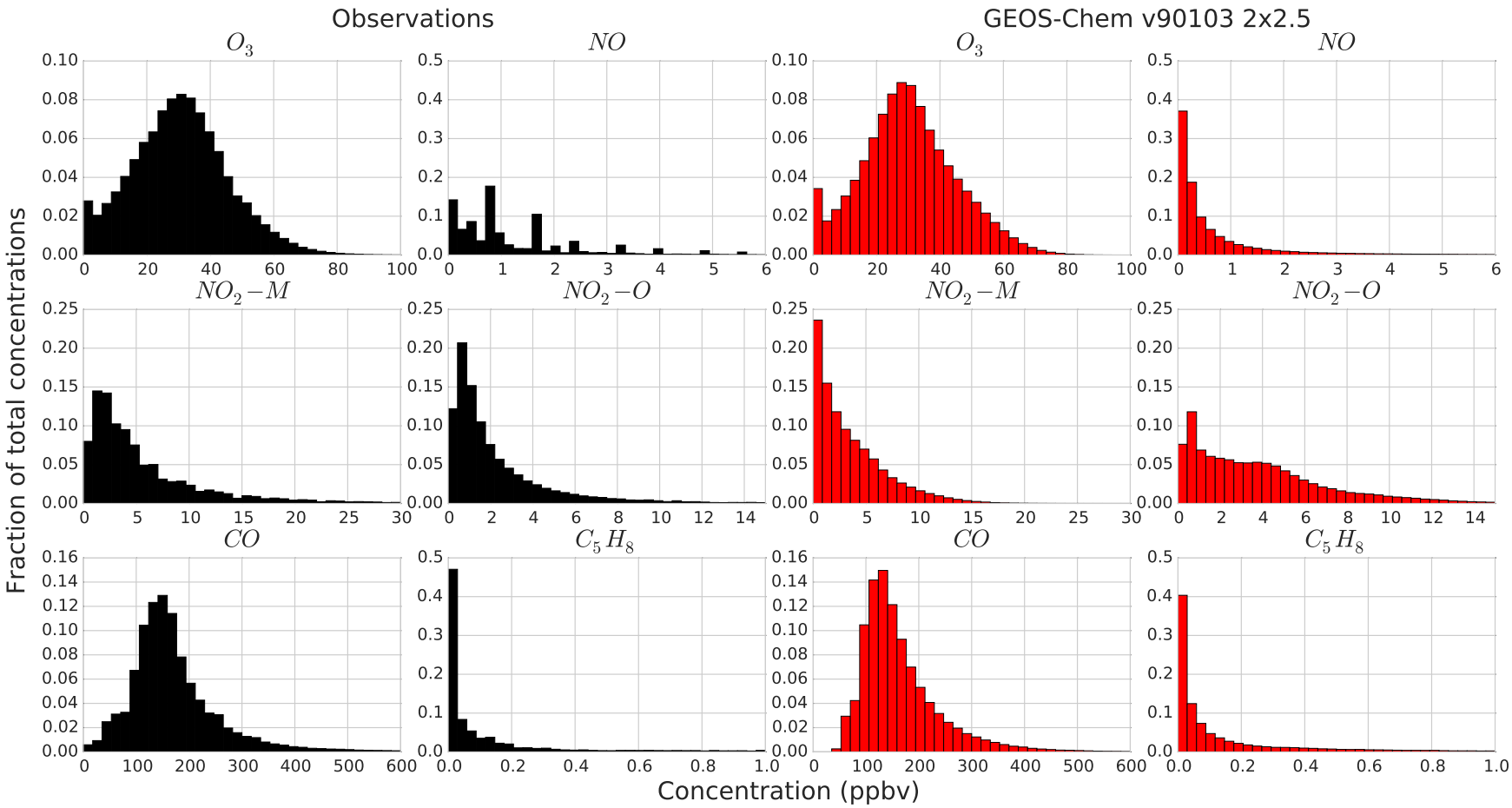


Fig. 2.7 PDF of all valid data between 2005 and 2010, by species, for observations (left panels, and in black) and GEOS-Chem (right panels, and in red). The sum of the bars equals 1.

## 2.5 Statistical overview of observations

With the processed data sets finalised, different statistical aspects in the observed data can be investigated, creating metrics that can also be used in the evaluation of global models. Metrics are chosen to attempt to accurately capture the probability distribution of each set of data, namely: the moments of the distributions (mean, temporal standard deviation, skewness, kurtosis) and percentiles (25th percentile, median, 75th percentile, 95th percentile, 99th percentile), these metrics defined in Table 2.6.

By calculating these metrics for every valid site, spatial variation across the metrics for each different species set can be assessed. Figure 2.8 shows the mean, temporal standard deviation, skewness and kurtosis spatially by each species set between 2005 and 2010. Due to the density of sites in North America and Europe, we choose to limit the map projection to solely to these areas for each species set, except CO and $O_3$. CO average concentrations are broadly homogenous across the NH, with the exception of higher averages in Europe. There is a clear divide in the CO average by hemisphere, with the SH sites having a concentration of 100–200 ppbv lower than the NH sites. The greatest standard deviations in CO come predominately over Europe. For $O_3$, the greatest averages and standard deviations are located in continental regions, particularly in central Europe and the western USA. For NO, the greatest averages and standard deviations are co-located in southern Europe, in the Po Valley region. Similarly for $NO_2$–M, the largest averages and standard deviations are co-located in central Europe and the Central Valley in the western USA. There do not exist enough valid $NO_2$–O sites to assess the spatial variability of the different metrics. The largest averages and standard deviations for $C_5H_8$ occur in the eastern USA, an area with significant biogenic emissions (Guenther et al., 2006). For $O_3$, oceanic and high latitude sites generally have a negative skewness (i.e. left side of distribution is longer or fatter than the right side), whereas continental sites are positively skewed (i.e. right side of distribution is longer or fatter than the left side). Whereas for the kurtosis, the pattern is more mixed, the clearest pattern being positive kurtosis of sites in central Europe and Japan (i.e. narrow peak distribution and fatter tails). For the $O_3$ precursors, almost all sites for all species sets show strongly positive kurtosis and skewness. This reflects the log-normal distributions for each of these species, as shown by Fig. 2.7. The most strongly positive values for both the skewness and kurtosis, for each these species, occur over continental areas (i.e. more extreme log-normal distributions).

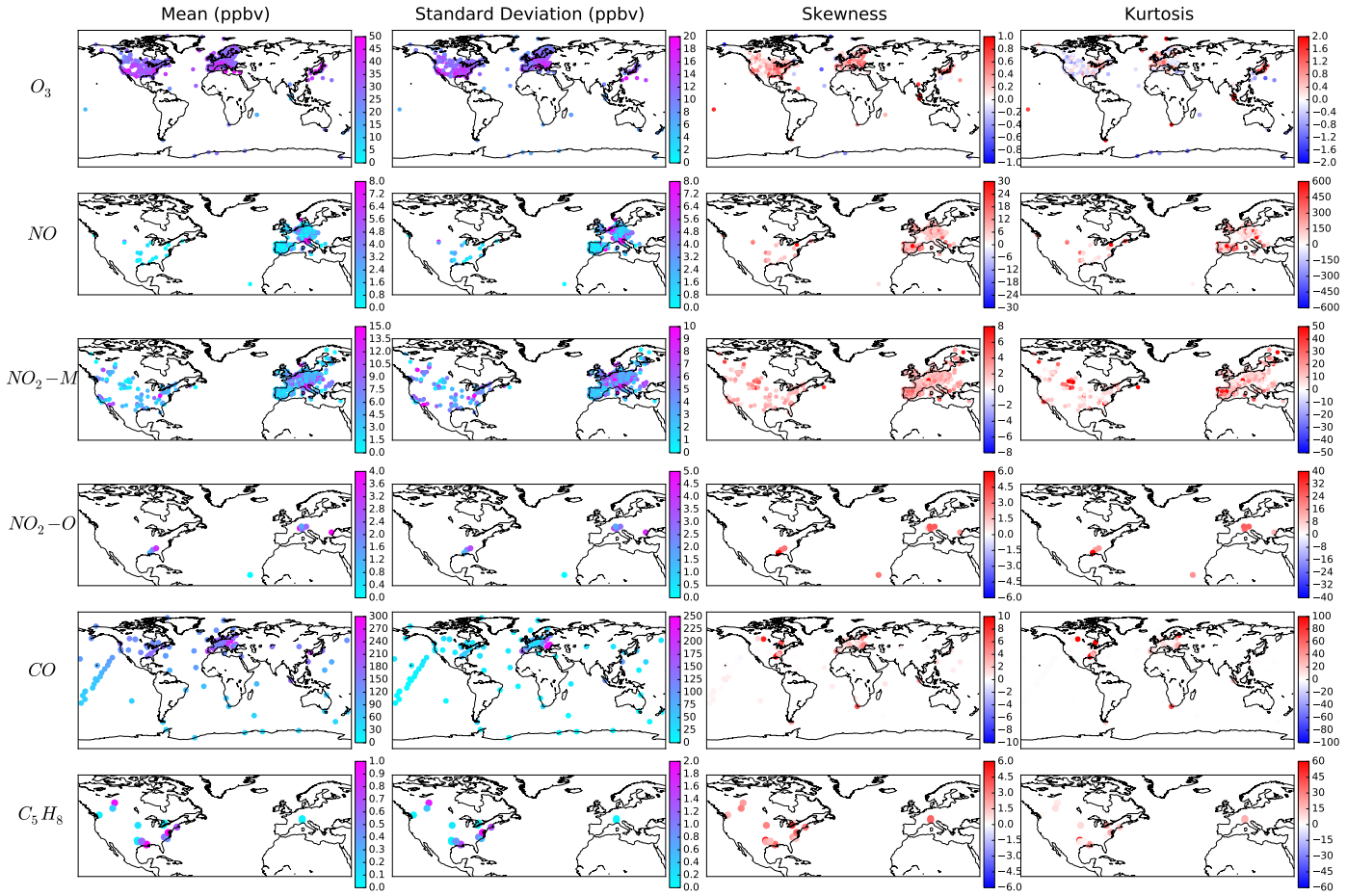


Fig. 2.8 Maps of observed statistical metrics (average, temporal standard deviation, skewness, kurtosis) for valid sites, by species, between 2005 and 2010.

| Primary Metric Filename | Definition |
|---|---|
| Mean_Gridded | Mean |
| Median_Gridded | Median |
| Skewness_Gridded | Pearson skewness |
| Kurtosis_Gridded | Zero-centred kurtosis |
| e.g. 25_Percentile_Gridded | 25th, 75th, 95th, and 99th percentiles |
| **Auxiliary Metric Filename** | **Definition** |
| Std_Dev_Time | Temporal standard deviation see Eq. (2.3) |
| Std_Dev_Sites | Spatial standard deviation, see Eq. (2.4) |
| count_Nsites | Number of sites, per grid box, per timestep |
| DataFrac | Fraction of hours represented, per grid box, per timestep |
| Mean_Altitude | Mean altitude of sites, per grid box, per timestep |

Table 2.6 Metrics prescribed for model evaluation via the BADC.

| Resolution | Grid details | Bottom left grid edge (°)* | |
|---|---|---|---|
| $1° \times 1°$ | Centred on 0° | −180.5 | −90.5 |
| $1° \times 1°$ | Centred on 0.5° | −180 | −90 |
| $2° \times 2°$ | ACCMIP (Lamarque et al., 2013) common resolution | −180 | −90 |
| $2° \times 2.5°$ | GEOS-Chem (Bey et al., 2001) | −181.25 | −91 |
| $2° \times 2.5°$ | GISS ModelE (Miller et al., 2014) | −178.75 | −90 |
| $2.5° \times 3.75°$ | UKCA (O'Connor et al., 2014) | −180 | −90 |
| $4° \times 5°$ | GEOS-Chem (Bey et al., 2001) | −182.5 | −92 |
| $4° \times 5°$ | GEOS-Chem/GCAP (Wu et al., 2008) | −182.5 | −90 |
| **Time Period** | **Notes** | | |
| Monthly | Calendar months; February has 28 or 29 days. | | |
| Annual | Calendar year; leap years are 366 days. | | |

*Latitudes less than −90° indicate half-boxes at poles

Table 2.7 Spatial and temporal resolutions of metrics available for model evaluation via the BADC.

## 2.6 Gridding data for model evaluation

In order to directly evaluate the reproducibility of the metrics outlined in Sect. 2.5 by CTMs/ESMs, a method for fairly comparing the observations with gridded model data must first be determined. Two options are available for this. Either model data solely in the grid boxes containing observations can be selected, or otherwise observations can be averaged onto a grid the resolution of the model. The latter approach is chosen as it provides a method for us to simply redistribute the compiled data sets without violating the rights of the original data providers. Further, metrics are calculated in each grid box over set periods (monthly and annual), giving robust metrics that can be fairly compared with equivalent model derived metrics, both spatially and temporally.

Multiple primary metrics are thus calculated (outlined in Sect. 2.5, and defined in Table 2.6) in each grid box derived from all valid hourly data over set time intervals from all sites contained within each grid box, designed to fairly capture the probability distribution of concentrations over each gridded period. Metrics are calculated over a range spatial grid configurations (grids of $1^\circ \times 1^\circ$ or coarser) and temporal resolutions (monthly and annual), detailed by Table 2.7. All calculated metics are output in a standalone gridded netCDF file for each spatial/temporal combination, for each species set. This culminates in 80 different output files.

Additionally, several auxiliary metrics are output that allow determination of the representivity of the gridded primary metrics, again defined in Table 2.6. The first metric is the temporal standard deviation of the data going into each gridded period (i.e. monthly or annual), termed "Std_Dev_Time" in the output files, given by:

$$\sigma_{\bar{x}} = \sqrt{\frac{1}{N-1}\sum_{t}^{N}(\overline{c_x}(t) - \bar{c})^2}, \tag{2.3}$$

where $\overline{c_x}(t)$ is the average concentration $c$ over all $M$ sites in the grid box, at a given hour $t$ for $N$ hours within the time interval (e.g. year). $\bar{c}$ represents the grid box average over all $M$ sites and $N$ hours. A high value of $\sigma_{\bar{x}}$ suggests a large degree of variability associated the the grid box temporal average, and therefore that any model-measurement disagreement in this grid box can possibly be attributed to excessive temporal averaging.

The second auxiliary metric provided is the spatial standard deviation of the data over the different sites going into each gridded period, termed "Std_Dev_Sites" in the output files, given by:

$$\overline{\sigma_x} = \frac{1}{N}\sum_{t}^{N}\sqrt{\frac{1}{M-1}\sum_{x}^{M}(c(x,t) - \overline{c_x}(t))^2}, \tag{2.4}$$

where $c(x,t)$ is the concentration $c$ at site $x$ of $M$ sites in the grid box at time $t$ of $N$ hours in the time interval (e.g. year). A high value of $\overline{\sigma_x}$ suggests there is large variability between the data from the multiple sites in the gridded period, and that any model–measurement disagreement in this grid box can be potentially attributed to sub-grid

scale variability in the observations, which might not be resolved by the model. This metric is set as NaN If there is only a single site contained in a grid box.

Additional auxiliary metrics output are: the number of sites going into each gridded period, termed "count_Nsites"; the fraction of hours in each gridded time interval that have a minimum of one valid measurement across all sites, termed "DataFrac"; and the average altitude of the sites going into each gridded period, termed "Mean_Altitude".

Each output file also contains additional core variables: "latitude" and "longitude" values for the grid (centres of grid boxes) and "time" (seconds from 1970). A metadata dictionary is also included (defined in Sect. 2.3.2 and shown by Fig. 2.1) associated with every valid site in each data set, given by the "meta_values" variable, the names of the respective field names given by the "meta_fields" variable. Valid measurement methodologies for each site are reported by the "methods" variable, along with the timespan of their usage by the "methods_times" variable (seconds from 1970). The gridded data sets are made publicly available in netCDF-4 via the British Atmospheric Data Centre (BADC). The data sets are openly available, only requiring free registration with the Centre for Environmental Data Archival (CEDA) for access.

The application of the final gridded data sets for the stated aim of model evaluation is now briefly demonstrated through comparison with GEOS-Chem, shown in Fig. 2.9. Gridded monthly metrics (average, temporal standard deviation, skewness, kurtosis), for each species set, are compared with equivalently calculated output from the model, between 2005 and 2010. Each point is coloured by the observed spatial standard deviation ("Std_Dev_Sites") to potentially highlight reason for any model–measurement disagreement. For $O_3$, GEOS-Chem generally well captures the monthly averages, despite considerable scatter. The monthly temporal standard deviations are also well captured, despite systematic underestimates of the highest observed values, these biases correlating well with the spatial standard deviations, suggesting biases may be associated with sub-grid scale variability in the observations that the model is not able to capture. The model significantly underestimates the majority of monthly averages and temporal standard deviations for both NO and $NO_2$–M, with deviation from the model increasing towards the high-end of the observational values, also correlating very well with the spatial standard deviations. Conversely, the model overestimates these metrics on average for the $NO_2$–O set. CO is the best represented species, with the model capturing a large amount of the monthly averages and temporal standard deviations, only tending to underestimate these metrics as they increase towards more extreme values. The model also does a reasonable job at capturing the monthly averages and temporal standard deviations for $C_5H_8$, again well capturing the low-end of values, underestimating values only as they become more extreme. The model shows very little skill in representing both the kurtosis and skewness, underestimating the majority of values for these metrics for most of the $O_3$ precursors, except $C_5H_8$, for which it overestimates.

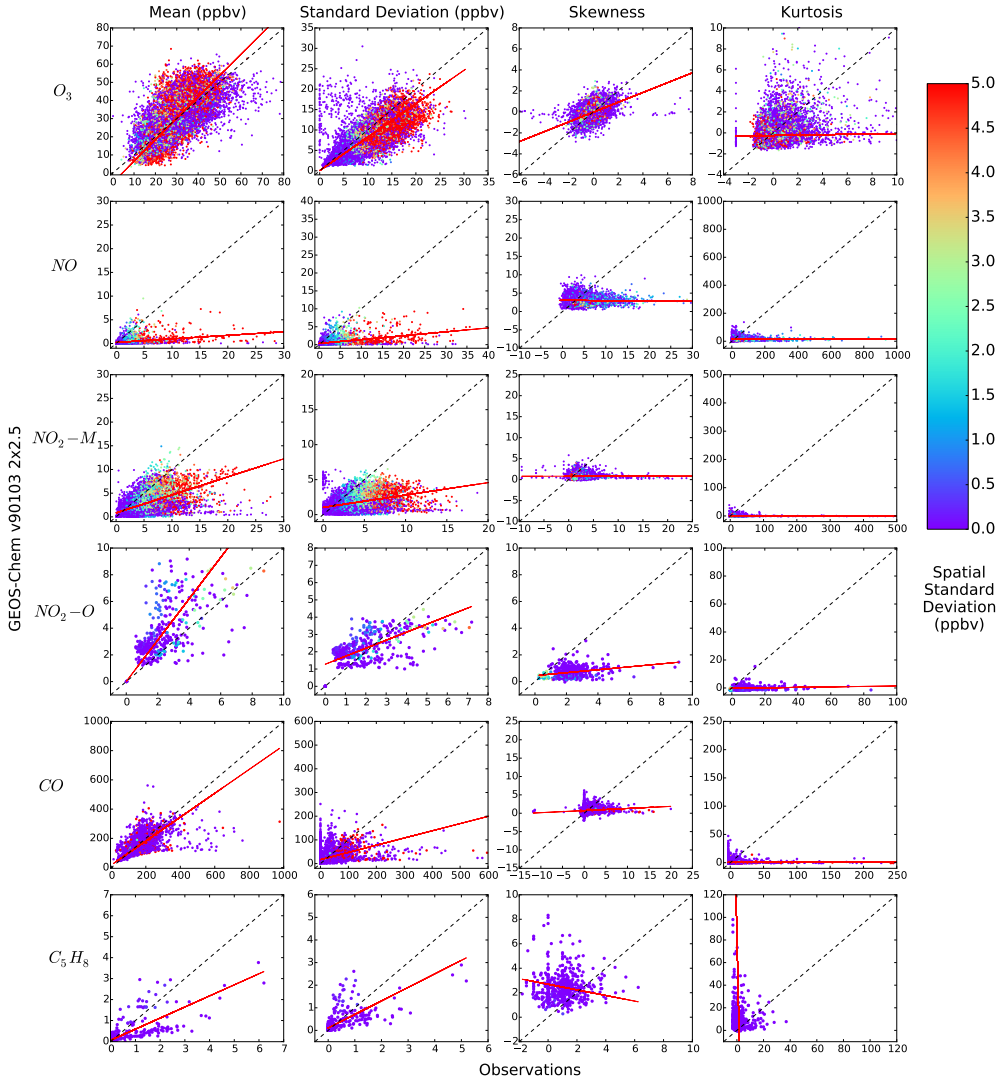


Fig. 2.9 Comparison of monthly gridded statistical metrics (average, temporal standard deviation, skewness, kurtosis) between observations (x axis) and GEOS-Chem (y axis) for the years 2005–2010, by species. Points are coloured by the spatial standard deviation between sites going into each gridded metric. The red best-fit line is the orthogonal least-squares regression.

## 2.7 Recommendations for data providers

The work undertook during this evaluation has revealed a number of issues associated with the reporting of data and or metadata. These issues have taken a significant time resolving and in many instances significantly increase the uncertainty on measurements, and in some cases make large amounts of data unusable. Recommendations are thus provided to the atmospheric chemistry measurement community based on experiences gleaned through this work.

Significant work in this evaluation has involved the determination and subsequent standardisation of measurement methodologies. Separating the $NO_2$ measurements using either molybdenum or photolytic converters for example was a hugely time consuming task caused in main by a lack of information reported in the metadata regarding the type of converter used, with any determination achieved solely through manually checking instrumental manuals. Additional methodological details are also rarely given. A lack of detail in general regarding calibration procedures for example is inherent across the networks with the exception of WMO GAW, which brings uncertainty in cases on measurements. For example, the uncertainty associated with the calibration of CO, with potentially multiple different scales adopted by different data networks, can not be estimated due to a lack of information given regarding the calibration procedures by most networks. In all cases the reporting of additional methodological details reduces uncertainty associated with measurements, and any additional details should be reported in all cases. Significant effort was also spent standardising methods across all data networks, with inconsistencies inherent even in-network, with 1000s of different methods by syntax. In some cases the measurement methodologies reported can be entirely meaningless, leading associated data to be screened out. Internal network processing that standardises methods and thus prevents the reporting of erroneous metadata would reduce end user efforts and save having to throw away significant chunks of potentially valid data.

Limits of detections are also rarely reported in the metadata (with the exception of AQS, which tend to be applied inconsistently). In some instances data plateaus at fixed concentrations, where the instrument hits the limit of detection, imposing a high average bias. A semi-automatic quality check is applied that removes instances like this, however the reporting of limits of detections by each network for each measurement point would be able to resolve these instances more simply.

Another source of uncertainty discovered in this work was the reporting of sampling times. Some daily/monthly stated resolution data was forced to be discarded from the AirBase network due to a lack of confidence that the measurements are representative over the stated resolution. Manual analysis was needed to assure $C_5H_8$ AQS measurements were truly representative over the sample times stated. Manual filling of sample times was necessary also for some WMO GAW network measurements using the GAWSIS web platform. Indications of actual sampling times would be useful for all networks.

The choice of AQS to report the majority of CO data at 100 ppbv resolution makes valid CO data sparse in the USA. NO is also reported in coarse intervals ($> 1$ ppbv) by a

variety of networks, leading to minimal NO data over the western USA in the late 2000s. There is clearly a disconnect between the purpose of data being measured for air quality purposes and that to better the understanding of NOx/CO and $O_3$ chemistry. It is not known if data is measured at a higher resolution and simply not reported, however, the measurement and reporting of the data at a higher resolution would satisfy both legislative and scientific purposes.

The lack of a consistent definition of an "urban" site imposes significant uncertainty on any model–measurement comparison. What one network or person deems to determine an "urban" site can vary significantly. This is attempted to be defined using a 3 step process: using the network provided land use classifications, a global anthropogenic land use classification and a final semi-automatic extreme average screening check. This level of detail was deemed necessary when a preliminary data set produced for CO showed huge deviations with GEOS-Chem, particularly in Europe. On further investigation it turned out some sites in Europe, located in the close proximity of major roads, were majorly biasing the data set. This underlines the importance of the accurate removal of urban influenced sites. More complex classification efforts have been undertaken using spectral analysis to group sites based on the likeness of their spectral components into urban, suburban and rural classes (Solazzo and Galmarini, 2015). Any effort that could be made to strictly define what constitutes an urban site, or to provide a global land use classification data set by a global coordinative network (i.e. WMO GAW) or project group (i.e. Tropospheric Ozone Assessment Report) would be a great help in standardising the numerous model evaluations that are undertaken each year, and would be greatly appreciated by the atmospheric chemistry community.

# Chapter 3

# Spectral analysis: a framework for application to atmospheric composition data

## 3.1 Introduction

Depending on the emphasis of the study, a range of methodologies have been applied to model–measurement comparisons for $O_3$. Many have used comparisons to "long-term" surface $O_3$ observations as a basis (Tanimoto et al., 2005; Jonson et al., 2006; Oltmans et al., 2006; Derwent et al., 2008; Cooper et al., 2012; Logan et al., 2012; Hess and Zbinden, 2013; Oltmans et al., 2013; Parrish et al., 2013, 2014). Typically, these observations are averaged onto a monthly timescale and compared to a similarly averaged model output, and the two compared as a function of time. This offers some advantages. The averaged measurement and modelled data sets are small, making comparisons compact and easy to understand. It also removes the short-term variability ($<$ monthly) that may not be of interest to the researchers. Additionally, the uncertain data quality of higher resolution measurements can be improved through the averaging process.

However, this approach also suffers from a range of limitations. Processes occurring on timescales shorter than monthly include photochemistry, deposition, transport, and emission, all of which are important to the success of the model. By focusing on the monthly variability alone other timescales are ignored, which may lead to an insufficiently robust analysis of model performance. What is required is a methodology to assess model fidelity on a range of timescales simultaneously. Spectral methods offer this approach, but in atmospheric chemistry have only been used in a small number of studies, and specifically for $O_3$ in a limited sense, fitting stand-alone sine waves to time series (Schnell et al., 2015) and applied to a small selection of coarse monthly average data (Parrish et al., 2016).

In this chapter, a methodology for the spectral analysis of atmospheric composition data is outlined. In Section 3.2 the mathematical basis and workings of the Discrete Fourier Transform are detailed (the fundamental cornerstone of spectral analysis). Section 3.3 describes an extension of the Discrete Fourier Transform methods, enabling handling of

significantly gapped time series, though use of the Lomb-Scargle Periodogram. Section 3.4 details a major limitation of all spectral methods: spectral leakage, and describes how this issues is handled though this work. In Sect 3.5 synthetic data is used to test the validity the described spectral methods.

## 3.2 DFT/FFT

Across the universe there are numerous examples of periodic oscillations. Planets rotate around stars, planets rotate on their axes, sound is carried through oscillations of air molecules etc. When measuring any variable, relevant periodic processes impose variability across multiple frequencies, of a range of magnitudes. Every time series can therefore be thought of as a combination of simpler waves. The decomposition of a time series into a set of orthogonal periodic functions was first suggested by Joseph Fourier in 1822. The method translates information from the time domain to the frequency domain, splitting the time series into multiple sinusoidal waveforms of many frequencies. This allows the variability imposed by independent periodic processes across the time series to be quantified, or even recognised. This technique is used extensively in disciplines such as engineering and geophysics. Using a computer to compute this decomposition is termed the Discrete Fourier Transform (DFT). However, this method is computationally intense, which led to the development of the Fast Fourier Transform (FFT).

### 3.2.1 Founding

The FFT produces the same output as the DFT, the only difference being the speed taken for the calculation, with the FFT optimised to run on modern computers. The principles behind the DFT are well founded. They stem from the finding of the 19th century physicist Joseph Fourier that any continuous periodic time series signal can be represented as a set of sinusoidal functions. The equation for the DFT is given by:

$$DFT[k] = \frac{1}{N}\sum_{n=1}^{N} y(t_n)\cdot e^{xi} \tag{3.1}$$

$$x = k\frac{n}{N}2\pi, \tag{3.2}$$

where $N$ is the total number of time series samples, $n$ is the time series sample number, and $y(t_n)$ is a time series sample at time $t_n$. The complex exponential $e^{xi}$ provides a succinct way of describing circular rotation, with $x$ representing the phase angle of the rotation (in radians), at the $k^{\text{th}}$ frequency (of $N$ total frequencies). Equations 3.1 and 3.2 show the output of the DFT is derived from the multiplication of a time series with complex exponential functions of multiple frequencies. Leonhard Euler derived the fundamental identity:

$$e^{xi} = \cos(x) + \sin(x)i \tag{3.3}$$

Which for the case of $x = \pi$ gives the following expression:

$$e^{i\pi} + 1 = 0 \tag{3.4}$$

Eq. 3.3 demonstrates that the output of the DFT can be equivalently derived by multiplication with pairs of sine and cosine waves of multiple frequencies. Both forms of notation provide mathematically identical, but conceptually different methods for the translation of a time series into sinusoidal functions of multiple frequencies. Multiplication by $e^{xi}$ can be thought of as breaking a time series into cosine waves of multiple frequencies, each with a specific amplitude (half peak to trough difference) and a phase shift ($\theta$, point in cycle of the peak of the sinusoid, in radians). Whereas multiplication by $\cos(x) + \sin(x)i$ can be thought of as breaking the time series into pairs of sine and cosine waves of multiple frequencies, each with specific amplitudes. The workings of the DFT are generally represented in complex form. Complex numbers uniquely allow the representation of two variables as a single vector, allowing elegant representation of the mathematics of the DFT.

Both of the terms of Eq. 3.3 provide different forms of notation for the description of circular rotation as a function of the phase angle $x$ (analogous to time), representing the unit circle when visualised in two dimensions on the complex plane. Figure 3.1 provides an illustration of the equivalency of both forms of notation, demonstrating the close relationship between the sinusoidal functions (sine and cosine) and the unit circle on the complex plane. If we place a point on a circle, the position of this point can be described in terms of x and y coordinates, or in complex space as real and imaginary coordinates termed rectangular notation. The unit circle is defined as having a radius of 1. Through the rotation of a point around the unit circle (i.e. changing $x$, analogous to the evolution of time), the change in the rectangular coordinates describing this point, allows the periodic nature of the cosine and sine functions to be understood. The change in the y-coordinate (given by the red line in Fig. 3.1a) as a function of $x$, represents the periodic oscillation of a sine wave (Fig. 3.1b). The change in the x-coordinate as a function of $x$ (given by the blue line in Fig. 3.1a), represents the oscillation of a cosine wave (Fig. 3.1c). Therefore, the position of any point on a circle can also be defined trigonometrically, with the y-coordinate given by $\sin(x)$, and the x-coordinate is given by $\cos(x)$. On the complex plane, these coordinates can be generalised as:

$$A\cos(x) + B\sin(x)i, \tag{3.5}$$

where $A$ and $B$ are the amplitudes of the cosine and sine waves (half peak to trough difference), both 1 in the DFT process, therefore Eq. 3.5 simplifies to $\cos(x) + \sin(x)i$, as in Eq. 3.3.

The position of a point on a circle can also be described in terms of amplitude (radius of circle, 1 for unit circle), and phase angle ($x$), termed polar notation. On the complex plane, this notation can be generalised as:

$$Ce^{xi}, \tag{3.6}$$

where $C$ represents the amplitude of the complex exponential function, which is 1 in the DFT process, with Eq. 3.6 therefore simplifying to $e^{xi}$, as in Eq. 3.3.

The rectangular and polar representations are mathematically equivalent, with the conversion between these simply achieved through trigonometry. Although the polar form is typically used when interpreting the output of the DFT, the rectangular form is useful for understanding its workings.

### 3.2.2 Correlation

Focusing on the rectangular notation, the output of the DFT can be seen as being calculated by performing dot products of the time series with pairs of sine and cosine waves at multiple frequencies. The dot products quantitatively measure the degree to which the time series is correlated with both sine and cosine waves at a specific frequency. A resultant value greater than 0 can only be obtained if there is a degree of correlation, indicating there is periodic variability contained in the time series at the frequency of interest.

Just as sinusoidal functions can be described through rectangular and polar notation as a function of $x$, the DFT produces output that can be equivalently be thought of in rectangular and polar terms, but rather as a function of frequency ($f$) (i.e. the number of cycles of $x$ over $t$). The resultant dot products at each frequency give rectangular coordinates that represent the amplitudes of sine and cosine waves found in the time series signal at that frequency, which in the complex domain can be represented as:

$$A\cos(2\pi ft) + B\sin(2\pi ft)i, \tag{3.7}$$

where $A$ and $B$ are the amplitudes of the cosine and sine waves, $t$ is time and $f$ is the frequency (i.e. the number of cycles of $x$ over $t$). This can be equivalently thought of in polar terms, with the addition of a pair of cosine and sine waves of the same frequency producing a cosine wave that can be described with an amplitude and phase shift ($\theta$), which in the complex domain can be represented as:

$$C\cos(2\pi ft + \theta)i, \tag{3.8}$$

where $C$ is the amplitude of the cosine wave, and $\theta$ is the phase shift (point in cycle of the peak of the sinusoid, in radians). Both notations therefore allow sinusoids at each frequency to be described by simply 2 values. Dot products are taken with both sine and cosine waves at each frequency as this results in a derived amplitude (in polar terms) at each frequency that is constant, no matter the phase shift of the time series. The resultant dot products are additionally multiplied by the $\frac{1}{N}$ term to normalise for the length of the time series.

The output of the DFT/FFT is typically given in rectangular form, with the dot product pairs at each frequency reported as a complex number, with the cosine dot product representing the real term, and the sine dot product representing the imaginary term. An illustration of the correlation calculation step at a specific frequency ($\frac{1}{365}$ cycles per day) is given by Fig. 3.2. The equivalency of the output rectangular notation to the polar

representation is demonstrated on the complex plane by Fig. 3.2d. Figure 3.3 expands on this, plotting the waveforms that the DFT output describes (over 1 cycle of $x$), both in rectangular (Fig. 3.3b) and polar form (Fig. 3.3c).

The mathematical relationship between the sine and cosine waveforms forms the basis of the DFT, they are always $\frac{\pi}{2}$ radians out of phase with one another, said to be orthogonal, mathematically defined as having a dot product of 0. Therefore the correlation with each sinusoid at a frequency is independent of the other. Sine and cosine waveforms at frequencies multiples of one another are also orthogonal. Therefore in the entire DFT calculation, there is no duplicate information encoded, with the resultant energy in the frequency domain equal to that in the time domain (after normalisation), known as Parseval's theorem. This is shown by:

$$\sum_{n=1}^{N} y(t_n)^2 = \frac{1}{N} \sum_{k=1}^{N} Amplitudes(k)^2 \tag{3.9}$$

The left hand side of the equation represents the energy contained in the time domain, and the right hand side represents the energy in the frequency domain. Energy is proportional to the amplitude squared, so the sum of the squared individual time series samples is equivalent to the sum of the amplitudes squared in the frequency domain (after normalisation). Therefore, the addition of the polar described sinusoids at each frequency (with the appropriate normalisation) will reform the original time series.

### 3.2.3 Frequencies

Each complex number output from the DFT relates to a particular frequency estimated at. The number of frequencies is determined by the number of time series samples ($N$), with $\frac{N}{2}$ integer frequencies (i.e. 1 cycle over $N$, 2 cycles over $N$,...) between 0 and half the sampling frequency ($f_s$), termed the Nyquist limit ($f_{Nq}$), and a mirrored set of negative frequencies. Waveforms at the $f_{Nq}$ limit thus make $\frac{N}{2}$ complete cycles over $N$ points. The $f_{Nq}$ limit comes from the Nyquist–Shannon sampling theorem, that dictates that the sampling frequency should be at least twice that of the highest frequency of variability contained in the signal. Sampling data at frequencies less than twice of this will result in the high frequency variability being under-sampled, making it appear as if it has a different frequency, potentially interfering with the estimation of variability existing at the frequencies it is shifted to. This issue is commonly termed "aliasing". It is therefore necessary to tailor sampling based on the signal wished to be analysed. As it is not possible for any valid information to be derived on frequencies greater than $f_{Nq}$, frequencies of the DFT only run to this limit. The DFT output at a frequency of zero represents a special case. Where $f = 0$, a cosine wave is a constant 1, and a sine wave is a constant 0. This results in the real term of the complex number representing the average of the time series (after normalisation), and the imaginary term equalling zero.

Complex exponential functions can rotate both forwards and backwards in time (i.e. $e^{xi}$ can rotate clockwise or anti-clockwise on the unit circle), this gives rise to the idea of negative frequencies. As both types of rotation are equally valid representations, every

complex exponential function is the product of an equal contribution of positive and negative frequency components. The negative frequency components are an exact mirror of the positive frequency components, and by convention are almost always discarded. As a result, a multiplication by a scaling factor of $\frac{2}{N}$ is needed to be applied for the positive frequency output, to correct for the loss of this information.

As the frequencies estimated at can not be set manually, a spectral technique termed zero-padding is often used to increase the frequency resolution, achieved by appending large numbers of zeros to the end of the time series. This technique relates to the nature of the DFT, in that it is actually a sampled form of Joseph Fourier's derived theorem (referred to as the Fourier Series), which specifically states that a continuous periodic signal (which extends from negative to positive infinity) can be equally represented in terms of an infinite sum of sine and cosine functions. Computers can only handle data which is finite and discrete, therefore the DFT provides a computationally viable method of estimating the Fourier Series. Zero-padding simply provides a method to sample more finely the theoretical Fourier Series.

### 3.2.4 Limitations

One of the major limitations of the DFT is that it is cannot accurately handle datasets with irregular time intervals. In the presence of data gaps the orthogonality of the sinusoids breaks down, and thus so does the DFT. Some kind of interpolation is needed to provide data on a regular time interval which biases results (particularly at high frequencies) (Press et al., 1992; Schulz and Stattegger, 1997; Musial et al., 2011; Rehfeld et al., 2011). Atmospheric observations inherently have irregular time intervals due to instrumental issues (power breaks, instrument failures, calibration times etc.) so another numerical method is needed to investigate the spectral information they contain.

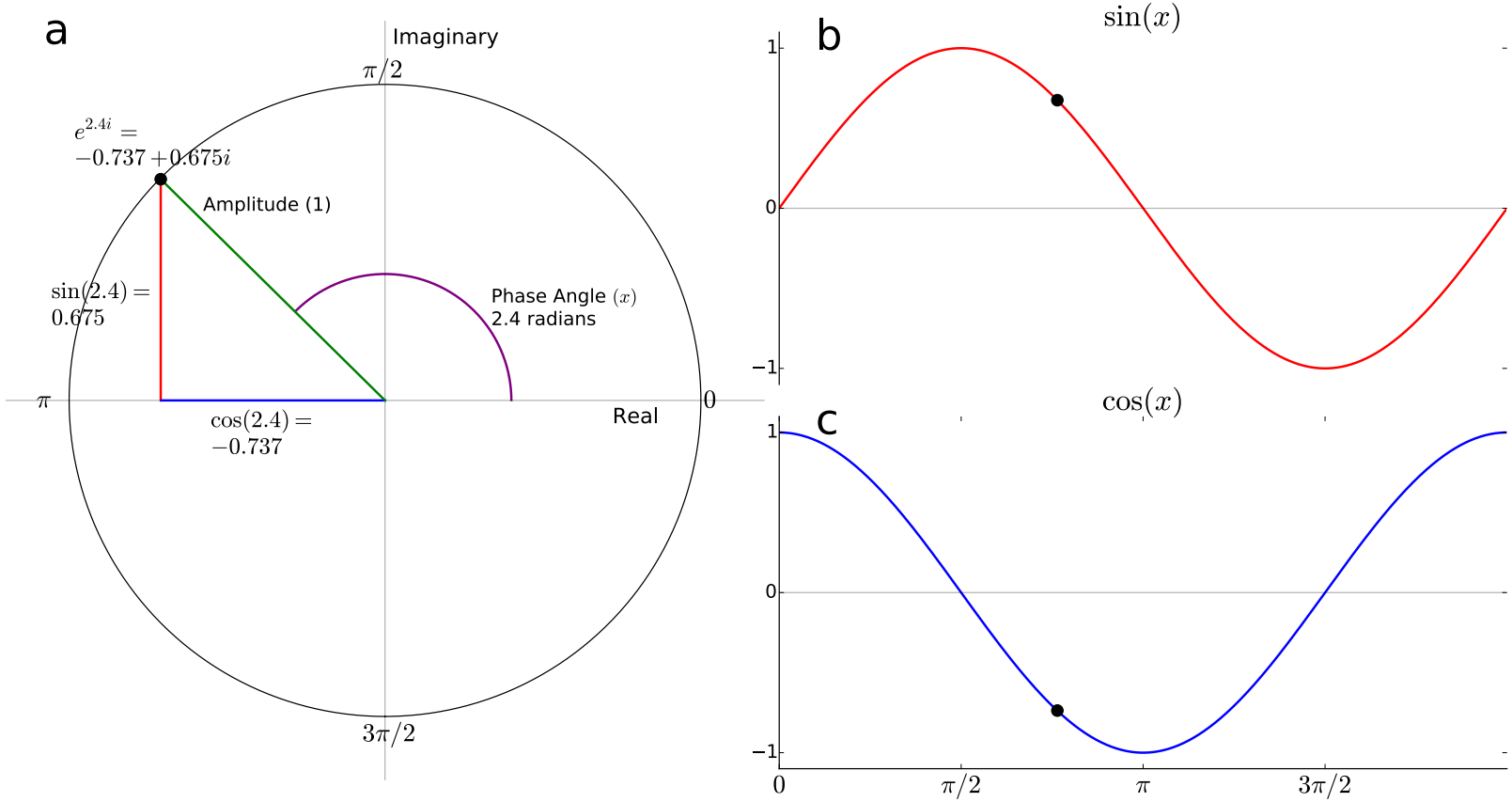


Fig. 3.1 Demonstration of the close relationship between the unit circle and the sine and cosine functions. **(a)** Unit circle in complex space illustrating the equality between the representation of periodic circular rotation by a complex exponential (polar notation) and in terms of sine and cosine (rectangular notation). **(b)** Illustration of the evolution of $\sin(x)$ with rotation of a point around the unit circle, representing the sine function. **(c)** Illustration of the evolution of $\cos(x)$ with rotation of a point around the unit circle, representing the cosine function.

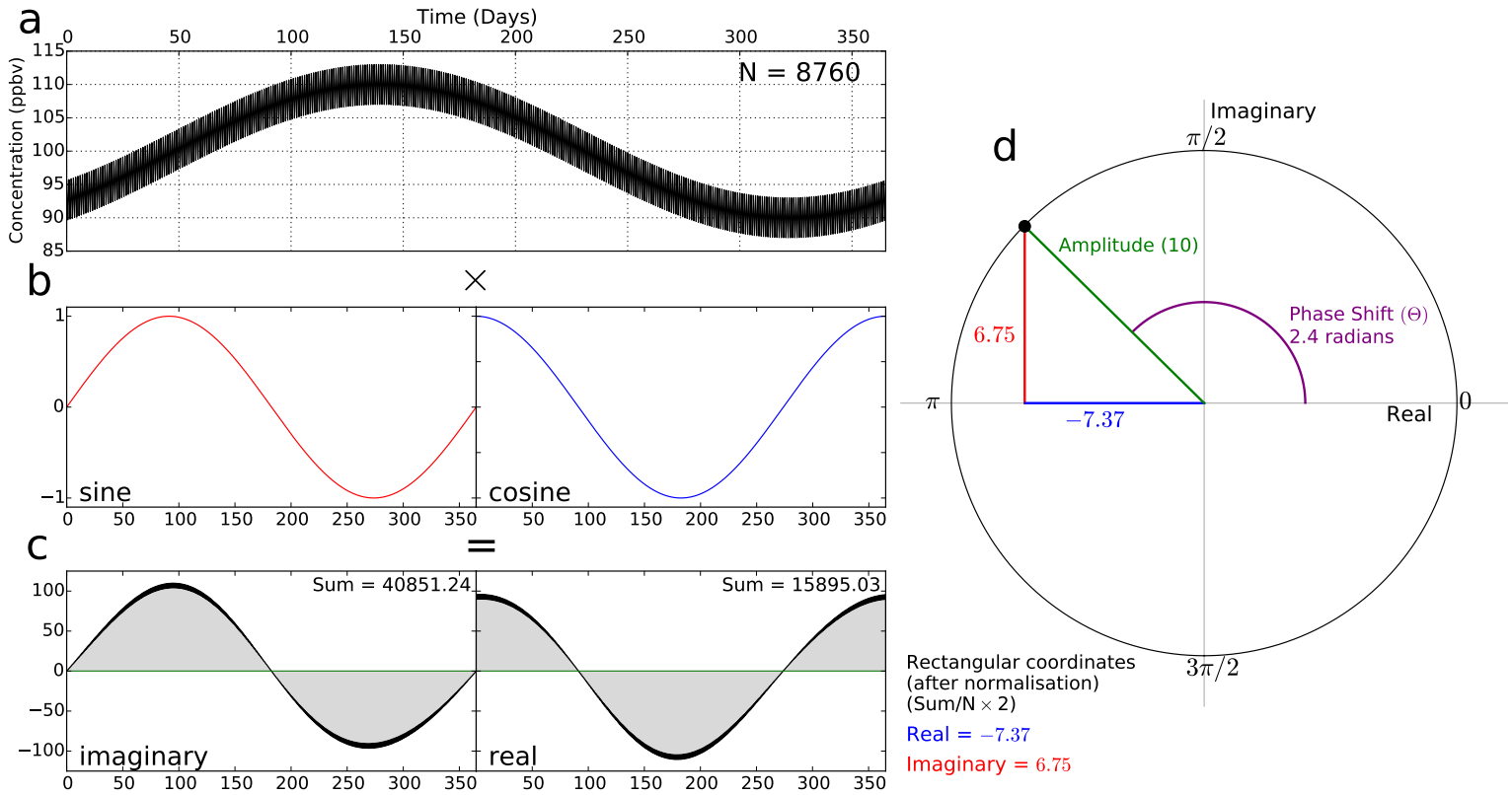


Fig. 3.2 Demonstration of the calculation of the complex number output of the DFT, at a single frequency ($\frac{1}{365}$ cycles per day). **(a)** Synthetic time series composed of annual and daily repeating sinusoids spanning 365 days. Annual sinusoid given a amplitude of 10 ppbv and phase of 2.4 radians. **(b)** Time series is multiplied by a pair of sine and cosine functions with a frequency of $\frac{1}{365}$ cycles per day. **(c)** The products of both multiplications are then summed, and after normalisation, the real and imaginary terms of the complex output are derived. **(d)** Through conversion to polar notation, it can be shown the DFT correctly derives the variability contained in the time series at a frequency of $\frac{1}{365}$ cycles per day.

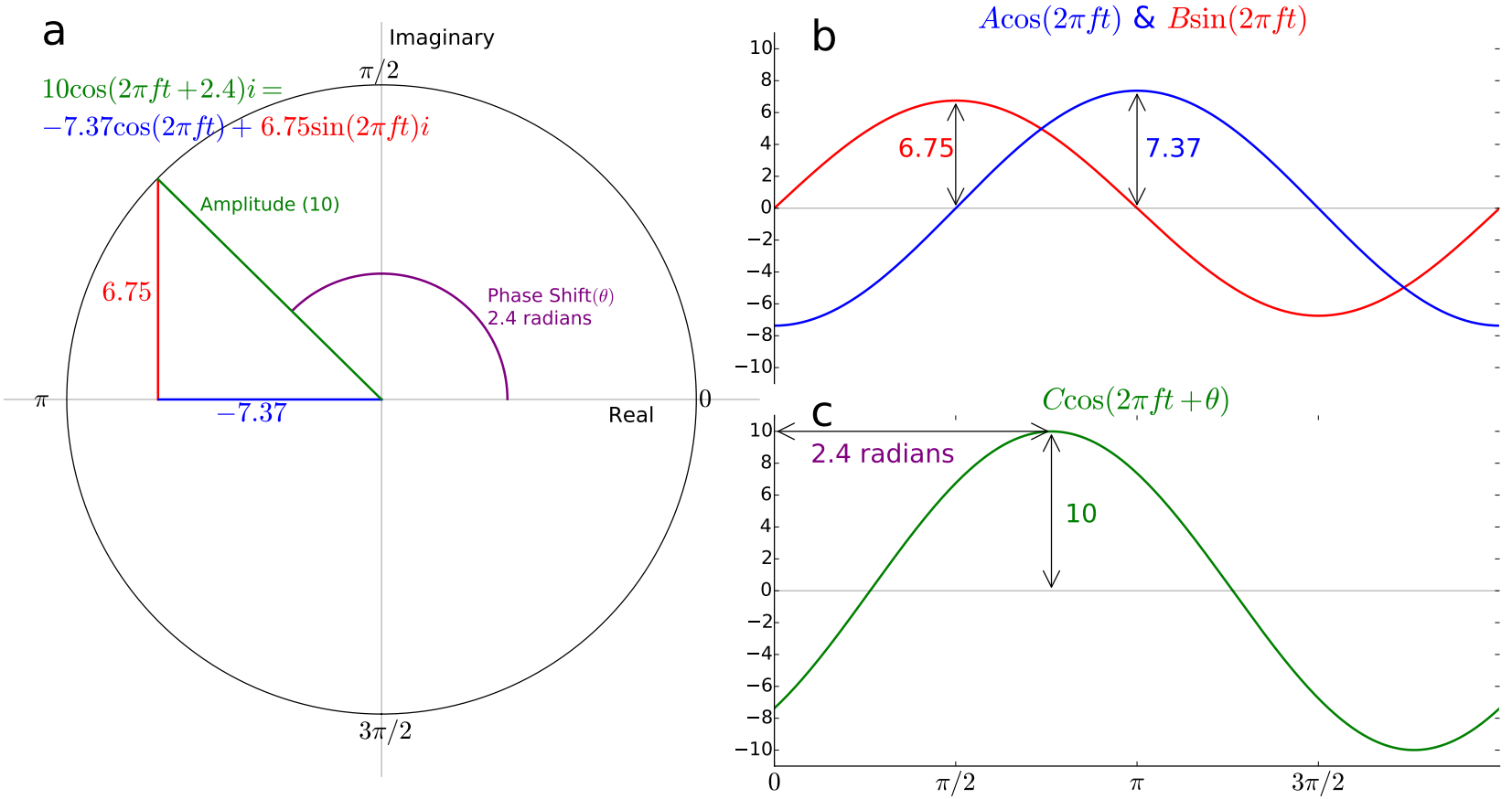


Fig. 3.3 Physical illustration of the output derived from the DFT at a specific frequency. **(a)** Representation of the output of the DFT at a specific frequency in complex space (the derivation of which is shown in Fig. 3.2). **(b)** Representation of the cosine and sine functions described by the rectangular output of the DFT, over one full oscillation in $x$. **(c)** Representation of the sinusoidal function described by the polar output of the DFT, over one full oscillation in $x$.

## 3.3 Lomb–Scargle periodogram

The Lomb–Scargle periodogram (LSP) is a spectral analysis method designed to handle gapped datasets (Lomb, 1976; Scargle, 1982; Horne and Baliunas, 1986; Press and Rybicki, 1989; Press et al., 1992), which has been applied in a small number of instances to air quality data (Dutton et al., 2010; Stefan et al., 2010). It can be formulated as a modified DFT (Scargle, 1982; Press et al., 1992), and also equivalently by the least squares of fit of sine and cosine waveforms to a time series centred around zero (Lomb, 1976). For an equally spaced time series the modified DFT formulation is equal to that of the DFT, but with different subsequent normalisation. In the presence of data gaps, the pairs of sine and cosine functions at each frequency multiplied by are modified to be exactly orthogonal by an additional phase parameter $\Theta$ (Scargle, 1982), making the estimation invariant to shifts in time of the input time series (i.e. data gaps). In the presence of data gaps the LSP does not conform to Parseval's theorem, as despite the exact orthogonality of the pairs of sine and cosine functions at each frequency, this does not hold between sinusoids of different frequencies, making estimates at different frequencies not independent. However, when frequencies estimated at are well chosen, the degree of dependence between different frequencies is very small (Scargle, 1982). The LSP is commonly represented in its normalised form (in units of Power Spectral Density), e.g. (Press et al., 1992), as:

$$P(\omega) = \frac{1}{2\sigma^2}\left(\frac{\left[\sum_{n=1}^{N} y(t_n)\cos\left(\omega t_n - \Theta\right)\right]^2}{\sum_{n=1}^{N}\cos^2\left(\omega t_n - \Theta\right)} + \frac{\left[\sum_{n=1}^{N} y(t_n)\sin\left(\omega t_n - \Theta\right)\right]^2}{\sum_{n=1}^{N}\sin^2\left(\omega t_n - \Theta\right)}\right), \quad (3.10)$$

where $y(t_n)$ is a time series sample at time $t_n$, $\omega$ is the angular frequency, and $\sigma^2$ is the variance of the time series. The LSP is typically used for the identification of periods with significant variability relative to the noise (periods with no variability), and thus its units are given as Power Spectral Density, giving an estimate of the normalised power (amplitude$^2$) contained on each frequency, amplifying separation between peaks at significant frequencies and the noise level. When data gaps exist, the normalisation by $\sigma^2$ (rather than $N$ for the DFT) returns an exponential distribution for pure Gaussian noise, equivalent to that of the equal spaced case. The phase shift $\Theta$ is calculated with the four quadrant inverse tangent:

$$\Theta = \frac{1}{2}\arctan\left(\sum_{n=1}^{N}\sin\left(2\omega t_n\right), \sum_{n=1}^{N}\cos\left(2\omega t_n\right)\right) \quad (3.11)$$

The LSP does not output any phase information natively. However, Hocke (1998) gave a method to modify the LSP algorithm to output real and imaginary components (or amplitude and phase), as resultant from the DFT, which is applied in this work.

## 3.4 Spectral leakage

There are some problems in accurately identifying the amplitude and phase of periodic components. The main issue is termed "spectral leakage". Typically, Lomb–Scargle methods calculate power at integer frequencies (i.e. 1 cycle over $N$, 2 cycles over $N$...) equally spaced between zero and one-half of the average sampling frequency (termed "average Nyquist frequency"), reflecting the DFT frequencies. However, if strong periodicity exists on a frequency not an integer integral of the span of the time series, then its power would lie between two of the frequencies, resulting in leakage of that power throughout the rest of the spectrum. Atmospheric time series are not typically integer year long. For example, if the time series was 10.5 years long the spectrum would consist of the periods: 10.5, 5.25, 3.5, 2.1, ...,1.16 1.05, 0.955 years etc. Therefore, if large variability were contained on exactly a 1 year cycle, the LSP would spread that power throughout the spectrum.

The leakage effect is a product of the mathematics underpinning the DFT. As referenced in Sect. 3.2, the DFT produces a sampled version of the Fourier Series, which makes the assumption that the time series is one period of an infinitely periodic signal. When the periodicity of interest is non-harmonic with the total span of the time record, there is a discontinuity, which results in power associated with that period spilling out across all frequencies (Horne and Baliunas, 1986).

To ensure the power leakage from multiple periodic components does not contaminate the entire spectrum, the input time series can be multiplied by a window function (Harris, 1978). The window is shaped so that it is zero at beginning and end, and has some defined shape in between. The window effectively changes the shape of the leakage in the frequency domain, limiting its impact to only a few frequencies around the frequency of interest, providing a trade-off between peak resolution (the width of the spectral peak associated with variability at a frequency) and spectral leakage (the amplitude of the tails of the leakage), with different windows altering the peaks of the spectrum in different ways. In this work a Hanning window was chosen as it offers an acceptable trade-off between peak resolution and spectral leakage (Harris, 1978).

Although the shape of the leakage can be altered, the peak amplitude will still be underestimated as there are no frequencies that estimate exactly at the frequency of interest. However, the LSP methodology (unlike the DFT) allows estimation at any frequency, allowing the exact capturing of the top of the peak. Thus, if significant cycles are known a priori (e.g. annual, daily etc.) their variability can be calculated very accurately.

## 3.5 Validation of methods

The validity of the outlined LSP methodology for the analysis of atmospheric observations is now tested using synthetic data. Firstly, the major stated advantage of the LSP, being able to handled gapped data, is evaluated relative to output from the FFT. A five year synthetic time series is created through the summation of daily (1 day) and annual (365.25 days) repeating sinusoids. The annual waveform is given an amplitude of 10 ppbv and phase of

0 radians, whereas the daily waveform is given an amplitude of 3 ppbv and phase of 0 radians. Random gaps are incrementally imposed across the time series, and the derived amplitude and phase bias for both periods is plotted as a function of the % gaps, shown in Fig. 3.4. Multiple versions of both the FFT and LSP methods are evaluated, allowing assessment of the incremental advances of the methodologies. For the FFT, these versions are the standard code, with a Hanning window applied to the time series, and with both zero padding (four times the original number of frequencies) and windowing. For the LSP, these versions are the standard code, with a Hanning window applied to the time series, and with both windowing and estimation at specific frequencies/periods (1 day and 365.25 days). For analysis by the FFT, the time series is linearly interpolated across time to remove data gaps.

For both the FFT and LSP, biases decrease with the increasing complexities of the methods, with specific frequency estimation and zero padding most notably lowering biases. The LSP method with both windowing and specific frequency estimation (purple line) is consistently the best performing, with significant biases only notable with greater than 80 % gaps when estimating the daily amplitude (up to 40 %). Noticeably on the daily timescale, with increasing % gaps the amplitude bias for all FFT methods increases significantly (particularly after 40 %).

Next, the performance of the LSP methods when determining periodicity in extreme amounts of random noise is evaluated. The same synthetic time series (un-gapped) is iteratively added with random noise of an increasing standard deviation (up to to 25 $\sigma$), with the derived amplitude and phase bias on both annual and daily timescales plotted as a function of $\sigma$, shown in Fig. 3.5. The LSP method with specific frequency estimation and windowing (purple line) again gives the minimal bias for both the amplitude and phase components, on both timescales. The only notable biases associated with this method come when estimating the daily amplitude with noise greater than 10 $\sigma$ (up to 40 %).

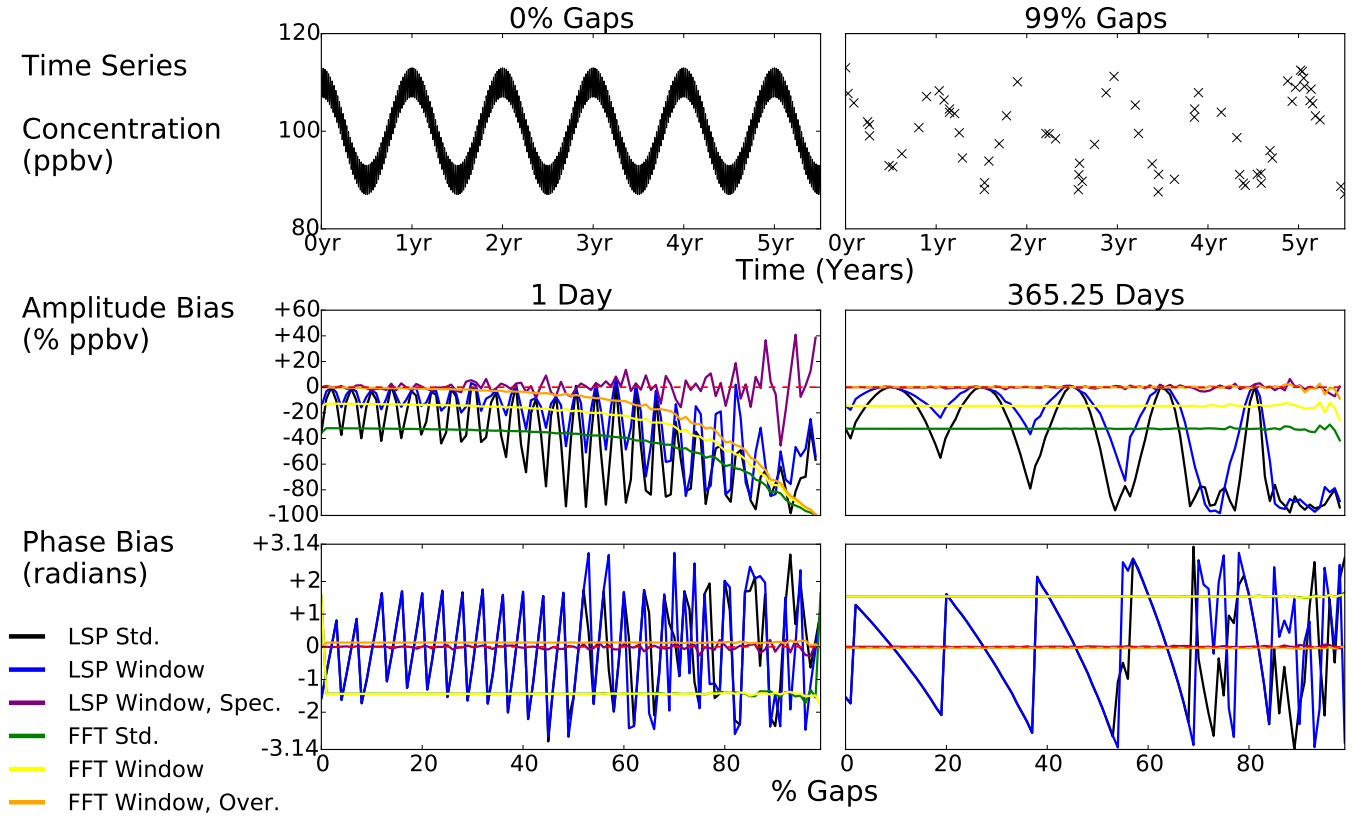


Fig. 3.4 Evaluation of the amplitude and phase biases for multiple versions of the FFT and LSP methodologies, as a function of % data gaps. A 5 year synthetic time series consisting of daily and annual repeating sinusoids (amplitudes – 3 and 10 ppbv, phases both 0 radians) is incrementally filled with random gaps, and the amplitude and phase biases for both periods, associated with multiple FFT and LSP methods are iteratively calculated. FFT methods are the standard code (FFT Std.), with windowing (FFT Window), and with both zero padding and windowing (FFT Window, Over.). LSP methods are the standard code (LSP Std.), with windowing (LSP Window), and with both specific frequency estimation and windowing (LSP Window, Spec.).

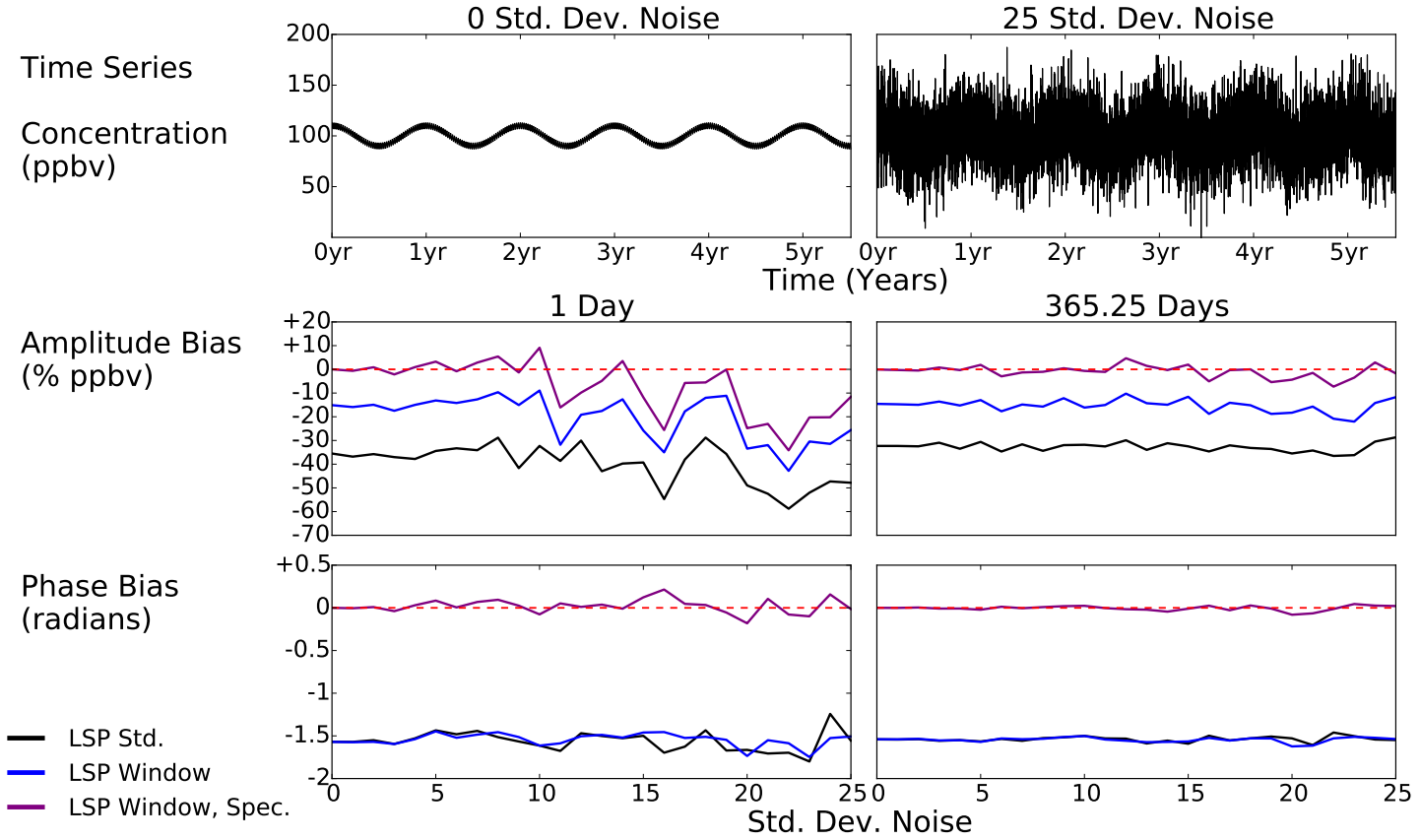


Fig. 3.5 Evaluation of the amplitude and phase biases for multiple versions of the LSP method, as a function of random noise (up to 25 $\sigma$). A 5 year synthetic time series consisting of daily and annual repeating sinusoids (amplitudes – 3 and 10 ppbv, phases both 0 radians) is incrementally added with random noise (up to 25 $\sigma$), and the amplitude and phase biases for both periods, associated with multiple versions of the LSP method are iteratively calculated. LSP methods are the standard code (LSP Std.), with windowing (LSP Window), and with both specific frequency estimation and windowing (LSP Window, Spec.).

# Chapter 4

# Spectral analysis of surface ozone: a model–measurement evaluation

## 4.1 Introduction

To this point, this work has described the collection of numerous surface composition data, collated specifically for global model evaluation purposes (Chapter 2), and has detailed a spectral methodology allowing determination of the independent periodic components of a time series (Chapter 3), only so far applied to synthetic data. This chapter describes a synthesis of this work, with the Lomb-Scargle Periodogram (LSP) being applied to real atmospheric data, specifically, to the collated surface $O_3$ measurements of Chapter 2, and further used to diagnose systematic periodic biases in the simulation of surface $O_3$ by a CTM.

The application of the LSP methodology to two contrasting surface $O_3$ sites is first described in detail in Sect. 4.2, outlining the dominant periodic variabilities of surface $O_3$ and detailing an approach for the spectral evaluation of $O_3$ at multiple sites. The findings of this multi-site application are described in Sect 4.3. The same approach is then used to spectrally evaluate reciprocally located surface $O_3$ in a CTM (Sect. 4.4). Finally, these results are then compared, and potential reasons for biases are discussed (Sect. 4.5).

## 4.2 Lomb–Scargle periodogram of surface $O_3$

Figure 4.1 shows the time series of hourly surface $O_3$ mixing ratios collected at Cape Verde (Carpenter et al., 2010) and Lompoc together with equivalent model output (see Sect. 4.4). Cape Verde (16.51° N, 24.52° W), is a small remote island country consisting of 10 islands situated in the tropical eastern North Atlantic Ocean, 570 km off the west African coast. It represents one of the only $O_3$ measurement stations in the tropics, and is relatively undeveloped, making it one of the small number of baseline oceanic measurement sites also. It is maintained by the atmospheric chemistry group at the University of York, and thus presents a readily available dataset for analysis. Lompoc (34.73° N, 120.43° W), is a EPA AQS rural continental site located on the USA Californian west coast.

Using the Lomb–Scargle methodology, the time series at Cape Verde and Lompoc can be transformed into a number of sinusoidal waves across a range of periods, with associated amplitudes and phases. Figure 4.2 shows the spectral amplitude (ppbv) of these waveforms as a function of their period (days). The spectra for both sites have a range of characteristic features. There are broadly linear regions from 2 hours to 10 days and from 10 days to the last period of 1826 days. There are also sets of peaks which occur at characteristic timescales (i.e. 1 day and 1 year). The identification of these linear regimes is initially discussed, followed by discussion associated with the identification of spectral peaks.

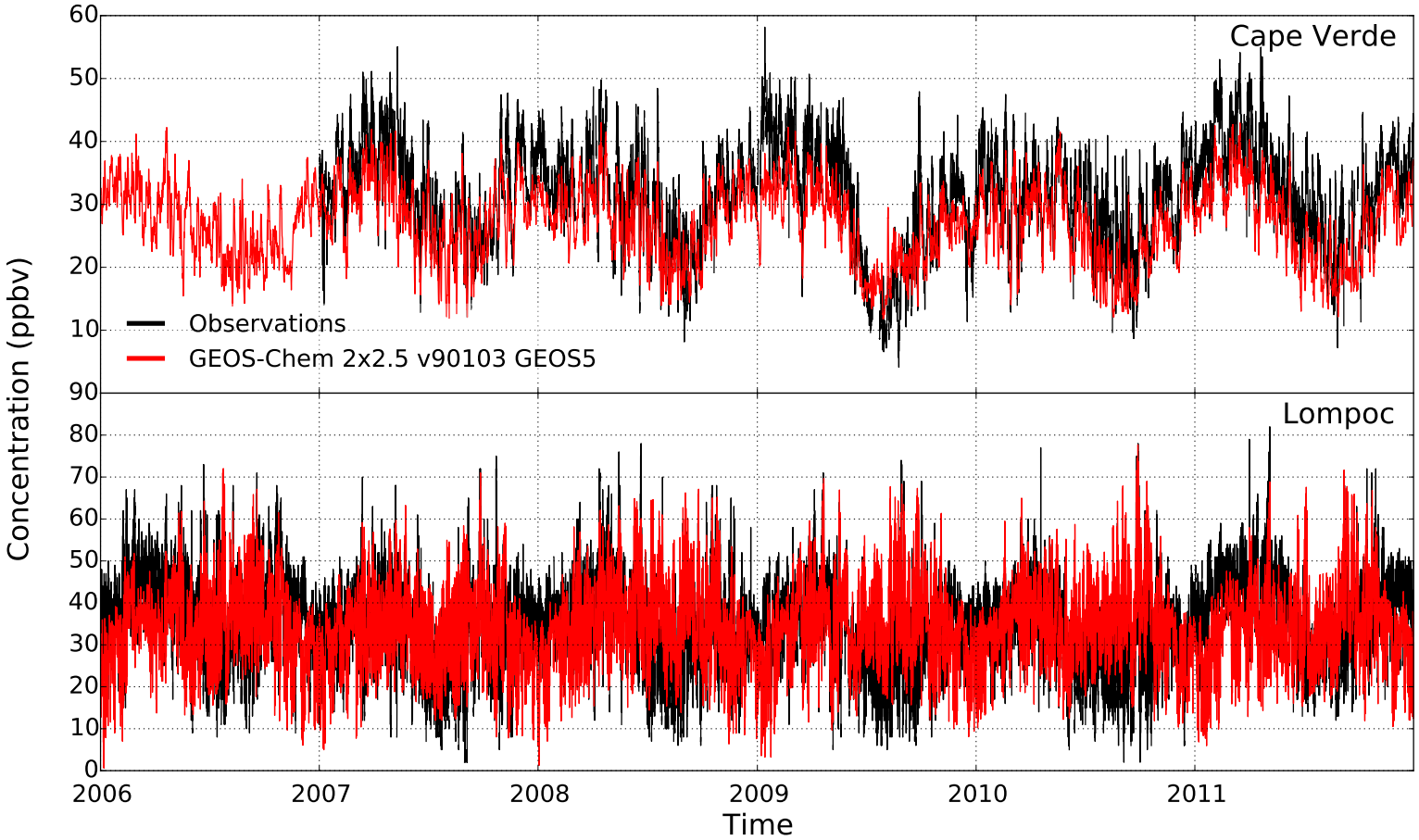


Fig. 4.1 Time series of surface $O_3$ at Cape Verde (16.51° N, 24.52° W) and Lompoc (34.73° N, 120.43° W) for the observations (black) and the GEOS-Chem model (red), between 2006 and 2012.

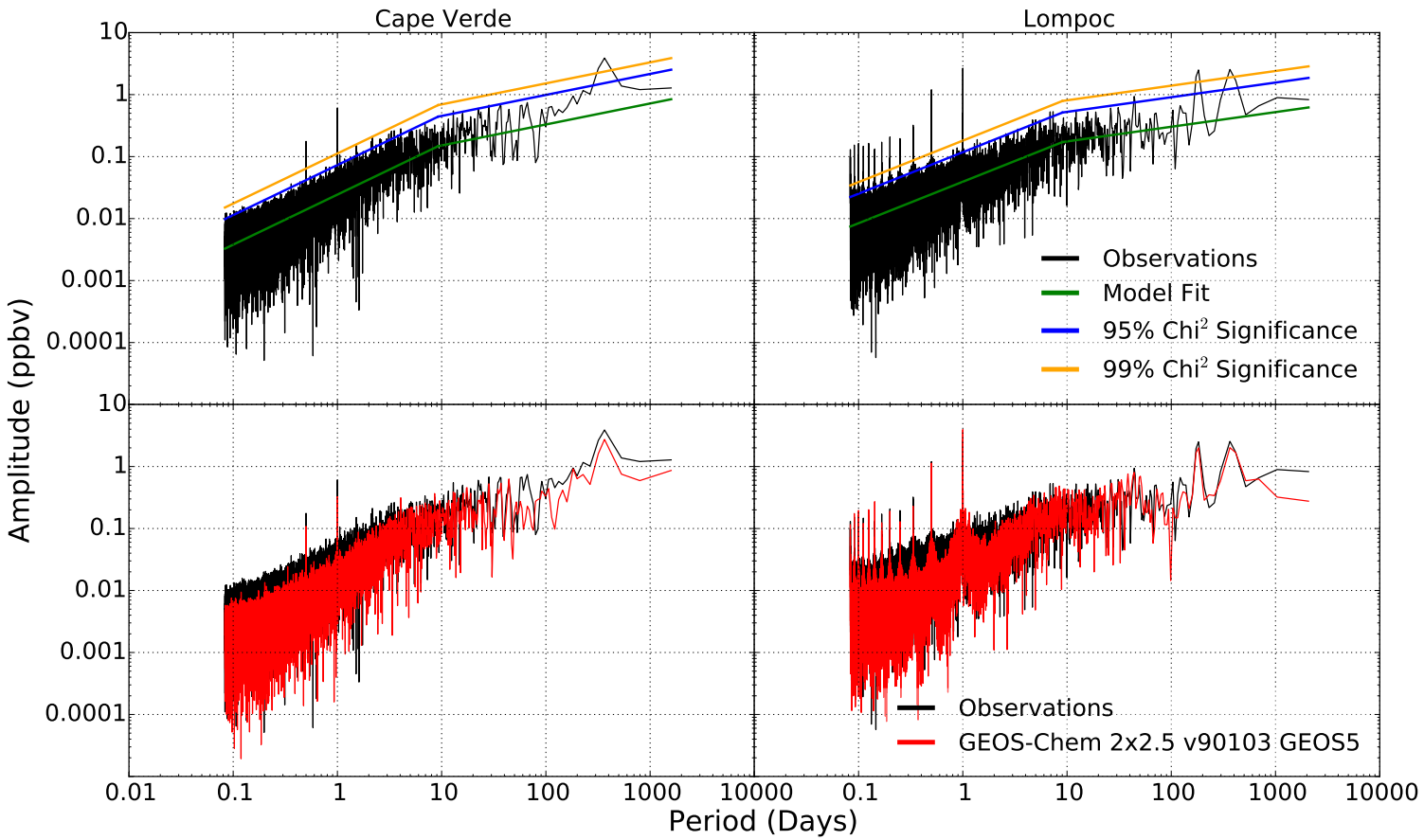


Fig. 4.2 Lomb–Scargle periodogram spectra for surface $O_3$ at Cape Verde (16.51° N, 24.52° W) and Lompoc (34.73° N, 120.43° W), between 2006 and 2012. The upper panels shows the observed data spectra together with chi-squared false-alarm levels for significant periodicity based on linear piecewise fits to the spectra. The lower panels compare the spectra of the observations (black) and the GEOS-Chem model (red).

### 4.2.1 Meteorological regimes

Figure 4.2 shows two distinct linear regimes for both sites' spectral amplitudes, which meet at around 10 days. Very similar spectra are seen in physical parameters in the atmosphere (Lovejoy and Schertzer, 2013a,b). There are 3 main scaling regimes of meteorological variability (Lovejoy and Schertzer, 2013a,b): "weather", "macroweather" and "climate", with each regime being the outcome of different dynamical processes.

Weather processes range from microscale local turbulence to planetary scale weather systems, with the temporal lifetimes of these features roughly proportional to their spatial scale (Lovejoy and Schertzer, 2013b). The variability induced on $O_3$ also scales accordingly to these, thus the weather regime for $O_3$ is represented by a steep spectral gradient (on the log–log spectrum – Fig. 4.2) from 2 hours to $\sim$10 days, after which there is a sharp transition to a flatter gradient. The change in the gradient at around 10 days is physically caused by the finite size of the Earth giving a limit to the lifetime of the biggest planetary scale weather systems. After $\sim$ 10 days the flat spectral gradient is a result of being the average of the largest planetary scale weather systems, being no more than low-frequency weather, with no new dynamical elements or forcing mechanism, the statistics of this regime being well captured by unforced "control" runs of General Circulation Models (GCMs) (Lovejoy and Schertzer, 2013a). The regime has been shown for metrological spectra to extend out to 10–100 years, and is termed "macroweather" (Lovejoy and Schertzer, 2013b). The final regime is characterised by a steep increase from the flat macroweather gradient between 10–100 years caused by new (internal) low-frequency nonlinear interactions or (external) solar, volcanic or anthropogenic forcings, and represents long term changes of the macroweather. Human induced changes would be termed "climate change". As this work only uses time series of 5 years in length, no evidence of any climate regime is seen in the spectra. Therefore, only 2 regimes are found necessary to describe the impact of meteorology on surface $O_3$ variability: weather (2 hours–10 days) and macroweather ($>10$ days).

These regimes can be described by fitting a model of two joint piecewise linear functions in log–log space to the spectrum (minimising the residuals). The transition point is set at 10 days, as the theoretical maximum lifetime for the largest planetary scale weather systems (Lovejoy and Schertzer, 2013b). Only periods less than 100 days are used, for the few points beyond this value are noisy and can often introduce significant variability into the fitting. The upper panels of Fig. 4.2 show the linear fits (green line) to the observed surface $O_3$ spectra for both Cape Verde and Lompoc.

To find periods which deviate from these fits, the fitted models are scaled by percentiles of the chi-squared probability distribution to obtain false-alarm levels (Schulz and Mudelsee, 2002). Peaks exceeding these false-alarm levels indicate non-model components in the time series, and should be considered significant (Schulz and Mudelsee, 2002). Frequencies that have an amplitude above the 99th percent confidence level are taken to be significant. Attention now focuses on these significant frequencies, namely the annual and daily peaks (and their harmonics).

### 4.2.2 Annual and daily cycles

From Fig. 4.2 it is evident that there are significant peaks on annual and daily timescales for both Cape Verde and Lompoc. There are also additional significant harmonic peaks ($\frac{1}{2}$ daily for Cape Verde; $\frac{1}{2}$, $\frac{1}{3}$, $\frac{1}{4}$, $\frac{1}{5}$, $\frac{1}{6}$, $\frac{1}{7}$, $\frac{1}{8}$, $\frac{1}{9}$, $\frac{1}{10}$, $\frac{1}{11}$, $\frac{1}{12}$ daily and $\frac{1}{2}$ annual for Lompoc). These periodic cycles are driven by the planetary processes of the Earth‘s rotation around its own axis and its rotation around the sun both of which changes the predominant driving force for the atmosphere, solar radiation. Variability in solar radiation is not sinusoidal in nature, and the atmosphere is not linear in its response. Thus any harmonics are a product of the non-sinusoidal shape of the daily and annual cycles of $O_3$ (Valenzuela and Pontt, 2009). Parrish et al. (2016) finds that the annual and half-annual cycles are enough to characterise the seasonal variability of marine boundary layer $O_3$, and that the forcing responsible for the half-annual cycle a priori is attributable to the 2nd harmonic of the photolysis rate of $O_3$. It is important to note however that the the harmonics do not have to have independent physical forcings. The power of the harmonics can simply be a function of the mathematics. These harmonics can sometimes extend to frequencies beyond the Nyquist limit ($f_{Nq}$), and are thus aliased to other frequencies, potentially biasing output. However, harmonics beyond this point are typically very small and have a negligible impact.

For the surface $O_3$ observational dataset described in Chapter 2, almost all sites are found to show significant peaks at the fundamentals (and most harmonics) of the annual and daily timescales. It is notable that no sites are found that show significance of a 7 day cycle (Altshuler et al., 1995; Marr and Harley, 2002; Beirle et al., 2003). Application of this approach to longer time series may also allow the investigation of other characteristic timescales such as NAO or ENSO (Ziemke et al., 2015).

#### Definition of “seasonal” and “diurnal” cycles

For all of the sites investigated, the amplitude of the daily cycle is always significantly larger than any of its harmonics. However, this is not true for the annual cycle, as the magnitude of the half-annual cycle can sometimes compete with that of the annual cycle. To bring together the fundamental and the harmonics, the fundamental and the harmonic signals are superposed to create “seasonal” and “diurnal” cycles. An example of this is shown in Fig. 4.3, where the average, 1st (fundamental), 2nd, 3rd and 4th harmonics are superposed to create the net waveform. Superposition is done down to the 12th harmonic for the diurnal cycle, and 4th harmonic for the seasonal cycle, as they are the highest harmonics for each periodicity that significance is found ($>$ 99th percent confidence level). The superposed cycles are characterised with their amplitude being half the peak to trough height and their phase being the timing of the maxima. The LSP code is modified to ensure estimation is precisely at 1 day (and 2nd to 12th harmonics) and 365.25 days (and 2nd, 3rd and 4th harmonics), to ensure accurate estimation of these cycles. From this point onwards all references to the “seasonal” or “diurnal” cycle refer to the superposition of the

respective fundamental and harmonics, and any "annual" and "daily" references refer to solely the fundamental terms.

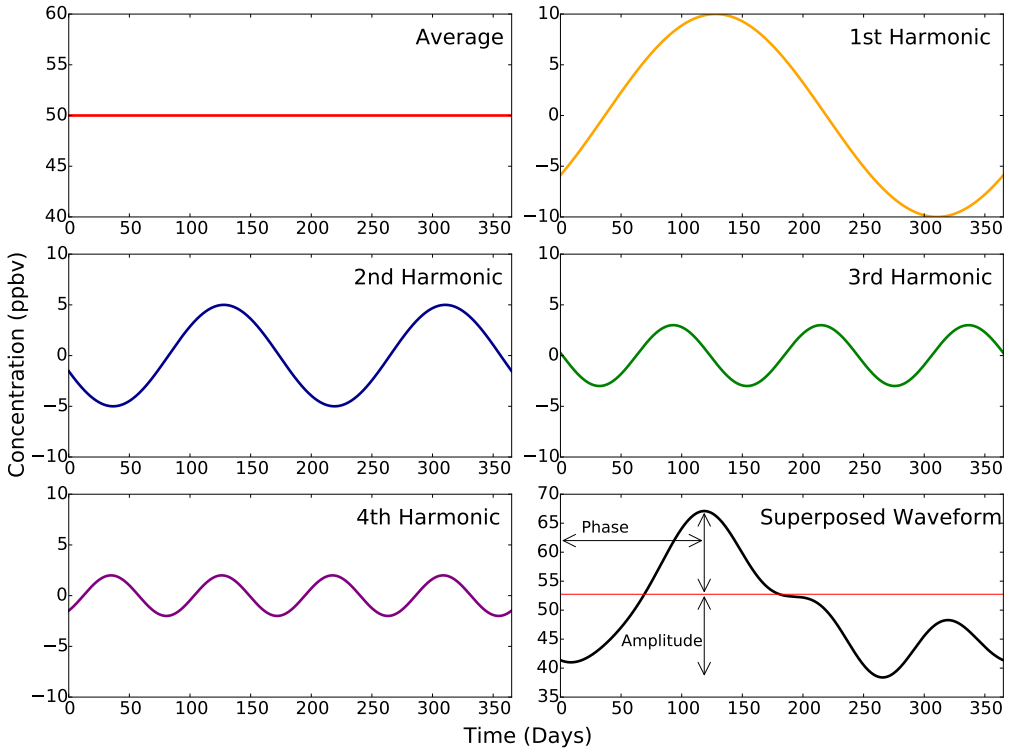


Fig. 4.3 Example of spectral superposition of the average, fundamental frequency and the harmonics for a frequency of interest.

### Fraction of total variance associated with a periodicity

The significance of the diurnal or seasonal cycles varies by location. The fractional variance ($\sigma^2$) that both periodic waveforms contribute to the raw time series variance can be calculated. This is done by extending both periodic waveforms to be the span of the raw time series, and then taking the fraction of the $\sigma^2$ of each waveform to the time series $\sigma^2$. Going further, superposing the extended diurnal and seasonal waveforms gives a periodic waveform representative of the total periodic $\sigma^2$. In the same way as previous, the fraction of the total periodic $\sigma^2$ is taken to the time series $\sigma^2$. Removing the total periodic waveform (including gaps) from the raw time series gives a time series which is solely derived of the weather and macroweather "noise". The variances of these periodic and noise time series are essentially additive so that $\sigma^2(\text{diurnal}) + \sigma^2(\text{seasonal}) + \sigma^2(\text{noise}) = \sigma^2(\text{timeseries})$.

## 4.3 Application to observations

These methods are now applied to the the long-term surface $O_3$ dataset described in Chapter 2. For simplicity the period between 2005 and 2010 is focused on, as this

represents the most comprehensively observed time period. To ensure accuracy of the LSP calculations, sites with data gaps of more than 365 days in this period or data gaps greater than 60 days in 3 or more years are removed. Figure 4.4 shows the location of the 710 valid sites. Most of the sites are from the US EPA AQS and EU AirBase datasets which leads to an over representation of northern continental mid-latitude locations and an under representation of other areas of world.

The Lomb–Scargle derived diurnal and seasonal cycles for these sites are now investigated.

Fig. 4.4 Map of valid surface sites reporting surface $O_3$ between 2005 and 2010 used in this work, coloured by the providing data network.

### 4.3.1 Significance of seasonal and diurnal cycles

Figure 4.5 shows the fraction of the variance at each site that is explained by the seasonal, diurnal and combined total periodic waveforms, as well as the weather and macroweather (meteorological) regimes. For most locations the seasonal cycle represents a much larger fractional variance than the diurnal cycle.

The greatest contribution to total variance from the seasonal cycle is for the Antarctic site (85 %) and the oceanic and continental SH sites (30–60 %). This reflects the lack of anthropogenic influence and spatial homogeneity of these regions leading to small spatial gradients in $O_3$. Without spatial gradients to advect, weather systems cannot induce much variability, thus diurnal and seasonal variability dominates. For high NOx regions in the north-eastern USA, southern and central Europe and Japan (Fig. 4.15c), the seasonal cycle contributes 30–50 % of the total variance. In the southern central USA, contribution from the seasonal cycle to the total variability is very small (2–10 %).

For the oceanic, polar and sites in low NOx areas in the extra-tropics (i.e. Cape Point (34.21° S, 18.29° E) – the most south-westerly point of Africa) the diurnal cycle is negligible. These diurnal cycles are typically small as $O_3$ production and loss in these low NOx environments is small. However, it is a major contributor (20–40 %) to the total variability for some low latitude regions in North America and Europe where high NOx concentrations and photolysis rates lead to significant diurnal cycles.

Superposition of the diurnal and seasonal cycles gives a measure of the fraction of total variance induced from periodicity. For most sites the percentage contribution is between 40 and 60 %. The highest value being for the Antarctic site (85 %). The site with the lowest % contribution from periodicity is in Indonesia (15 %), almost on the equator, where there is very little variability in the solar radiation.

The meteorological regimes contribute a large majority of the total variance for a large number of sites, particularly across the southern USA and north-west Europe (up to 80 %), and for the Indonesian site (85 %).

From this analysis it is evident that forcing of the atmosphere from seasonal and diurnal processes (changes in solar irradiation, chemistry, emissions etc.) are for responsible for at most 50 % of the variability seen at these sites. The remaining 50 % of the variability is attributable to changes on the weather or macroweather timescales due to processes such as boundary layer mixing, synoptic systems, changing emissions etc. We now describe in more detail the seasonal and diurnal cycles seen at different locations.

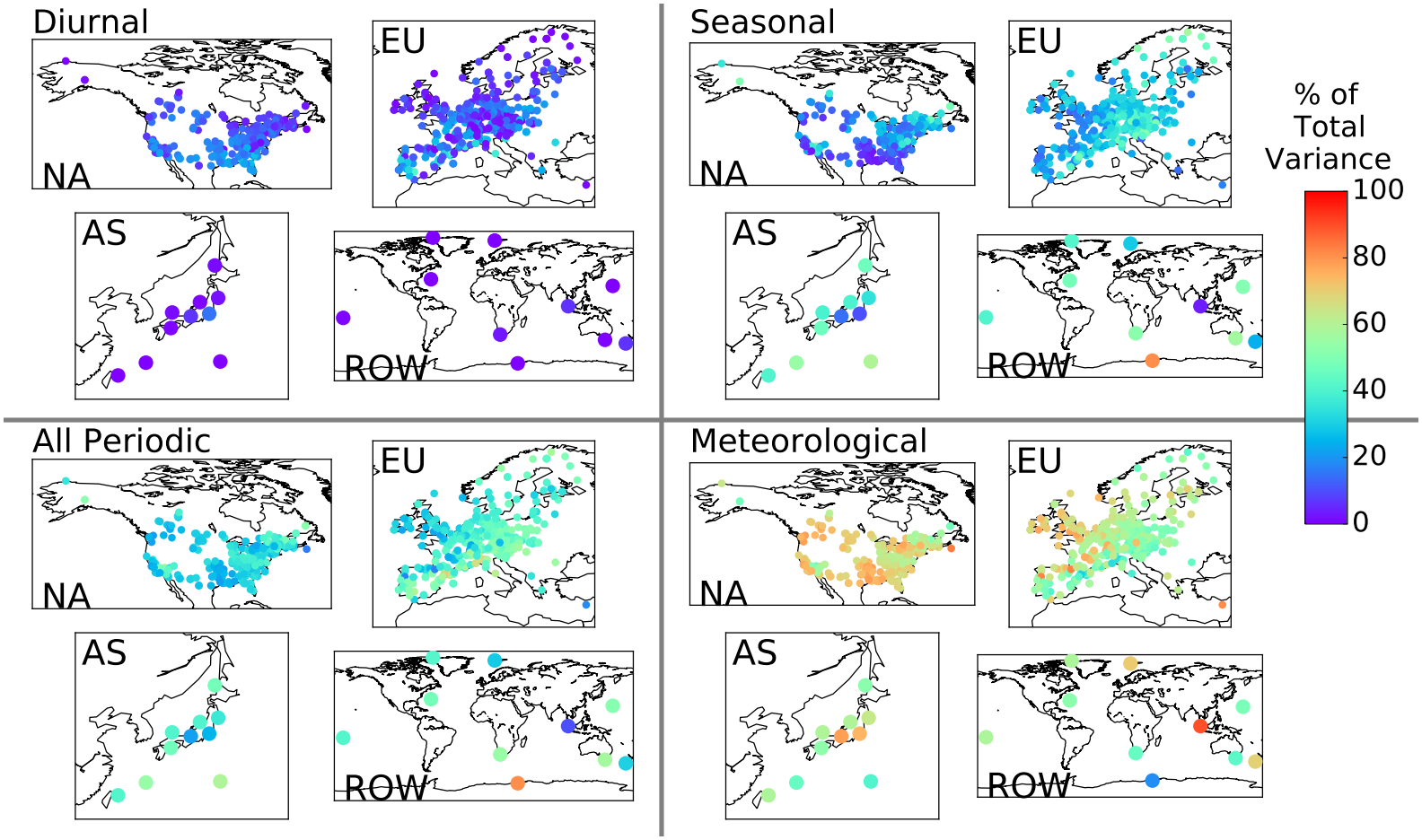


Fig. 4.5 Observational fractional variance of time series by site from diurnal, seasonal and total periodicity, as well as the weather and macroweather (meteorological) regimes. NA is North America, EU is Europe, AS is Asia, and ROW is rest of world.

### 4.3.2 Seasonal cycle

The seasonal cycle of $O_3$ has been subject to much discussion (Derwent and Davies, 1994; Logan, 1985; Monks et al., 2000; Monks, 2000; Tanimoto et al., 2005; Cooper et al., 2010, 2014; Carpenter et al., 2010; Parrish et al., 2013; Clifton et al., 2014; Parrish et al., 2016). In general, NH mid-latitude continental sites in the late 2000's show a springtime maxima, which has shifted from a broad summertime peak in the 1990's (Cooper et al., 2014). This change is strongly associated with NOx emission reductions in Europe and North America due to air quality legislation (Parrish et al., 2013; Clifton et al., 2014), however some of the most polluted urban sites still show a summertime peak (Cooper et al., 2014). Extra-tropical baseline sites show a consistent winter–spring maxima and tropical baseline sites a small winter maxima.

The findings in this work are consistent with the literature. The upper panels of Fig. 4.6 show the amplitudes of the seasonal waveforms for the observations. In general, most amplitudes are in the range of 5–15 ppbv. Sites influenced by highly polluted outflow such as the Central Valley in the US and the Po Valley in Italy show large amplitudes (up to 22 ppbv). High amplitudes can also be seen in the Asian sites downwind of China, particularly to the south of Japan (up to 23 ppbv).

The maxima in the observed seasonal waveforms (upper panels of Fig. 4.7) occurs in the spring (April, May) for most of the continental sites, with a tendency for later peaks in southern Europe. The small number of continental sites in the SH show peaks 3–6 months out of phase compared to the NH, peaking in the SH late winter to spring (August–October). The SH oceanic site, American Samoa (14.27° S, 170.13° W), has a winter phase (July), whereas the two NH oceanic sites have springtime phases (March and April). This is suggestive that the lower pollution associated with the SH sites generally leads to an earlier seasonal peak in $O_3$.

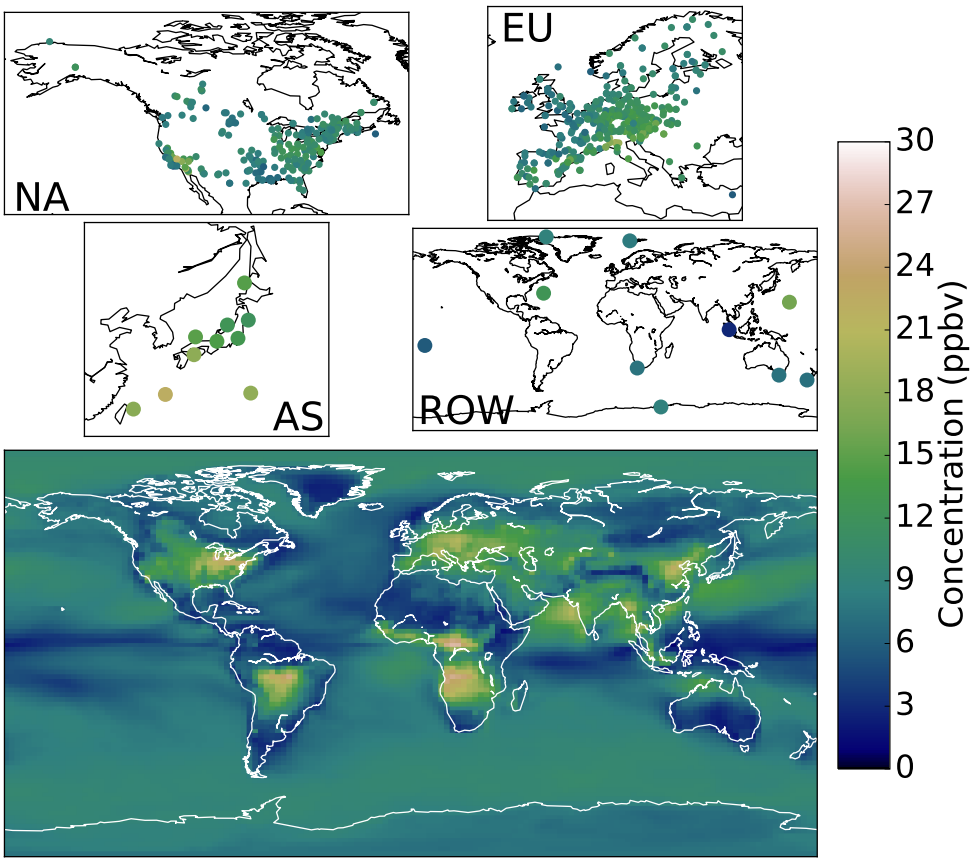


Fig. 4.6 Seasonal amplitudes of observations (upper panels) and model (lower panel). NA is North America, EU is Europe, AS is Asia, and ROW is rest of world.

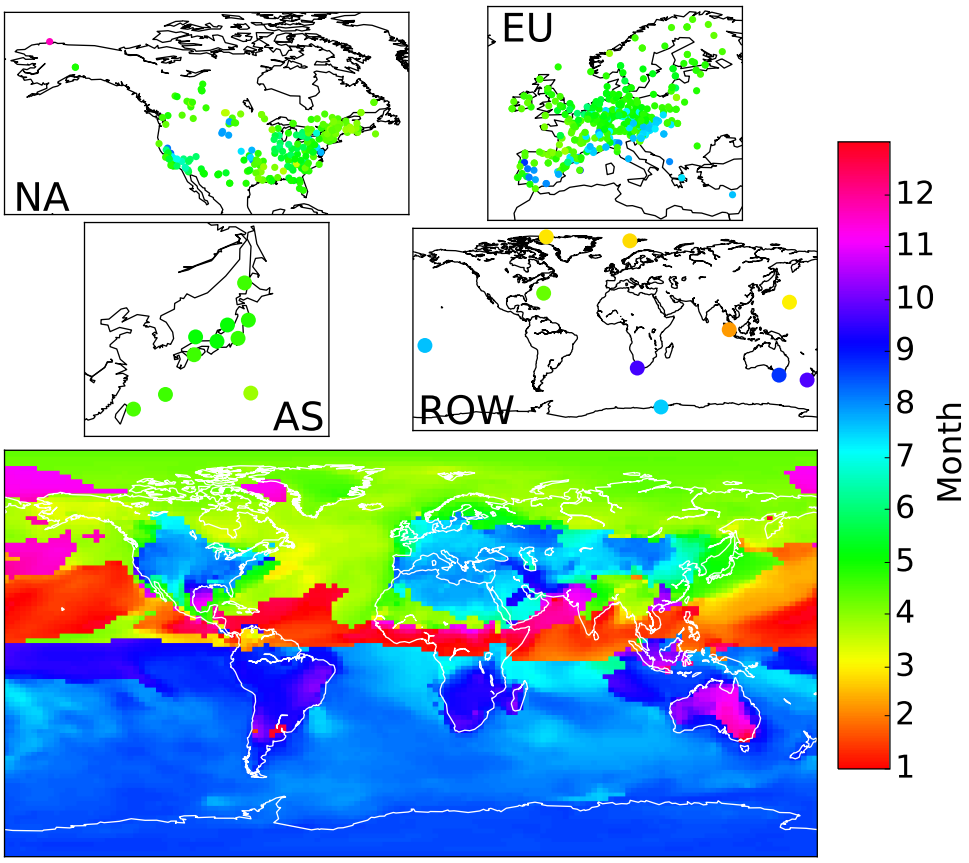


Fig. 4.7 Seasonal phases of observations (upper panels) and model (lower panel). NA is North America, EU is Europe, AS is Asia, and ROW is rest of world.

### 4.3.3 Diurnal cycle

The upper panels of Fig. 4.8 show the observational amplitudes of the diurnal cycle. In most of the locations this is in the range of 0–15 ppbv, with a tendency for larger amplitudes towards the tropics where solar radiation is more intense. There are also higher amplitudes in regions with higher NOx emissions (Fig. 4.15c), with again the Central and Po Valleys being evident.

Significant differences between sites can be seen in the phases of the diurnal cycle (upper panels of Fig. 4.9). Baseline sites (i.e. American Samoa) show a phase which peaks close to dawn, reflecting photochemical $O_3$ destruction during the day and $O_3$ build up at night. Continental sites (i.e. Lompoc) show maxima in the early afternoon due to photochemical $O_3$ production during the day.

The amplitude and phase of the diurnal and seasonal waveforms give a compact method of summarising much of the variability seen in surface $O_3$ sites. It is now explored how a global CTM represents these observations.

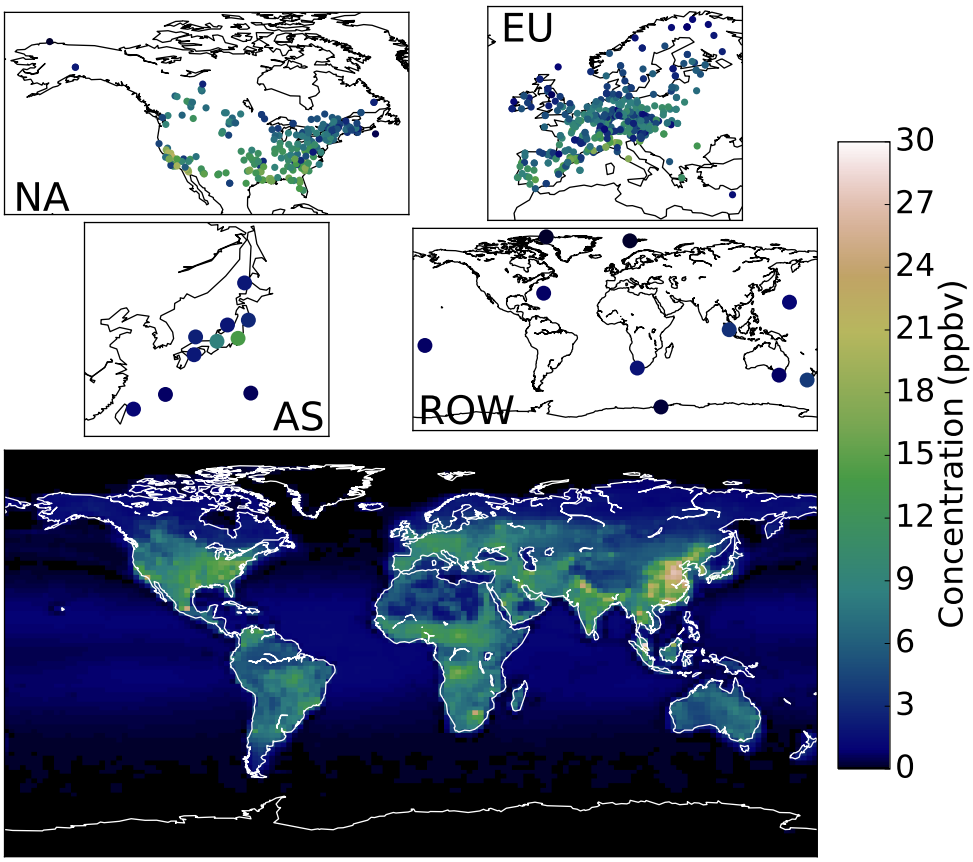


Fig. 4.8 Diurnal amplitudes of observations (upper panels) and model (lower panel). NA is North America, EU is Europe, AS is Asia, and ROW is rest of world.

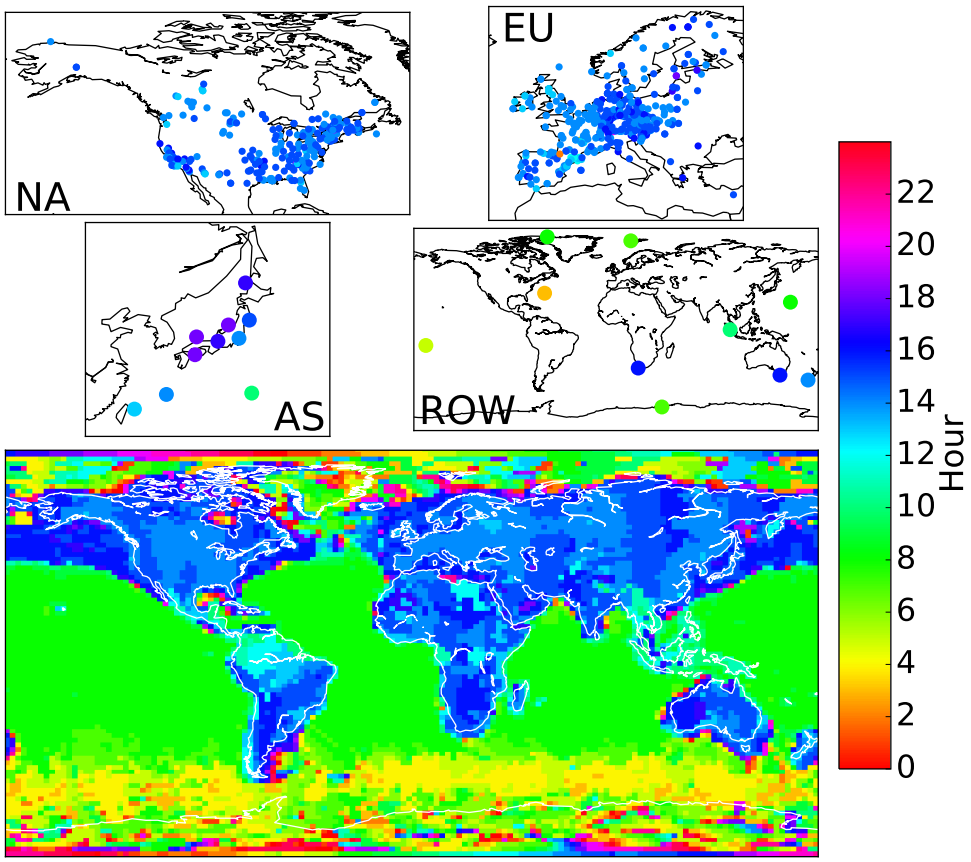


Fig. 4.9 Diurnal phases of observations (upper panels) and model (lower panel). NA is North America, EU is Europe, AS is Asia, and ROW is rest of world.

## 4.4 Model perspective

GEOS-Chem is a global 3-D CTM driven by assimilated meteorological observations from the Goddard Earth Observing System (GEOS) of the NASA Global Modelling Assimilation Office (GMAO). The basic model is described in Bey et al. (2001). Version v9.01.03, using GEOS5 analysed meteorology at $2^\circ \times 2.5^\circ$ resolution, is run for 5 years between 2005 and 2010, outputting surface hourly $O_3$ in each gridbox. Global anthropogenic emissions of CO, NOx, and $SO_2$ are from the global EDGAR v3.2 inventory (Olivier et al., 2005). Global anthropogenic emissions of NMVOCs are from the RETRO monthly global inventory for the year 2000, as described by Hu et al. (2015), except for ethane (Xiao et al., 2008) and global biofuel emissions (Yevich and Logan, 2003). Inventories are scaled for individual years on the basis of economic data. Regional inventories are used in certain regions where there is improved information, as described by van Donkelaar et al. (2008). There are also inputs of NOx from additional sources i.e. aircraft (Wang et al., 1998), ships (Vinken et al., 2011) and biomass burning (Giglio et al., 2010). Inputs from lightning and soil NOx are calculated online (Yienger and Levy, 1995; Murray et al., 2012). Biogenic VOC emissions are from the global MEGAN v2.1 inventory (also calculated online) (Guenther et al., 2006). STE is handled as a parameterised climatological representation of species sources and sinks (McLinden et al., 2000; Murray et al., 2012). Boundary layer mixing is parameterised using a non-local scheme which considers different states of mixing within the boundary layer, as determined by the static instability (Holtslag and Boville, 1993; Lin and McElroy, 2010).

### 4.4.1 Modelled power spectrum

The power spectra for the modelled surface $O_3$ at Cape Verde and Lompoc are shown in the lower panels of Fig. 4.2. As with the observed spectra, the weather and macroweather regimes are visibly separated at around 10 days. The model underestimates the amplitude on the shortest timescales for both sites ($< 3$ days). This is unsurprising given the model spatial scale ($2^\circ \times 2.5^\circ$, approx. 250 km) and the timescale for model meteorological field updates (3 or 6 hours). As the timescale increases, the power in the model increases until it is comparable to that observed. This occurs at roughly 3 days. After this point the model appears to well simulate the power spectrum for both the weather and macroweather regimes. Thus care needs to be taken in interpreting output of this model on timescales of less than around 3 days, as much of the meteorological variability will be missing. In general this will be true for all models. Therefore, on some timescales the model cannot be expected to interpret the observed variability, and this limitation should be considered when preparing model experiments.

As with the observations there are peaks at 365.25 days and 1 day, with appropriate harmonics. As per the observations the daily and annual fundamentals are superposed with their harmonics to produce seasonal and diurnal signals, which are described with a phase and amplitude. The amplitude and phase of the modelled diurnal and seasonal cycles are now investigated.

### 4.4.2 Significance of seasonal and diurnal cycles

Figure 4.10 shows the fraction of the total time series variance in each gridbox that is explained by the seasonal, diurnal and combined total periodic waveforms, as well as the weather and macroweather (meteorological) regimes.

Across the SH oceans and polar regions the seasonal cycle contributes $> 80\,\%$ of the total variance, reflecting the lack of anthropogenic influence and spatial homogeneity in these regions. The highest contributions from the seasonal cycle over mainland continental areas come in the biomass burning regions of central Africa and the high NOx emitting central Europe (60–70 %). A very small contribution from the seasonal cycle is notable over eastern China and Australia ($< 10\,\%$).

Contributions to the total variance from the diurnal cycle are negligible over all the oceans and polar regions. The highest fractions of total variance from the diurnal cycle occur in the low latitudes of central Africa (60–80 %), eastern Southern America and the Middle East (30–50 %). Total periodicity contributes $> 80\,\%$ of the total variance over the SH oceans, polar regions and central Europe; and 30–60 % in most other continental regions.

The weather and macroweather regimes contribute a large majority of the total variance near the eastern North American and western European coastlines (70–100 %), areas where there are significant gradients in the surface $O_3$ concentrations between land and sea. There is also a large fraction of variability from meteorological processes over the equator (60–100 %), an area where there is little variability in solar radiation and again large gradients in the concentrations of $O_3$, due to the shifting of the intertropical convergence zone (ICTZ) by season.

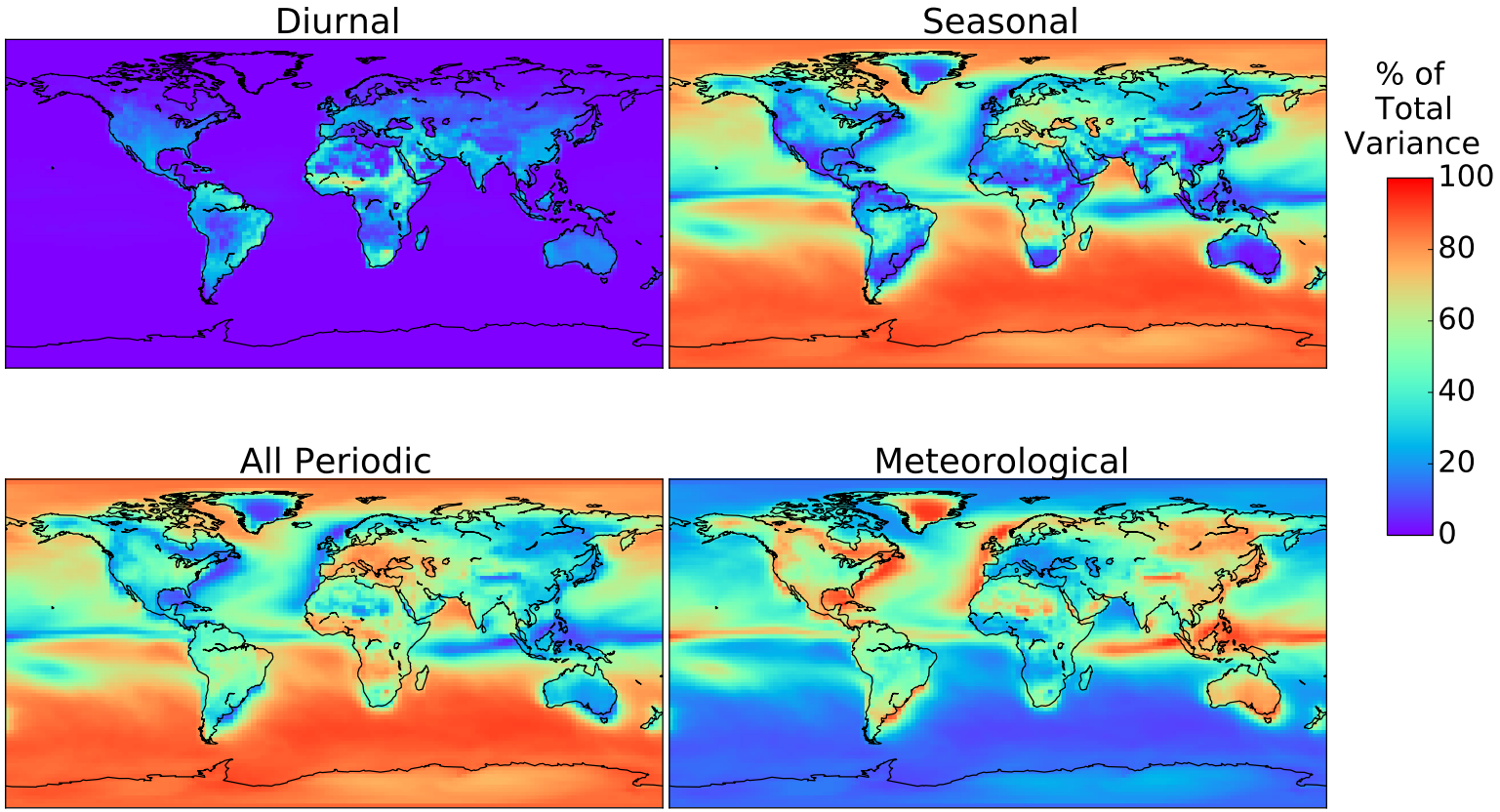


Fig. 4.10 Modelled fractional variance of time series from diurnal, seasonal and total periodicity, as well as the weather and macroweather (meteorological) regimes.

### 4.4.3 Seasonal cycle

The lowest panel of Fig. 4.6 shows the modelled amplitude for the seasonal cycle of surface $O_3$. As with the observations, the model shows large amplitudes over regions with significant anthropogenic NOx emissions (Fig. 4.15c) such as North America, Europe and Asia (up to 26 ppbv). Regions with significant seasonal cycles in the NOx emissions, such as from biomass burning in the Amazon and central Africa also have large cycles (up to 27 ppbv). These large amplitudes can be seen to extend away from the source regions into the Pacific and Indian oceans. Over the remote tropical oceans the seasonal cycle is very small (1 ppbv). Due to a scarcity of observations, many of these features are unobserved.

Figure 4.7 shows the global seasonal phase of modelled surface $O_3$ (lower panel). There are distinct bands of phases. Over polluted NH continental regions a July–September maximum is calculated, with the cleaner northern extra-tropics showing a April–May maximum and the clean tropics a December–February maximum. In the SH there is a September–December maximum for continental regions, and a July–September maximum over the oceans and Antarctica.

### 4.4.4 Diurnal cycle

The largest diurnal amplitudes (lower panel of Fig. 4.8) are found in eastern China (up to 28 ppbv) where the emissions of NOx are greatest. This leads to large diurnal photochemical production of $O_3$ but also large titration by NO at night. High diurnal amplitudes are also found over the polluted north-eastern USA (13–17 ppbv), central Europe (10–13 ppbv) and India (11–15 ppbv). Again, regions with significant seasonal cycles in the NOx emissions from biomass burning also have large amplitudes i.e. Amazon, Indonesia and central Africa.

Figure 4.9 shows the global diurnal phases of modelled surface $O_3$ (lower panel). As with the observations the 2 distinct clean and polluted regimes emerge. The polluted areas almost all have diurnal cycle peaking at 14:00 or 15:00 local solar time. This band includes all continental regions (except Greenland and polar regions). It also includes a band across the northern Pacific and northern Atlantic Oceans. The clean areas almost all have a phase at 08:00, the exception being a circumpolar band of phases which peak at 04:00 around Antarctica. The diurnal phase at the poles looks incoherent, which is predominantly due to the very small amplitudes in these regions, thus the phase becomes practically irrelevant.

## 4.5 Model – measurement comparisons

The previous sections investigate the absolute amplitude and phase of the seasonal and diurnal cycle. In this section these parameters are used to investigate model performance against observations.

### 4.5.1 Significance of seasonal and diurnal cycles

Figure 4.11 shows the difference between the observed and modelled fractional total variance explained by the seasonal, diurnal and combined total periodic waveforms, and meteorological regimes. The fractional variance from the seasonal cycle is overestimated by the model significantly over central Europe and north-eastern America (20–50 %), whereas it is underestimated in northern Europe, Canada and Japan (20–40 %). These findings are reversed with regards to the fractional contribution from the meteorological regimes. The fraction of total variance from the diurnal cycle is generally well captured by the model, with the exception being overestimation of the diurnal contribution over Europe (10–20 %).

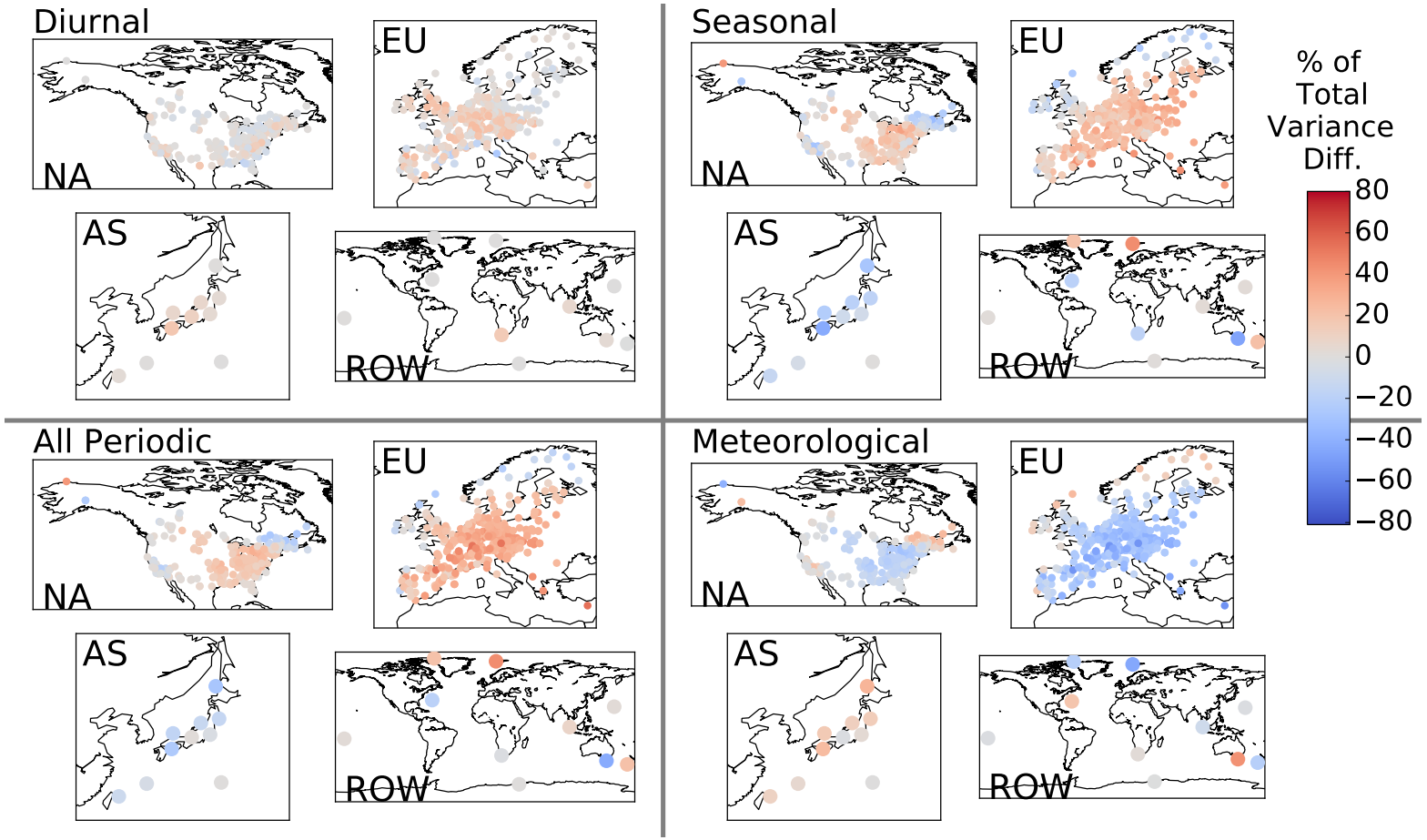


Fig. 4.11 Fractional variance differences of diurnal, seasonal and total periodicity, and weather and macroweather (meteorological) regimes, between observations and the GEOS-Chem model. NA is North America, EU is Europe, AS is Asia, and ROW is rest of world.

### 4.5.2 Seasonal cycle

Figure 4.14 shows the polar representation of the seasonal cycle for the observations, model and the difference between the two. North American and European site seasonal amplitudes are on average overestimated, (up to 16 ppbv). The seasonal phase also shows biases with most sites‘ phases in North America and Europe peaking 1–5 months later than the observations, in mid-late summer rather than mid-late spring. Seasonal amplitudes for the African, Antarctic, Arctic, Asian, Oceania and oceanic sites are all underestimated (up to 10 ppbv) but their phases show generally good agreement with the observations.

Figure 4.12 shows the spatial distribution of the difference for the seasonal amplitudes and phases. The biggest model overestimations for the amplitudes (upper panels) are in regions with very high $O_3$ precursors, i.e. north-eastern USA (up to 16 ppbv) and mainland central Europe (to to 11 ppbv); both generally at sites inland, away from oceanic influence. In contrast, it is the coastal and oceanic sites where the model underestimations are greatest, with the largest coming in Asia (5–10 ppbv) and eastern Canada (up to 8 ppbv).

The lower panels of Fig. 4.12 show in mainland Europe the seasonal phases are generally 1–3 months too late in the model and 2–4 months too late in the north-eastern/south-eastern USA. The biggest phase differences come in the central-southern USA with the model phases approximately 4–5 months too late (a region where the seasonal cycle contributes very little to the total variance, Fig. 4.5).

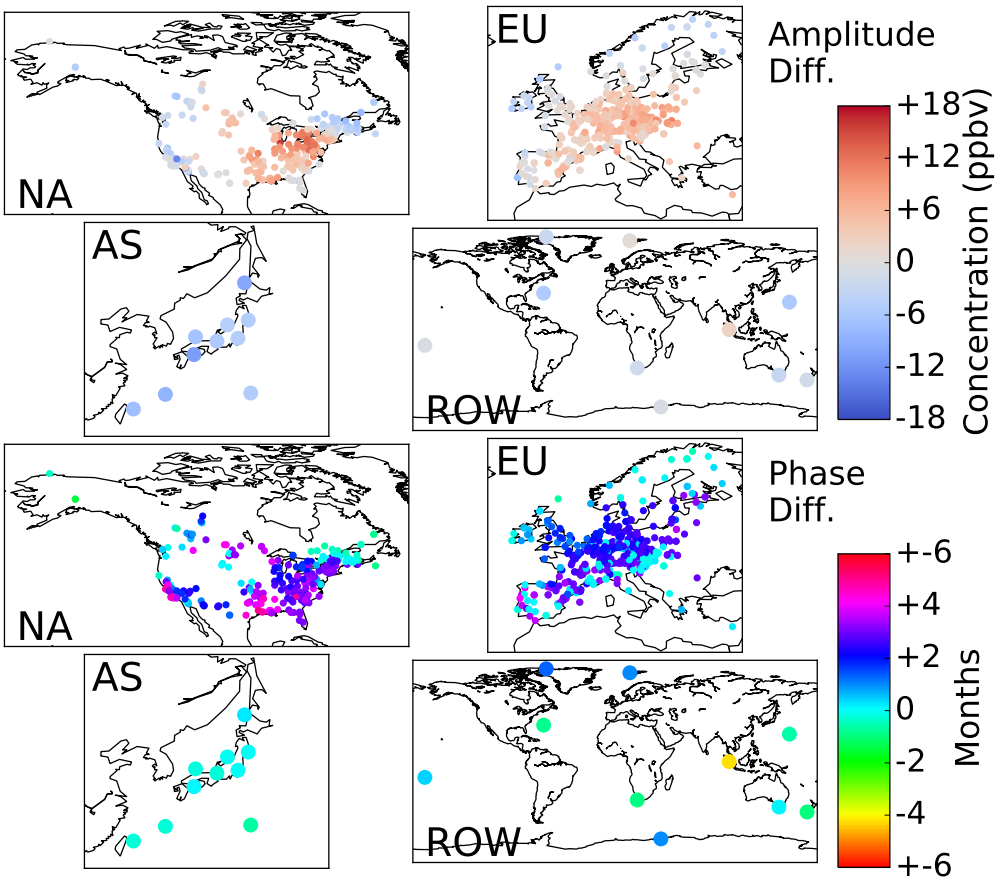


Fig. 4.12 Seasonal amplitude (upper panel) and phase (lower panel) differences between observations and the GEOS-Chem model. NA is North America, EU is Europe, AS is Asia, and ROW is rest of world.

### 4.5.3 Diurnal cycle

Figure 4.14 also shows the polar representation of the diurnal cycle observations, model and difference. The model has some skill in determining the diurnal amplitudes. There is on average an overestimation of North American, European and Asian diurnal amplitudes (up to 17 ppbv). Amplitudes for the clean oceanic sites are well estimated, with the rest of the sites in Oceania, Africa, Antarctic and Arctic displaying reasonable agreement. The model has generally good skill for simulating the diurnal phases (ignoring the polar sites), however notable biases show in the oceanic and Asian sites with the model up to 5 hours late, and up to 4 hours early respectively for the groupings. Additionally for the North American and European groupings, the model simulates the vast majority of phases in a narrow band, where there is a broader grouping of phases in the observations. This may represent issues with the timing of processes such as boundary layer mixing which is suggested to be excessive (Travis et al., 2016).

Spatially, Fig. 4.13 upper panels, the biggest overestimations in the amplitudes are again in regions with high emissions of $O_3$ precursors: Central Valley USA (up to 17 ppbv), north-eastern USA (up to 14 ppbv), Japan (up to 11 ppbv) and mainland central Europe (up to 11 ppbv). The biggest underestimations come in coastal regions i.e. USA west coast (up to 11 ppbv) and southern Europe (up to 10 ppbv).

The lower panels of Fig. 4.13 show the model in the high NOx emitting regions of north-eastern USA and central Europe to have too early a phase also ($-1$ to 2 hours). The largest phase offsets (excluding polar sites) are found in the oceanic sites of Bermuda and American Samoa ($+3$ and $+5$ hours).

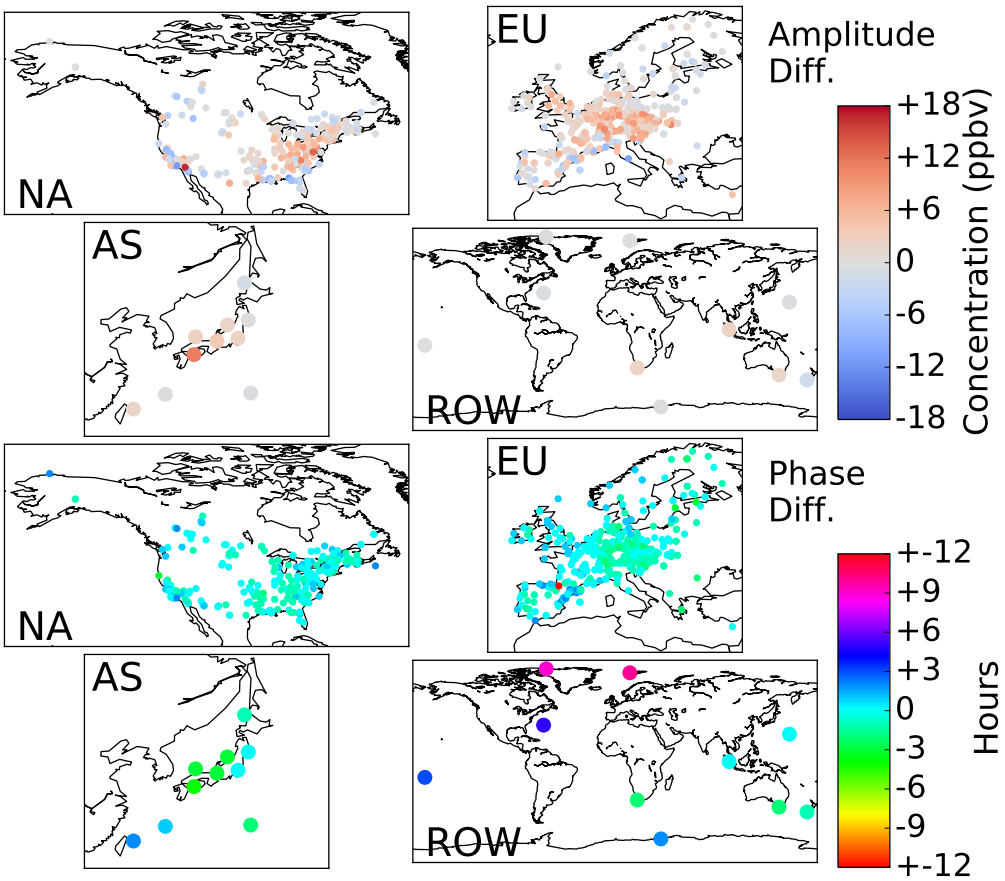


Fig. 4.13 Diurnal amplitude (upper panel) and phase (lower panel) differences between observations and the GEOS-Chem model. NA is North America, EU is Europe, AS is Asia, and ROW is rest of world.

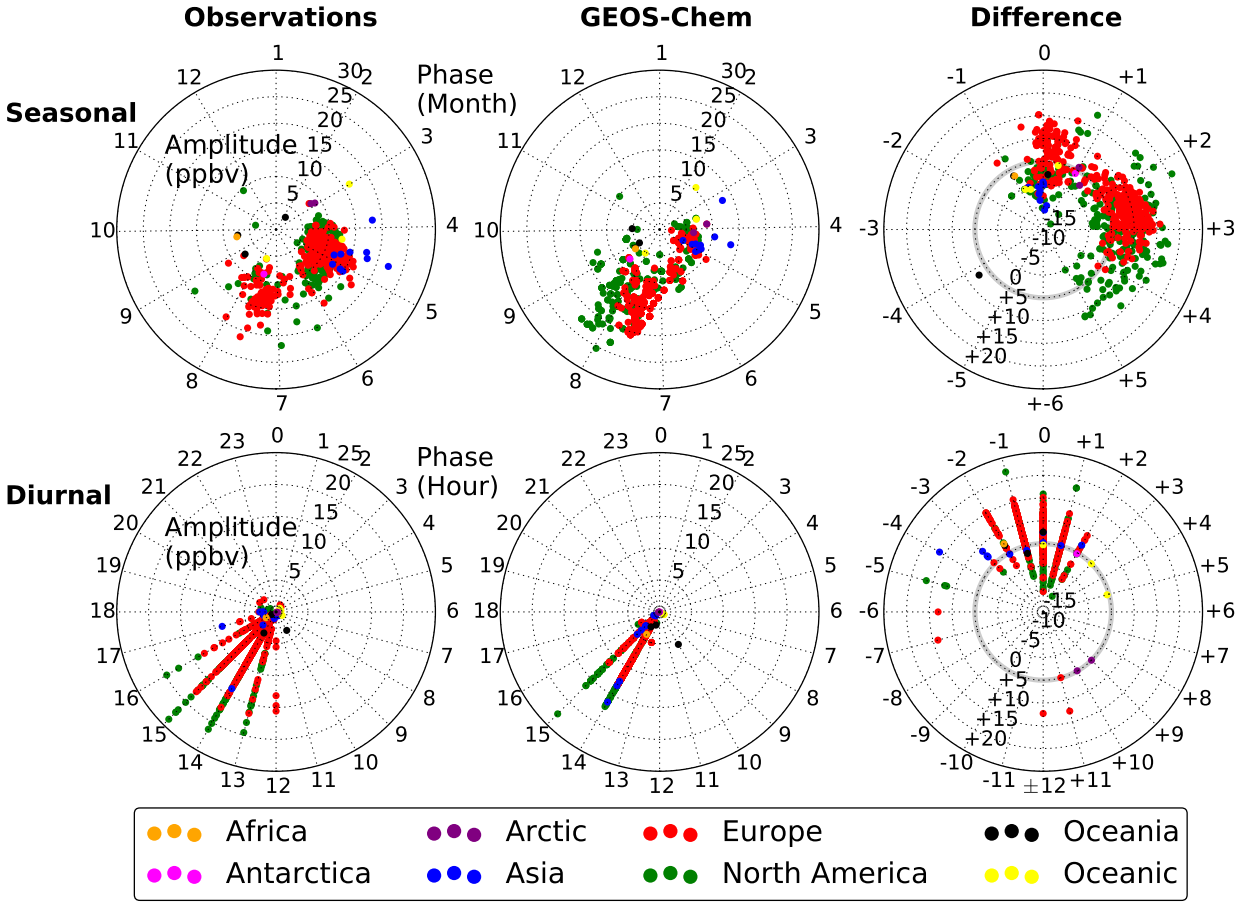


Fig. 4.14 Polar plot of the diurnal and seasonal amplitudes and phases for observations and the GEOS-Chem model, and the differences between them. Circle colour indicates the location of the site.

### 4.5.4 Possible causes of biases

A range of model biases are evident in this analysis. These may be explained by a range of model errors/uncertainties in the emissions, deposition, chemistry, photolysis rates, boundary layer mixing, stratospheric transport, tropospheric transport, resolution etc.

The most discussed uncertainties lie in the emissions. Probably the most accurate emission estimates are for North America and Europe, but even here significant uncertainties exist. Anderson et al. (2014) finds the anthropogenic USA National Emissions Inventory (NEI) 2005 NOx emissions (projected to 2011) in the mid-eastern USA to be 51–70 % too high compared with measurements taken on the DISCOVER-AQ field campaign. The NEI 2011 emissions appear to be overestimated by an even larger margin. Vestreng et al. (2009) finds $\pm$8–25 % uncertainties in European NOx emissions. Stein et al. (2014) also recently found wintertime systematic underestimates in NH CO by a global CTM, best offset by increases in winter CO road traffic emissions together with an improved CO dry deposition scheme. As anthropogenic NOx decreases, the relative importance of lightning and soil NOx is much greater and the importance of low-NOx $C_5H_8$ chemistry increases (Palmer, 2003; Fiore et al., 2014). Millet et al. (2008) show the MEGAN v2.1 biogenic emission inventory in the USA overestimates emissions of isoprene in areas where it specifies high emission factors.

The correlations between the modelled spectral biases for $O_3$ and NOx concentrations are briefly assessed. Figure 4.15 shows the modelled seasonal $O_3$ amplitude and phase biases are plotted against the average 2005–2010 model NOx. For the seasonal cycle, the greatest overestimates of the amplitude generally correlate with the highest NOx concentrations in the model (panel a), however this is not true for the largest biases in the phase (panel b). Although the phase biases are not linear with NOx emissions, from the amplitude biases it is clear that evaluation of NOx emissions would be a sensible place to start in trying to correct biases. Evaluations of modelled emissions and other parameters are touched on in much greater detail in Chapter 5, where a large-scale sensitivity study is used to attempt to minimise the NH seasonal biases of surface $O_3$.

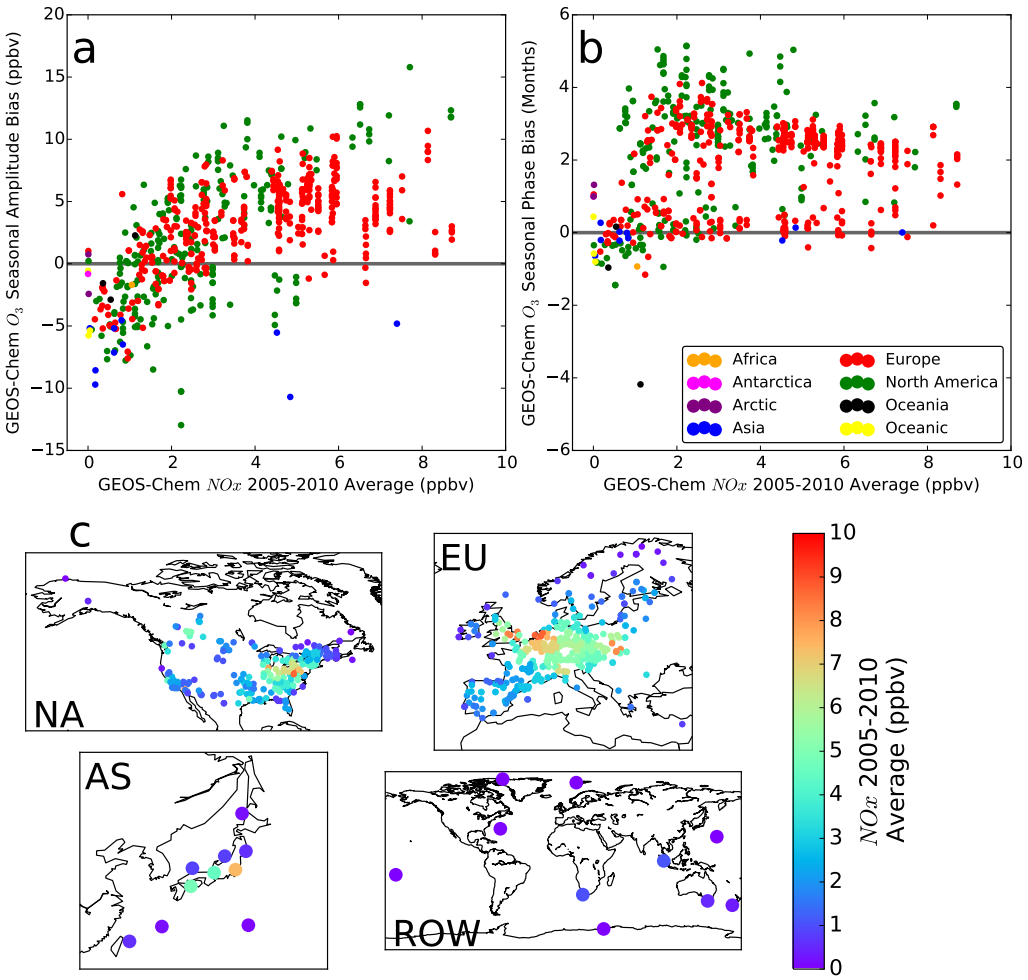


Fig. 4.15 **(a)** Seasonal amplitude bias vs. 2005–2010 Average GEOS-Chem model $NO_x$, **(b)** Seasonal phase bias vs. 2005–2010 Average GEOS-Chem model $NO_x$, **(c)** 2005–2010 Average GEOS-Chem model $NO_x$ by observational site. NA is North America, EU is Europe, AS is Asia, and ROW is rest of world.

# Chapter 5

# Summertime surface ozone bias: a problem with emissions?

## 5.1 Introduction

There is a general problem in present day CTMs/ESMs of a summertime overestimate of surface $O_3$ in the NH continental mid-latitudes (Murazaki and Hess, 2006; Fiore et al., 2009; Reidmiller et al., 2009; Lamarque et al., 2012; Brown-Steiner et al., 2015; Katragkou et al., 2015; Canty et al., 2015; Travis et al., 2016). For example, Brown-Steiner et al. (2015) find fourth-highest daily maximum 8-hour average surface $O_3$ biases of 15-35 ppbv in the eastern USA between 1995 and 2005 using the CESM CAM-Chem model, and Katragkou et al. (2015) find monthly mean summer biases of 5–10 ppbv in most areas over Europe between 2003 and 2012 using the MACC global model. This problem is additionally characterised with a failure to correctly capture the seasonality of surface $O_3$, with current CTMs/ESMs in the 2000s showing a general summertime peak in $O_3$ in the NH mid-latitudes, in contrast to a general observed springtime peak, as demonstrated in Chapter 4.

These biases may be explained by a range of model errors/uncertainties in the emissions, deposition, chemistry, photolysis rates, boundary layer mixing, stratospheric transport, tropospheric transport, resolution, etc. Biases in NOx emissions are widely cited (Vestreng et al., 2009; Fujita et al., 2012; Anderson et al., 2014; Travis et al., 2016). Low biases in modelled wintertime CO are partially attributed to underestimates in winter CO road traffic emissions (Stein et al., 2014). Significant uncertainties are associated with NMVOC chemistry, particularly for $C_5H_8$, with multiple presently used $C_5H_8$ oxidation schemes differing over the sign of the response of $O_3$ to NOx and $C_5H_8$ emissions (Squire et al., 2015). Liang and Jacobson (2000) suggest coarse horizontal resolution results in significant overestimate of surface $O_3$, whereas Wild and Prather (2006); Schaap et al. (2015) find that an increase in horizontal resolution does not reduce model bias to significant levels. Lin et al. (2009); Huang et al. (2013); Brown-Steiner et al. (2015) find that greater vertical resolution reduces model surface $O_3$ biases due to enhanced representation of the near-surface meteorology. Schwede et al. (2011); Wu et al. (2011); Walker (2014) suggest

that the dry deposition velocity of $O_3$ could be significantly underestimated in current CTMs/ESMs. Meteorological biases in temperature (Rasmussen et al., 2012), cloud fraction (Kim et al., 2015) and boundary layer mixing (Travis et al., 2016) have also been shown to impose biases on surface $O_3$. Sherwen et al. (2016) suggests halogen chemistry could be underestimated as a sink of $O_3$.

A large amount of surface $O_3$ model evaluations have been published, however only a small fraction of these evaluate the biases of $O_3$ and its precursors concurrently, due mainly to a lack of error free, global model comparable observations. Exploring the various postulated routes for model errors, while constraining both $O_3$ and its precursors with observations concurrently, would significantly reduce the number of viable pathways for reducing modelled seasonal surface $O_3$ biases. In the following sections the undertaking of a multi-species ($O_3$, NO, CO) model sensitivity study is described, using a global CTM (GEOS-Chem), evaluating multiple potential routes for model bias, resulting in optimised regional settings for the minimisation of seasonal biases for both $O_3$ and its precursors.

Section 5.2 describes the observational and model data used for evaluation, with detailed discussion of the model setup. Section 5.3 describes the current modelled seasonal biases of $O_3$ at the surface, evaluating model performance with a variety of different model setups. Section 5.4 outlines the framework and results of a sensitivity study designed to understand the sensitivity of seasonal $O_3$ biases to emissions and deposition. Section 5.5 describes an extension of the sensitivity study, evaluating NO and CO seasonal biases at the surface. Section 5.6 describes the sensitivity of modelled biases to the joint constraints of $O_3$, NO and CO. Section 5.7 describes the results of a model run with derived optimised scalings applied, and Sect 5.8 discusses the implications of these findings.

## 5.2 Measurements and model

### 5.2.1 Observations

Surface observations are taken from hourly versions of the long term $O_3$, NO and CO data sets described in Chapter 2. Data is limited to between 2009 and 2011, as this represents the most comprehensively observed time period over a two year window. Data is not taken from the $NO_2$ and $C_5H_8$ data sets, due to associated measurement biases (Steinbacher et al., 2007) and small numbers of observational stations respectively. Data is spectrally analysed (using LSP), therefore to ensure accuracy of the spectral estimates, any sites with data gaps greater than 60 days in a year are removed. Focus is placed on the three most well sampled regions in the NH mid-latitudes: North America, Europe and Japan. Figure 5.1 shows the location of the valid sites for each species, coloured by the reporting monitoring network.

The emphasis of this study is to evaluate the macro-scale modelled seasonality of surface $O_3$, therefore results are averaged by area to assess regional differences. Due to the large geographical size of North America (NA) and Europe (EU), these regions are separated into several smaller areas, with this separation predominantly weighted by the spatial availability of observations. This results in a total of 14 different areas, shown by Fig 5.2. North America is split into 7 areas: south western (SW NA), north western (NW

NA), central (C NA), north eastern (NE NA), central eastern (CE NA), south eastern (SE NA) and southern (S NA). Europe is split into 6 areas: south western (SW EU), north western (NW EU), northern (N EU), eastern (E EU), central (C EU) and southern (S EU). Japan is classed as a standalone area.

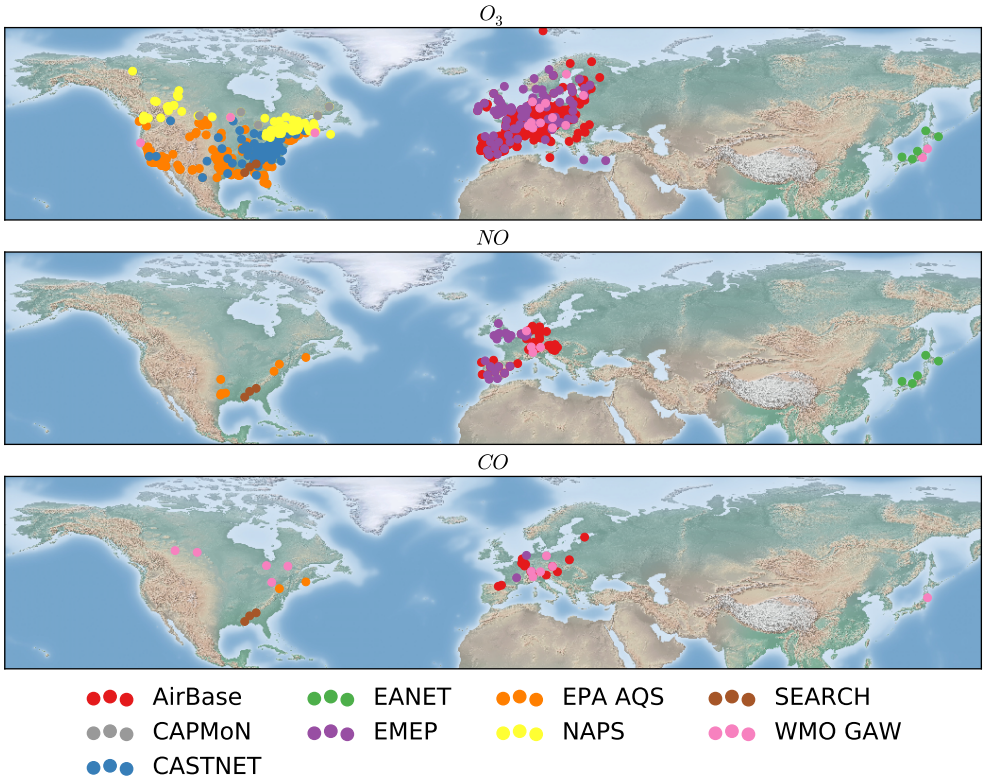


Fig. 5.1 Valid observational sites between 2009 and 2011 for $O_3$, NO and CO, coloured by the reporting monitoring network.

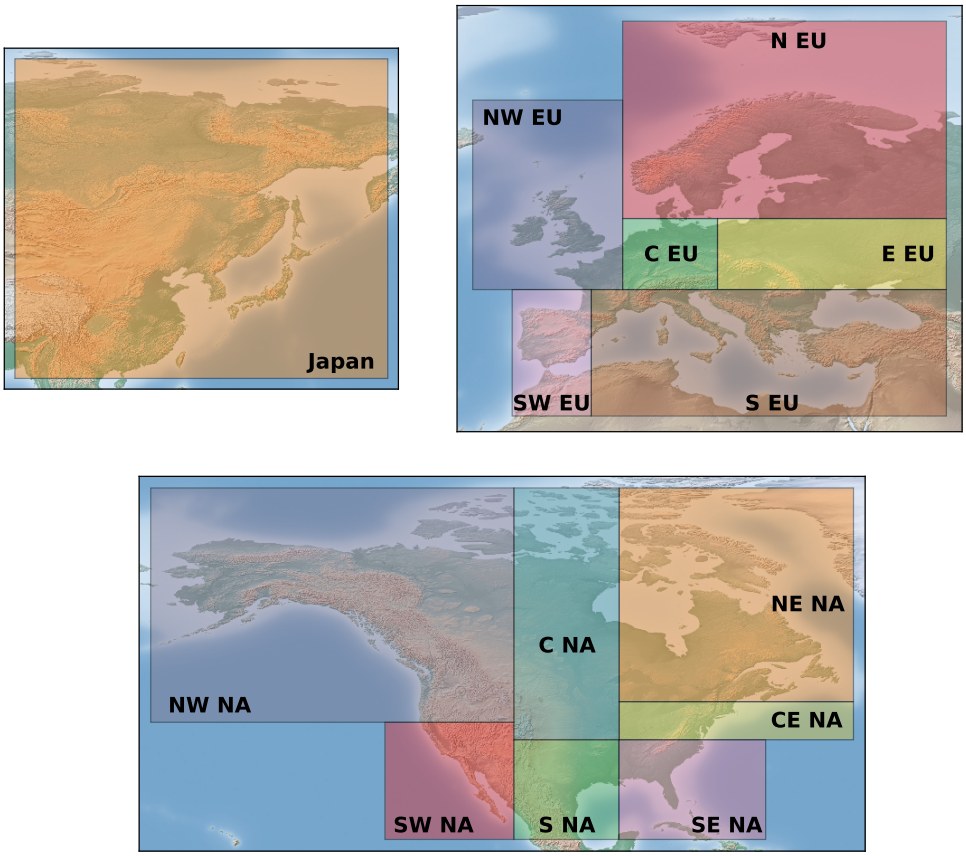


Fig. 5.2 Set areas for averaging results regionally, predominantly defined by the spatial availability of observations. North America is split into 7 regions: south western (SW NA), north western (NW NA), central (C NA), north eastern (NE NA), central eastern (CE NA), south eastern (SE NA) and southern (S NA). Europe is split into 6 regions: south western (SW EU), north western (NW EU), northern (N EU), eastern (E EU), central (C EU) and southern (S EU). Japan is classed as a standalone area.

### 5.2.2 GEOS-Chem model description

For model data, an updated version (v10.01.) of the GEOS-Chem global 3-D CTM is used (Bey et al., 2001). Between 2009 and 2011, the model is dynamically driven using globally assimilated meteorological data from a choice of two data sets: the Modern Era Retrospective Analysis for Research and Applications (MERRA) or Goddard Earth Observing System version 5 (GEOS5), both of which are produced by the NASA Global Modelling Assimilation Office (GMAO), using the GEOS5.2.0 assimilation system. MERRA was intended to assist long term model evaluation (30 years), and in order to reduce the volume of data produced (and other technical concerns), the vertical and horizontal resolution of many MERRA data fields (most 3-D fields and moist quantities) are reduced in contrast with GEOS5. Meteorological updates are 3 hours and 6 hours respectively for 3-D parameters (e.g. temperature, wind), and 1 hour and 3 hours respectively for 2-D parameters (e.g. surface parameters, mixing depths). The model is able to run globally at horizontal resolutions of $4^\circ \times 5^\circ$ and $2^\circ \times 2.5^\circ$. Higher resolution can be obtained only in regional simulations. Model time steps for chemistry and mixing are directly related to the horizontal resolution, 30 minutes for mixing, 60 minutes for emissions at $4^\circ \times 5^\circ$ resolution, and 15 minutes for mixing, 30 minutes for emissions at $2^\circ \times 2.5^\circ$ resolution. The model has 47 vertical levels, 13 below 2 km.

#### Chemistry

The major features of the current chemical mechanism are explained in detail by Mao et al. (2010, 2013). Recent updates have been focused on $C_5H_8$ oxidation, the principal NMVOC. The discovery of OH regeneration in low NOx environments prompted a new $C_5H_8$ oxidation mechanism to be implemented, described by Mao et al. (2013).

Oxidation of $C_5H_8$ by OH produces $C_5H_8$ peroxy radicals ($ISOPO_2$). In a low NOx atmosphere $ISOPO_2$ dominantly reacts with $HO_2$ or other organic peroxy radicals producing $C_5H_8$ hydroperoxides (ISOPOOH) (Paulot et al., 2009a). ISOPOOH is rapidly lost through deposition, previously thought to terminate HOx (Jacob and Wofsy, 1988), however observations from numerous field campaigns do not show such a loss of HOx (Tan et al., 2001; Stone et al., 2010; Whalley et al., 2011). This is corrected for in GEOS-Chem through the oxidation of ISOPOOH by OH producing epoxydiols (Paulot et al., 2009b), and fast isomerisation of $ISOPO_2$ leading to the production of hydroperoxyaldehydes (HPALDs) (Peeters et al., 2009; Peeters and Müller, 2010; Wolfe et al., 2012), with both pathways subsequently regenerating OH.

In a high NOx environment $ISOPO_2$ reacts dominantly with NO through two pathways. The major pathway produces $NO_2$ and subsequently $O_3$ (Paulot et al., 2009a). The minor pathway leads to $C_5H_8$ nitrate formation, typically thought to terminate both HOx and NOx chains (Ito et al., 2009; Paulot et al., 2012). However, $C_5H_8$ nitrates have been found to be partly recycled back to NOx through oxidation to more stable secondary nitrates. This has led to confusion over whether this minor pathway acts as a sink or reservoir of NOx, which has subsequent consequence for the tropospheric budget of $O_3$ (Von Kuhlmann et al.,

2004; Ito et al., 2009; Paulot et al., 2009a, 2012). The decomposition of secondary $C_5H_8$ nitrates are set to return a weighted average yield of 55 % of NOx within GEOS-Chem. Additionally, organic nitrates have been found to be significantly produced via nighttime oxidation of $C_5H_8$ by the nitrate radical ($NO_3$) (Rollins et al., 2009; Xie et al., 2013). Within GEOS-Chem the $C_5H_8$+$NO_3$ reaction is set to return a 70 % yield of carbonyl nitrates.

The net result of these changes is enhanced $O_3$, as OH is no longer titrated by $C_5H_8$, and more NOx is recycled from $C_5H_8$ nitrates (Mao et al., 2013). Work is still ongoing in this field, and significant uncertainties are still associated with the parameterised $C_5H_8$ oxidation mechanisms applied in global models. Squire et al. (2015) found multiple presently used $C_5H_8$ oxidation schemes differ in the response of ozone to NOx and $C_5H_8$ emissions, and Mao et al. (2012) find significant uncertainties regarding the validity of measured OH in low NOx environments. Further updates to the $C_5H_8$ oxidation mechanism have been suggested (Fisher et al., 2016; Marais et al., 2016; Travis et al., 2016), but have not been applied here. We do not further consider the uncertainty of the chemical mechanism in this work.

### Emissions

Emissions fields are sourced from a variety of global and regional bottom-up emission inventories, at a range of horizontal and temporal resolutions, the details of which are summarised in Table 5.1. Emissions are implemented at run-time using the HEMCO module (Keller et al., 2014).

The Emission Database for Global Atmospheric Research (EDGAR) v4.2 inventory provides global annual anthropogenic emissions of CO, NOx and $NH_3$ between 1970 and 2008 (Olivier et al., 2005), calculated based on the energy balance statistics of the International Energy Agency (IEA) (IEA, 2010). Monthly global anthropogenic emissions of NMVOCs for the year 2000 are from the Reanalysis of the Tropospheric chemical composition (RETRO) global inventory (lumping anthropogenic and biofuel emissions) as described by Hu et al. (2015), except for ethane which is provided globally by Xiao et al. (2008). Global annual biofuel emissions (for the year 1985) are taken from Yevich and Logan (2003) (for species not provided by RETRO).

Regional inventories are used in certain regions where there is improved information. The Big Bend Regional Aerosol and Visibility Observational Study Emissions Inventory (BRAVO) in Mexico and Criteria Air Contaminants (CAC) in Canada both provide annual regional emissions for CO and NOx (for 1999, and 2002–2009 respectively). EMEP provides european annual regional emissions for CO, NOx and $NH_3$ (1990–2013), and for a number of NMVOCs (1980, 1985–2000). MIX (Li et al., 2015) provides monthly Asian emissions between 2008 and 2011, derived by harmonising various emission inventories from multiple regions. The National Emissions Inventory 2011 (NEI2011) inventory provides hourly resolution emissions over the USA for 2011, with species specific annual scaling factors provided between 2006 and 2014.

Emissions from open fires are calculated online, based on monthly global emissions from the Global Fire Emissions Database version 4 (GFED4) (1998–2015) (Giglio et al., 2010). Monthly global aircraft emissions of CO, NOx and acetone for 2005 are taken from the Aviation Emissions Inventory Code (AEIC) (Stettler et al., 2011). Global monthly ship emissions of CO and NOx for 2002 are taken from the International Comprehensive Ocean-Atmosphere Data Set (ICOADS), as described by Lee et al. (2011). Improved annual estimates of ship emissions for CO and NOx in Europe are taken from EMEP (1990–2013). Ship NOx emissions are processed online to adjust for $O_3$ and $HNO_3$ production in the plume (Vinken et al., 2011; Holmes et al., 2014). Additional inputs of NOx from lightning (Price and Rind, 1992; Murray et al., 2012) and soil (Hudman et al., 2012) are also calculated online. Biogenic NMVOC (BNMVOC) emissions are calculated online using the global Model of Emissions of Gases and Aerosols from Nature (MEGAN) v2.1 inventory, computed using annual emission factors for plant functional types adjusted as a function of meteorological variables (temperature, solar radiation, leaf area index and leaf age) (Guenther et al., 2006, 2012). Notably, biogenic emissions of CO are not included in the model, assumed to balance with loss by dry deposition to soils (Müller and Brasseur, 1995). Oceanic emissions of acetone assume fixed annual concentrations as described by Fischer et al. (2012). $CH_4$ is not emitted, rather, concentrations are fixed annually in 4 zonal bands (90°S–30°S, 30°S–0°S, 0°N–30°N, 30°N–90°N) using averaged observed data from the National Oceanic and Atmospheric Administration (NOAA) (http://www.esrl.noaa.gov/gmd/).

In years outside of the prescribed emissions ranges, and where annual scaling factors are not provided (e.g. NEI2011), NOx and CO emissions are annually scaled (relative to the first or last year) on the basis of economic data (van Donkelaar et al., 2008) by a global $1^\circ \times 1^\circ$ scaling map, available for years between 1985 and 2011. Trend estimates from specific regions are incorporated where available (in Asia, Canada, Europe and the USA). Otherwise, scaling factors are derived based on $CO_2$ trends from the Carbon Dioxide Information Analysis Center (http://cdiac.ornl.gov/) (van Donkelaar et al., 2008).

Due to the coarse temporal resolution of the majority of emissions fields, a variety of seasonal and diurnal scaling factors are applied to make emissions appropriate for application in a global model. Diurnal scaling is applied to all anthropogenic emissions except from NEI2011 (which have native hourly resolution), ship and aircraft emissions. For NOx this is done per grid cell based on the weighted average of the diurnal variation of NOx from each source type (provided by the EDGAR inventory), relative to the source contribution to total NOx in each grid cell (van Donkelaar et al., 2008). All fossil fuel emissions (i.e. CO and NMVOCs) are scaled by hourly factors derived from the Global Emissions Inventory Activity (GEIA) data set. EDGAR NOx emissions are scaled monthly based on the seasonality of GEIA NOx. EMEP emissions of NOx, CO and $NH_3$ are seasonally scaled by monthly scaling factors derived from the Generation of European Emission Data for Episodes (GENEMIS) project (Reis et al., 2004), coordinated by the Institute of Energy Economics and the Rational Use of Energy (IER) at the University of Stuttgart. Factors are derived for the year 1994, not accounting for changes to the seasonal

variation of emissions in subsequent years (e.g. decreases in the winter/summer ratios of electricity consumption (Grennfelt and Hov, 2005)). Additionally CO and acetone emissions from biofuels, BRAVO, CAC, EDGAR, EMEP and RETRO are modified by fixed ratios to more accurately speciate between emissions from fossil fuels, biomass and biofuels.

The current implementation of emissions in GEOS-Chem has a number of other notable limitations. BRAVO, biofuels, CAC (except $NH_3$), EDGAR CO, EMEP NMVOCs, EMEP ship and Xiao ethane emissions are not seasonally scaled. No annual scalings are applied for biofuel emissions, RETRO and Xiao ethane emissions, and no ship emissions of NMVOCs are included.

The patchwork nature of emission inventories and temporal scalings applied within global models has led to consistent attribution of modelled surface $O_3$ biases to issues with emissions. The most detailed emission estimates come from North America and Europe, but even here significant uncertainties exist. Anderson et al. (2014) find July anthropogenic NEI2005 NOx emissions (annually scaled to 2011) in the mid-eastern USA to be 51–70 % too high compared with aircraft and surface measurements, with NEI2011 emissions overestimated by an even larger margin. Travis et al. (2016) find summertime (August–September) daytime surface $O_3$ biases in the south-east USA to be partly attributable to a $\sim$50% overestimate of NOx emissions in NEI2011. NOx emission uncertainties from power plants are small across the USA due to the use of continuous emission monitoring systems (Duncan et al., 2013). Rather, errors are found to be dominantly from overestimates of mobile sources (Fujita et al., 2012; Brioude et al., 2013; Anderson et al., 2014; Travis et al., 2016).

Annual EMEP emissions are estimated to have a 8–23 % uncertainty in western Europe and $\sim$ 25 % in eastern Europe (Vestreng et al., 2009). Schöpp et al. (2005) indicate that the specific sector uncertainty of emissions is higher, and might be as much as three times larger for emissions from petroleum using cars and diesel using heavy duty vehicles. The overall uncertainty on Asian NOx emissions is estimated to be up to 37 %, with growing uncertainty over time due to a higher fraction of emissions from mobile sources (Streets et al., 2003; Zhang et al., 2007, 2009). Emissions from China in particular are thought to be suspect due to a lack of local emission factors (Zhao et al., 2011), with an estimated uncertainty of 16 % in 2012 for the Multi-resolution Emission Inventory for China (MEIC) (Hong et al., 2016). In 2008, Asian emissions of NOx from EDGAR are 20 % lower than from MIX (Li et al., 2015).

Top-down satellite measurements have been frequently used to assess bottom-up emissions of NOx. Top-down estimates are associated with significant uncertainties, with tropospheric $NO_2$ column uncertainties estimated to be 30 % and 60 % under clear sky and cloudy conditions respectively (Boersma et al., 2004; Lamsal et al., 2010). $NO_2$ generated from lightning in the upper troposphere significantly contributes to the tropospheric $NO_2$ column, and therefore requires correcting for when estimating surface NOx emissions, corrections which can be extensively complicated (Travis et al., 2016). Miyazaki et al. (2012) using assimilated Ozone Monitoring Instrument (OMI) column $NO_2$ from the

NASA AURA satellite, find anthropogenic NOx emissions are mostly underestimated globally, finding it necessary to increase NOx emissions from EDGAR (2005 and 2006) in eastern China, eastern USA and central eastern Europe by factors of 1.4 to 2.5. Spatial variations in the sign of necessary emissions changes over Europe are notable, with positive changes needed in northwestern Europe and negative changes over eastern and south western Europe. Lu et al. (2015) find good agreement between USA NEI emissions and OMI column $NO_2$ estimates, however they assume an error on NEI emissions of 50 %. Lin et al. (2012) find eastern Chinese OMI column $NO_2$ to be underestimated in GEOS-Chem by 20 % in July 2006 and by 36 % in January 2006, using the INTEX-B inventory (Zhang et al., 2009).

Anderson et al. (2014) find July NEI2005 CO emissions (annually scaled to 2011) in the mid-eastern USA to be overestimated by 15 $\pm$ 11 % through comparison with lowermost tropospheric CO from the Measurement of Pollution in the Troposphere Instrument (MOPITT) onboard the NASA TERRA satellite (Deeter et al., 2013), and surface observations. Stein et al. (2014) through model analysis with a combination of satellite derived CO columns (from MOPITT and the Infrared Atmospheric Sounding Interferometer (IASI) onboard the European Space Agency MetOp satellite), aircraft and surface observations find 2008 wintertime anthropogenic CO emissions, from traffic or other combustion processes, to be underestimated in Europe and North America in the MACCity inventory (Granier et al., 2011). Increases in wintertime CO traffic emissions by factors of up to 4.5 and 2 in Europe and North America respectively are necessary to minimise model biases. This is in agreement with Kopacz et al. (2010), who through an inversion of GEOS-Chem v7.04.11. with multiple satellite CO columns (in 2004 and 2005), find significant regional seasonal scalings of CO emissions are necessary to reduce model biases in the NH mid-latitudes, with most notably European (EMEP) and USA (NEI1999) winter emissions needing to be increased by factors of 1.5–2. Fu et al. (2016) find uncertainties on measurements of lowermost tropospheric CO from MOPITT to be $\pm$ 14 %.

Robust evaluations of NMVOC emissions are limited by the small amount of valid observations that have been made, either from aircraft or at the surface. Emissions of $C_5H_8$ by different inventories have been found to differ by factors of two or more (Warneke et al., 2010; Hogrefe et al., 2011). Satellite measurements of formaldehyde (HCHO), an intermediate product from the oxidation of most NMVOCs, have been most commonly used to estimate emissions of NMVOCs (Palmer, 2003). Millet et al. (2008), using OMI column HCHO, find MEGAN overestimates BNMVOC emissions (by 30 % to 50 %) in areas where it specifies particularly high emission factors (e.g. the Ozarks region of the south east USA), backed up by in situ observations (Carlton and Baker, 2011). Curci et al. (2010) find a general underestimate of the seasonal amplitude of European OMI column HCHO, attributed to biases in MEGAN BNMVOC emissions. MEGAN $C_5H_8$ emissions are found to be too high by 40 % and 20 % over the Balkans and southern Germany respectively, and too low by 20 % over the Iberian peninsula and Italy. However, Zhu et al. (2016) find all HCHO satellite retrievals to be biased low on average by 20–51 %.

| Emissions Inventory | Type | Period | Temporal Resolution | Horizontal Resolution | Species |
|---|---|---|---|---|---|
| Aircraft (AEIC) | Global | 2005 | Monthly | $1° \times 1°$ | NOx, CO, SOx, Acetone |
| Biofuel | Global | 1985 | Annual | $4° \times 5°$ | NOx, CO, Acetaldehyde, Acetone, Ethane, Formaldehyde, Lumped >= C4 Alkanes, Lumped >= C3 Alkenes, Methyl Ethyl Ketone, Propane |
| BRAVO | Regional (Mexico) | 1999 | Annual | $1° \times 1°$ | NOx, CO, SOx |
| CAC | Regional (Canada) | 2002–2009 | Annual | $1° \times 1°$ | NOx, CO, SOx, $NH_3$ |
| EDGARv4.2 | Global | 1970–2009 | Annual | $0.1° \times 0.1°$ | NOx, CO, SOx, $NH_3$ |
| EMEP (AQ) | Regional (Europe) | 1990–2013 | Annual | $0.1° \times 0.1°$ | NOx, CO, SOx, $NH_3$ |
| EMEP (VOCs) | Regional (Europe) | 1980, 1985–2000 | Annual | $1° \times 1°$ | Acetaldehyde, Lumped >= C4 Alkanes, Lumped >= C3 Alkenes, Methyl Ethyl Ketone |
| GFED4 (online) | Global | 1998–2015 | Monthly | $0.25° \times 0.25°$ | NOx, CO, SOx, $NH_3$, Acetaldehyde, Acetone, Ethane, Formaldehyde, Lumped >= C4 Alkanes, Lumped >= C3 Alkenes, Methyl Ethyl Ketone, Propane |
| Lightning (online) | Global | – | – | $4° \times 5°$ | NOx |
| MEGAN (online) | Global | – | – | $1° \times 1°$ | Acetaldehyde, Acetone, Ethylene, Isoprene, Lumped >= C3 Alkenes |
| MIX | Regional (Asia) | 2008–2011 | Monthly | $0.25° \times 0.25°$ | NOx, CO, SOx, $NH_3$, Acetaldehyde, Acetone, Ethane, Formaldehyde, Lumped >= C4 Alkanes, Lumped >= C3 Alkenes, Methyl Ethyl Ketone, Propane |
| NEI2011 | Regional (USA) | 2011 | Hourly | $0.1° \times 0.1°$ | NO, $NO_2$, HONO, CO, $SO_2$, $SO_4$, $NH_3$, Acetaldehyde, Acetone, Aldehyde, Benzene, Ethane, Ethylene, Formaldehyde, Lumped >= C3 Alkenes, Methacrolein, Toluene, Xylene |
| Oceanic (online) | Global | – | – | $1° \times 1°$ | Acetone |
| RETRO | Global | 2000 | Monthly | $1° \times 1°$ | Acetaldehyde, Acetone, Benzene, Ethane, Ethylene, Formaldehyde, Lumped >= C4 Alkanes, Lumped >= C3 Alkenes, Methyl Ethyl Ketone, Propane, Toluene, Xylene |
| Soil (online) | Global | – | – | $0.5° \times 0.5°$ | NOx |
| Ship (ARCTAS) | Global | 2008 | Annual | $1° \times 1°$ | SOx |
| Ship (EMEP) | Regional (Europe) | 1990–2013 | Annual | $0.1° \times 0.1°$ | NOx (processed online), CO, SOx |
| Ship (ICOADS) | Global | 2002 | Monthly | $1° \times 1°$ | NOx (processed online), CO |
| Xiao (Ethane) | Global | 1985 | Annual | $1° \times 1°$ | Ethane |

Table 5.1 Summary of global and regional emissions inventories used in GEOS-Chem v10.01. Regional emissions overwrite global emissions of the same species. Emission grids are interpolated on the fly to the resolution of the model run by the HEMCO emissions component (Keller et al., 2014).

### Dry deposition

Several different dry deposition mechanisms are employed in CTMs/ESMs. The dry deposition mechanism in GEOS-Chem is based on the resistance-in-series scheme described by Wesely (1989) and implemented by Wang et al. (1998), termed a "big leaf model", analogous to Ohm's law in electrical circuits, represented by equations 5.1 and 5.2:

$$F = V_d \cdot C \tag{5.1}$$

$$V_d = \frac{1}{R_a + R_b + R_c} \tag{5.2}$$

The deposition flux of a species of interest ($F$) to the surface is assumed to be proportional to the concentration of the species ($C$) near the surface. $F$ is then modified to account for boundary layer mixing in each discrete time step. The proportionality constant is termed the dry deposition velocity ($V_d$), which is modelled as a set of different resistances: the aerodynamic resistance above the surface ($R_a$), the resistance to molecular diffusion through a quasi-laminar layer just above the surface ($R_b$), and the bulk canopy resistance to physical, biological and chemical interactions with the surface ($R_c$) (Wesely and Hicks, 2000). The effects of $R_a$ and $R_b$ are typically small (Zhang et al., 2002) and well constrained (Walker, 2014), whereas large uncertainties arise from the calculation of $R_c$, which accounts for all deposition resistances to the surface, summed in parallel (i.e. stomatal resistance, cuticular resistance, resistance based on canopy height and density, lower canopy resistance, and ground surface resistance). Surface resistances vary significantly by land cover. Specific values for each surface resistance term are explicitly set in GEOS-Chem, for 11 different land cover classes taken from Wesely (1989), except for tropical rainforests (Jacob and Wofsy, 1990) and tundra (Jacob et al., 1992). The multiple surface resistances are fractionally weighted onto a global grid using the Olson 1992 data set (Olson, 1994; Loveland et al., 2000), which reports globally gridded fractional land cover classes (a total of 74) at native $1^\circ \times 1^\circ$ resolution (i.e. many of the classes share the same depositional characteristics). Each surface resistance term is then subsequently modified dependent on the chemical reactivity of the species in question (scaled relative to the high reactivity of $O_3$).

30–90 % of the $F$ for $O_3$ is estimated to occur via the plant stomata (Fowler et al., 2001; Cieslik, 2004; Fowler et al., 2009), and consequently stomatal resistance dominantly contributes to the uncertainty of $R_c$ for $O_3$. Stomatal resistance is calculated based on a Jarvis method of parametrisation (Jarvis, 1976), where a specified minimum resistance is multiplied by the product of independent environmental stress factors (i.e. temperature (Wesely, 1989) and solar insolation (Baldocchi et al., 1987; Guenther et al., 1995)), suppressed at night due to stomatal closure (Finkelstein et al., 2000). The minimum stomatal resistance is difficult to represent as it can not be measured independently (Niyogi et al., 2009) and has significant diurnal and seasonal variability (Avissar, 1993). Wu et al. (2011), evaluating a regional atmospheric model (WRF-Chem) using a Wesely (1989) scheme, find significant underestimation of $O_3$ $V_d$ in Autumn over a mixed deciduous forest

(Harvard Forest), a factor of 4 in daylight hours, directly attributed to an overestimate of the minimum stomatal resistance. Setting a minimum stomatal resistance of 70 s $m^{-1}$ (with a comparable set value of 200 s $m^{-1}$ in GEOS-Chem), produces much better model estimates of $O_3$ $V_d$. Similarly, Val Martin et al. (2014) find the CESM-CAM ESM (using a modified Wesely (1989) scheme), significantly overestimates the minimum stomatal resistance in the summertime over a broadleaf deciduous forest in Canada (Padro, 1996), by a factor of 5.

Non-stomatal surface resistances can also lead to significant biases. $O_3$ $F$ has been found to increase significantly (up to a factor a 3) in wet conditions (Zhang et al., 2002), with the variety of circumstances involving wet vegetation surfaces (i.e. rainy, humid, dewy) notably difficult to model (Wesely and Hicks, 2000). Persistent underestimates of $O_3$ $V_d$ at night (factors of 2–8) have also been attributed to an overestimation of nighttime non-stomatal surface resistance (Charusombat et al., 2010; Wu et al., 2011). Schwede et al. (2011) compare the big leaf deposition model to the multilayer deposition model, finding differences on the order of 2–3, attributed to uncertainties associated with non-stomatal surface resistances (soil and cuticular). Notably, canopy based resistances and ground surface resistances (i.e. soil, leaf litter, water, snow) do not account for seasonal changes in leaf area index in GEOS-Chem, and additionally the impacts of surface wetness or soil moisture are not represented.

Hardacre et al. (2015) evaluate the $O_3$ $F$ globally using 15 CTMs from the Hemispheric Transport of Air Pollution intercomparison project (HTAP) for the year 2001, which mostly all use variants of the Wesely (1989) scheme. The annual $O_3$ $F$ is found to range from 818 Tg $yr^{-1}$ to 1256 Tg $yr^{-1}$ by model (with GEOS-Chem v.07. on the low end of the distribution). The seasonal amplitude of the $O_3$ $F$ also varies substantially across the models, particularly in forested regions (4–9 Tg $yr^{-1}$ for deciduous forests). Compared with observations, the models are found to overestimate/underestimate monthly $O_3$ $V_d$ by as much as factors of two, year round. Walker (2014) undertake an inversion study using GEOS-Chem over North America, constraining modelled $O_3$ by ozonesonde and surface $O_3$ observations, finding that enhanced $O_3$ $F$ (by as much as factors of 3) provides a valid pathway to reduce modelled surface $O_3$ biases over eastern North America from 17 ppbv to 5.6 ppbv.

Emitted NOx is dominantly lost through wet deposition (Sparks et al., 2007). Zhang et al. (2012) find GEOS-Chem well reproduces observed oxidised nitrogen (NOy) wet deposition fluxes over North America. NOx is also significantly lost through dry deposition (up to 43 % over North America (Shannon and Sisterson, 1992)), through a variety of NOy compounds ($NO_2$, $N_2O_5$, $HNO_3$, PAN). The chemical reactivity of PAN is set equal to $O_3$, 10 % that of $O_3$ for $NO_2$, and set as 0 for $HNO_3$ and $N_2O_5$ (as they are rapidly deposited). Wu et al. (2011) find the $V_d$ for NOy is dominated by the deposition of $HNO_3$, controlled by the atmospheric resistances ($R_a$ and $R_b$). Modelled NOy $V_d$ is found to generally agree well with observations in summer–autumn over a mixed deciduous forest, but significant modelled underestimates are found at night (10–20 %) (Wu et al., 2011).

Mao et al. (2013) updated the chemical reactivity of all oxygenated VOCs (OVOCs) to be the same as $O_3$ following Karl et al. (2010), and included deposition of ISOPOOH and epoxydiols. Nguyen et al. (2015) find $R_c$ for $H_2O_2$ and certain OVOCs are overestimated in GEOS-Chem over a mixed forest, leading to underestimates in $V_d$, however $O_3$ production is not significantly affected. No dry deposition of CO or hydrocarbons is included in GEOS-Chem (Müller and Brasseur, 1995). Stein et al. (2014) find modelled underestimates of NH mid-latitude CO can be improved through reduced estimates of CO dry deposition.

**Boundary layer mixing/transport**

Transport in GEOS-Chem is handled using the TPCORE advection algorithm of Lin et al. (1996). Convective transport is computed from the convective mass fluxes prescribed in the meteorological data set (i.e. GEOS5), as described by Wu et al. (2007). Stratosphere/troposphere exchange is handled as a parameterised representation of species sources and sinks. The Linoz algorithm of McLinden et al. (2000) is used for $O_3$, and monthly average source and sink rate constants are used for other stratospheric species (Murray et al., 2012).

Boundary layer mixing is handled using a non-local parameterisation (Holtslag and Boville, 1993), implemented in GEOS-Chem by Lin and McElroy (2010). Previously, the boundary layer in GEOS-Chem was assumed to be fully mixed, with concentrations, emissions, and dry deposition evenly distributed below a set boundary layer height (taken from meteorological fields, i.e. GEOS5). This is a reasonable assumption when the boundary layer is extremely unstable (e.g. hot summer afternoon with clear sky). However, when the boundary layer is stable or moderately stable/unstable (e.g. cool summer nighttime with clear sky) mixing will be significantly overestimated (Lin and McElroy, 2010). In stable conditions the non-local scheme reverts to a first-order local mixing scheme based on K-theory (e.g. Louis et al. (1982)). It is assumed that mixing of water vapour, heat and chemical species only occurs between adjacent vertical layers, with the magnitude of mixing determined by a calculated eddy diffusion coefficient and the local gradients of respective scalars. In unstable conditions (determined by the net heat flux and the vertical gradient of virtual potential temperature), a non-local term is introduced to account for enhanced vertical mixing (Lin et al., 2008).

The non-local scheme has been shown to reduce the GEOS-Chem bias in surface $O_3$ at $2^\circ \times 2.5^\circ$ resolution by 2–5 ppbv in the afternoon, and by more than 10 ppbv at night (Lin and McElroy, 2010). Travis et al. (2016) find the non-local scheme may provide excessive mixing to the surface in the summertime afternoon over the south east USA, contributing to overestimates in surface $O_3$. Species concentrations in the boundary layer are also strongly related to the boundary layer depth, with greater depths diluting concentrations (Lin et al., 2008). The non-local scheme is capable of calculating the boundary layer height interactively, but is set to use the height provided by the meteorological data set by default.

### Model updates

GEOS-Chem is run in its current version (v10.01.), as well as in its previous 2 versions (v09.01.03., v09.02.), to evaluate how model biases have evolved though version iterations. Major revisions from v09.01.03. to v09.02. are: a new soil NOx module (Hudman et al., 2012), new aircraft emissions inventory (AEIC) (Stettler et al., 2011), inorganic chemistry updates, updated $C_5H_8$ chemistry scheme (Mao et al., 2013), increase of $NO_3$ and $HO_2$ uptake by aerosol (Mao et al., 2013), inhibition of $N_2O_5$ uptake by nitrate aerosol, change to $RO_2$+$HO_2$ rate constant, and updates to the anthropogenic annual scaling factors through 2010. Notable revisions from v09.02. to v10.01. are: a new unified emissions module (HEMCO) (Keller et al., 2014), updated open fire emissions (GFED4), EDGAR emissions updated to v4.2, updates to MEGAN v2.1 biogenic emissions (Guenther et al., 2012), updates to PARANOX ship NOx chemistry (Holmes et al., 2014), new anthropogenic Asian emissions inventory (MIX) (Li et al., 2015), new anthropogenic USA emissions inventory (NEI2011), and reprocessed EMEP emissions for 1990–2012.

In the next section modelled seasonal surface $O_3$ biases in the NH mid-latitudes are evaluated in detail. The sensitivity of biases in GEOS-Chem to different configurations of model version, driven meteorology, horizontal resolution and boundary layer mixing are explored. In total 7 configurations are evaluated, with setup details summarised in Table 5.2. Each model simulation is for 2 years between 2009 and 2011, spun up for 6 months prior. Additionally, surface $O_3$ day/night biases, and biases in multiple other CTMs/ESMs are evaluated.

| Simulation | Version | Resolution | Meteorology | Boundary layer mixing scheme | Additional details |
|---|---|---|---|---|---|
| Base | v10.01. | $4° \times 5°$ | GEOS5 | Non-Local | |
| Base-1 | v09.02. | $4° \times 5°$ | GEOS5 | Non-Local | |
| Base-2 | v09.01.03. | $4° \times 5°$ | GEOS5 | Non-Local | |
| BaseHR | v10.01. | $2° \times 2.5°$ | GEOS5 | Non-Local | |
| MERRA | v10.01. | $4° \times 5°$ | MERRA | Non-Local | |
| FMBL | v10.01. | $4° \times 5°$ | GEOS5 | Fully Mixed | |
| IBLH | v10.01. | $4° \times 5°$ | GEOS5 | Non-Local* | Boundary layer height is set interactively |

Table 5.2 Description of simulations exploring the sensitivity of seasonal surface $O_3$ in GEOS-Chem to changes in model version, driven meteorology, horizontal resolution and boundary layer mixing. Each simulation is for 2 years between 2009 and 2011, spun up for 6 months prior.

## 5.3 Modelled seasonal ozone biases

### 5.3.1 Spectral methodology

The seasonality of the observed and modelled surface $O_3$ is spectrally determined using the Lomb–Scargle periodogram (LSP), as described in Chapter 4. The LSP is applied to the time series of each valid observational site contained within the bounds of the areas defined in Fig. 5.2, between 2009 and 2011. Rather than taking the amplitudes and phases of the resultant seasonal waveforms, the entire waveforms for each site are averaged by area. This process is repeated with model data, taking the LSP of each modelled surface $O_3$ time series in the reciprocal grid boxes of each valid site, and again taking the average seasonal waveform by area. This results in observed and modelled regionally representative seasonal waveforms, separated from noisy meteorological processes, that are able to be fairly compared.

### 5.3.2 GEOS-Chem biases by version

Figure 5.3 shows the average spectrally derived observed surface seasonal $O_3$ waveforms for 2009–2011, across the Fig 5.2 defined areas in North America, Europe and in Japan (black lines), compared with correspondingly derived output from GEOS-Chem $4^\circ \times 5^\circ$ GEOS5 v10.01 (red lines), v09.02 (green lines) and v09.01.03 (blue lines). Across all versions, in most areas, the most notable biases occur in the summertime (June–September), with very large modelled overestimates of $O_3$. This bias is particularly striking in the eastern USA, where in v10.01 July $O_3$ is overestimated in CE NA by 19 ppbv and in SE NA by 23 ppbv, areas with substantial BNMVOC emissions (Guenther et al., 2006). Modelled summertime overestimates are smaller over Europe generally, however in v.10.01. July biases still exceed 10 pbbv in all areas. Summertime $O_3$ is also overestimated in Japan, with a July 13 ppbv bias in v10.01.

The summertime bias significantly alters the seasonal representation of modelled surface $O_3$, in all versions. In the USA and northern Europe, $O_3$ has a modelled summer (June–September) peak, compared with an observed springtime peak (March–May), as seen for the majority of sites in Chapter 4. Observed $O_3$ in continental Europe has a broad summertime peak, which is reasonably well represented by the model. The observed springtime peak (April–May) in Japan is also well simulated by the model, a feature which is dominantly controlled by the east Asian monsoonal system, with strong westerly outflow from the continent in the spring and weakly reversed maritime inflow in the summer (Tanimoto, 2002; Creilson et al., 2003; Tanimoto et al., 2005). The modelled summertime overestimate also ensures the seasonal amplitude over most areas is overestimated, again consistent with the findings for the majority of sites in Chapter 4.

Despite the increasing chemical complexity with version number, the simulation of summertime surface $O_3$ is increasingly worse in all areas by version. Assuming changes made to chemistry improve the modelled representation of $O_3$, these are being offset by other modifications (e.g. emissions). The North American and Japanese summertime bias

gets significantly worse from v09.01.03. to v09.02. (e.g. July 6 ppbv change in NW NA), and in Europe from v09.02. to v10.01. (e.g. July 6 ppbv change in C EU). In no areas does v10.01. represent the best model version for minimising the integrated absolute seasonal $O_3$ biases.

In other seasons all model versions display less biases, however there is still a general overestimate of $O_3$ in the spring (March–June) and autumn (September–December), particularly in the USA and Japan (e.g. in v10.01. an October 19 ppbv overestimate in SE NA). There is a general underestimation of winter (December–March) $O_3$ in Europe, most notably in C EU and E EU (e.g. in v10.01. a January 14 pbbv underestimate in C EU). Winter underestimates are also seen in CE NA (3 ppbv in January in v10.01.). The C EU, E EU and CE NA areas have the largest population densities, and therefore also the greatest density of emissions. Winter underestimates in these regions could therefore be linked to issues with resolution, with observations potentially more urban influenced than the modelled regional grid box estimate. All wintertime underestimates are exacerbated in v09.02.

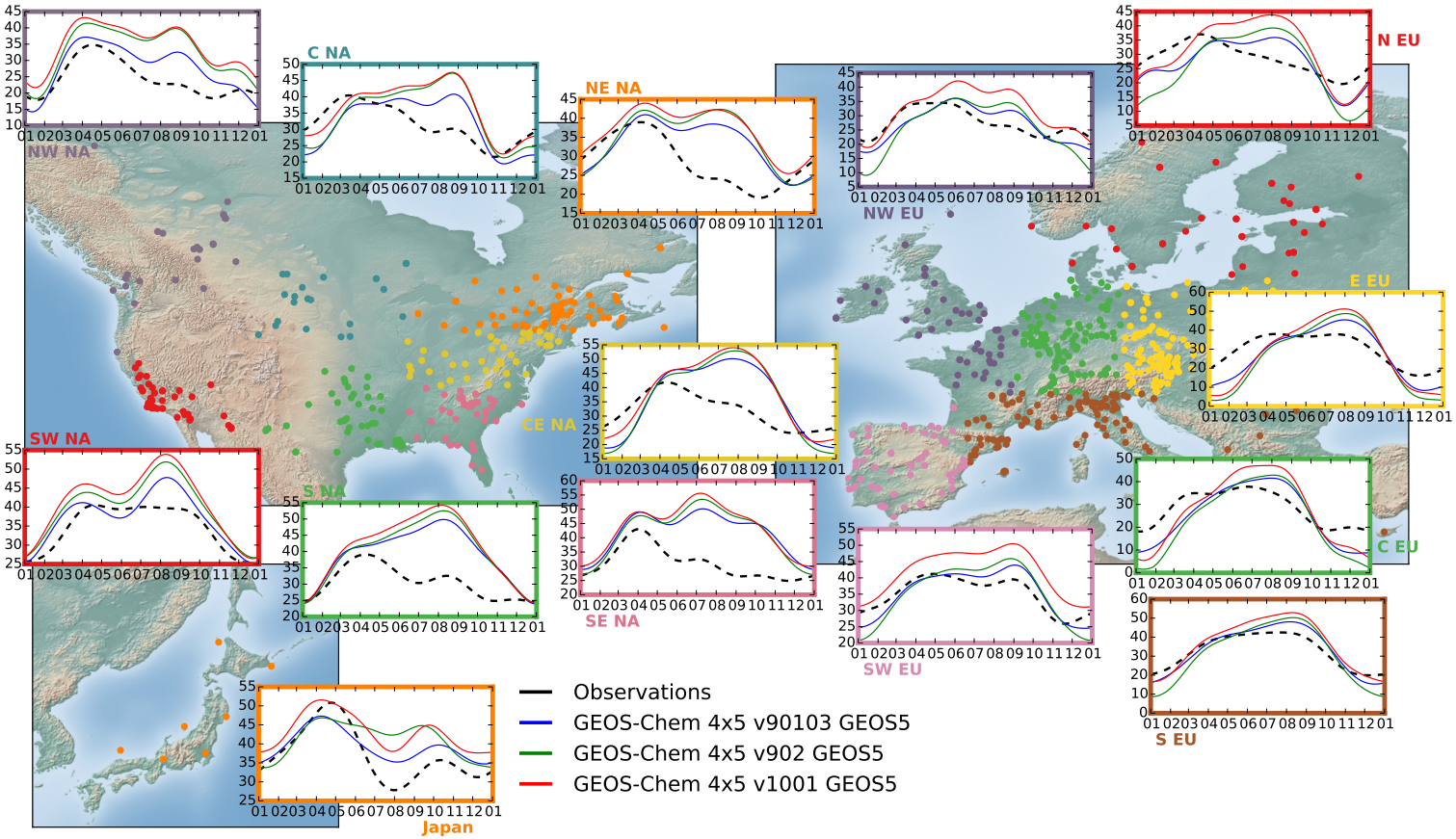


Fig. 5.3 Comparison of average spectrally derived seasonal surface $O_3$ waveforms (for 2009–2011) between observations (black lines) and iterative versions of GEOS-Chem 4° × 5° GEOS5 (v09.01.03. – blue lines; v09.02. – green lines; v10.01. – red lines), in multiple areas in North America, Europe and Japan.

### 5.3.3 GEOS-Chem biases by setup

Figure 5.4 shows the regional comparison of the observed average surface seasonal $O_3$ waveforms (black lines) with correspondingly derived output from multiple different configurations of GEOS-Chem v10.01., exploring the sensitivity of modelled biases to driven meteorology, horizontal resolution, and boundary layer mixing settings.

Running with a $2^\circ \times 2.5^\circ$ horizontal resolution (blue lines) reduces the modelled overestimate in spring–autumn in almost all areas (except Japan) relative to the standard $4^\circ \times 5^\circ$ GEOS 5 configuration (red lines), but not significantly (by 1–3 pbbv). In the wintertime, in all areas but Japan, higher horizontal resolution has a negligible impact on modelled biases, notably not improving the wintertime underestimates in regions with high densities of emissions (C EU, E EU, CE NA). In Japan, higher resolution significantly reduces $O_3$ in the winter and spring (e.g. by 8 ppbv in April), improving the wintertime estimate (4 ppbv overestimate to a negligible difference in January), but degrading the springtime estimate (1 ppbv overestimate to a 5 ppbv underestimate in April). The strong seasonal sensitivity is most probably attributed to the improved resolution better resolving the meteorological features of the east Asian monsoonal system (Tanimoto, 2002; Tanimoto et al., 2005).

Driving the model with MERRA meteorology (green lines) imposes an additional 5–10 pbbv of $O_3$ in all months, in all areas, relative to running with GEOS5 meteorology (with the exception of the summer for S NA and SE NA, where increases reach 20 ppbv). This significantly worsens the simulation in all areas through spring–autumn, and most areas in the wintertime (except C EU and E EU). The major difference between GEOS5 and MERRA is the lower vertical and horizontal resolution of many MERRA data fields (most 3-D fields and moist quantities), demonstrating the importance of accurate meteorology in the simulation of $O_3$.

Running with interactively calculated boundary layer heights (orange lines), rather than using GEOS5 archived meteorological heights, reduces year round $O_3$ concentrations in all areas by 1–5 ppbv, reducing modelled summertime overestimates in all areas, but worsening wintertime estimates in many areas also (e.g. all areas in Europe).

Running with a fully mixed boundary layer (purple lines), rather than with the non-local scheme, adds an additional 1–7 pbbv of $O_3$ in May–October in all areas, and 1–3 ppbv in October–May in North America. This is consistent with the findings of Lin and McElroy (2010), with the non-local scheme parameterising the variability in mixing, reducing modelled biases, particularly at night.

In summary, the only configuration found to consistently reduce modelled seasonal biases year round is running at $2^\circ \times 2.5^\circ$ resolution, however the magnitude of improvement is small (1–3 pbbv). Most notably, the modelled summertime overestimates in all regions cannot be significantly reduced by any configuration.

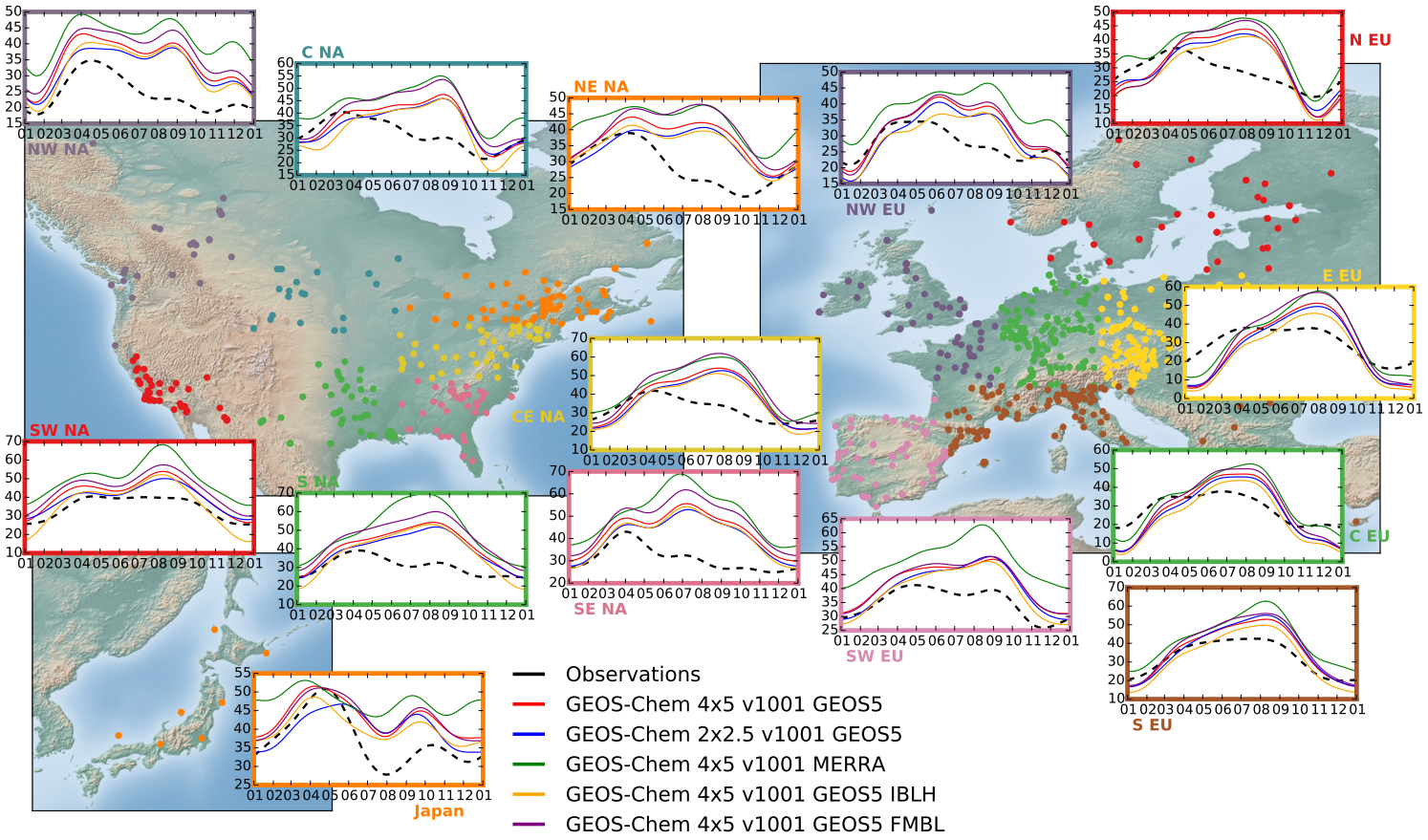


Fig. 5.4 Comparison of average spectrally derived seasonal surface $O_3$ waveforms (for 2009–2011) between observations (black lines) and multiple configurations of GEOS-Chem v10.01. (standard $4° \times 5°$ GEOS5 – red lines; $2° \times 2.5°$ horizontal resolution – blue lines; MERRA meteorology – green lines; interactive boundary layer height – orange lines; fully mixed boundary layer – purple lines), in multiple areas in North America, Europe and Japan.

### 5.3.4 Day/night biases in GEOS-Chem

Most model evaluative studies of surface $O_3$ have focused on solely daytime values (e.g. maximum daily 8-hour average), due to a typical emphasis on daytime air quality exceedances. However, evaluating $O_3$ wholly in a diurnal context allows for analysis of the diurnal timing of modelled errors, aiding understanding of the fundamental basis of errors. Spectrally, the diurnal sensitivity of biases can be evaluated in two ways. Firstly, the seasonal waveforms can be derived using only day or nighttime data. The distinction between day and night is made in the same way as described in Chapter 2, using the astronomical python package (PyEphem), which determines the integer number of day and nighttime hours (based on the angle of the centre of the sun to the horizon, from the surface) for each different day of the year.

Figure 5.5 shows the comparison of the observed regionally averaged surface seasonal $O_3$ waveforms (black lines) with correspondingly derived output from GEOS-Chem v10.01. $4^\circ \times 5^\circ$ GEOS5 (red lines), using solely daytime values (solid lines) and nighttime values (dashed lines). Both observed and modelled seasonal nighttime $O_3$ is consistently lower in concentration, relative to daytime values, in all areas across the year (by 2–15 ppbv), with differences at a maximum in the summer months (when diurnal $O_3$ production is at a maximum). Modelled daytime summer $O_3$ has a high bias in all areas, most significantly in North America (up to 20 ppbv in July for S NA) and Japan (11 ppbv in July), but also in Europe (2–8 ppbv in July). Modelled nighttime summer $O_3$ has a high bias in all areas in North America and Japan (by 3–12 pbbv in July), generally smaller than daytime biases. Modelled European summer nighttime $O_3$ biases are negligible to positive (3 ppbv in July). Spring and autumn $O_3$ is overestimated equally across the day in North America (3–20 ppbv). Peak springtime Japanese $O_3$ is underestimated in the day and night, equally in magnitude (by 4 pbbv in May). Winter modelled biases in Europe and northern regions of North America (CE NA, NE NA, C NA, NW NA) have a systematic nighttime bias. Winter daytime biases in these regions are negligible to negative (4 ppbv in January), whereas the model significantly underestimates winter nighttime $O_3$ (6–13 ppbv). In southern regions of North America and Japan, winter $O_3$ is well simulated across the day.

The direct diurnal periodicity of surface $O_3$ can also be derived spectrally. Taking the same approach as for the seasonal cycle, the average observed and modelled diurnal waveforms of surface $O_3$ are calculated by area. This is done twice, using solely summer (July–September) and winter values (December–March), to isolate differences in seasonal chemistry. Figure 5.6 shows the average diurnal periodicity for the observations (black lines) compared with the GEOS-Chem v10.01. $4^\circ \times 5^\circ$ GEOS5 (red lines), in the summer (solid lines) and winter (dashed lines). In both seasons, the amplitudes and phases of the observed diurnal waveforms are well represented by the model in most areas, with amplitudes only significantly overestimated in CE NA, C EU and E EU (in the summer by 6–8 pbbv, and in the winter by 2–5 pbbv), over producing $O_3$ in the day. Modelled biases across the day are consistently offset, dominantly controlled by seasonal average biases (i.e. homogenous summertime high bias), rather than diurnal processes. The only notable systematic diurnal bias is associated with the night–day transition (when $O_3$ starts

to be produced significantly with the availability of energetic photons), with the model starting to significantly produce $O_3$ 1–2 hours later than the observations, most probably associated with the coarse temporal updates in meteorological fields (6 hours for 3D parameters, 3 hours for 2D parameters). Notably, the significant modelled winter nighttime underestimates in Europe and northern North America in Fig 5.5, are not replicated in the diurnal waveform comparisons, and is evidently a dominantly seasonal issue.

In summary, the diurnal variability of surface $O_3$ is well represented by the model. Day and nighttime biases are dominantly controlled by seasonal average biases, which require further exploration.

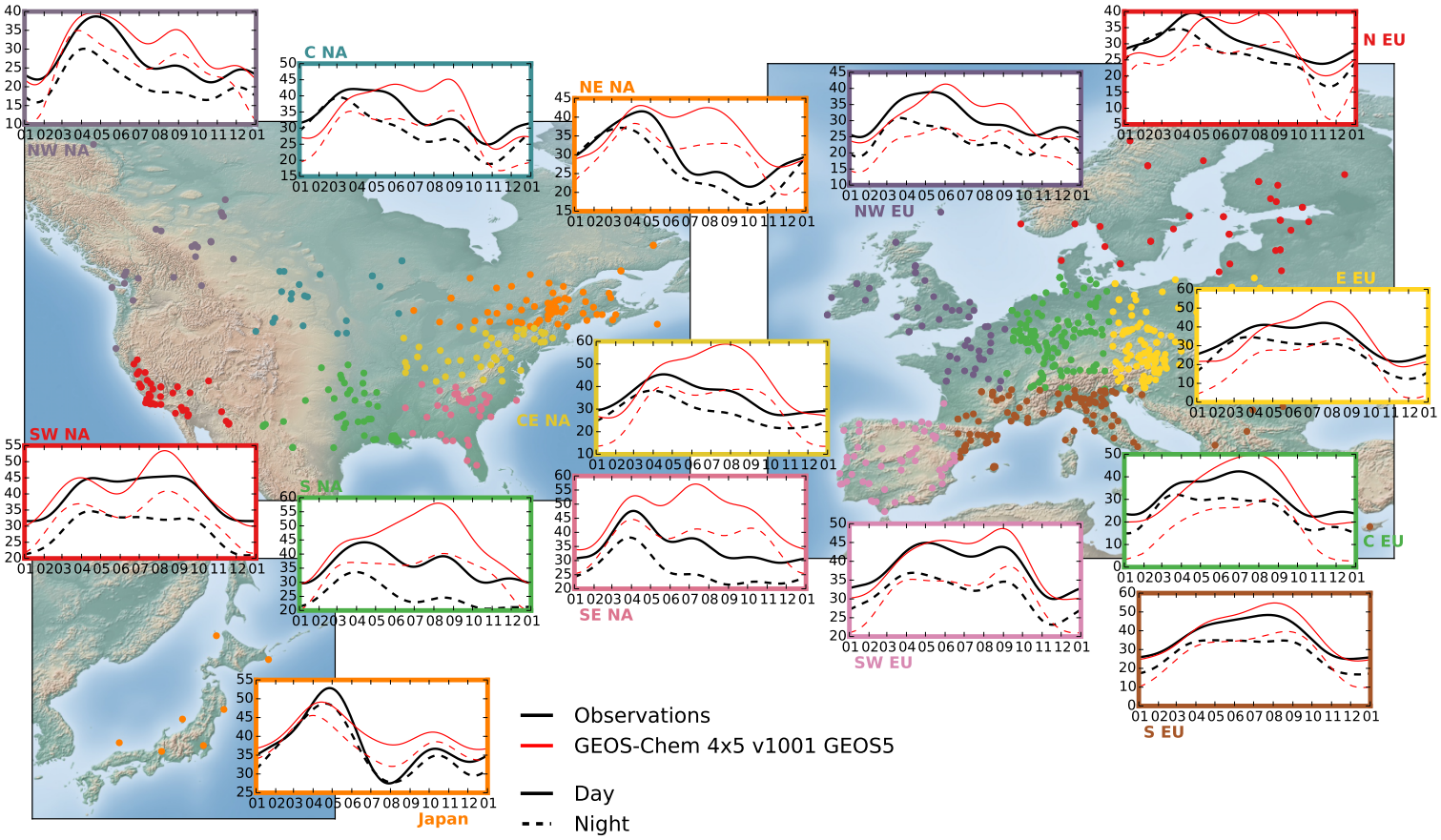


Fig. 5.5 Comparison of average spectrally derived seasonal surface $O_3$ waveforms (for 2009–2011) between observations (black lines) and GEOS-Chem v10.01. $4° \times 5°$ GEOS5 (red lines), in the day (solid lines) and at night (dashed lines), in multiple areas in North America, Europe and Japan.

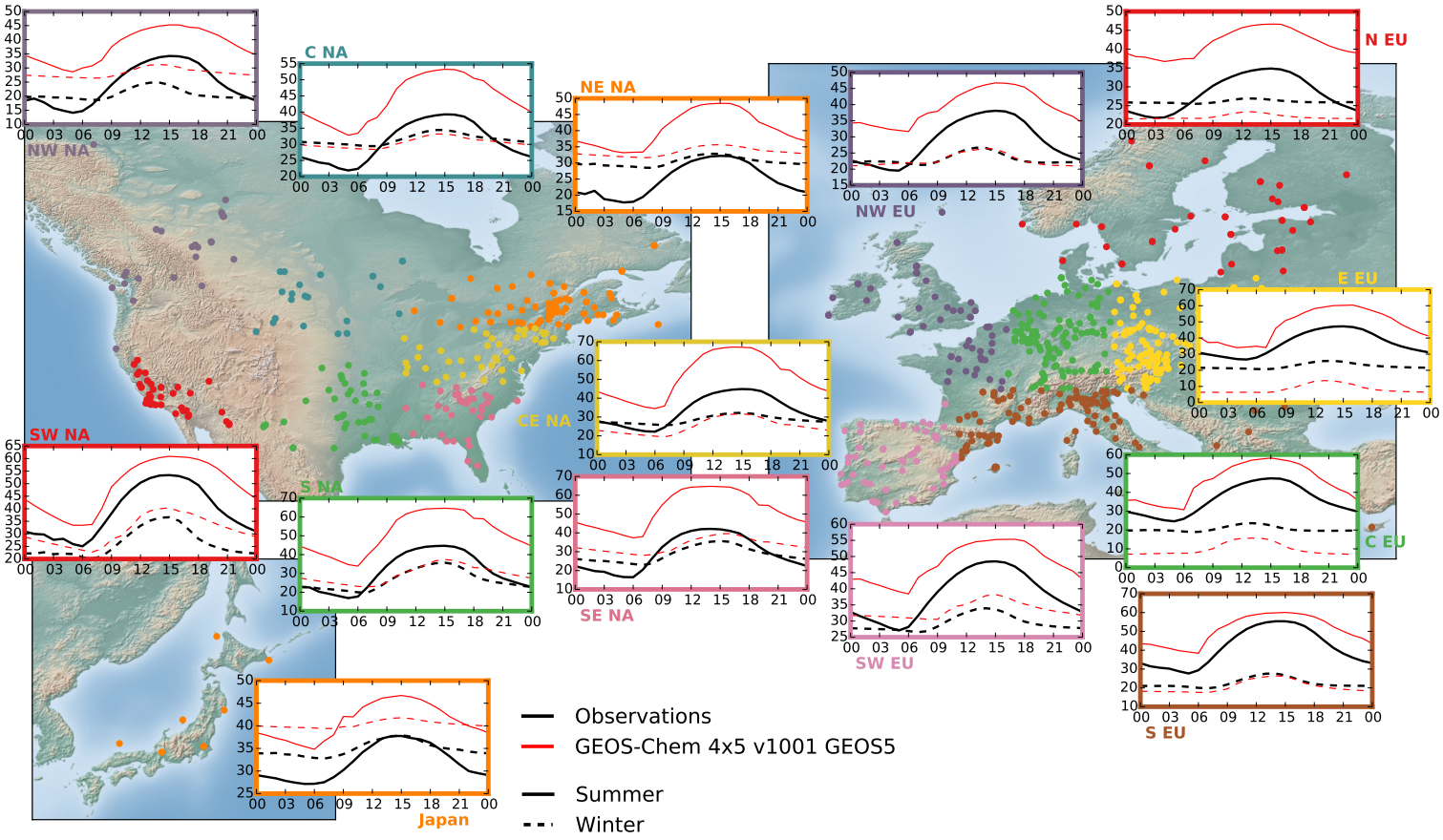


Fig. 5.6 Comparison of average spectrally derived diurnal surface $O_3$ waveforms (for 2009–2011) between observations (black lines) and GEOS-Chem v10.01. $4° \times 5°$ GEOS5 (red lines), in the summer (solid lines) and in the winter (dashed lines), in multiple areas in North America, Europe and Japan.

### 5.3.5 ACCMIP biases

Multiple evaluations of other CTMs/ESMs have also reported summertime high biases of surface $O_3$, e.g. Reidmiller et al. (2009); Lamarque et al. (2012); Brown-Steiner et al. (2015); Katragkou et al. (2015). Comparison of GEOS-Chem surface $O_3$ seasonality with other atmospheric chemistry models can reveal if biases are GEOS-Chem isolated, or systematic across all models.

The Atmospheric Chemistry and Climate Model Intercomparison Project (ACCMIP) (Lamarque et al., 2013; Young et al., 2013) used 15 global models of a wide range of horizontal and vertical resolutions, chemical mechanisms and dynamics, to evaluate the state of current understanding for tropospheric $O_3$. Anthropogenic and biomass burning emissions are fixed across all models, but natural emissions vary. 6 models return hourly surface $O_3$ data between 2005 and 2010: CESM-CAM-Superfast, CMAM, GEOSCCM, GFDL-AM3, GISS-E2-R and MIROC-CHEM.

In the same way as previous, the regional average seasonal waveforms are spectrally derived from observations and the 6 hourly reporting ACCMIP models (as well as GEOS-Chem) in the period of 2005–2010. Observations are again taken from an hourly version of the surface $O_3$ data set described in Chapter 2, with any sites with data gaps greater than 60 days in 3 or more years removed to ensure accuracy of the spectral estimates.

Figure 5.7 shows the comparison of the observed regionally averaged seasonal surface $O_3$ waveforms (black lines) for 2005–2010, with the median of the correspondingly derived output from the ACCMIP models (purple lines), the range of the ACCMIP model output (light blue), and GEOS-Chem v10.01. $4^\circ \times 5^\circ$ GEOS5 (red lines). The median of the ACCMIP spread overestimates surface $O_3$ at almost all times, in all areas. Summer $O_3$ (June–September) specifically is significantly overestimated in North America (4–17 ppbv in July) and Japan (9 pbbv in July), but also in Europe (2–10 ppbv). The most notable biases however are in the winter, with the ACCMIP median overestimating January $O_3$ in the range of 1–20 ppbv in North America, 7–11 ppbv in Europe, and 15 ppbv in Japan. GEOS-Chem summer overestimates are greater than the ACCMIP median in all areas, by varying magnitudes (1–10 ppbv in July). Conversely, GEOS-Chem simulates wintertime $O_3$ much better than the ACCMIP median in almost all areas (aside from the densely populated C EU, E EU, and CE NA), with significantly lower winter concentrations (by 4–13 ppbv in January).

Despite anthropogenic emissions being fixed across models, the range of the ACCMIP spread is significant (up to 47 ppbv). The observed seasonal waveforms are generally within the range of the ACCMIP spread in each area, but are almost always on the low end of the distribution. The models with the lowest individual summertime biases are CESM-CAM-Superfast and CMAM, models which have the most simplistic NMVOC chemistry. $C_5H_8$ is the sole NMVOC in CESM-CAM-superfast, and CMAM uses extra CO emissions as a surrogate for zero NMVOCs (Young et al., 2013).

Through the spectral evaluations of this section and in Chapter 4, it is evident that the seasonality of surface $O_3$ in current state of art atmospheric chemistry models is poorly constrained. Specifically, dependent on region, the modelled summertime or winter $O_3$

shows significant biases. The rest of the work in this chapter focuses on the minimisation of seasonal surface $O_3$ biases, exploring the sensitivity of biases to alterations in emissions and the $O_3$ dry deposition flux, which as detailed, carry significant uncertainties. In the next section, a sensitivity study designed to understand the controlling influences on the modelled seasonal biases of surface $O_3$ is detailed.

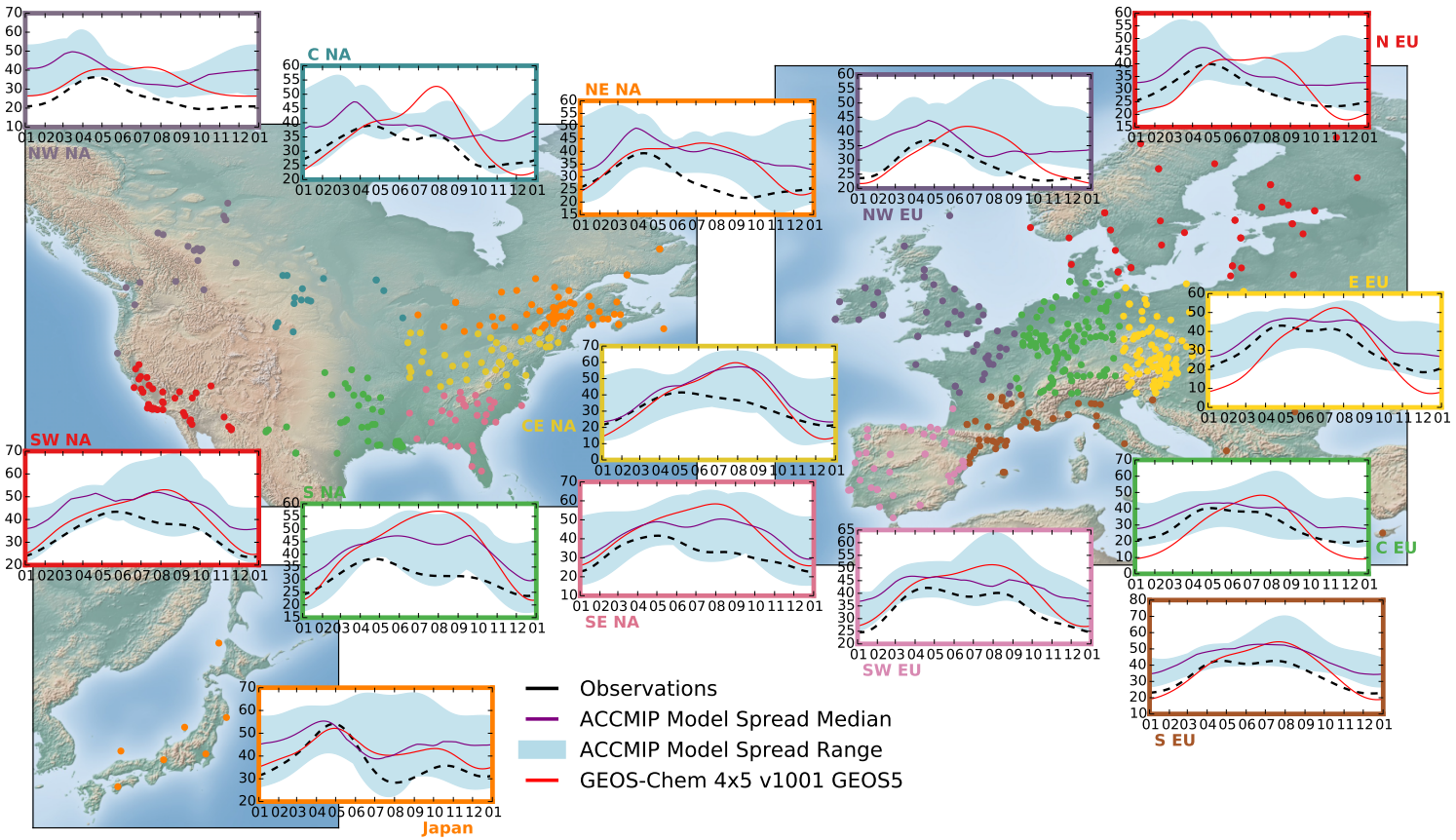


Fig. 5.7 Comparison of average spectrally derived seasonal surface $O_3$ waveforms (for 2005–2010) between observations (black lines), GEOS-Chem v10.01. $4^\circ \times 5^\circ$ GEOS5 (red lines), median of the ACCMIP model spread (purple lines), and the range of the ACCMIP model spread (light blue), in multiple areas in North America, Europe and Japan.

## 5.4 Ozone sensitivity to emissions/dry deposition

In this section, the sensitivity of modelled surface $O_3$ to changes of its major source and sink terms: precursor emissions and dry deposition, is explored. An extensive sensitivity study is designed, scaling a range of parameters, resulting in 106 total simulations. The setup details of this study are first detailed.

### 5.4.1 Sensitivity study setup

The sensitivity of surface $O_3$ to 6 different parameters is explored. These are: anthropogenic NMVOC emissions (ANMVOC), biogenic NMVOC emissions (BNMVOC), anthropogenic CO emissions (ACO), zonal $CH_4$ concentrations, the $O_3$ dry deposition flux, and anthropogenic NOx emissions (ANOx).

Multiple simulations of GEOS-Chem v10.01. $4^\circ \times 5^\circ$ GEOS5 are run over 2 years (between 2009 and 2011), spun up for 6 months prior, with each simulation featuring different scaling configurations of the 6 parameter sets. All parameters except zonal $CH_4$ are globally scaled by factors of: 0.25, 0.5, 2 and 4. $CH_4$ zonal concentrations are scaled by factors of: 0.98, 0.99, 1.01 and 1.02, decreed from the estimated range of regional observational uncertainties (Bruhwiler et al., 2014). Firstly, each different parameter set is independently globally scaled by all scaling factors (24 simulations: 4 different scaled simulations for each of the 6 parameter sets). Secondly, all parameter sets are globally scaled in matrices along with global scalings of ANOx (which carries the greatest cited uncertainties), resulting in 81 additional simulations. The standard unscaled GEOS-Chem v10.01. $4^\circ \times 5^\circ$ GEOS5 is the final simulation, resulting in 106 total simulations.

A summary of the parameter sets is given in Table 5.3, detailing the specific species scaled from given emission inventories. Biofuel and open fire emissions (GFED4) are classed as anthropogenic. Notably, naturally emitted NOx from soil or lightning is not scaled, as focus is placed on constraining the most cited anthropogenic emission biases, e.g. Vestreng et al. (2009); Fujita et al. (2012); Anderson et al. (2014); Travis et al. (2016).

Regionally averaged seasonal surface $O_3$ waveforms are spectrally determined from each different simulation, with the LSP applied on model data from all grid boxes that observational sites are contained in. This results in a plethora of output that is extensively synthesised to enable useful scientific consumption. Both the observed and modelled regionally averaged seasonal waveforms are first averaged by month. The observed monthly averages are then subtracted from all respective modelled monthly average values, and the absolute percentage differences from the base observational averages are then calculated. This results in 106 modelled average absolute percentage differences from observations, per month, per area.

| Scaling Set | Emission Inventories | Species/Parameters |
|---|---|---|
| ANMVOCs | Aircraft (AEIC), Biofuel, BRAVO, CAC, EMEP (VOCs), GFED4, MIX, NEI2011, RETRO, Xiao (Ethane) | Acetaldehyde, Acetone, Aldehyde, Benzene, Ethane, Ethylene, Formaldehyde, Lumped >= C4 Alkanes, Lumped >= C3 Alkenes, Methacrolein, Methyl Ethyl Ketone, Propane, Toluene, Xylene |
| BNMVOCs | MEGAN, Oceanic (online) | Acetaldehyde, Acetone, Ethylene, Isoprene, Lumped >= C3 Alkenes |
| ACO | Aircraft (AEIC), Biofuel, BRAVO, CAC, EDGAR, EMEP (AQ), GFED4, MIX, NEI2011, Ship (EMEP), Ship (ICOADS) | CO |
| ANOx | Aircraft (AEIC), Biofuel, BRAVO, CAC, EDGAR, EMEP (AQ), GFED4, MIX, NEI2011, Ship (EMEP), Ship (ICOADS) | NO, $NO_2$, NOx |
| Zonal $CH_4$ | – | $CH_4$ |
| $O_3$ Dry Deposition | – | $O_3$ Dry Deposition Flux |

Table 5.3 Description of each of the parameter sets that are scaled in GEOS-Chem. ANMVOCs, BNMVOCs, ACO, ANOx, and the $O_3$ dry deposition flux are globally scaled by factors of: 0.25, 0.5, 2 and 4. Zonal $CH_4$ is scaled by factors of: 0.98, 0.99, 1.01 and 1.02.

### 5.4.2 Example output

Output can be visually represented as a series of $5 \times 5$ gridded matrices, where output from scalings of ANMVOC, BNMVOC, ACO, zonal $CH_4$ and the $O_3$ dry deposition flux are plotted relative to output from scalings of ANOx, per month, per area. The colour of each square in the gridded matrix in this framework represents the modelled surface $O_3$ average absolute percentage difference from observations. This $5 \times 5$ gridded matrix can be interchangeably represented as a contour plot, interpolating between the 25 matrix squares.

Figure 5.8 provides an evolving graphical demonstration of this representation. Figure 5.8a displays a contour plot of the spectrally derived modelled average absolute percentage differences from observations, in January, in the C EU region, through multiple parameter scalings. The darkest plotted blue represents a monthly average absolute percentage difference of 0 %, whereas the darkest red represents a 200 % difference, with differences above this limit whited out. The x-axis represents scalings of ANMVOC emissions, and the y-axis represents scalings of ANOx emissions, e.g. the bottom left corner of the box represents output from where ANMVOC and ANOx emissions have been scaled by a factor of 0.25, and the top right corner represents output from where ANMVOC and ANOx emissions have been scaled by a factor 4. The centre of the box represents where no scalings have been applied. In this case, the bottom right of the box represents the optimal scalings for the minimisation of the monthly modelled bias ($< 10$ %), where ANMVOC emissions are scaled by a factor of 4, and ANOx emissions by a factor of 0.25.

Figure 5.8b expands on Figure 5.8a, showing modelled sensitivities to scalings of of ANMVOC and ANOx emissions across all months of the year in C EU. It is immediately evident the optimal scalings for the minimisation of modelled biases change significantly over the year.

Figure 5.8c expands on Figure 5.8b, where each row represents output from scalings of different x-axis parameters, going top to bottom: A–ANMVOCs, B–BNMVOCs, C–ACO, D–$O_3$ dry deposition. The y-axis always represents scalings of ANOx. This representation efficiently synthesises output from all scaled simulations, allowing multi-area monthly evaluation of the sensitivities of modelled surface $O_3$ biases to changes of the multiple emission/deposition parameters.

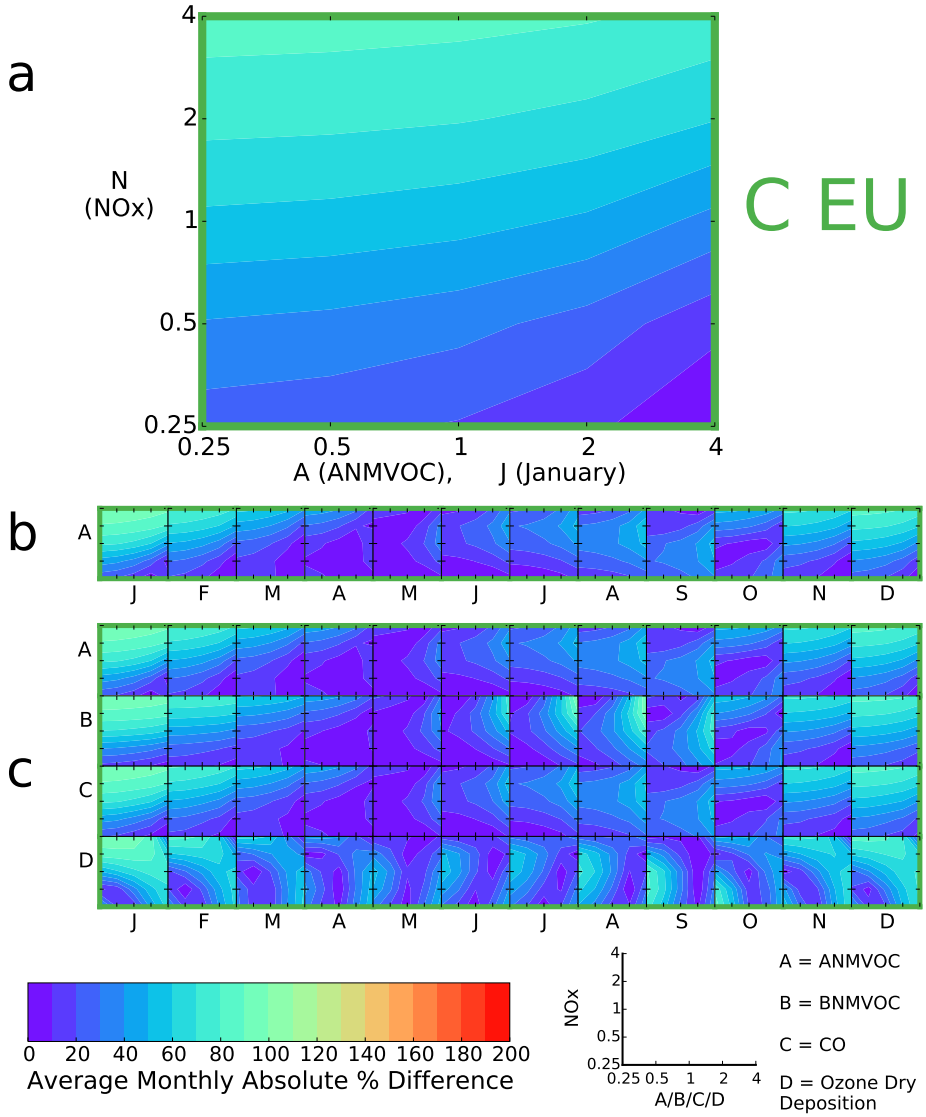


Fig. 5.8 Evolving representation of the output from a large-scale study using GEOS-Chem v10.01. $4° \times 5°$ GEOS5, designed to evaluate the sensitivity of regional spectrally determined monthly modelled surface $O_3$ biases to changes in emissions and the $O_3$ dry deposition flux (between 2009 and 2011). This figure shows output specifically for the defined C EU area. **(a)** Contour plot showing the January modelled surface $O_3$ biases resultant from multiple scalings of ANMVOC and ANOx emissions, in C EU. The plotted colour represents the spectrally derived monthly average absolute percentage difference from observations. The y-axis represents scalings of ANOx emissions, and the x-axis represents scalings of ANMVOC emissions. The centre of the box represents where no scalings have been applied. The scalings across both axes are 0.25, 0.5, 1, 2 and 4. **(b)** Expansion of (a), with multiple contour plots showing the modelled surface $O_3$ biases resultant from scalings of ANMVOC and ANOx emissions, across all months of the year, in C EU. **(c)** Expansion of (b), where each row represents output from scalings of different x-axis parameters, going top to bottom: A–ANMVOCs, B–BNMVOCs, C–ACO, D–$O_3$ dry deposition. The y-axis always represents scalings of ANOx.

### 5.4.3 Sensitivity study results

Through initial analysis, surface $O_3$ was found to be negligibly sensitive to changes in the zonal $CH_4$ concentration in all months, even at levels outside of the estimated level of uncertainty, i.e. $\pm$ 4 % (Bruhwiler et al., 2014), therefore changes to zonal $CH_4$ are not focused on again in this work.

Figure 5.9 expands on Figure 5.8c, showing the regional spectrally derived monthly modelled surface $O_3$ biases, resultant from scalings of ANMVOC, BNMVOC, ACO and ANOx emissions, and the $O_3$ dry deposition flux, across all Fig 5.2 defined regions. The over-plotted white x marks represent the optimal monthly scalings for the minimisation of modelled biases, per region.

In all areas, and in all months, modelled surface $O_3$ biases are able to be reduced to being small to negligible ($< 5$ % absolute differences) through various scalings. Surface $O_3$ is found to be dominantly sensitive to changes of the $O_3$ dry deposition flux and ANOx emissions across all regions, in most months. In very few instances does the standard unscaled model version provide the optimal pathway for minimising biases. The sensitivity of surface $O_3$ to changes of ANMVOC, BNMVOC and ACO emissions is small, and almost identical in response. Therefore in all areas, surface $O_3$ is dominantly NOx sensitive, as opposed to VOC sensitive.

In the summer months (June–September), surface $O_3$ is dominantly sensitive to dry deposition, with an increasing flux (by factors of 2–4) in all areas significantly reducing modelled biases (e.g. reducing a SE NA July 70 % bias to 2 %, though a factor of 4 increase). Summer biases are also sensitive to changes in ANOx, with reductions of ANOx (typically by factors of 0.25) also significantly reducing modelled biases (e.g. reducing a SE NA July 70 % bias to 11 %, through scaling ANOx emissions by 0.25). In many areas (i.e SE NA, CE NA) the optimal scalings in the summer months involve the scaling of both $O_3$ dry deposition and ANOx emissions in tandem, often allowing scalings of one or both parameters to be reduced in magnitude. Decreasing summer ANMVOC, BNMVOC, or ACO emissions (by factors of 4) provides a slight improvement to the simulation of surface $O_3$, most effectively when reduced in tandem with decreasing ANOx. In regions with large biogenic emissions (e.g. SE NA, CE NA), there is a greater sensitivity to summer reductions of BNMVOC emissions, than from reductions of ANMVOC or ACO emissions (10–30 % minimum bias difference), this being the only systematic difference between the biases resultant from scalings of these parameter sets.

In other seasons, when modelled biases are generally small in the standard simulation (as shown in Fig 5.3), surface $O_3$ is also very sensitive to dry deposition, however the magnitude of change necessary for minimising biases is smaller to negligible. Small improvements to biases are available through a range of scaling combinations of ANOx and ANMVOCs/BNMVOCs/ACO. For example in Japan, all scalings of ANMVOCs/BNMVOCs/ACO between 0.25 and 1, in tandem with scalings of ANOx between 0.25 and 2, produce January biases of $< 10$ %. However, scalings of ANOx are almost always the dominant factor in minimising modelled biases, with additional changes to ANMVOCs, BNMVOCs or ACO only slightly further decreasing biases.

The optimal scalings in all regions are therefore significantly variable across all months but in the summer, where decreasing ANOx emissions and an increasing $O_3$ dry deposition flux are in almost all cases the optimal scalings.

Figure 5.10 shows the comparison of regional spectrally derived observed monthly averaged seasonal surface $O_3$ waveforms, with correspondingly derived output from GEOS-Chem v10.01. $4^\circ \times 5^\circ$ GEOS5 (red lines), median of reciprocal output from all 106 scaled simulations (purple lines), range of reciprocal output from all scaled simulations (light blue), and the optimal of reciprocal output from all scaled simulations (green x marks). The median seasonal $O_3$ of the scaled simulation spread is almost identical with the standard model output in almost all cases, except for Japan, where the median better simulates winter $O_3$. Therefore seasonal output from the standard version of the model lies very centrally in the range of output produced from all scalings. This range is substantive in all areas (22–78 ppbv), particularly in the summer (e.g. 78 ppbv in July for SE NA). The optimal monthly average $O_3$ matches the observed monthly average $O_3$ almost exactly in all areas, in all months ($< 5$ % absolute difference). However the substantial variability of the scalings necessary to produce this optimised output (as shown by the white x marks in Fig 5.9), makes the likelihood of many of these scalings being physically realistic small.

In all areas, and in most months, there are typically 2 or more available scaling configurations that substantially minimise biases (e.g. modelled absolute differences of $< 10$ %). Potentially, any of these configurations could be physically viable. Therefore, further observational constraints are necessary to reduce the number of viable scaling configurations, and provide confidence in results. In the next section, surface NO and CO are incorporated into the analysis.

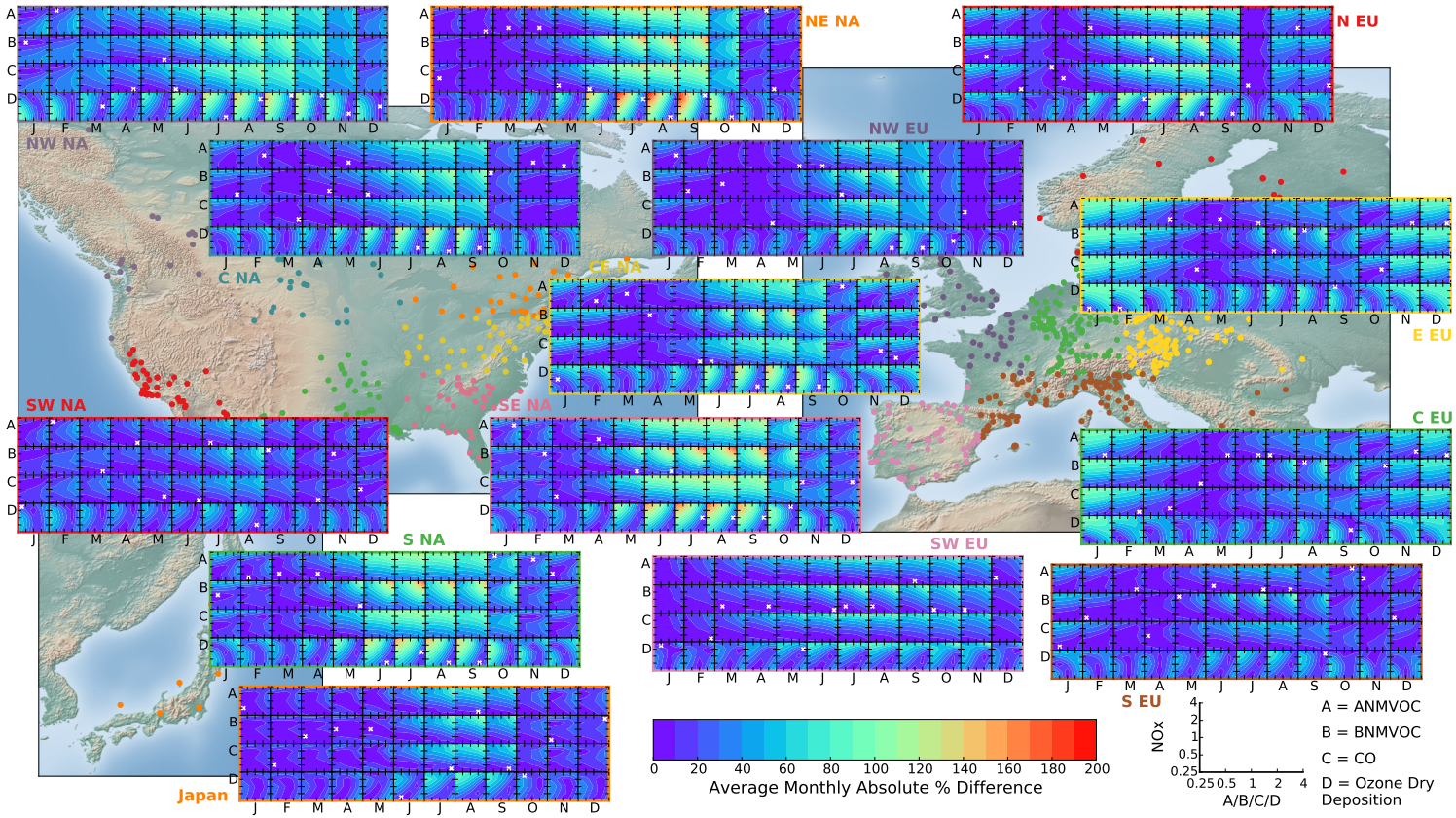


Fig. 5.9 Contour plots showing the sensitivity of regional spectrally derived monthly surface $O_3$ biases of GEOS-Chem v10.01. $4^\circ \times 5^\circ$ GEOS5, resultant from scalings of multiple emissions/deposition parameters (for 2009–2011). Each individual box represents the regional average monthly modelled biases from scalings of ANOx emissions (y-axis) and a changing x-axis parameter (ANMVOCs, BNMVOCs, ACO, $O_3$ dry deposition). Design of figure is explained in detail by Fig 5.8. The over-plotted white x marks represent the optimal monthly scalings for the minimisation of modelled biases, per region.

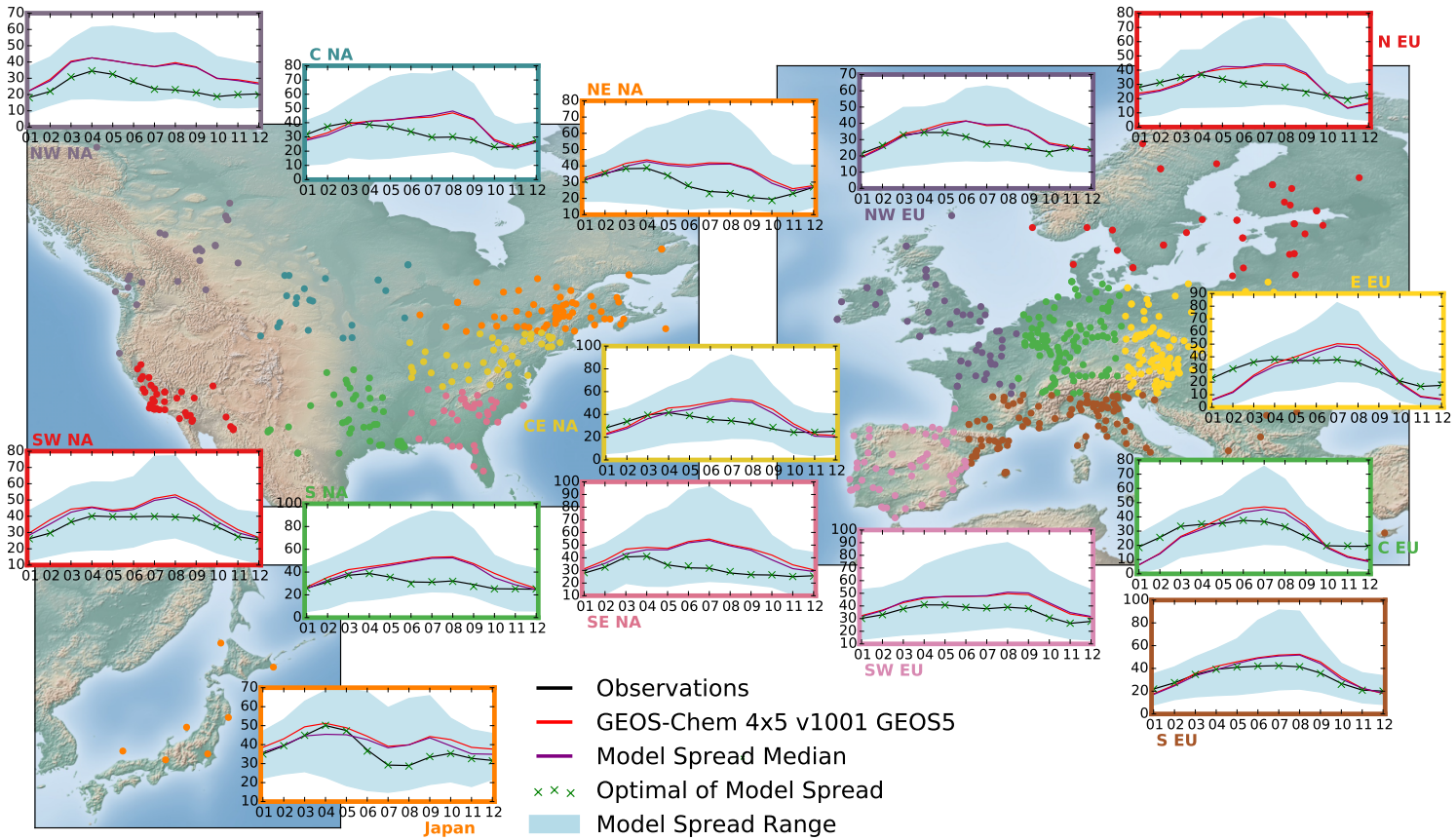


Fig. 5.10 Comparison of regional spectrally derived seasonal surface $O_3$ monthly averages (for 2009–2011) between observations (black lines) and GEOS-Chem v10.01. $4° \times 5°$ GEOS5 (red lines), median of output from all 106 scaled simulations (purple lines), optimal model output of scaled simulations (green x marks), and the range of output from all scaled simulations (light blue), in multiple areas in North America, Europe and Japan.

## 5.5 Nitric oxide/carbon monoxide sensitivity to emissions/dry deposition

As discussed in Chapter 2, the availability of high quality, global model comparable NO and CO surface observations are limited (relative to $O_3$), however enough regions are represented to allow for an extended multi-species sensitivity study, enabling the number of viable pathways for the minimisation of seasonal surface $O_3$ biases to be reduced. In this section, spectrally derived modelled biases of NO and CO are discussed, as well as their sensitivities to scalings of emissions/$O_3$ dry deposition.

### 5.5.1 Nitric Oxide

#### Current GEOS-Chem seasonal biases

To present, as far as this author is aware, no global model evaluations of surface NO have been undertaken. NO cannot be measured from satellites, and is typically very low in concentration in rural areas (e.g. $< 1$ ppbv), meaning it is hard to accurately measure. Evaluations of modelled $NO_2$ using measurements from satellites and at the surface are more common (e.g. Miyazaki et al. (2012)), but as outlined previously (in Chapter 2 and Sect 5.2.2), both measurement methods carry substantial uncertainties. Through the substantive data collection and processing undertaken in Chapter 2, GEOS-Chem modelled surface NO is able to be fairly evaluated in multiple areas across the NH using surface NO observations.

Hourly surface NO observations from the Chapter 2 dataset are limited solely to the daytime (using the same day/night separation algorithm as described in Sect 5.3.4), due to uncertainties regarding the inclusion of zeros and negative concentrations, which led to an initial high bias in concentration when averaged temporally (described in greater detail in Chapter 2). The minimum limit of detection accepted for NO measurements was set at 0.099 ppbv in Chapter 2, with sites with years of data all above this limit manually screened. The minimum data resolution allowed (i.e. minimum difference between points) was set to be 0.3 pbbv, imposing a 0.15 pbbv uncertainty on all measurements. Taking the sum of these two potential biases results in a maximum uncertainty on any given observational point of approximately 0.25 pbbv. However this bias is generally lower in actuality, as site data resolutions are almost all $< 0.1$ ppbv, with NW NA being the only area with site data resolutions exceeding 0.2 ppbv.

Figure 5.11 shows the average spectrally derived observed surface seasonal NO waveforms for 2009–2011, across the defined areas in North America, Europe and in Japan (black lines), compared with correspondingly derived output from GEOS-Chem v10.01 $4^\circ \times 5^\circ$ GEOS5 (red lines). Zero NO observations are located in SW NA, NW NA, C NA or N EU, and therefore no comparisons are shown in these regions. Surface NO is overestimated in the winter (December–March) in all regions except SW EU and NW EU (by 40–300 % in January). The greatest winter overestimates occur in the areas with the greatest density of emissions (CE NA, C EU, E EU), showing a direct correlation with the

significant winter underestimates of $O_3$ in the same regions. As with $O_3$, this bias is not improved by higher horizontal resolution ($2^\circ \times 2.5^\circ$), as shown in Fig. B.1 in Appendix B.

In the summer (June–September) modelled NO is generally underestimated, with the exception of CE NA, most significantly in C EU and NW EU (by 0.9–1 ppbv in July). The observed winter phase of surface NO in most areas is simulated well, however the general modelled winter overestimates and summer underestimates result in the modelled seasonal amplitudes being too high in most areas (by 50–550 %). The seasonal amplitude of modelled NO in Japan is very small (0.07 ppbv), significantly underestimating the observed seasonal amplitude (0.20 ppbv), and additionally not capturing the observed summer phase.

As undertaken in Sect 5.4 for surface $O_3$, the sensitivity of modelled seasonal surface NO to scalings of ANMVOC, BNMVOC, ACO and ANOx emissions, and the $O_3$ dry deposition flux is now explored.

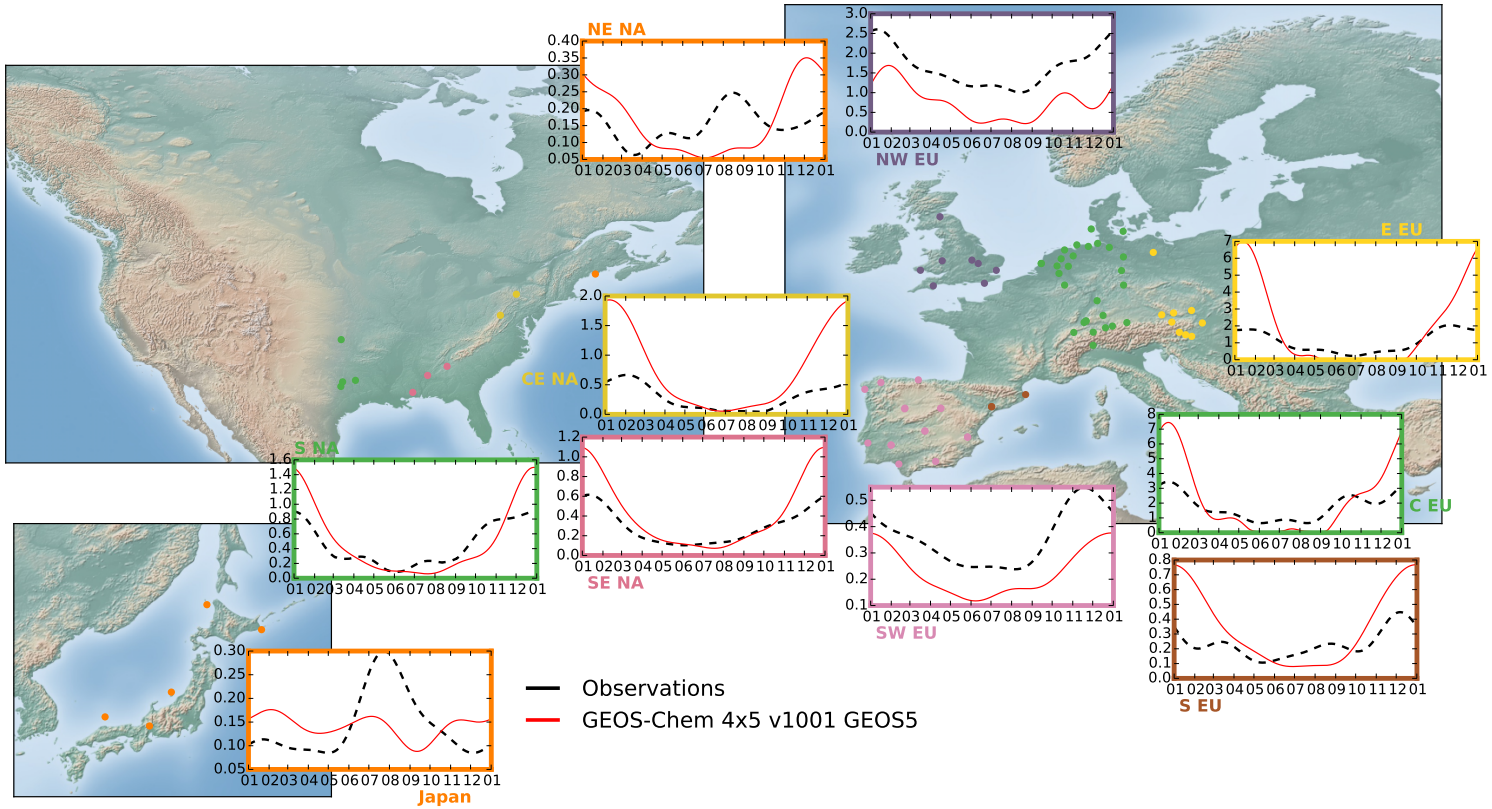


Fig. 5.11 Comparison of average spectrally derived seasonal surface NO waveforms (for 2009–2011) between observations (black lines) and GEOS-Chem v10.01. 4° × 5° GEOS5 (red lines), in multiple areas in North America, Europe and Japan.

### Sensitivity study results

Figure 5.12 shows the regional spectrally derived monthly modelled surface NO biases resultant from multiple scalings of emissions and $O_3$ dry deposition, calculated as outlined in Sect 5.4. It is immediately evident that greater monthly differences from observations are able to be generated than for $O_3$, with multiple monthly scaling configurations being whited out (absolute biases $> 200\,\%$), in all regions. Modelled NO biases are dominantly sensitive to scalings of ANOx emissions in all areas, in almost all months.

In the summer months, the optimal scaling settings are more variable per region than for $O_3$, however increases to both ANOx emissions and the $O_3$ dry deposition flux generally provide the optimal routes for minimising modelled biases (e.g. in SW EU). In E EU and C EU the observed summer NO cannot be well matched through any scaling configurations (e.g. a July optimal absolute percentage bias of 90 % in C EU). Modelled NO is generally insensitive to scalings of ANMVOCs/BNMVOCs/ACO, however there is enhanced sensitivity to these parameters in the summer months, which is significantly variable across regions and also between the parameter sets (e.g. in SE NA July, a reduction of BNMVOC emissions by a factor of 4, and an increase of ANMVOC emissions by a factor of 4, both results in biases $< 20\,\%$).

From October–March modelled NO is almost exclusively controlled by changes in ANOx emissions, with reductions of ANOx emissions (typically by a factor of 0.5) generally being the optimal path for minimising biases. Increases of ANOx emissions by any factor in these months leads to very large modelled biases, with most configurations associated with increasing ANOx in these months whited out.

Figure 5.13 shows the comparison of regional spectrally derived observed monthly averaged seasonal surface NO waveforms, with correspondingly derived output from GEOS-Chem v10.01. $4^\circ \times 5^\circ$ GEOS5 (red lines), median of reciprocal output from all 106 scaled simulations (purple lines), range of reciprocal output from all scaled simulations (light blue), and the optimal of reciprocal output from all scaled simulations (green x marks). The median NO seasonality of the scaled output is almost identical with the standard modelled seasonality in most regions, except for in the southern USA (S NA and SE NA), where the median underestimates observed summer NO by a larger magnitude than the standard model output. Therefore, as with $O_3$, NO seasonality in the standard version of the model lies centrally in the range of output produced from all scalings. This range can be extremely large in the winter in certain areas (e.g. C EU, E EU, CE NA), requiring the y-axes of Fig 5.13 to be logged to display the full range of variability (e.g. 0.2–90 ppbv in January for C EU). In the summer months the range of variability is reduced in all areas to between 0.01 and 2 ppbv, and even lower in some instances (e.g. in E EU between 0.01 and 0.1 ppbv in July).

As was the case for $O_3$, the optimal monthly average NO matches the observed monthly average NO almost exactly, in almost all instances ($< 5\,\%$ absolute difference). However, in the summer months for E EU and C EU, no simulations can adequately replicate the observed monthly concentrations, significantly underestimating NO in these months (e.g. for July in E EU, the optimal simulation is 0.5 ppbv below the observed value). The scaling

configurations used to derive the optimal modelled output are again fairly sporadic per month, per region (white x marks in Figure 5.12).

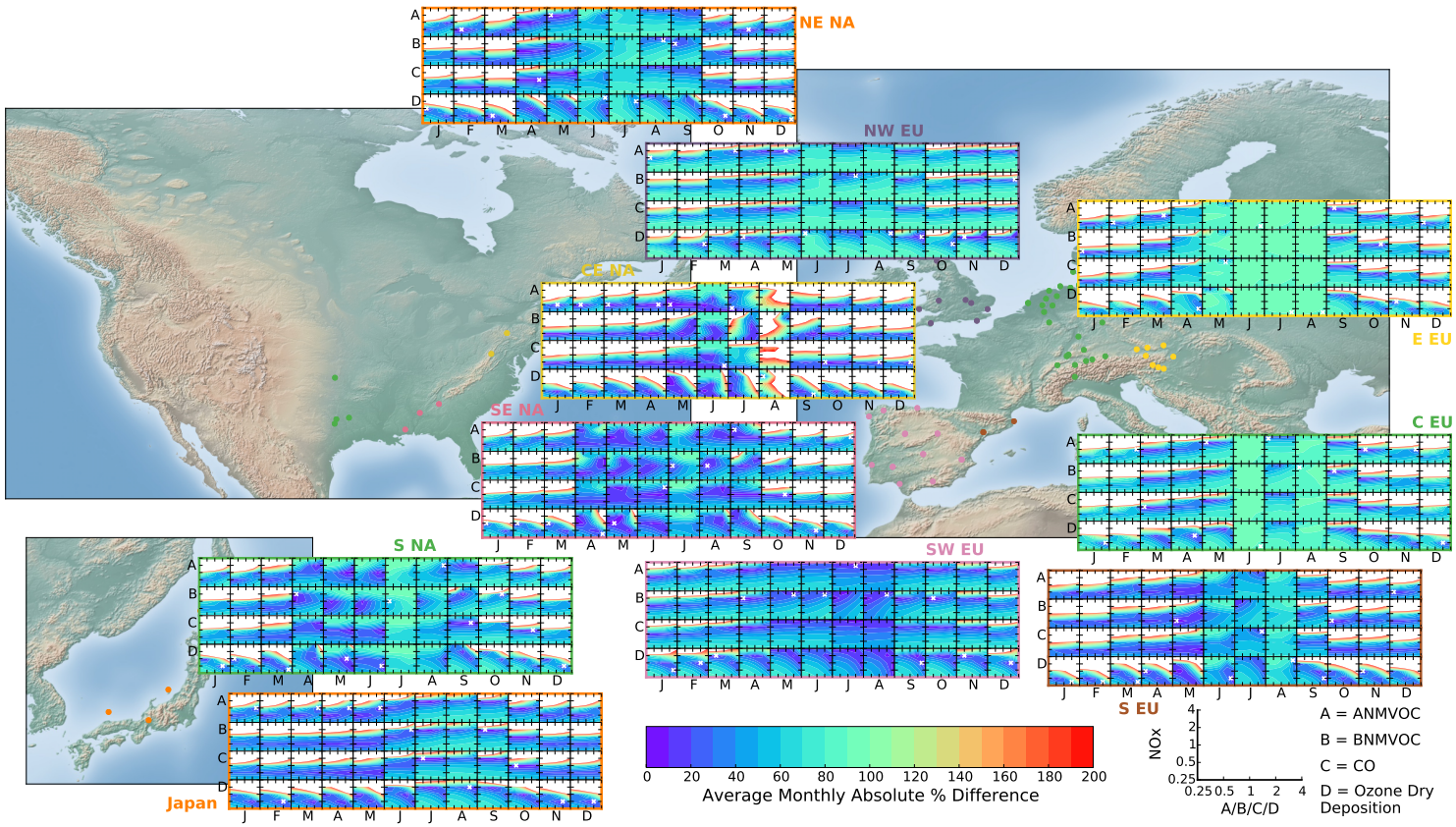


Fig. 5.12 Contour plots showing the sensitivity of regional spectrally derived monthly surface NO biases of GEOS-Chem v10.01. $4° \times 5°$ GEOS5, resultant from scalings of multiple emissions/deposition parameters (for 2009–2011). Each individual box represents the regional average monthly modelled biases from scalings of ANOx emissions (y-axis) and a changing x-axis parameter (ANMVOCs, BNMVOCs, ACO, $O_3$ dry deposition). Design of figure is explained in detail by Fig 5.8. The over-plotted white x marks represent the optimal monthly scalings for the minimisation of modelled biases, per region.

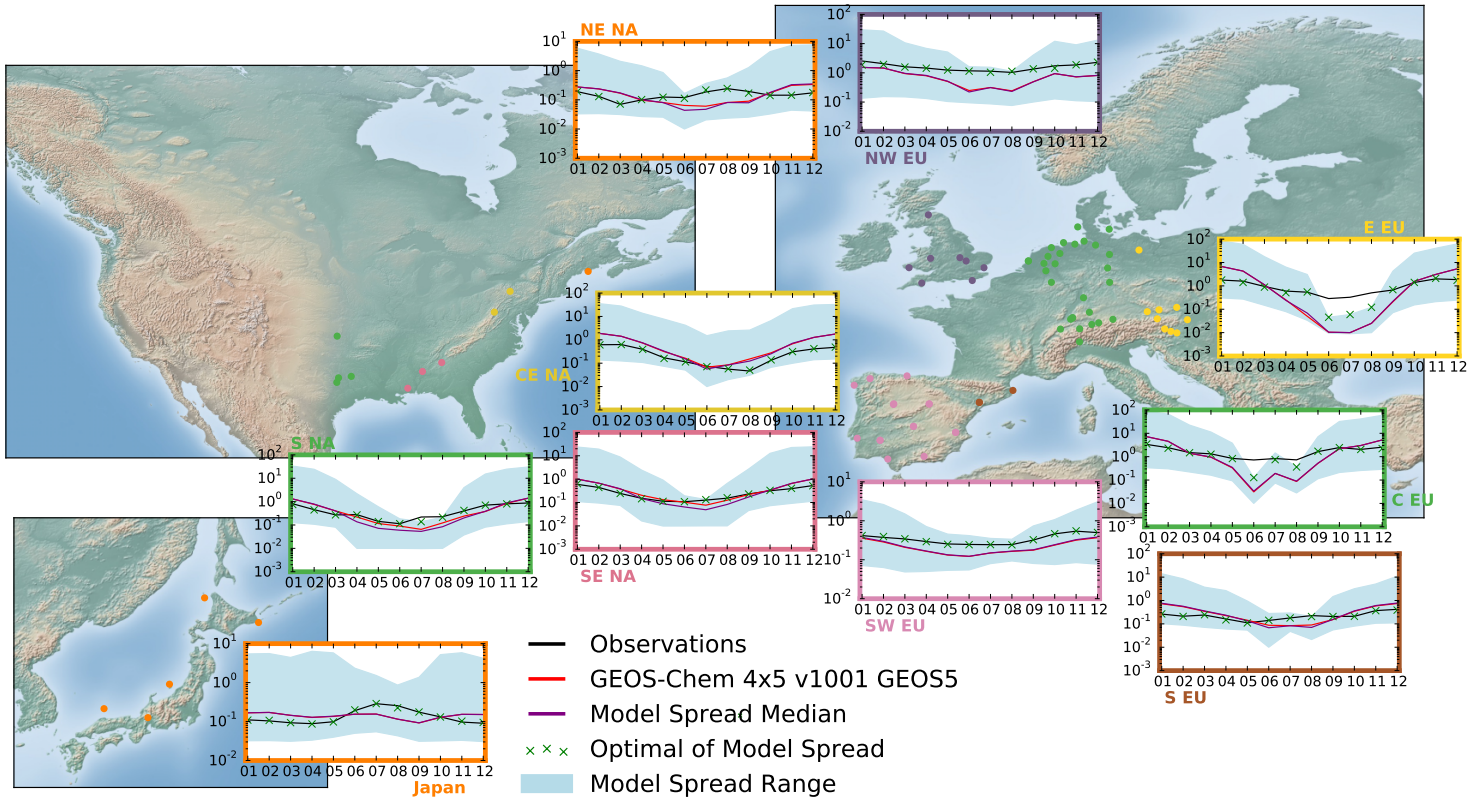


Fig. 5.13 Comparison of regional spectrally derived seasonal surface NO monthly averages (for 2009–2011) between observations (black lines) and GEOS-Chem v10.01. 4° × 5° GEOS5 (red lines), median of output from all 106 scaled simulations (purple lines), optimal model output of scaled simulations (green x marks), and the range of output from all scaled simulations (light blue), in multiple areas in North America, Europe and Japan.

### 5.5.2 Carbon monoxide

#### Current GEOS-Chem seasonal biases

Globally modelled surface CO has been evaluated in numerous studies e.g. Williams et al. (2013); Stein et al. (2014); Strode et al. (2015). The most commonly reported finding is a systematic low bias of CO in the NH, particularly in the winter–spring, suggested to be associated with a range of factors: underestimates of winter ACO emissions from traffic or combustion sources (Stein et al., 2014), overestimates of CO dry deposition to soils (Stein et al., 2014), and a low bias of the $CH_4$ lifetime (and consequently a high bias of OH) (Strode et al., 2015). Taking hourly surface CO from the Chapter 2 dataset, the seasonality of GEOS-Chem CO is spectrally evaluated in the same manner as done for $O_3$ and NO.

Figure 5.14 shows the average spectrally derived observed surface seasonal CO waveforms for 2009–2011, across the defined areas in North America, Europe and in Japan (black lines), compared with correspondingly derived output from GEOS-Chem v10.01 $4^\circ \times 5^\circ$ GEOS5 (red lines). No CO observations are made in SW NA, S NA or NW EU, and therefore no comparisons are shown in these regions.

Modelled surface CO is generally overestimated in North America, most extensively in the winter (e.g. in January by 140 ppbv in CE NA, and 30 ppbv in SE NA). Modelled CO in CE NA is overestimated year round (by 25– 140 ppbv), however there is only a single observational site in this region. Conversely, CO is generally underestimated in all regions in Europe, across the year, most significantly in March–December (by 10–60 ppbv). The seasonality of Japanese CO is excellently simulated by the model, with consistent small underestimates ($< 20$ ppbv), agreeing with findings by Stein et al. (2014). The winter observed seasonal phase is well captured by the model in most areas, except for C NA and NE NA, where a strong modelled summertime peak skews the seasonality and imposes a large summer overestimate (of approximately 60 ppbv). The modelled seasonal amplitudes are well estimated in Europe and Japan, but overestimated in all areas in North America (by 20–75 %).

The difference in findings from previous CO model evaluations over North America could be associated with a number of factors: using spectral analysis to derive seasonality, the extensive screening of observational sites and lack of inclusion of flask sites ,or model variability in the representation of surface CO.

The regional spectrally derived monthly modelled surface CO biases resultant from multiple scalings of emissions and $O_3$ dry deposition are now explored.

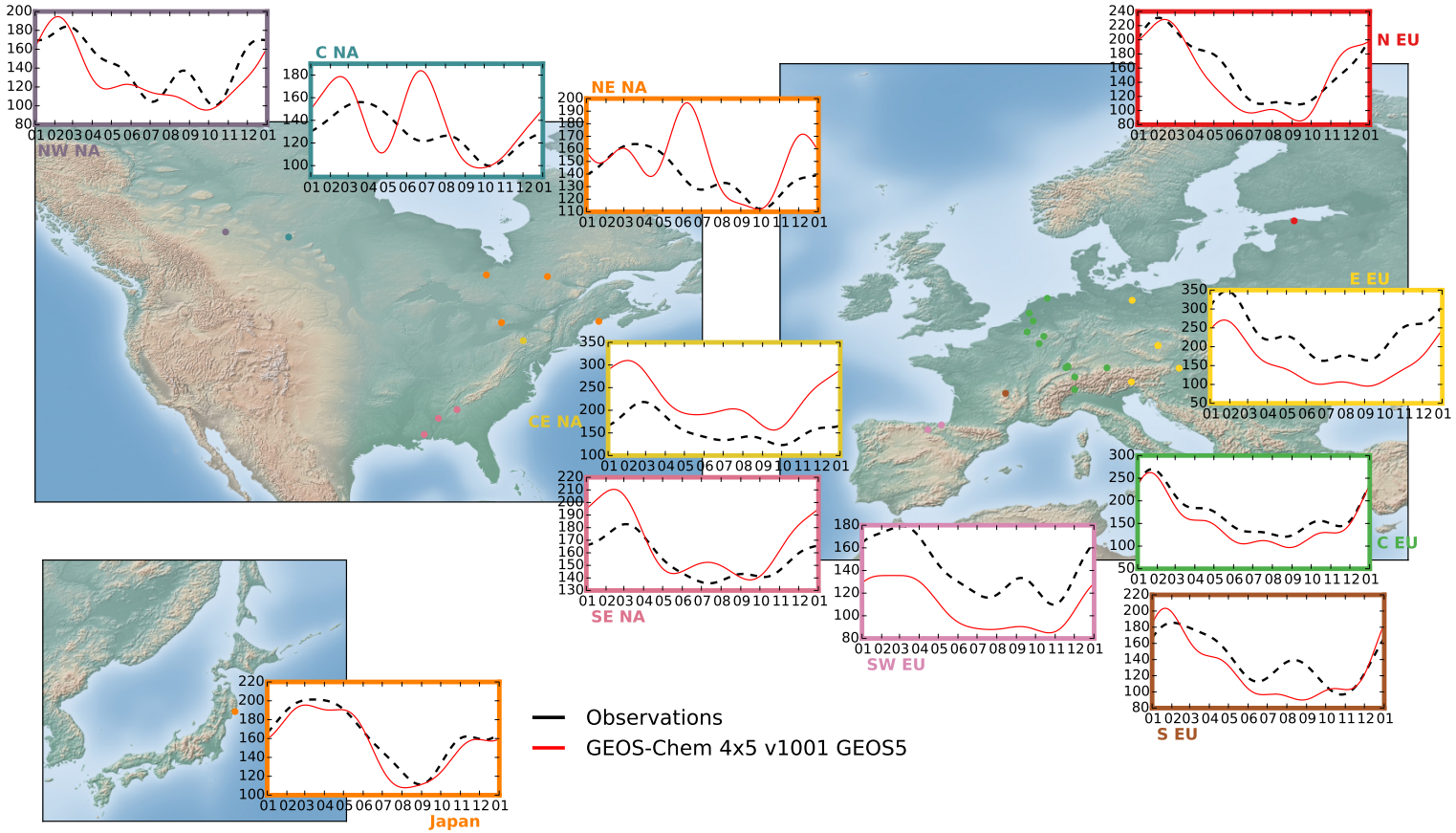


Fig. 5.14 Comparison of average spectrally derived seasonal surface CO waveforms (for 2009–2011) between observations (black lines) and GEOS-Chem v10.01. 4° × 5° GEOS5 (red lines), in multiple areas in North America, Europe and Japan.

### Sensitivity study results

Figure 5.15 shows the regional spectrally derived monthly modelled surface CO biases resultant from the multiple scalings of emissions and $O_3$ dry deposition, calculated as outlined in Sect 5.4. In all areas and in all months, surface CO is almost exclusively sensitive to scalings of ACO emissions. Scaling ACO emissions by any factors outside of the optimal value, leads to very large biases, particularly when increasing emissions (e.g. scaling Japan July ACO emissions by factors of 2 and 4, compared with the optimal factor of 1, changes a 4 % bias to be 110 % and 230 % respectively). In most areas the optimal pathway for minimising biases is leaving ACO emissions unscaled, however in some areas (e.g. CE NA, E EU) scalings by factors of 2 (by both signs) are necessary in some months. CO has much smaller sensitivities to scalings of ANMVOC and BNMVOC emissions across the entire year, and even less so for ANOX, however, as the changes induced on modelled CO through scalings of these parameters is much smaller than from scalings of ACO, when modelled CO does not need to be significantly modified, the optimal simulations generally involve a variety of scalings involving these parameters, with little consistency of configurations across the year, in any region. CO is completely insensitive to scalings of the $O_3$ dry deposition flux.

Figure 5.16 shows the comparison of regional spectrally derived observed monthly averaged seasonal surface CO waveforms, with correspondingly derived output from GEOS-Chem v10.01. $4^\circ \times 5^\circ$ GEOS5 (red lines), median of reciprocal output from all 106 scaled simulations (purple lines), range of reciprocal output from all scaled simulations (light blue), and the optimal of reciprocal output from all scaled simulations (green x marks). The standard modelled seasonality is almost identical with the median seasonality from all scaled simulations in all regions (as with $O_3$ and NO), and therefore the standard simulation output again lies centrally in the the range of output from all scaled simulations. Factor of 4 increases in ACO emissions allow huge amounts of CO to be produced, particularly in the winter, yielding huge ranges of monthly average concentrations in all areas (between 550 and 1100 ppbv in January). This range approximately halves in the summer in all areas, except C NA and NE NA (which are impacted by a large anomalous summer peak, as described previously). The optimal monthly average CO matches the observed monthly average $O_3$ almost exactly, in almost all instances ($< 5$ % absolute difference). The optimal scaling configurations are again significantly variable, with very little consistency of scalings across the year, per area (white x marks in Figure 5.15).

To briefly recap, through independent sensitivity studies of surface $O_3$, NO and CO to scalings of emissions/ $O_3$ dry deposition, modelled seasonal biases of each species can be almost entirely eliminated, in all regions. However, because of the significant variability of the optimal scaling configurations, little confidence can be placed in these findings being realistic. In the next section, the multi-species sensitivities are combined, resulting in significant reductions in the number of viable scaling pathways.

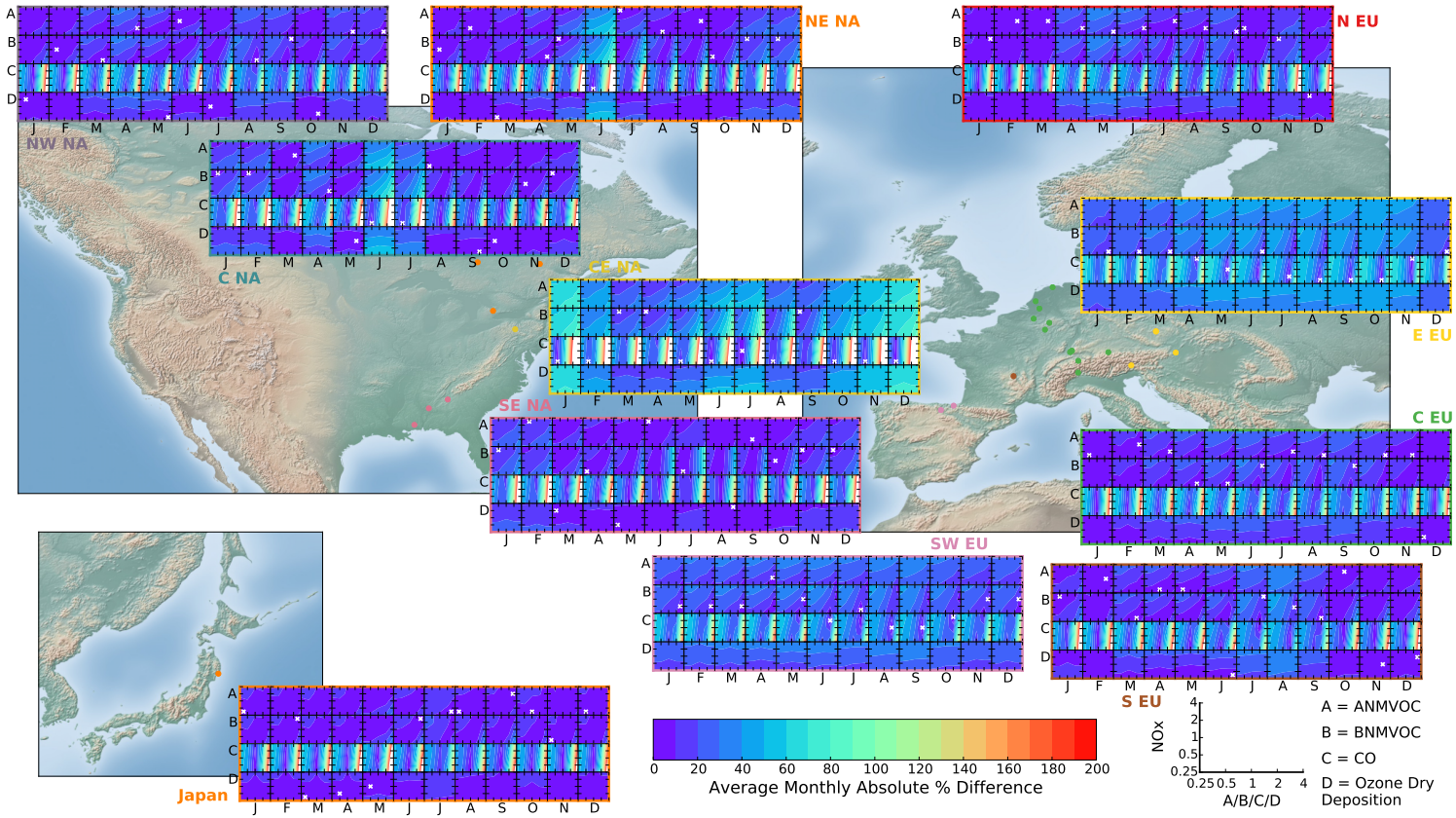


Fig. 5.15 Contour plots showing the sensitivity of regional spectrally derived monthly surface CO biases of GEOS-Chem v10.01. $4^\circ \times 5^\circ$ GEOS5, resultant from scalings of multiple emissions/deposition parameters (for 2009–2011). Each individual box represents the regional average monthly modelled biases from scalings of ANOx emissions (y-axis) and a changing x-axis parameter (ANMVOCs, BNMVOCs, ACO, $O_3$ dry deposition). Design of figure is explained in detail by Fig 5.8. The over-plotted white x marks represent the optimal monthly scalings for the minimisation of modelled biases, per region.

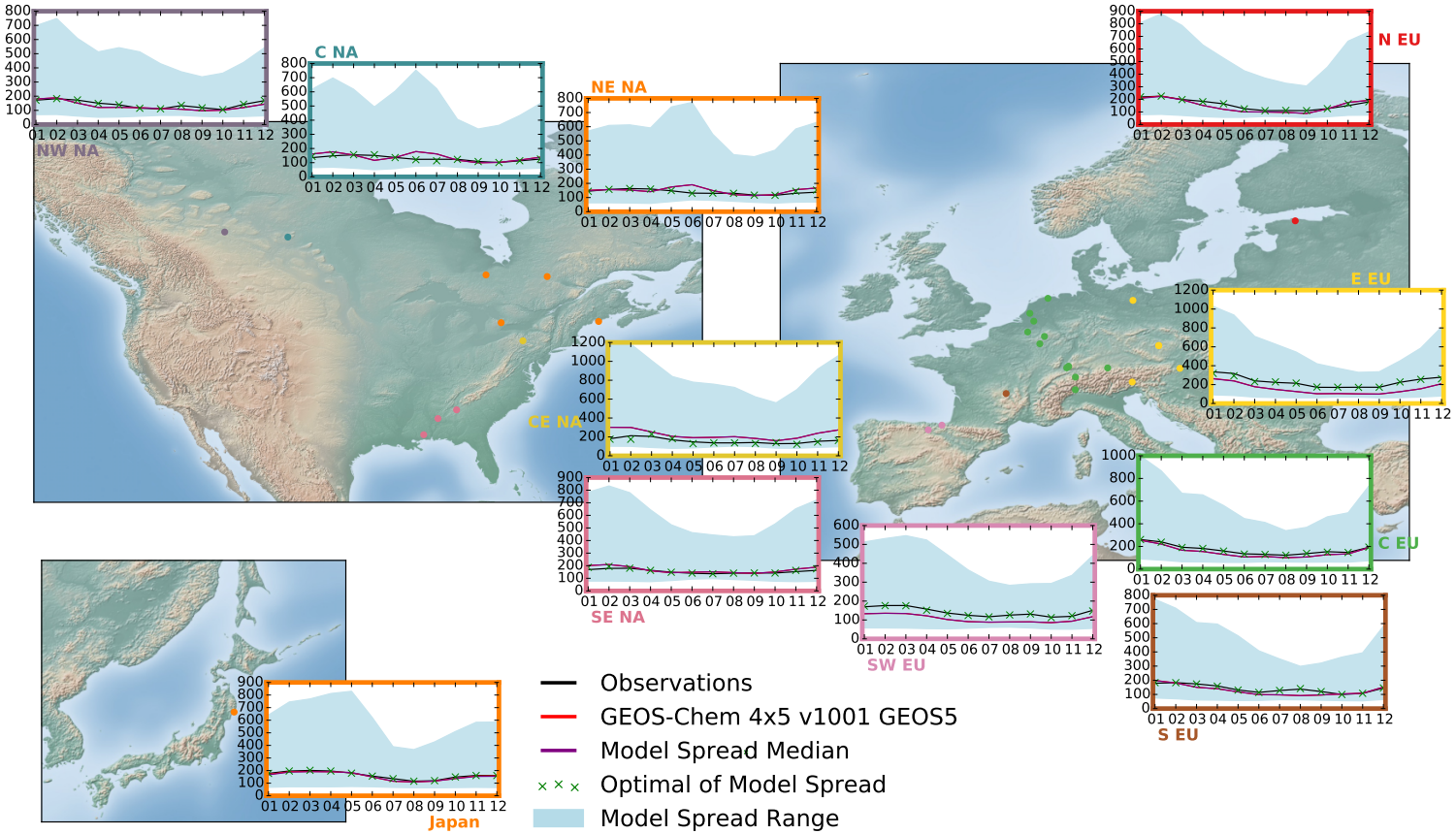


Fig. 5.16 Comparison of regional spectrally derived seasonal surface CO monthly averages (for 2009–2011) between observations (black lines) and GEOS-Chem v10.01. 4° × 5° GEOS5 (red lines), median of output from all 106 scaled simulations (purple lines), optimal model output of scaled simulations (green x marks), and the range of output from all scaled simulations (light blue), in multiple areas in North America, Europe and Japan.

## 5.6 Integrated species sensitivity to emissions/dry deposition

Taking the integrated biases across all species, from all model scalings (i.e. summing the species independent biases shown in Fig 5.9, Fig 5.12 and Fig 5.15), gives the joint-species sensitivity to emissions/$O_3$ dry deposition scalings, shown Fig 5.17. No output is shown in areas where there are no CO or NO observations (SW NA, NW NA, C NA, NW EU, N EU). In this section the results of this composite plot are described in detail, and sensible optimised monthly regional scaling settings for each region are attempted to be derived.

### 5.6.1 Composite sensitivity study results

In Fig 5.17, the number of instances where joint species biases are $< 5$ % are very small in number, and almost entirely limited to the winter, spring and autumn seasons. Bias minimisations in these seasons are most commonly achieved through reductions of ANOx emissions (typically by a factor of 2) and a variable form of change to ANMVOC emissions.

Summer biases (June–September) are notably very hard to minimise, with increases to the $O_3$ dry deposition flux (typically by a factor of 4), in tandem with some change of ANOx emissions (generally an increase in Europe, and decrease in North America), being the optimal, and generally only viable route for summer bias minimisations across all areas. In the SE NA and SW NA regions the optimal configurations year round involve a factor of 2–4 increase of the $O_3$ dry deposition flux.

The joint species sensitivities to scalings of ANMVOC and BNMVOC emissions are generally small and very similar, with the exception of the summer months, when reductions of BNMVOCs in some regions (e.g. SE NA) can significantly reduce biases (e.g. in SE NA July, reducing BNMVOC emissions by a factor of 4 reduces biases from 120 % to 50 %), but never as optimally as resultant from changes to $O_3$ dry deposition.

Across the year in SE NA and CE NA, the optimal settings for scaling ANOx are reductions by a minimum factor of 2, and by a factor of 4 in CE NA in the summer months, consistent with results from recent evaluations of NOx emissions in these areas (Anderson et al., 2014; Travis et al., 2016). In C EU and E EU, the joint summer minimum biases are never less than 60 %, with the modelled unresolvable NO underestimates (Fig 5.12) imposing the majority of this bias. The sensitivities to scalings of ANOx emissions in these regions are significantly variable over the year, with factors of 2 reductions necessary in the winter, and factor of 2 increases necessary in the early and late summer (May and September). The significant modelled CO biases in the CE NA and E EU areas (Fig 5.14), results in these areas being strongly sensitive to changes in ACO emissions, with factor of 2 scalings (of opposite signs by region) necessary across most months.

In Japan, the optimal scalings are very consistent. ANOx and ANMVOC emissions must be consistently reduced in magnitude in all months (always 0.5 for ANOx), except in the summer where biases are optimally reduced through increased $O_3$ dry deposition (by factors of 2–4).

In general, the number of viable configurations for minimising biases across all areas, in all seasons, have significantly decreased through the multi-species constraints of $O_3$,

NO, and CO. The variability of the optimal scalings (white x marks in Fig 5.17) reflects this, being significantly more consistent across the year in each region. Through this multi-species approach therefore, the legitimacy of potential scalings is heightened.

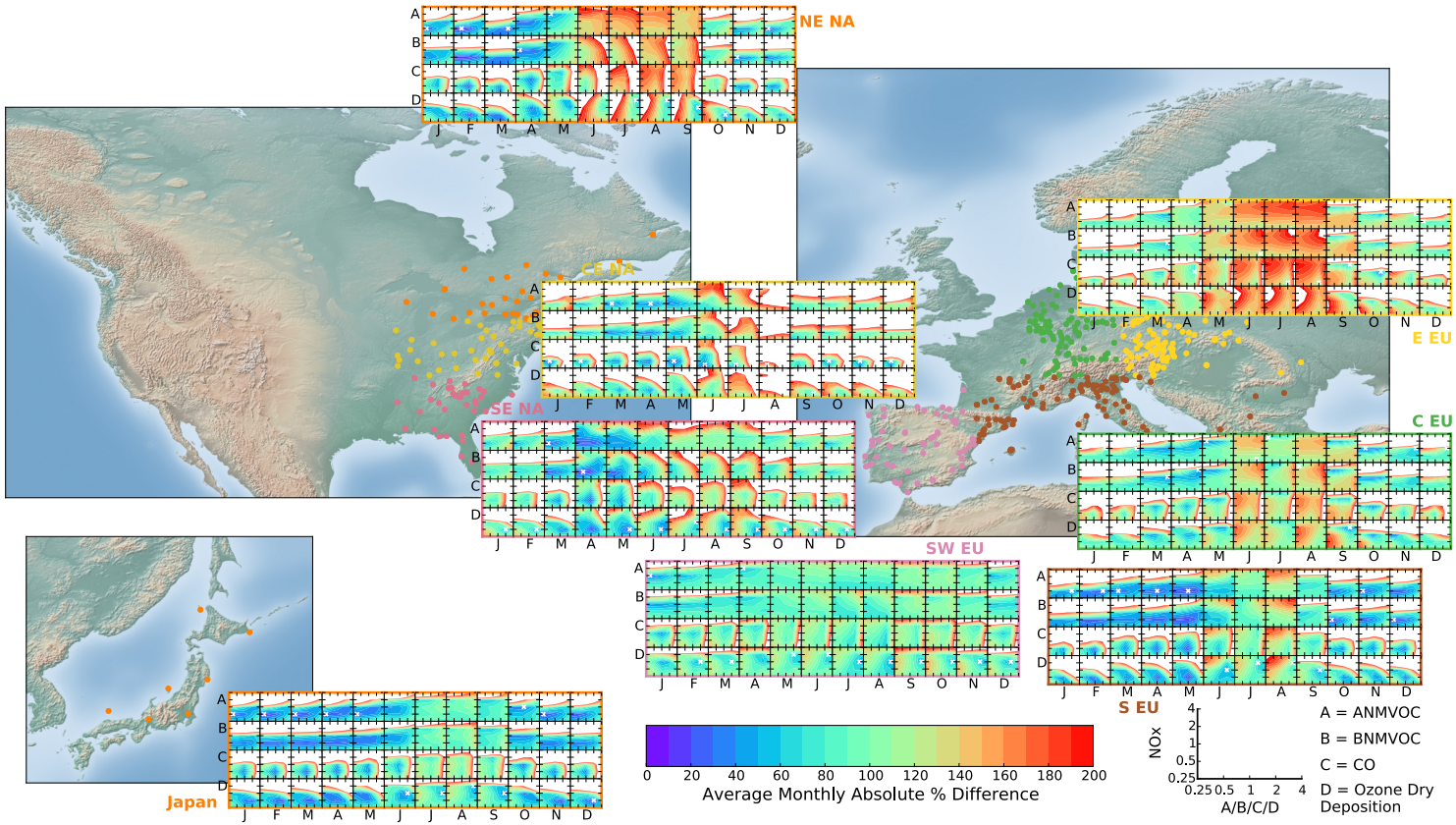


Fig. 5.17 Contour plots showing the sensitivity of regional spectrally derived monthly surface $O_3$+NO+CO biases of GEOS-Chem v10.01. $4^\circ \times 5^\circ$ GEOS5, resultant from scalings of multiple emissions/deposition parameters (for 2009–2011). Each individual box represents the regional average monthly modelled biases from scalings of ANOx emissions (y-axis) and a changing x-axis parameter (ANMVOCs, BNMVOCs, ACO, $O_3$ dry deposition). Design of figure is explained in detail by Fig 5.8. The over-plotted white x marks represent the optimal monthly scalings for the minimisation of modelled biases, per region.

### 5.6.2 Optimal scalings

If we make the assumption that local emissions, deposition and photochemistry predominantly control the concentration of $O_3$ in each defined area, then regionally scaling emissions/$O_3$ dry deposition in a single GEOS-Chem simulation by the optimal monthly scaling configurations, should theoretically result in a model simulation which concurrently minimises the seasonal biases of surface $O_3$, NO and CO, across all defined regions. This of course is an oversimplification, and neglects the impact of transport, which in some regions can be be very important to the local concentrations, e.g. in western North America (Cooper et al., 2010). Despite this, the veracity of optimised scalings are evaluated through the concurrent regional monthly scaling of these parameters in a single GEOS-Chem simulation. For this purpose, monthly global $4^\circ \times 5^\circ$ scaling grids are composed for each separate scaleable parameter, with regionally specific scalings set within each of the defined regions of Fig 5.2.

However, rather than simply taking taking the optimal configurations directly from Fig 5.17, a systematic methodology is employed to ensure all chosen scalings are sensible, conservative and consistent. Although the optimal configurations shown in Fig 5.17 produce the minimum integrated biases, some of these configurations can lie outside literature estimates (e.g. reducing ANOx emissions in Europe by factor of 4), and can still be somewhat erratic month to month (e.g. in C EU). In many instances the optimal monthly scalings are easily chosen (e.g. increase of $O_3$ dry deposition flux in the summer), however, despite the multi-species constraints, multiple viable pathways are still available on occasion (defined as configurations which yield a difference in bias of $< 15\,\%$). In these cases, a modest approach is taken. If there are configurations that yield a bias within 15 % of the optimal solution, and require a smaller total magnitude of changes, then the configuration that requires the minimum of changes is always taken. Biases resultant from scalings of ANMVOC and BNMVOC emissions are very similar in all instances other than in the summer (when biases can be reduced though the reduction of BNMVOC emissions). In all months other than the summer therefore, whenever a specific ANMVOC scaling is optimal, an almost identical bias can be produced by scaling BNMVOC emissions by the same magnitude. In all these instances, ANMVOC emissions are preferentially chosen to be scaled for consistency. This ultimately results in zero scalings ofBNMVOC emissions, in any area. Literature estimates regarding the uncertainty of emissions/$O_3$ dry deposition (reported in Sect 5.2.2), are also taken into consideration (i.e. it is unlikely that ANOx emissions need to scaled by a factor of 4 in magnitude, by either sign, whereas $O_3$ dry deposition uncertainties have been reported up to a factor of 4 in the day, and a factor of 8 at night.) It is decided that both ANMVOC and ANOx emissions are not allowed to be scaled by more than a factor of 2 (by either sign). Finally, it is also very unlikely that emissions will be need to be scaled one month to next by magnitudes of differing signs, but there are a few instances of this shown in Fig 5.17 (e.g. CE EU optimal ANOx scalings in June and July both being factors of 4, but differing in sign). Changes in scalings month to month are attempted to be made smooth (i.e. no more than a 1 level of magnitude change allowed month to month).

In areas where there are no NO observations, the composite plot of $O_3$ and CO biases is used to derive optimal regional scalings (Fig. B.3 in Appendix B). In areas with no CO observations, the composite contour plot of $O_3$ and NO is used instead (Fig. B.2 in Appendix B). In SW NA, there are only $O_3$ observations, therefore scalings in this region are solely derived using the output from Fig. 5.9. Figure B.4 in Appendix B additionally shows the composite plot of NO and CO biases. This process ultimately results in the monthly regional scaling factors given by Fig 5.18. The colour and intensity of the plotted circles represents the sign and magnitude of the scalings, respectively.

Close evaluation of Fig 5.18 reveals some consistent continental patterns. $O_3$ dry deposition is increased in the summer in all areas, typically by a factor of 4 in peak summer (August). In NW NA, SW NA, SE NA and SW EU, $O_3$ dry deposition is increased in most months of the year. Across North America, ANOx emissions are generally reduced in the winter (by a factor of 2). In SE NA, CE NA and N EU, ANOx emissions are reduced year round. In C EU and E EU, ANOx is positively scaled in the summer, and negatively scaled in the winter. Scalings to ANMVOC emissions are only made in the winter–spring (almost always reduced by a factor of 2), applied in most cases over North America and Japan.

These regional scaling parameters are incorporated into the outlined monthly global $4^\circ \times 5^\circ$ scaling grids, and then used to scale emissions/$O_3$ dry deposition in a final optimised simulation of GEOS-Chem, the output of which is described in the next section.

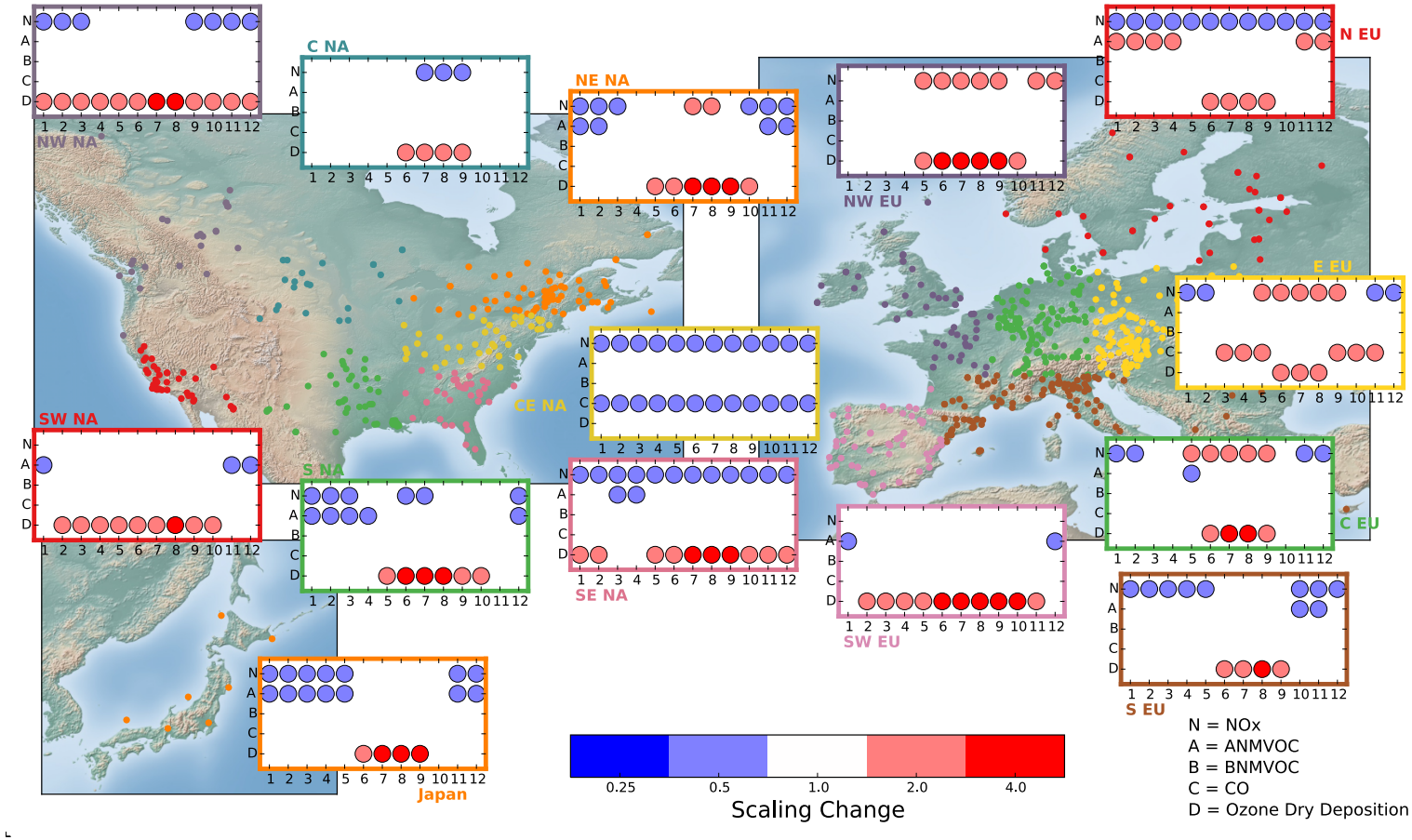


Fig. 5.18 Optimal monthly scalings of emissions/$O_3$ dry deposition parameters (between 2009 and 2011) in GEOS-Chem v10.01. $4° \times 5°$ GEOS5, for the minimisation of surface $O_3$+NO+CO biases. Plotted colour represents sign and intensity of scaling change.

## 5.7 Optimised simulation

The composed monthly global $4^\circ \times 5^\circ$ scaling grids are used to scale emissions/$O_3$ dry deposition in GEOS-Chem v10.01. $4^\circ \times 5^\circ$ GEOS5. The model is ran over the same time period as previous (2009–2011), again spinning up for 6 months prior (with global scalings applied in these times also). Figures 5.19, 5.20 and 5.21 respectively show the comparisons of the observed regionally averaged, spectrally derived seasonal surface $O_3$, NO and CO waveforms (black lines) for 2009–2011, with correspondingly derived output from GEOS-Chem v10.01. $4^\circ \times 5^\circ$ GEOS5 (red lines), and from the optimally scaled simulation (blue lines).

Despite the simple nature of scalings performed (i.e. neglecting transport), the modelled seasonality of both surface $O_3$ and NO is significantly improved in all areas in the optimally scaled simulation. Most notably, the modelled summertime overestimates of surface $O_3$ are removed almost entirely, across all continents (Fig 5.19). In North America and Japan, there is in fact a small general underestimate of $O_3$ in the summer (e.g. by 5 ppbv in SE NA July). In CE NA and CE NA these underestimates are more severe (e.g. by 11 ppbv in CE NA July), however, these worst case biases, in absolute terms, are still a factor of 2 lower than the previous overestimates. In Europe, the modelled winter underestimates are removed completely in the N EU and S EU regions, but can not be entirely removed in C EU and E EU (with a 7–8 ppbv January underestimate in both areas), however these biases are halved in magnitude from previous. Despite previous modelled summer $O_3$ overestimates being smaller in Europe than in other areas, these biases are also reduced, by at least a factor of 2 in almost all areas (except NW NA).

Most notably for surface NO, the modelled wintertime overestimates in most areas are removed almost entirely (e.g. in January E EU, a 5 ppbv overestimate to a 0.1 ppbv underestimate) (Fig 5.20). Winter NO is still overestimated in S EU (by 0.3 ppbv), but this bias is halved in magnitude from previous. The smaller modelled summer underestimates in most areas are also improved (i.e. 1 ppbv increase in CE EU July), however in CE NA a previously negligible bias is degraded to a 0.3–0.4 ppbv summer overestimate, representing one of only very few instances where where the optimised simulation compares less favourably with output from the standard model. The lack of modelled NO seasonality in Japan and NE NA is also corrected, now both showing a summer peak. For Japan in particular, seasonal integrated biases are almost negligible. In NE NA, the August peak of the seasonality is captured, but is overestimated in magnitude (by 0.15 ppbv).

The reductions of modelled summertime $O_3$ also mean the modelled seasonal amplitudes and phases across all continents are much better represented (e.g. a modelled springtime peak in $O_3$ across North America, as seen in observations). This is also the case for NO, with the elimination of the modelled winter overestimates and summer underestimates in most areas, significantly improving the modelled amplitudes.

Significant improvements to CO are only made in CE NA (Fig 5.21), an area where ACO emissions are explicitly scaled in all months, with winter modelled CO overestimates

reduced by 80 ppbv. The reduction of surface $O_3$ and NO seasonal biases therefore have a negligible impact on the modelled representation of CO.

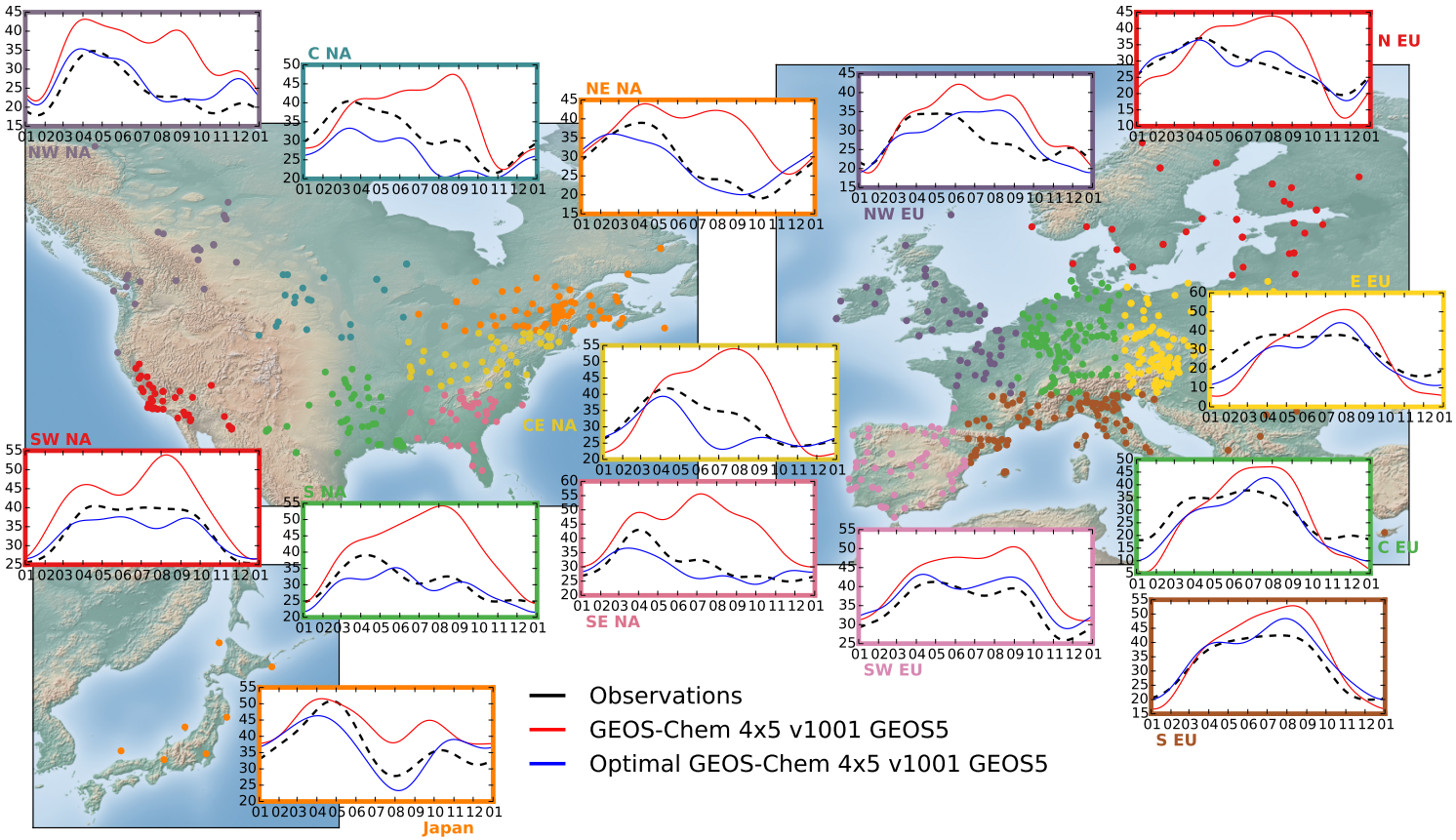


Fig. 5.19 Comparison of average spectrally derived seasonal surface $O_3$ waveforms (for 2009–2011) between observations (black lines), GEOS-Chem v10.01. $4° \times 5°$ GEOS5 (red lines), and an optimal regionally scaled version of the same model (using scalings shown in Fig 5.18) (blue lines), in multiple areas in North America, Europe and Japan.

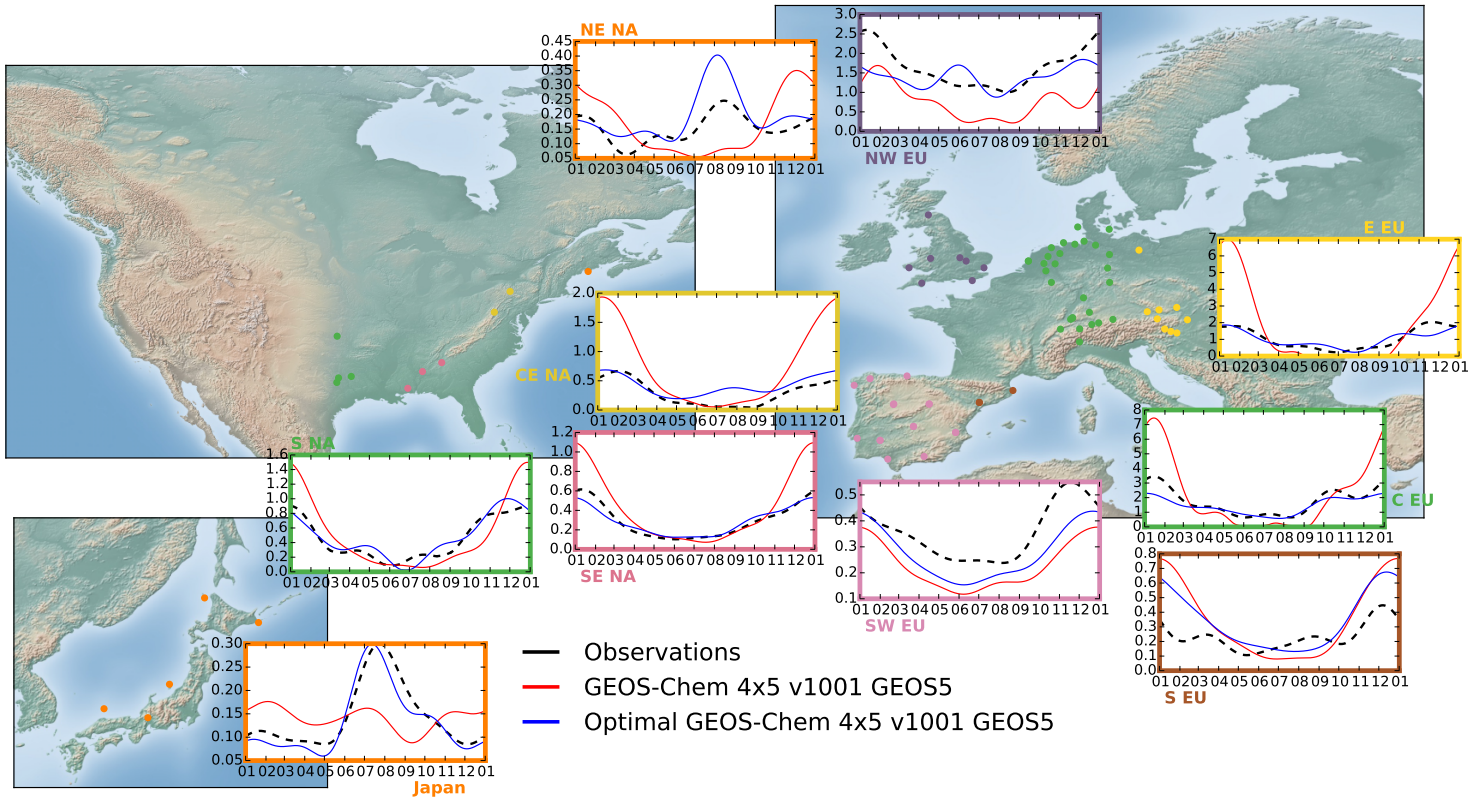


Fig. 5.20 Comparison of average spectrally derived seasonal surface NO waveforms (for 2009–2011) between observations (black lines), GEOS-Chem v10.01. $4^\circ \times 5^\circ$ GEOS5 (red lines), and an optimal regionally scaled version of the same model (using scalings shown in Fig 5.18) (blue lines), in multiple areas in North America, Europe and Japan.

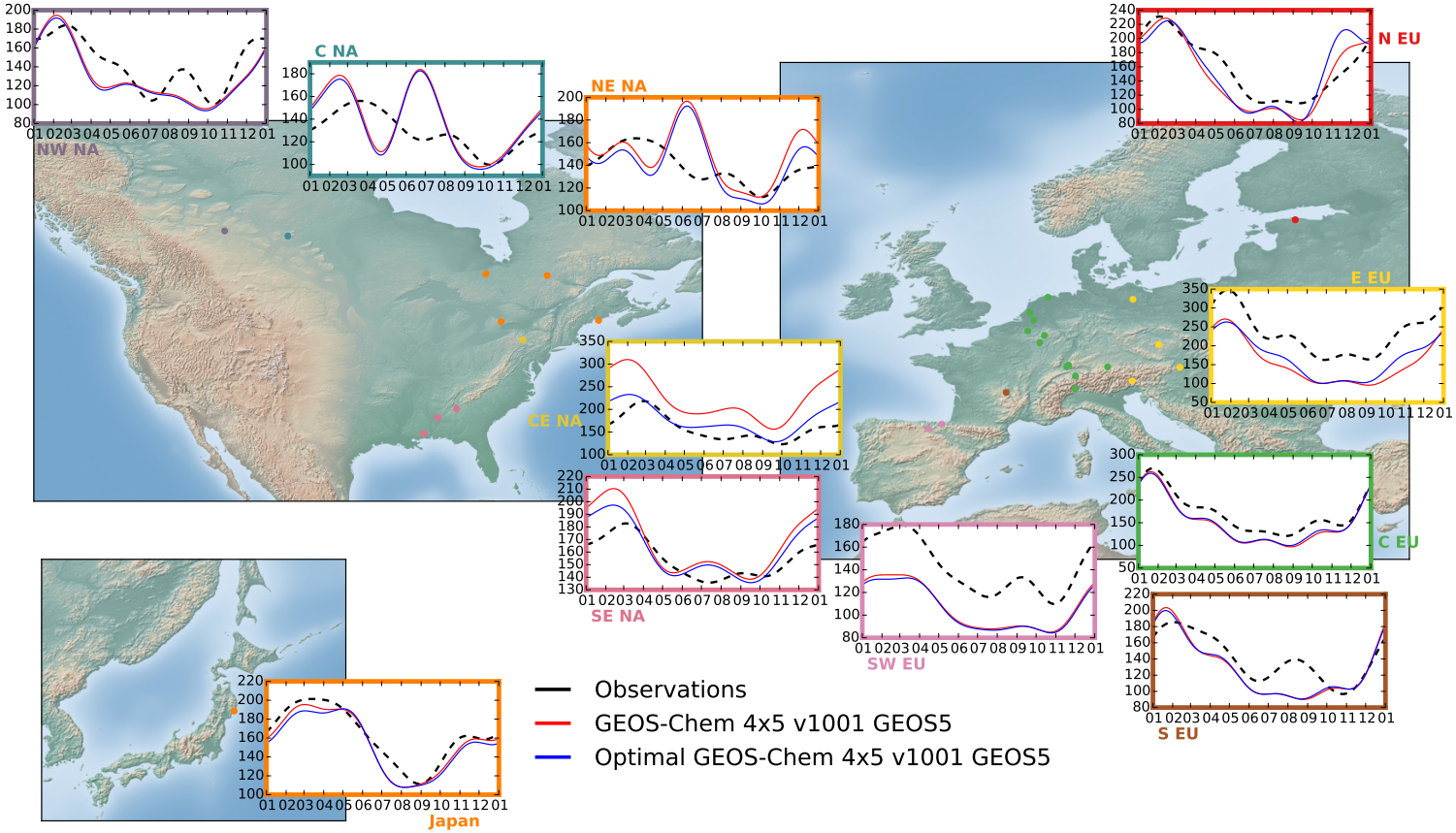


Fig. 5.21 Comparison of average spectrally derived seasonal surface CO waveforms (for 2009–2011) between observations (black lines), GEOS-Chem v10.01. $4° \times 5°$ GEOS5 (red lines), and an optimal regionally scaled version of the same model (using scalings shown in Fig 5.18) (blue lines), in multiple areas in North America, Europe and Japan.

## 5.8 Discussion

In short, through an extensive global sensitivity study (using joint observational constraints of $O_3$, NO and CO), it is demonstrated that with optimised monthly regional scalings of anthropogenic emissions and the $O_3$ dry deposition flux, the modelled seasonality of surface $O_3$ and NO in the northern hemisphere can be significantly improved. Surface $O_3$ is found to be NOx sensitive in all regions, with scalings of VOC emissions (anthropogenic or natural) generally not imparting significant change on $O_3$. Surface $O_3$ is found to be sensitive to scalings of ACO emissions, however in almost all areas, changes of ACO emissions lead to greater modelled $O_3$ biases.

The most notable finding from this work is that increases to the summertime $O_3$ dry deposition flux provide the only viable route for substantial reduction of the modelled summertime surface $O_3$ bias in all evaluated regions. Despite frequent attribution of modelled surface $O_3$ biases to uncertainties of emissions, the findings of this work show it is not possible to entirely eliminate summertime surface $O_3$ biases in any region by solely optimising emissions. Additionally, generally found modelled winter underestimates of surface $O_3$, and overestimates of NO (particular notable in densely populated areas: CE NA, C EU) are able to be simultaneously eliminated in main through reductions of ANOx emissions. ANOx emissions are generally needed to be reduced by a factor of 2 in the winter months in North America, consistent with results from recent evaluations (Anderson et al., 2014; Travis et al., 2016).

Emission inventories used by global models are typically originally compiled for legislative purposes, not with atmospheric chemistry research in mind. The variant forms of horizontal resolutions, temporal resolutions and species provided over different areas ensures emissions in global models as present are essentially a patchwork. Emissions in Europe (EMEP), Canada (CAC) and Mexico (BRAVO) specifically are natively provided with an annual resolution, and are well constrained bottom-up estimates of the total emitted quantities over the year. Seasonal scaling factors are then applied to the native annual estimates in these regions. The sensitivity to ANOx emissions in C EU and E EU (areas with some of the largest density of emissions), is strongly variant by season (change in sign between the winter and summer), suggestive of issues with the seasonal scaling factors in these regions.

Further work needs to be undertaken to evaluate the uncertain seasonality of $O_3$ dry deposition. The parameterisation of dry deposition in GEOS-Chem is based on code and a land class map, that are now both over 20 years old (Wesely, 1989; Olson, 1994). Most other global CTMs/ESMs also use a similar Wesely (1989) type parameterisation for dry deposition, and therefore biases in the modelled representation of dry deposition could therefore be at least partly responsible for the persistent NH summertime surface $O_3$ overestimate across most models. Recent work has demonstrated substantive improvements to $O_3$ dry deposition (and subsequently the estimation of $O_3$) through online coupling of dry deposition to the evolving vegetation phenology simulated by a land model (Val Martin et al., 2014). GEOS-Chem is now fully capable of being run as the atmospheric chemistry

component of an ESM, therefore a direct comparison between the standard offline and online approaches to dry deposition is able to be made. However, extensive observations of the $O_3$ dry deposition flux, by land class, are needed to truly validate the findings in this work, observations of which are extremely limited as present.

The optimal configurations derived in this work could almost certainly be further improved through finer finesse of scalings, and with greater numbers of parameters being scaled in tandem. However, the already substantive number of model runs undertaken through this work (106) precluded this. Applying an adjoint inversion methodology (e.g. 4-D VAR (Keller, 2014; Walker, 2014)) would allow the sensitivity of surface $O_3$ to a vast range of parameter configurations to be evaluated. This approach would also allow for the effects of transport between regions to be implicitly incorporated into regional scalings, and would therefore be the sensible next progression of this analysis. Greater numbers of high quality surface NO and CO observations would be necessary to allow an inversion to be stable across the entirety of North America, Europe and Japan however, and running for 2.5 years (as done in this work) would be computationally expensive. Going forwards in the short term, additional constraints of $O_3$ dry deposition rates, VOCs, etc.. would help in further minimising biases. Recent findings of excessive boundary layer mixing in GEOS-Chem (Travis et al., 2016), contributing to summer surface $O_3$ biases in the south east USA, also need to be evaluated.

# Chapter 6

# Conclusions

All work in this thesis was undertaken with the ultimate aim of reducing uncertainty of global modelled tropospheric $O_3$ in CTMs/ESMs, for which persistent biases have been regularly cited. In order for globally modelled $O_3$ to be evaluated, high quality model comparable observations were first required.

The first major chapter of this work describes the collection of hourly, daily and monthly surface measurements of $O_3$ and some of its major precursors (NO, $NO_2$, CO, $C_5H_8$) from all publicly available data sets. 1,033,463,750 measurements from 16,996 sites are processed through a number of rigorous data quality checks (i.e. screening of bad of measurement methodologies, removing urban sites). It was found necessary to split $NO_2$ observations into 2 sets ($NO_2$–M and $NO_2$–O) due to the bias associated with chemiluminescence instruments which use molybdenum converters. Final processed data totals 206,930,222 observations from 3112 sites, of high enough quality appropriate for global model evaluation. The majority of observations are made in the northern hemisphere mid-latitudes, particularly in Europe and the USA, with generally sparse coverage over the rest of the world (with the exception of CO – due to the flask measurement network). Observations of $O_3$ precursors are found to spatially limited, relative to $O_3$, with many observations of these species needing to be discarded due to being coarsely resolved, attributable to measurements being made for legislative purposes as opposed to scientific.

Specific focus is placed on the macro-scale evaluation of the periodic (seasonal and diurnal) variability of surface $O_3$ in a global CTM (GEOS-Chem). A spectral methodology, the Lomb-Scargle periodogram, is applied for this purpose, transforming data from the time domain to the frequency domain. This technique mathematically isolates the variability encoded in the transformed time series across multiple frequencies (or periods), allowing the key frequencies for which $O_3$ has substantial periodic variability on to be determined, and magnitude of variability quantified. The Lomb-Scargle periodogram is designed to natively handle gapped data, and therefore is appropriate for application to atmospheric (typically gapped) data.

Using the Lomb-Scargle periodogram to spectrally analyse observed hourly surface $O_3$ at any given site produces spectra which show distinct relationships between magnitude and period, attributable to meteorological processes (weather and macroweather), as well

as peaks on daily and annual timescales (and harmonics). A methodology for multi-site periodic analysis is built, superposing the spectral information encoded on both daily and annual timescales with associated harmonics, yielding waveforms solely derived from the periodic seasonal and diurnal variability encoded in the time series. These waveforms are described simply by two terms, the amplitude (half peak to trough difference) and phase (timing of peak of waveform). Spectrally analysing the entirety of the collated hourly observed $O_3$ data between 2005 and 2010 reveals the amplitude and phase on both seasonal and diurnal timescales to significantly vary by site, but with coherent geographical patterns.

The correspondingly derived periodic variability of surface $O_3$ in GEOS-Chem is evaluated, most notably revealing substantial model biases associated with the seasonal cycle in the mid-latitude northern hemisphere, with a general overestimation of the seasonal amplitudes in North America and Europe (by up to 16 ppbv), together with delayed phase maxima by 1–5 months. Smaller biases are found for the modelled diurnal cycle of surface $O_3$, but the majority of amplitudes in Europe and North America are found to be overestimated (by up to 17 ppbv).

Going further, for data between 2009 and 2011, the regionally averaged seasonal waveforms of surface $O_3$ for all areas in North America, Europe and in Japan are found to be significantly biased in all recent versions of GEOS-Chem. Specifically, summertime $O_3$ is overestimated in all areas by a minimum of 10 ppbv, with the greatest overestimates being located in the eastern USA, up to 23 ppbv in July. This bias leads to a general modelled northern hemisphere summer peak in $O_3$, and is the major cause of the identified seasonal amplitude and phase biases. These seasonal biases are not significantly improved through changes to the model configuration, i.e. changes in driven meteorology, horizontal resolution and boundary layer mixing scheme. Equivalent analysis of the seasonality of hourly reporting models in the ACCMIP model spread reveal similar seasonal biases to GEOS-Chem. A substantive literature review to determine potential causation of this modelled bias is undertaken, with uncertainties associated with the magnitude of anthropogenic emissions and the $O_3$ dry deposition flux being most the regularly cited issues.

An extensive global sensitivity study is undertaken using GEOS-Chem to evaluate the sensitivity of modelled surface $O_3$ seasonal biases to scalings of anthropogenic emissions (NOx, CO, NMVOCs), biogenic emissions (NMVOCs, i.e. $C_5H8$), zonal $CH_4$, and the $O_3$ dry deposition flux. GEOS-Chem is run 106 times, using a multitude of differing global scaling configurations. Surface $O_3$, NO and CO output from each simulation are spectrally analysed to produce regionally averaged seasonal waveforms, with seasonal model biases for each species determined through comparison with correspondingly spectrally processed observational constraints. The independent minimisation of the modelled biases for each species reveals multiple divergent viable scaling configurations, which for each respective species also wildly vary by month. For each species, by taking the best case simulation each month (and thus neglecting advection), modelled seasonal biases across all regions are able be entirely removed. The optimal scalings derived in each region however vary significantly across the year, for each species, meaning little confidence can be placed

in results. In almost no circumstances does the standard version of the model represent the best case scenario for simulating surface $O_3$. Additionally, modelled surface $O_3$ is found to be very insensitive to changes in zonal $CH_4$, even outside estimated uncertainty boundaries.

Constraining jointly by $O_3$, NO and CO observations allows convergence on scalings which improve the modelled chemical representation as a whole, not just for individual species. This approach significantly reduces the number of viable scaling configurations, and produces regionally consistent optimal monthly scaling settings, heightening confidence in the physical validity of results. These derived factors are used to regionally scale a final optimised simulation of GEOS-Chem (with the impacts of advection now implicitly included). This results in a simulation which significantly improves the modelled northern hemisphere seasonality of surface $O_3$ and NO. Most notably, the modelled summertime overestimates of surface $O_3$ are removed almost entirely, across all continents, in fact leading a small general summer underestimate of $O_3$ in North America and Japan (e.g. by 5 ppbv in SE NA July). The reduction in modelled summertime surface $O_3$ is dominantly controlled through increases to the summer $O_3$ dry deposition flux (by factors of 2–4), with increases to this flux providing the only viable pathway for substantial reduction of the modelled summertime bias, in all evaluated regions. Despite frequent attribution of modelled surface $O_3$ biases to uncertainties of emissions, the findings of this work show it is not possible to entirely eliminate summertime surface $O_3$ biases in any region by solely optimising emissions.

Surface $O_3$ is found to be NOx sensitive in all regions, with scalings of VOC emissions generally not imparting significant change on $O_3$. General modelled winter underestimates of surface $O_3$, and overestimates of NO (particularly notable in densely populated areas: CE NA, C EU) are able to be simultaneously removed, in main through reductions of NOx emissions (a factor of 2 decrease). Surface $O_3$ is found to be sensitive to scalings of CO emissions, however in almost all areas changes to CO emissions lead to greater modelled surface $O_3$ biases. Significant improvements to modelled surface CO are only made in CE NA, where ACO emissions are scaled by a factor of 0.5 in all months, leading to winter modelled CO overestimates being reduced by 80 ppbv. The reduction of the modelled seasonal biases for surface $O_3$ and NO have a negligible impact on the modelled representation of surface CO.

Further work needs to be undertaken to evaluate the uncertain seasonality of $O_3$ dry deposition. The parameterisation of dry deposition in GEOS-Chem is based on code and a land class map, that are now both over 20 years old (Wesely, 1989; Olson, 1994). Most other global CTMs/ESMs also use a similar Wesely (1989) type parameterisation for dry deposition, and therefore biases in the modelled representation of dry deposition could therefore be at least partly responsible for the persistent northern hemisphere summertime surface $O_3$ overestimate across most models. Recent work has demonstrated substantive improvements to $O_3$ dry deposition (and subsequently the estimation of surface $O_3$) through online coupling of dry deposition to the evolving vegetation phenology simulated by a land model (Val Martin et al., 2014). GEOS-Chem is now fully capable of being run as

the atmospheric chemistry component of an ESM, therefore a direct comparison between the standard offline and online approaches to dry deposition is able to be made. However, extensive observations of the $O_3$ dry deposition flux, by land class, are needed to truly validate the findings in this work, observations of which are extremely limited as present.

The optimal configurations derived in this work could almost certainly be further improved through finer finesse of scalings, and with greater numbers of parameters being scaled in tandem. However, the already substantive number of model runs undertaken through this work (106) precluded this. Applying an adjoint inversion methodology (e.g. 4-D VAR (Keller, 2014; Walker, 2014)) would allow the sensitivity of surface $O_3$ to a vast range of parameter configurations to be evaluated. This approach would also allow for the effects of transport between regions to be implicitly incorporated into regional scalings, and would therefore be the sensible next progression of this analysis. Greater numbers of high quality surface NO and CO observations would be necessary to allow an inversion to be stable across the entirety of North America, Europe and Japan however, and running for 2.5 years (as done in this work) would be computationally expensive. Going forwards in the short term, additional constraints of $O_3$ dry deposition rates, VOCs, etc.. would help in further minimising biases. Recent findings of excessive boundary layer mixing in GEOS-Chem (Travis et al., 2016), contributing to summer surface $O_3$ biases in the south east USA, also need to be evaluated.

# Appendix A

| Measurement Method | Reason |
|---|---|
| **$O_3$** | |
| Electrochemical Concentration Cell | Method more typically used by ozonesondes, than at the surface. Concerns also regarding the use of different sensing solutions strongly influencing performance (Boyd et al., 1998). |
| Ethylene Chemiluminescence | Significant water vapour interferences (Kleindienst et al., 1993). Method used to be supported by U.S.A EPA, but is no longer. |
| GCFID | Method not typically associated with species. |
| Photometric Flame Photometry | Method not typically associated with species. |
| **NO** | |
| GCFID | Method not typically associated with species. |
| NDIR | Method not typically associated with species. |
| UV Absorption Spectrophotometry | Method not typically associated with species. |
| **$NO_2$** | |
| GCFID | Method not typically associated with species. |
| Integrative Active – Liquid Phase Sampling & Colorimetry / Spectrophotometry | Concerns regarding the sensitivity of the sampling conditions, most notably the gas impingement rate (Goyal, 2002). |
| Passive – Diffusive Sampler & Colorimetry / Ion Chromatography | Multiple potential biases: type of sampler, exposure setting (i.e. sheltered or not), exposure time and chemical interference (Tang et al., 2001; Theo et al., 2009). |
| Photometric Flame Photometry | Method not typically associated with species. |
| UV Absorption Spectrophotometry | Method not typically associated with species. |
| **CO** | |
| Coulometry | Method not typically associated with species. |
| Ion Chromatography | Method not typically associated with species. |
| Photometric Flame Photometry | Method not typically associated with species. |
| UV Absorption Spectrophotometry | Method not typically associated with species. |

Table A.1 Omitted measurement methodologies for all species.

# Appendix B

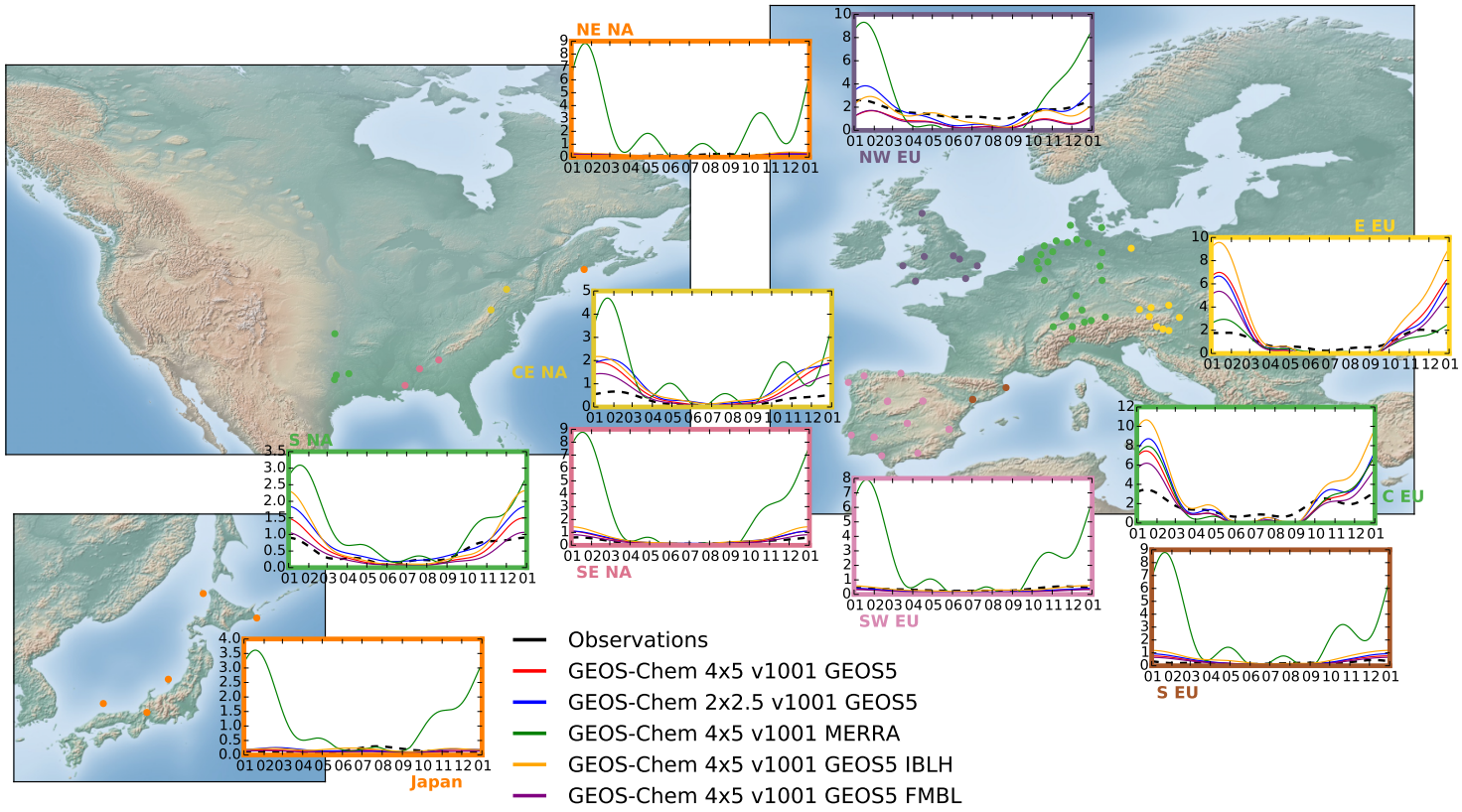


Fig. B.1 Comparison of average spectrally derived seasonal surface NO waveforms (for 2009–2011) between observations (black lines) and multiple configurations of GEOS-Chem v10.01. (standard $4^\circ \times 5^\circ$ GEOS5 – red lines; $2^\circ \times 2.5^\circ$ horizontal resolution – blue lines; MERRA meteorology – green lines; interactive boundary layer height – orange lines; fully mixed boundary layer – purple lines), in multiple areas in North America, Europe and Japan.

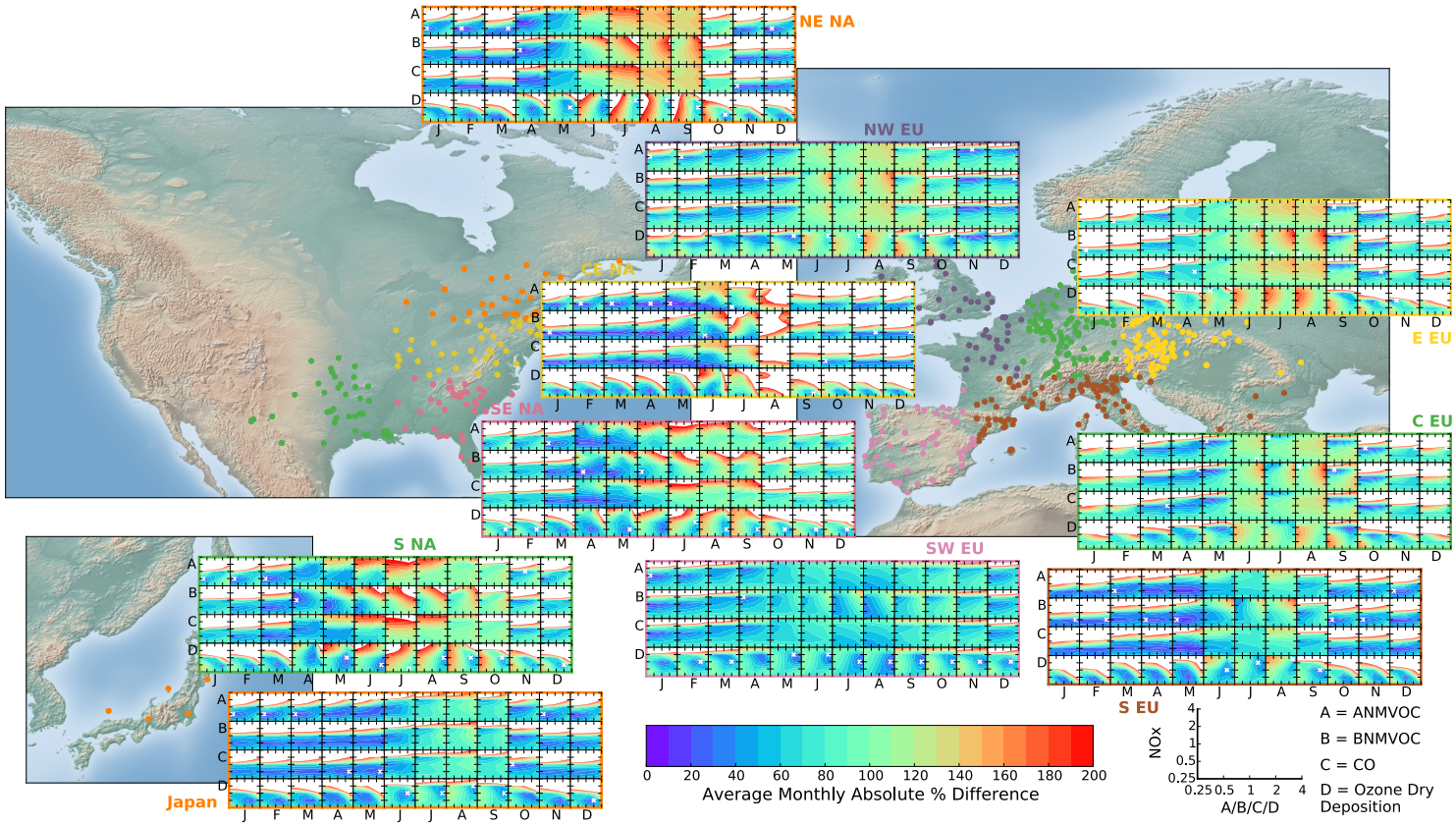


Fig. B.2 Contour plots showing the sensitivity of regional spectrally derived monthly surface $O_3$+NO biases of GEOS-Chem v10.01. 4° × 5° GEOS5, resultant from scalings of multiple emissions/deposition parameters (for 2009–2011). Each individual box represents the regional average monthly modelled biases from scalings of ANOx emissions (y-axis) and a changing x-axis parameter (ANMVOCs, BNMVOCs, ACO, $O_3$ dry deposition). Design of figure is explained in detail by Fig 5.8. The over-plotted white x marks represent the optimal monthly scalings for the minimisation of modelled biases, per region.

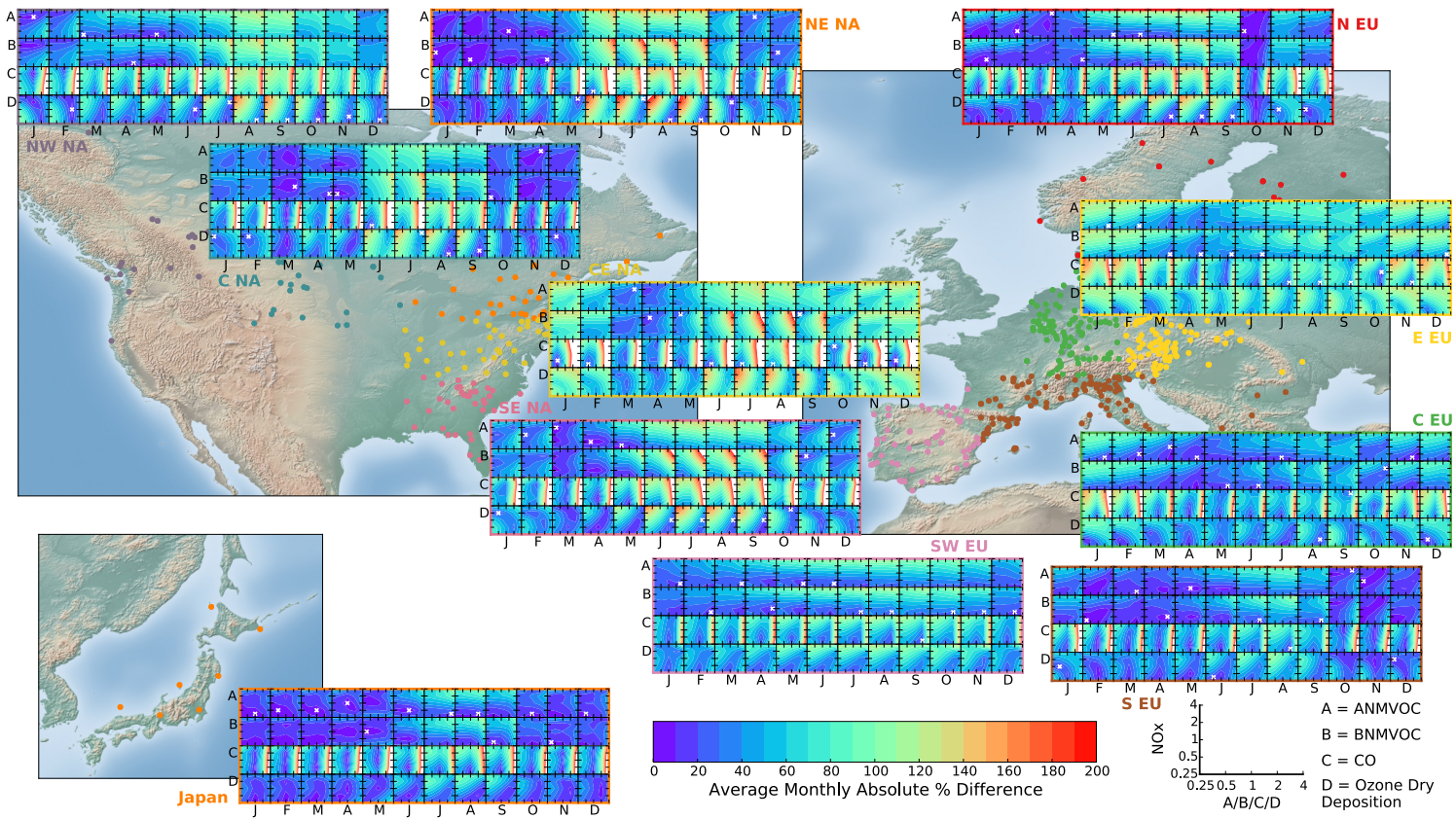


Fig. B.3 Contour plots showing the sensitivity of regional spectrally derived monthly surface $O_3$+CO biases of GEOS-Chem v10.01. 4° × 5° GEOS5, resultant from scalings of multiple emissions/deposition parameters (for 2009–2011). Each individual box represents the regional average monthly modelled biases from scalings of ANOx emissions (y-axis) and a changing x-axis parameter (ANMVOCs, BNMVOCs, ACO, $O_3$ dry deposition). Design of figure is explained in detail by Fig 5.8. The over-plotted white x marks represent the optimal monthly scalings for the minimisation of modelled biases, per region.

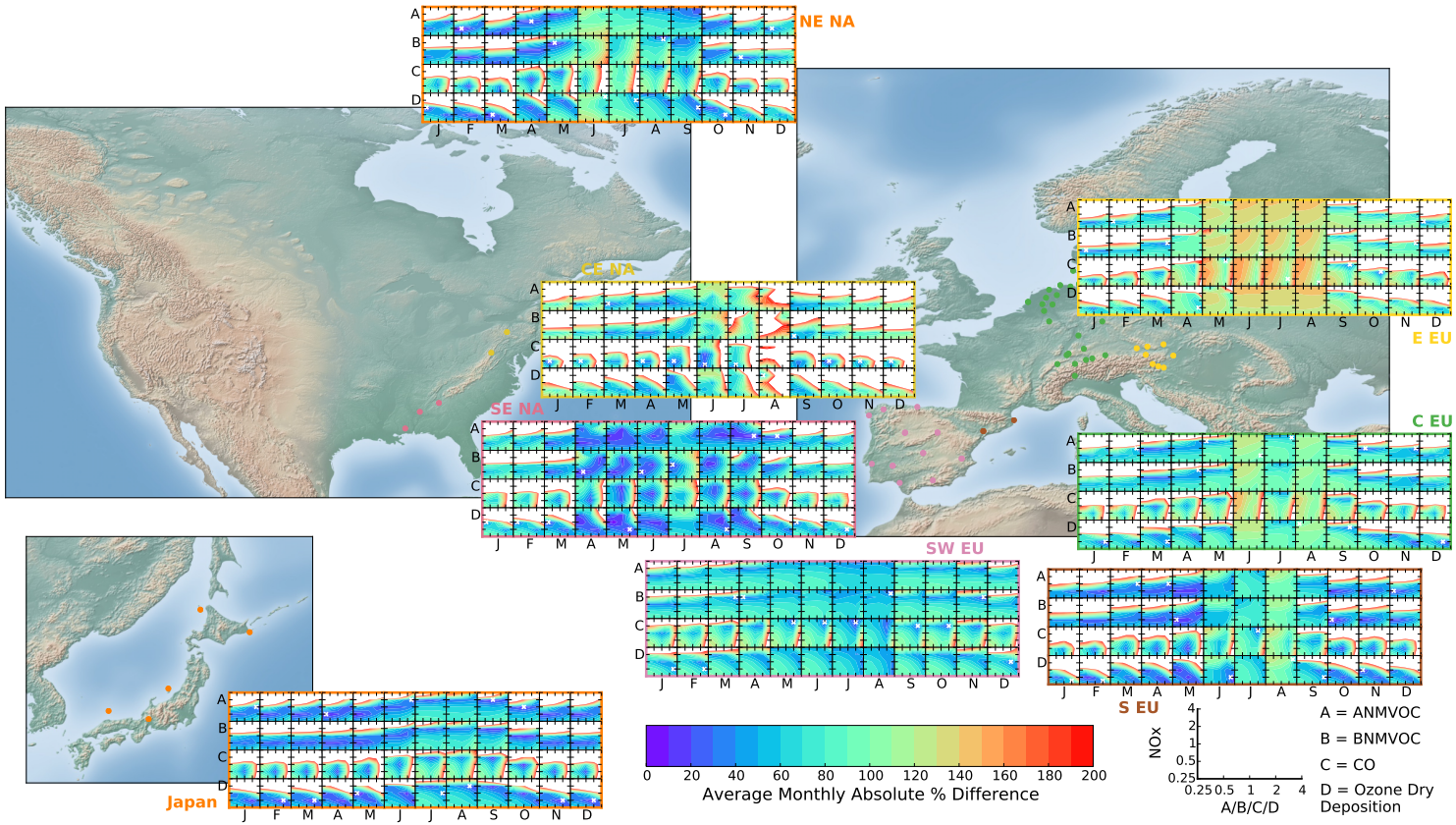


Fig. B.4 Contour plots showing the sensitivity of regional spectrally derived monthly surface NO+CO biases of GEOS-Chem v10.01. 4° × 5° GEOS5, resultant from scalings of multiple emissions/deposition parameters (for 2009–2011). Each individual box represents the regional average monthly modelled biases from scalings of ANOx emissions (y-axis) and a changing x-axis parameter (ANMVOCs, BNMVOCs, ACO, $O_3$ dry deposition). Design of figure is explained in detail by Fig 5.8. The over-plotted white x marks represent the optimal monthly scalings for the minimisation of modelled biases, per region.

# Nomenclature

**Acronyms / Abbreviations**

| | |
|---|---|
| ACCENT | Atmospheric Composition Change: the European Network of excellence |
| ACCMIP | Atmospheric Chemistry and Climate Model Intercomparison Project |
| AEIC | Aviation Emissions Inventory Code |
| AQS | Air Quality System |
| BADC | British Atmospheric Data Centre |
| BRAVO | Big Bend Regional Aerosol and Visibility Observational Study Emissions Inventory |
| BVOC | biogenic non–methane volatile organic compound |
| CAC | Criteria Air Contaminants |
| CAPMoN | Canadian Air and Precipitation Monitoring Network |
| CASTNET | Clean Air Status and Trends Network |
| CEDA | Centre for Environmental Data Archival |
| CLRTAP | Convention on Long Range Transboundary Air Pollution |
| CTM | chemical transport model |
| DFT | Discrete Fourier Transform |
| EANET | Acid Deposition Monitoring Network in East Asia |
| EDGAR | Emission Database for Global Atmospheric Research |
| EEA | European Economic Area |
| EMEP | European Monitoring and Evaluation Programme |
| EPA | Environmental Protection Agency |
| ESM | earth system model |

| | |
|---|---|
| EU | European Union |
| FFT | Fast Fourier Transform |
| GAW | Global Atmospheric Watch |
| GCM | general circulation model |
| GEIA | Global Emissions Inventory Activity |
| GENEMIS | Generation of European Emission Data for Episodes |
| GEOS | Goddard Earth Observing System |
| GFED4 | Global Fire Emissions Database version 4 |
| GHG | greenhouse gas |
| GMAO | Global Modelling Assimilation Office |
| HPALDs | hydroperoxyaldehydes |
| HTAP | Hemispheric Transport of Air Pollution intercomparison project |
| IASI | Infrared Atmospheric Sounding Interferometer |
| ICOADS | International Comprehensive Ocean-Atmosphere Data Set |
| ICTZ | intertropical convergence zone |
| IEA | International Energy Agency |
| MEGAN | Model of Emissions of Gases and Aerosols from Nature |
| IPCC | Intergovernmental Panel on Climate Change |
| LSP | Lomb–Scargle periodogram |
| MBL | marine boundary layer |
| MEIC | Multi-resolution Emission Inventory for China |
| MERRA | Modern Era Retrospective Analysis for Research and Applications |
| MOPITT | Measurement of Pollution in the Troposphere Instrument |
| NaN | not a number |
| NAPS | Canadian National Air Pollution Survey Program |
| NASA | National Aeronautics and Space Administration |
| NEI | National Emissions Inventory |
| NEI | USA National Emissions Inventory |

| | |
|---|---|
| NH | northern hemisphere |
| NMVOC | non–methane volatile organic compound |
| NOAA | National Oceanic and Atmospheric Administration |
| NOx | nitrogen oxides |
| OECD | Organisation for Economic Co-operation and Development |
| OMI | Ozone Monitoring Instrument |
| OVOCs | oxygenated volatile organic compounds |
| PAN | peroxyacetyl nitrate |
| PDF | probability distribution function |
| ppbv | parts per billion by volume ($1 \times 10^{-9}$) |
| ppmv | parts per million by volume ($1 \times 10^{-6}$) |
| pptv | parts per trillion by volume ($1 \times 10^{-12}$) |
| RETRO | Reanalysis of the Tropospheric chemical composition |
| RF | radiative forcing |
| SCION | Southern Oxidants Study |
| SEARCH | South Eastern Aerosol Research and Characterisation |
| SH | southern hemisphere |
| SOA | secondary organic aerosol |
| SRP | standard reference photometer |
| STE | Stratosphere–troposphere exchange |
| USA | United States of America |
| USNO | United States Naval Observatory |
| UTC | Coordinated Universal Time |
| UV | ultraviolet |
| VOC | volatile organic compound |
| WDCGG | World Data Center for Greenhouse Gases |
| WMO | World Meteorological Organisation |

# References


Ackermann-Liebrich, U., Leuenberger, P., Schwartz, J., Schindler, C., Monn, C., Bolognini, G., Bongard, J. P., Brändli, O., Domenighetti, G., Elsasser, S., Grize, L., Karrer, W., Keller, R., Keller-Wossidlo, H., Künzli, N., Martin, B. W., Medici, T. C., Perruchoud, A. P., Schöni, M. H., Tschopp, J. M., Villiger, B., Wüthrich, B., Zellweger, J. P., and Zemp, E. (1997). Lung function and long term exposure to air pollutants in Switzerland. Study on Air Pollution and Lung Diseases in Adults (SAPALDIA) Team. *American Journal of Respiratory and Critical Care Medicine*, 155(1):122–9.

Altshuler, S., Arcado, T., and Lawson, D. (1995). Weekday vs weekend ambient ozone concentrations - discussion and hypotheses with focus on northern California. *Journal of the Air & Waste Management Association*, 45(12):967–972.

AMEC Environment and Infrastructure Inc. (2014). Clean Air Status and Trends Network (CASTNET) 2012 Annual Report. Technical Report contract No. EP-W-09-028, U.S. Environmental Protection Agency, Washington DC.

Anderson, D. C., Loughner, C. P., Diskin, G., Weinheimer, A., Canty, T. P., Salawitch, R. J., Worden, H. M., Fried, A., Mikoviny, T., Wisthaler, A., and Dickerson, R. R. (2014). Measured and modeled CO and NOy in DISCOVER-AQ: An evaluation of emissions and chemistry over the eastern US. *Atmospheric Environment*, 96:78–87.

Anenberg, S. C., West, J. J., Fiore, A. M., Jaffe, D. A., Prather, M. J., Bergmann, D., Cuvelier, K., Dentener, F. J., Duncan, B. N., Gauss, M., Hess, P., Jonson, J. E., Lupu, A., MacKenzie, I. A., Marmer, E., Park, R. J., Sanderson, M. G., Schultz, M., Shindell, D. T., Szopa, S., Vivanco, M. G., Wild, O., and Zeng, G. (2009). Intercontinental Impacts of Ozone Pollution on Human Mortality. *Environmental Science and Technology*, 43(17):6482–6487.

Angelbratt, J., Mellqvist, J., Simpson, D., Jonson, J. E., Blumenstock, T., Borsdorff, T., Duchatelet, P., Forster, F., Hase, F., Mahieu, E., De Mazière, M., Notholt, J., Petersen, A. K., Raffalski, U., Servais, C., Sussmann, R., Warneke, T., and Vigouroux, C. (2011). Carbon monoxide (CO) and ethane (C2H6) trends from ground-based solar FTIR measurements at six European stations, comparison and sensitivity analysis with the EMEP model. *Atmospheric Chemistry and Physics*, 11(17):9253–9269.

Atkinson, R. and Arey, J. (2003). Gas-phase tropospheric chemistry of biogenic volatile organic compounds: a review. *Atmospheric Environment*, 37:197–219.

Aumont, O. and Bopp, L. (2006). Globalizing results from ocean in situ iron fertilization studies. *Global Biogeochemical Cycles*, 20(2):GB2017.

Avissar, R. (1993). Observations of leaf stomatal conductance at the canopy scale: An atmospheric modeling perspective. *Boundary-Layer Meteorology*, 64(1-2):127–148.

Avnery, S., Mauzerall, D. L., Liu, J., and Horowitz, L. W. (2011). Global crop yield reductions due to surface ozone exposure: 1. Year 2000 crop production losses and economic damage. *Atmospheric Environment*, 45(13):2284–2296.

Baldocchi, D. D., Hicks, B. B., and Camara, P. (1987). A canopy stomatal resistance model for gaseous deposition to vegetated surfaces. *Atmospheric Environment (1967)*, 21(1):91–101.

Beirle, S., Platt, U., Wenig, M., and Wagner, T. (2003). Weekly cycle of NO2 by GOME measurements: a signature of anthropogenic sources. *Atmospheric Chemistry and Physics*, 3:2225–2232.

Bejan, I., Abd El Aal, Y., Barnes, I., Benter, T., Bohn, B., Wiesen, P., and Kleffmann, J. (2006). The photolysis of ortho-nitrophenols: a new gas phase source of HONO. *Physical Chemistry Chemical Physics*, 8(17):2028.

Bell, M. L., Peng, R. D., and Dominici, F. (2006). The exposure-response curve for ozone and risk of mortality and the adequacy of current ozone regulations. *Environmental Health Perspectives*, 114(4):532–6.

Bey, I., Jacob, D. J., Yantosca, R. M., Logan, J. A., Field, B. D., Fiore, A. M., Li, Q. B., Liu, H. G. Y., Mickley, L. J., and Schultz, M. G. (2001). Global modeling of tropospheric chemistry with assimilated meteorology: Model description and evaluation. *Journal of Geophysical Research: Atmospheres*, 106(D19):23073–23095.

Boersma, K., Eskes, H., and Brinksma, E. (2004). Error analysis for tropospheric NO2 retrieval from space. *Journal of Geophysical Research: Atmospheres*, 109:D04311.

Bousquet, P., Ciais, P., Miller, J. B., Dlugokencky, E. J., Hauglustaine, D. A., Prigent, C., Van der Werf, G. R., Peylin, P., Brunke, E.-G., Carouge, C., Langenfelds, R. L., Lathière, J., Papa, F., Ramonet, M., Schmidt, M., Steele, L. P., Tyler, S. C., and White, J. (2006). Contribution of anthropogenic and natural sources to atmospheric methane variability. *Nature*, 443(7110):439–443.

Bowdalo, D. R. and Evans, M. J. (2016). Summertime surface ozone bias: a problem with emissions? *In prep. for submission to ACP*.

Bowdalo, D. R., Evans, M. J., and Sofen, E. D. (2016a). Spectral analysis of atmospheric composition: application to surface ozone model–measurement comparisons. *Atmospheric Chemistry and Physics*, 16(13):8295–8308.

Bowdalo, D. R., Sofen, E. D., and Evans, M. J. (2016b). Gridded global metrics for surface ozone precursor model evaulation. *In prep. for submission to ESSD*.

Boyd, I. S., Bodeker, G. E., Connor, B. J., Swart, D. P. J., and Brinksma, E. J. (1998). An assessment of ECC ozonesondes operated using 1cathode solutions at Lauder, New Zealand. *Geophysical Research Letters*, 25(13):2409–2412.

Brioude, J., Angevine, W. M., Ahmadov, R., Kim, S.-W., Evan, S., McKeen, S. A., Hsie, E.-Y., Frost, G. J., Neuman, J. A., Pollack, I. B., Peischl, J., Ryerson, T. B., Holloway, J., Brown, S. S., Nowak, J. B., Roberts, J. M., Wofsy, S. C., Santoni, G. W., Oda, T., and Trainer, M. (2013). Top-down estimate of surface flux in the Los Angeles Basin using a mesoscale inverse modeling technique: assessing anthropogenic emissions of CO, NOx and CO2 and their impacts. *Atmospheric Chemistry and Physics*, 13(7):3661–3677.

Brown-Steiner, B., Hess, P., and Lin, M. (2015). On the capabilities and limitations of GCCM simulations of summertime regional air quality: A diagnostic analysis of ozone and temperature simulations in the US using CESM CAM-Chem. *Atmospheric Environment*, 101:134–148.

Bruhwiler, L., Dlugokencky, E., Masarie, K., Ishizawa, M., Andrews, A., Miller, J., Sweeney, C., Tans, P., and Worthy, D. (2014). CarbonTracker-CH4: an assimilation system for estimating emissions of atmospheric methane. *Atmospheric Chemistry and Physics*, 14(16):8269–8293.

Butchart, N. (2014). The Brewer-Dobson circulation. *Reviews of Geophysics*, 52(2):157–184.

Canty, T. P., Hembeck, L., Vinciguerra, T. P., Anderson, D. C., Goldberg, D. L., Carpenter, S. F., Allen, D. J., Loughner, C. P., Salawitch, R. J., and Dickerson, R. R. (2015). Ozone and NOx chemistry in the eastern US: evaluation of CMAQ/CB05 with satellite (OMI) data. *Atmospheric Chemistry and Physics*, 15(19):10965–10982.

Carlton, A. G. and Baker, K. R. (2011). Photochemical Modeling of the Ozark Isoprene Volcano: MEGAN, BEIS, and Their Impacts on Air Quality Predictions. *Environmental Science & Technology*, 45(10):4438–4445.

Carpenter, L. J., Fleming, Z. L., Read, K. A., Lee, J. D., Moller, S. J., Hopkins, J. R., Purvis, R. M., Lewis, A. C., Muller, K., Heinold, B., Herrmann, H., Fomba, K. W., van Pinxteren, D., Muller, C., Tegen, I., Wiedensohler, A., Muller, T., Niedermeier, N., Achterberg, E. P., Patey, M. D., Kozlova, E. A., Heimann, M., Heard, D. E., Plane, J. M. C., Mahajan, A., Oetjen, H., Ingham, T., Stone, D., Whalley, L. K., Evans, M. J., Pilling, M. J., Leigh, R. J., Monks, P. S., Karunaharan, A., Vaughan, S., Arnold, S. R., Tschritter, J., Pohler, D., Friess, U., Holla, R., Mendes, L. M., Lopez, H., Faria, B., Manning, A. J., and Wallace, D. W. R. (2010). Seasonal characteristics of tropical marine boundary layer air measured at the Cape Verde Atmospheric Observatory. *Journal of Atmospheric Chemistry*, 67(2-3):87–140.

Charusombat, U., Niyogi, D., Kumar, A., Wang, X., Chen, F., Guenther, A., Turnipseed, A., and Alapaty, K. (2010). Evaluating a New Deposition Velocity Module in the Noah Land-Surface Model. *Boundary-Layer Meteorology*, 137(2):271–290.

Cieslik, S. A. (2004). Ozone uptake by various surface types: a comparison between dose and exposure. *Atmospheric Environment*, 38(15):2409–2420.

Clifton, O. E., Fiore, A. M., Correa, G., Horowitz, L. W., and Naik, V. (2014). Twenty-first century reversal of the surface ozone seasonal cycle over the northeastern United States. *Geophysical Research Letters*, 41(20):7343–7350.

Cooper, O. R., Gao, R.-S., Tarasick, D., Leblanc, T., and Sweeney, C. (2012). Long-term ozone trends at rural ozone monitoring sites across the United States, 1990-2010. *Journal of Geophysical Research: Atmospheres*, 117:D22307.

Cooper, O. R., Parrish, D. D., Stohl, A., Trainer, M., Nédélec, P., Thouret, V., Cammas, J. P., Oltmans, S. J., Johnson, B. J., Tarasick, D., Leblanc, T., McDermid, I. S., Jaffe, D., Gao, R., Stith, J., Ryerson, T., Aikin, K., Campos, T., Weinheimer, A., and Avery, M. A. (2010). Increasing springtime ozone mixing ratios in the free troposphere over western North America. *Nature*, 463:344–348.

Cooper, O. R., Parrish, D. D., Ziemke, J., Balashov, N. V., Cupeiro, M., Galbally, I. E., Gilge, S., Horowitz, L., Jensen, N. R., Lamarque, J.-F., Naik, V., Oltmans, S. J., Schwab, J., Shindell, D. T., Thompson, A. M., Thouret, V., Wang, Y., and Zbinden, R. M. (2014). Global distribution and trends of tropospheric ozone: An observation-based review. *Elementa: Science of the Anthropocene*, 2(1):000029.

Creilson, J., Fishman, J., and Wozniak, A. (2003). Intercontinental transport of tropospheric ozone: a study of its seasonal variability across the North Atlantic utilizing tropospheric ozone residuals and its relationship to the North Atlantic Oscillation. *Atmospheric Chemistry and Physics*, 3:2053–2066.

Crippa, M., Janssens-Maenhout, G., Dentener, F., Guizzardi, D., Sindelarova, K., Muntean, M., Van Dingenen, R., and Granier, C. (2016). Forty years of improvements in European air quality: regional policy-industry interactions with global impacts. *Atmospheric Chemistry and Physics*, 16(6):3825–3841.

Crutzen, P. (1973). A discussion of the chemistry of some minor constituents in the stratosphere and troposphere. *Pure and Applied Geophysics*, 106-108(1):1385–1399.

Curci, G., Palmer, P. I., Kurosu, T. P., Chance, K., and Visconti, G. (2010). Estimating European volatile organic compound emissions using satellite observations of formaldehyde from the Ozone Monitoring Instrument. *Atmospheric Chemistry and Physics*, 10(23):11501–11517.

Daniel, J. S. and Solomon, S. (1998). On the climate forcing of carbon monoxide. *Journal of Geophysical Research: Atmospheres*, 103(D11):13249–13260.

Danielsen, E. F. (1968). Stratospheric-Tropospheric Exchange Based on Radioactivity, Ozone and Potential Vorticity. *Journal of the Atmospheric Sciences*, 25(3):502–518.

Deeter, M. N., Martínez-Alonso, S., Edwards, D. P., Emmons, L. K., Gille, J. C., Worden, H. M., Pittman, J. V., Daube, B. C., and Wofsy, S. C. (2013). Validation of MOPITT Version 5 thermal-infrared, near-infrared, and multispectral carbon monoxide profile retrievals for 2000-2011. *Journal of Geophysical Research: Atmospheres*, 118(12):6710–6725.

Dentener, F., Stevenson, D., Ellingsen, K., van Noije, T., Schultz, M., Amann, M., Atherton, C., Bell, N., Bergmann, D., Bey, I., Bouwman, L., Butler, T., Cofala, J., Collins, B., Drevet, J., Doherty, R., Eickhout, B., Eskes, H., Fiore, A., Gauss, M., Hauglustaine, D., Horowitz, L., Isaksen, I. S. A., Josse, B., Lawrence, M., Krol, M., Lamarque, J. F., Montanaro, V., Müller, J. F., Peuch, V. H., Pitari, G., Pyle, J., Rast, S., Rodriguez, J., Sanderson, M., Savage, N. H., Shindell, D., Strahan, S., Szopa, S., Sudo, K., Van Dingenen, R., Wild, O., and Zeng, G. (2006). The Global Atmospheric Environment for the Next Generation. *Environmental Science & Technology*, 40(11):3586–3594.

Derwent, R. and Davies, T. (1994). Modelling the impact of NOx or hydrocarbon control on photochemical ozone in Europe. *Atmospheric Environment*, 28(12):2039–2052.

Derwent, R., Stevenson, D., Doherty, R., Collins, W., and Sanderson, M. (2008). How is surface ozone in Europe linked to Asian and North American NOx emissions? *Atmospheric Environment*, 42(32):7412–7422.

Dlugokencky, E. J., Houweling, S., Bruhwiler, L., Masarie, K. A., Lang, P. M., Miller, J. B., and Tans, P. P. (2003). Atmospheric methane levels off: Temporary pause or a new steady-state? *Geophysical Research Letters*, 30(19):1992.

Dlugokencky, E. J., Myers, R. C., Lang, P. M., Masarie, K. A., Crotwell, A. M., Thoning, K. W., Hall, B. D., Elkins, J. W., and Steele, L. P. (2005). Conversion of NOAA atmospheric dry air CH4 mole fractions to a gravimetrically prepared standard scale. *Journal of Geophysical Research: Atmospheres*, 110:D18306.

Dlugokencky, E. J., Nisbet, E. G., Fisher, R., and Lowry, D. (2011). Global atmospheric methane: budget, changes and dangers. *Philosophical Transactions of the Royal Society A: Mathematical, Physical and Engineering Sciences*, 369(1943):2058–2072.

Duncan, B. N., Logan, J. A., Bey, I., Megretskaia, I. A., Yantosca, R. M., Novelli, P. C., Jones, N. B., and Rinsland, C. P. (2007). Global budget of CO, 1988–1997: Source estimates and validation with a global model. *Journal of Geophysical Research: Atmospheres*, 112:D22301.

Duncan, B. N., Yoshida, Y., de Foy, B., Lamsal, L. N., Streets, D. G., Lu, Z., Pickering, K. E., and Krotkov, N. A. (2013). The observed response of Ozone Monitoring Instrument (OMI) NO2 columns to NOx emission controls on power plants in the United States: 2005–2011. *Atmospheric Environment*, 81:102–111.

Dutton, S. J., Rajagopalan, B., Vedal, S., and Hannigan, M. P. (2010). Temporal patterns in daily measurements of inorganic and organic speciated PM2.5 in Denver. *Atmospheric Environment*, 44(7):987–998.

Edner, H., Ragnarson, P., Spännare, S., and Svanberg, S. (1993). Differential optical absorption spectroscopy (DOAS) system for urban atmospheric pollution monitoring. *Applied Optics*, 32(3):327–333.

Ellis, E. C., Klein Goldewijk, K., Siebert, S., Lightman, D., and Ramankutty, N. (2010). Anthropogenic transformation of the biomes, 1700 to 2000. *Global Ecology and Biogeography*, 19(5):589–606.

Ellis, E. C. and Ramankutty, N. (2008). Putting people in the map: anthropogenic biomes of the world. *Frontiers in Ecology and the Environment*, 6(8):439–447.

Etheridge, D. M., Steele, L. P., Francey, R. J., and Langenfelds, R. L. (1998). Atmospheric methane between 1000 A.D. and present: Evidence of anthropogenic emissions and climatic variability. *Journal of Geophysical Research: Atmospheres*, 103(D13):15979–15993.

European Environment Agency (2002). Directive 2002/3/EC of the European Parliament and of the Council of 12 February 2002 relating to ozone in ambient air. *Official Journal of the European Communities*, L067:0014–0030.

European Topic Centre on Air Pollution and Climate Change Mitigation (2015). AirBase – the European air quality database. available at: http://www.eea.europa.eu/data-and-maps/data/ds_resolveuid/3c756b2021754f6bba40447397d67fdf (last updated: 15 August 2015).

Farman, J. C., Gardiner, B. G., and Shanklin, J. D. (1985). Large losses of total ozone in Antarctica reveal seasonal ClOx/NOx interaction. *Nature*, 315(6016):207–210.

Farquhar, G., Schulze, E., and Kuppers, M. (1980). Responses to Humidity by Stomata of Nicotiana glauca L. And Corylus avellana L. Are Consistent With the Optimization of Carbon Dioxide Uptake With Respect to Water Loss. *Australian Journal of Plant Physiology*, 7(3):315–327.

Finkelstein, P. L., Ellestad, T. G., Clarke, J. F., Meyers, T. P., Schwede, D. B., Hebert, E. O., and Neal, J. A. (2000). Ozone and sulfur dioxide dry deposition to forests: Observations and model evaluation. *Journal of Geophysical Research: Atmospheres*, 105(D12):15365–15377.

Fiore, A., Oberman, J., Lin, M., Zhang, L., Clifton, O., Jacob, D., Naik, V., Horowitz, L., Pinto, J., and Milly, G. (2014). Estimating North American background ozone in U.S. surface air with two independent global models: Variability, uncertainties, and recommendations. *Atmospheric Environment*, 96:284–300.

Fiore, A. M., Dentener, F. J., Wild, O., Cuvelier, C., Schultz, M. G., Hess, P., Textor, C., Schulz, M., Doherty, R. M., Horowitz, L. W., MacKenzie, I. A., Sanderson, M. G., Shindell, D. T., Stevenson, D. S., Szopa, S., Van Dingenen, R., Zeng, G., Atherton, C., Bergmann, D., Bey, I., Carmichael, G., Collins, W. J., Duncan, B. N., Faluvegi, G., Folberth, G., Gauss, M., Gong, S., Hauglustaine, D., Holloway, T., Isaksen, I. S. A., Jacob, D. J., Jonson, J. E., Kaminski, J. W., Keating, T. J., Lupu, A., Marmer, E., Montanaro, V., Park, R. J., Pitari, G., Pringle, K. J., Pyle, J. A., Schroeder, S., Vivanco, M. G., Wind, P., Wojcik, G., Wu, S., and Zuber, A. (2009). Multimodel estimates of intercontinental source-receptor relationships for ozone pollution. *Journal of Geophysical Research: Atmospheres*, 114:D04301.

Fischer, E. V., Jacob, D. J., Millet, D. B., Yantosca, R. M., and Mao, J. (2012). The role of the ocean in the global atmospheric budget of acetone. *Geophysical Research Letters*, 39:L01807.

Fischer, E. V., Jacob, D. J., Yantosca, R. M., Sulprizio, M. P., Millet, D. B., Mao, J., Paulot, F., Singh, H. B., Roiger, A., Ries, L., Talbot, R., Dzepina, K., and Pandey Deolal, S. (2014). Atmospheric peroxyacetyl nitrate (PAN): a global budget and source attribution. *Atmospheric Chemistry and Physics*, 14(5):2679–2698.

Fisher, J. A., Jacob, D. J., Travis, K. R., Kim, P. S., Marais, E. A., Chan Miller, C., Yu, K., Zhu, L., Yantosca, R. M., Sulprizio, M. P., Mao, J., Wennberg, P. O., Crounse, J. D., Teng, A. P., Nguyen, T. B., St. Clair, J. M., Cohen, R. C., Romer, P., Nault, B. A., Wooldridge, P. J., Jimenez, J. L., Campuzano-Jost, P., Day, D. A., Hu, W., Shepson, P. B., Xiong, F., Blake, D. R., Goldstein, A. H., Misztal, P. K., Hanisco, T. F., Wolfe, G. M., Ryerson, T. B., Wisthaler, A., and Mikoviny, T. (2016). Organic nitrate chemistry and its implications for nitrogen budgets in an isoprene- and monoterpene-rich atmosphere: constraints from aircraft (SEA4RS) and ground-based (SOAS) observations in the Southeast US. *Atmospheric Chemistry and Physics*, 16(9):5969–5991.

Flores, E., Idrees, F., Moussay, P., Viallon, J., Wielgosz, R., Fernández, T., Ramírez, S., Rojo, A., Shinji, U., Waldén, J., Sega, M., Sang-Hyub, O., Macé, T., Couret, C., Qiao, H., Smeulders, D., Guenther, F. R., Thorn III, W. J., Tshilongo, J., Ntsasa, N. G., Štovcík, V., Valková, M., Konopelko, L., Gromova, E., Nieuwenkamp, G., Wessel, R. M., Milton, M., Harling, A., Vargha, G., Tuma, D., Kohl, A., and Schulz, G. (2012). Final report on international comparison CCQM-K74: Nitrogen dioxide, 10 µmol/mol. *Metrologia*, 49(1A):08005.

Fontijn, A., Sabadell, A. J., and Ronco, R. J. (1970). Homogeneous chemiluminescent measurement of nitric oxide with ozone. Implications for continuous selective monitoring of gaseous air pollutants. *Analytical Chemistry*, 42(6):575–579.

Forster, P., Ramaswamy, V., Artaxo, P., Berntsen, T., Betts, R., Fahey, D. W., Haywood, J., Lean, J., Lowe, D. C., Myhre, G., Nganga, J., Prinn, R., Raga, G., Schulz, M., and Dorland, R. V. (2007). Changes in Atmospheric Constituents and in Radiative Forcing. In Solomon, S., Qin, D., Manning, M., Chen, Z., Marquis, M., Averyt, K., Tignor, M., and Miller, H., editors, *Climate Change 2007: The Physical Science Basis. Contribution of Working Group I to the Fourth Assessment Report of the Intergovernmental Panel on Climate Change*, pages 131–215. Cambridge University Press, Cambridge, U.K.

Fowler, D., Flechard, C., Cape, J. N., Storeton-West, R. L., and Coyle, M. (2001). Measurements of Ozone Deposition to Vegetation Quantifying the Flux, the Stomatal and Non-Stomatal Components. *Water, Air, and Soil Pollution*, 130:63–74.

Fowler, D., Pilegaard, K., Sutton, M., Ambus, P., Raivonen, M., Duyzer, J., Simpson, D., Fagerli, H., Fuzzi, S., Schjoerring, J., Granier, C., Neftel, A., Isaksen, I., Laj, P., Maione, M., Monks, P., Burkhardt, J., Daemmgen, U., Neirynck, J., Personne, E., Wichink-Kruit, R., Butterbach-Bahl, K., Flechard, C., Tuovinen, J., Coyle, M., Gerosa, G., Loubet, B., Altimir, N., Gruenhage, L., Ammann, C., Cieslik, S., Paoletti, E., Mikkelsen, T., Ro-Poulsen, H., Cellier, P., Cape, J., Horváth, L., Loreto, F., Niinemets, Ü., Palmer, P., Rinne, J., Misztal, P., Nemitz, E., Nilsson, D., Pryor, S., Gallagher, M., Vesala, T., Skiba, U., Brüggemann, N., Zechmeister-Boltenstern, S., Williams, J., O'Dowd, C., Facchini, M., de Leeuw, G., Flossman, A., Chaumerliac, N., and Erisman, J. (2009). Atmospheric composition change: Ecosystems–Atmosphere interactions. *Atmospheric Environment*, 43(33):5193–5267.

Fu, D., Bowman, K. W., Worden, H. M., Natraj, V., Worden, J. R., Yu, S., Veefkind, P., Aben, I., Landgraf, J., Strow, L., and Han, Y. (2016). High-resolution tropospheric carbon monoxide profiles retrieved from CrIS and TROPOMI. *Atmospheric Measurement Techniques*, 9(6):2567–2579.

Fuhrer, J. (2009). Ozone risk for crops and pastures in present and future climates. *Naturwissenschaften*, 96(2):173–194.

Fujita, E. M., Campbell, D. E., Zielinska, B., Chow, J. C., Lindhjem, C. E., DenBleyker, A., Bishop, G. A., Schuchmann, B. G., Stedman, D. H., and Lawson, D. R. (2012). Comparison of the MOVES2010a, MOBILE6.2, and EMFAC2007 mobile source emission models with on-road traffic tunnel and remote sensing measurements. *Journal of the Air & Waste Management Association*, 62(10):1134–1149.

Galbally, I. and Schultz, M. (2013). Guidelines for Continuous Measurements of Ozone in the Troposphere. Technical Report GAW Report No. 209, World Meteorological Organization.

Gauderman, W. J., Gilliland, G. F., Vora, H., Avol, E., Stram, D., McConnell, R., Thomas, D., Lurmann, F., Margolis, H. G., Rappaport, E. B., Berhane, K., and Peters, J. M. (2002). Association between air pollution and lung function growth in southern California children: results from a second cohort. *American Journal of Respiratory and Critical Care Medicine*, 166(1):76–84.

Gauderman, W. J., McConnell, R., Gilliland, F., London, S., Thomas, D., Avol, E., Vora, H., Berhane, K., Rappaport, E. B., Lurmann, F., Margolis, H. G., and Peters, J. (2000). Association between air pollution and lung function growth in southern California children. *American Journal of Respiratory and Critical Care Medicine*, 162(4):1383–1390.

Gerbig, C., Schmitgen, S., Kley, D., Volz-Thomas, A., Dewey, K., and Haaks, D. (1999). An improved fast-response vacuum-UV resonance fluorescence CO instrument. *Journal of Geophysical Research: Atmospheres*, 104(D1):1699–1704.

Giglio, L., Randerson, J. T., van der Werf, G. R., Kasibhatla, P. S., Collatz, G. J., Morton, D. C., and DeFries, R. S. (2010). Assessing variability and long-term trends in burned area by merging multiple satellite fire products. *Biogeosciences*, 7(3):1171–1186.

Goldstein, A. H. and Galbally, I. E. (2007). Known and Unexplored Organic Constituents in the Earth's Atmosphere. *Environmental Science & Technology*, 41(5):1514–1521.

Goyal, S. K. (2002). Comparison of Two Manual Methods of Nitrogen Dioxide Determination in Ambient Air. *Environmental Monitoring and Assessment*, 89(3):305–314.

Granier, C., Bessagnet, B., Bond, T., D'Angiola, A., Denier van der Gon, H., Frost, G. J., Heil, A., Kaiser, J. W., Kinne, S., Klimont, Z., Kloster, S., Lamarque, J.-F., Liousse, C., Masui, T., Meleux, F., Mieville, A., Ohara, T., Raut, J.-C., Riahi, K., Schultz, M. G., Smith, S. J., Thompson, A., van Aardenne, J., van der Werf, G. R., and van Vuuren, D. P. (2011). Evolution of anthropogenic and biomass burning emissions of air pollutants at global and regional scales during the 1980–2010 period. *Climatic Change*, 109(1-2):163–190.

Grennfelt, P. and Hov, O. (2005). Regional air pollution at a turning point. *Ambio*, 34(1):2–10.

Gryparis, A., Forsberg, B., Katsouyanni, K., Analitis, A., Touloumi, G., Schwartz, J., Samoli, E., Medina, S., Anderson, H. R., Niciu, E. M., Wichmann, H.-E., Kriz, B., Kosnik, M., Skorkovsky, J., Vonk, J. M., and Dörtbudak, Z. (2004). Acute effects of ozone on mortality from the "air pollution and health: a European approach" project. *American Journal of Respiratory and Critical Care Medicine*, 170(10):1080–1087.

Guenther, A., Hewitt, C. N., Erickson, D., Fall, R., Geron, C., Graedel, T., Harley, P., Klinger, L., Lerdau, M., Mckay, W. A., Pierce, T., Scholes, B., Steinbrecher, R., Tallamraju, R., Taylor, J., and Zimmerman, P. (1995). A global model of natural volatile organic compound emissions. *Journal of Geophysical Research: Atmospheres*, 100(D5):8873.

Guenther, A., Karl, T., Harley, P., Wiedinmyer, C., Palmer, P. I., and Geron, C. (2006). Estimates of global terrestrial isoprene emissions using MEGAN (Model of Emissions of Gases and Aerosols from Nature). *Atmospheric Chemistry and Physics*, 6(11):3181–3210.

Guenther, A. B., Jiang, X., Heald, C. L., Sakulyanontvittaya, T., Duhl, T., Emmons, L. K., and Wang, X. (2012). The Model of Emissions of Gases and Aerosols from Nature version 2.1 (MEGAN2.1): an extended and updated framework for modeling biogenic emissions. *Geoscientific Model Development*, 5(6):1471–1492.

Hardacre, C., Wild, O., and Emberson, L. (2015). An evaluation of ozone dry deposition in global scale chemistry climate models. *Atmospheric Chemistry and Physics*, 15(11):6419–6436.

Harden, J. W., Koven, C. D., Ping, C.-L., Hugelius, G., David McGuire, A., Camill, P., Jorgenson, T., Kuhry, P., Michaelson, G. J., O'Donnell, J. A., Schuur, E. A. G., Tarnocai, C., Johnson, K., and Grosse, G. (2012). Field information links permafrost carbon to physical vulnerabilities of thawing. *Geophysical Research Letters*, 39:L15704.

Harris, F. (1978). On the use of windows for harmonic analysis with the discrete Fourier transform. In *Proceedings of the IEEE*, volume 66, pages 51–83. Institute of Electrical and Electronics Engineers (IEEE).

Hegglin, M. I., Brunner, D., Wernli, H., Schwierz, C., Martius, O., Hoor, P., Fischer, H., Parchatka, U., Spelten, N., Schiller, C., Krebsbach, M., Weers, U., Staehelin, J., and Peter, T. (2004). Tracing troposphere-to-stratosphere transport above a mid-latitude deep convective system. *Atmospheric Chemistry and Physics*, 4:741–756.

Hegglin, M. I. and Shepherd, T. G. (2009). Large climate-induced changes in ultraviolet index and stratosphere-to-troposphere ozone flux. *Nature Geoscience*, 2(10):687–691.

Hess, P. G. and Zbinden, R. (2013). Stratospheric impact on tropospheric ozone variability and trends: 1990–2009. *Atmospheric Chemistry and Physics*, 13(2):649–674.

Hocke, K. (1998). Phase estimation with the Lomb-Scargle periodogram method. *Annales Geophysicae: Atmospheres, Hydrospheres and Space Sciences*, 16(3):356–358.

Hoffmann, T., Odum, J. R., Bowman, F., Collins, D., Klockow, D., Flagan, R. C., and Seinfeld, J. H. (1997). Formation of Organic Aerosols from the Oxidation of Biogenic Hydrocarbons. *Journal of Atmospheric Chemistry*, 26(2):189–222.

Hogrefe, C., Isukapalli, S. S., Tang, X., Georgopoulos, P. G., He, S., Zalewsky, E. E., Hao, W., Ku, J.-Y., Key, T., and Sistla, G. (2011). Impact of Biogenic Emission Uncertainties on the Simulated Response of Ozone and Fine Particulate Matter to Anthropogenic Emission Reductions. *Journal of the Air & Waste Management Association*, 61(1):92–108.

Holloway, J. S., Jakoubek, R. O., Parrish, D. D., Gerbig, C., Volz-Thomas, A., Schmitgen, S., Fried, A., Wert, B., Henry, B., and Drummond, J. R. (2000). Airborne intercomparison of vacuum ultraviolet fluorescence and tunable diode laser absorption measurements of tropospheric carbon monoxide. *Journal of Geophysical Research: Atmospheres*, 105(D19):24251–24261.

Holmes, C. D., Prather, M. J., and Vinken, G. C. M. (2014). The climate impact of ship NOx emissions: an improved estimate accounting for plume chemistry. *Atmospheric Chemistry and Physics*, 14(13):6801–6812.

Holton, J. R., Haynes, P. H., McIntyre, M. E., Douglass, A. R., Rood, R. B., and Pfister, L. (1995). Stratosphere-troposphere exchange. *Reviews of Geophysics*, 33(4):403.

Holtslag, A. A. M. and Boville, B. A. (1993). Local versus nonlocal boundary layer diffusion in a global climate model. *Journal of Climate*, 6(10):1825–1842.

Holzke, C., Dindorf, T., Kesselmeier, J., Kuhn, U., and Koppmann, R. (2006). Terpene emissions from European beech (shape Fagus sylvatica~L): Pattern and Emission Behaviour Over two Vegetation Periods. *Journal of Atmospheric Chemistry*, 55(1):81–102.

Hong, C., Zhang, Q., He, K., Guan, D., Li, M., Liu, F., and Zheng, B. (2016). Variations of China's emission estimates response to uncertainties in energy statistics. *Atmospheric Chemistry and Physics Discussions*.

Horne, J. H. and Baliunas, S. L. (1986). A prescription for period analysis of unevenly sampled time-series. *Astrophysical Journal*, 302(2):757–763.

Houweling, S., Kaminski, T., Dentener, F., Lelieveld, J., and Heimann, M. (1999). Inverse modeling of methane sources and sinks using the adjoint of a global transport model. *Journal of Geophysical Research: Atmospheres*, 104(D21):26137–26160.

Hsu, J. and Prather, M. J. (2009). Stratospheric variability and tropospheric ozone. *Journal of Geophysical Research: Atmospheres*, 114:D06102.

Hu, L., Millet, D. B., Baasandorj, M., Griffis, T. J., Travis, K. R., Tessum, C. W., Marshall, J. D., Reinhart, W. F., Mikoviny, T., Müller, M., Wisthaler, A., Graus, M., Warneke, C., and de Gouw, J. (2015). Emissions of C6-C8 aromatic compounds in the United States: Constraints from tall tower and aircraft measurements. *Journal of Geophysical Research: Atmospheres*, 120(2):826–842.

Huang, M., Carmichael, G. R., Chai, T., Pierce, R. B., Oltmans, S. J., Jaffe, D. A., Bowman, K. W., Kaduwela, A., Cai, C., Spak, S. N., Weinheimer, A. J., Huey, L. G., and Diskin, G. S. (2013). Impacts of transported background pollutants on summertime western US air quality: model evaluation, sensitivity analysis and data assimilation. *Atmospheric Chemistry and Physics*, 13(1):359–391.

Hudman, R. C., Moore, N. E., Mebust, A. K., Martin, R. V., Russell, A. R., Valin, L. C., and Cohen, R. C. (2012). Steps towards a mechanistic model of global soil nitric oxide emissions: implementation and space based-constraints. *Atmospheric Chemistry and Physics*, 12(16):7779–7795.

IEA (2010). *CO2 Emissions from Fuel Combustion 2010*. CO2 Emissions from Fuel Combustion. OECD Publishing.

Ito, A., Sillman, S., and Penner, J. E. (2009). Global chemical transport model study of ozone response to changes in chemical kinetics and biogenic volatile organic compounds emissions due to increasing temperatures: Sensitivities to isoprene nitrate chemistry and grid resolution. *Journal of Geophysical Research: Atmospheres*, 114:D09301.

Jacob, D. J., Fan, S.-M., Wofsy, S. C., Spiro, P. A., Bakwin, P. S., Ritter, J. A., Browell, E. V., Gregory, G. L., Fitzjarrald, D. R., and Moore, K. E. (1992). Deposition of ozone to tundra. *Journal of Geophysical Research: Atmospheres*, 97(D15):16473.

Jacob, D. J. and Wofsy, S. C. (1988). Photochemistry of biogenic emissions over the Amazon forest. *Journal of Geophysical Research: Atmospheres*, 93(D2):1477.

Jacob, D. J. and Wofsy, S. C. (1990). Budgets of reactive nitrogen, hydrocarbons, and ozone over the Amazon forest during the wet season. *Journal of Geophysical Research: Atmospheres*, 95(D10):16737.

Janssens-Maenhout, G., Petrescu, A. M. R., Muntean, M., and Blujdea, V. (2010). Verifying Greenhouse Gas Emissions. In *Greenhouse Gas Measurement and Management*, volume 1, chapter Methods, pages 132–133. National Academies Press, Washington, D.C.

Jarvis, P. G. (1976). The Interpretation of the Variations in Leaf Water Potential and Stomatal Conductance Found in Canopies in the Field. *Philosophical Transactions of the Royal Society B: Biological Sciences*, 273(927):593–610.

Jerrett, M., Burnett, R. T., Pope, C. A. I., Ito, K., Thurston, G., Krewski, D., Shi, Y., Calle, E., and Thun, M. (2009). Long-Term Ozone Exposure and Mortality. *New England Journal of Medicine*, 360(11):1085–1095.

Jonson, J., Simpson, D., Fagerli, H., and Solberg, S. (2006). Can we explain the trends in European ozone levels? *Atmospheric Chemistry and Physics*, 6(1):51–66.

Kaiser, J. W., Heil, A., Andreae, M. O., Benedetti, A., Chubarova, N., Jones, L., Morcrette, J.-J., Razinger, M., Schultz, M. G., Suttie, M., and van der Werf, G. R. (2012). Biomass burning emissions estimated with a global fire assimilation system based on observed fire radiative power. *Biogeosciences*, 9(1):527–554.

Karl, T., Guenther, A., Yokelson, R. J., Greenberg, J., Potosnak, M., Blake, D. R., and Artaxo, P. (2007). The tropical forest and fire emissions experiment: Emission, chemistry, and transport of biogenic volatile organic compounds in the lower atmosphere over Amazonia. *Journal of Geophysical Research: Atmospheres*, 112:D18302.

Karl, T., Harley, P., Emmons, L., Thornton, B., Guenther, A., Basu, C., Turnipseed, A., and Jardine, K. (2010). Efficient Atmospheric Cleansing of Oxidized Organic Trace Gases by Vegetation. *Science*, 330(6005).

Katragkou, E., Zanis, P., Tsikerdekis, A., Kapsomenakis, J., Melas, D., Eskes, H., Flemming, J., Huijnen, V., Inness, A., Schultz, M. G., Stein, O., and Zerefos, C. S. (2015). Evaluation of near-surface ozone over Europe from the MACC reanalysis. *Geoscientific Model Development*, 8(7):2299–2314.

Keller, C. A., Long, M. S., Yantosca, R. M., Da Silva, A. M., Pawson, S., and Jacob, D. J. (2014). HEMCO v1.0: a versatile, ESMF-compliant component for calculating emissions in atmospheric models. *Geoscientific Model Development*, 7(4):1409–1417.

Keller, M. (2014). *Mitigating Model Error in CO emission estimation*. PhD thesis, University of Toronto.

Kim, H. C., Lee, P., Ngan, F., Tang, Y., Yoo, H. L., and Pan, L. (2015). Evaluation of modeled surface ozone biases as a function of cloud cover fraction. *Geoscientific Model Development*, 8(9):2959–2965.

King, G. M. (1999). Characteristics and significance of atmospheric carbon monoxide consumption by soils. *Chemosphere - Global Change Science*, 1(1):53–63.

Kleindienst, T. E., Hudgens, E. E., Smith, D. F., McElroy, F. F., and Bufalini, J. J. (1993). Comparison of chemiluminescence and ultraviolet ozone monitor responses in the presence of humidity and photochemical pollutants. *Air & Waste: Journal of the Air & Waste Management Association*, 43(2):213–22.

Kleinman, L. I. (2005). The dependence of tropospheric ozone production rate on ozone precursors. *Atmospheric Environment*, 39(3):575–586.

Kopacz, M., Jacob, D. J., Fisher, J. A., Logan, J. A., Zhang, L., Megretskaia, I. A., Yantosca, R. M., Singh, K., Henze, D. K., Burrows, J. P., Buchwitz, M., Khlystova, I., McMillan, W. W., Gille, J. C., Edwards, D. P., Eldering, A., Thouret, V., and Nedelec, P. (2010). Global estimates of CO sources with high resolution by adjoint inversion of multiple satellite datasets (MOPITT, AIRS, SCIAMACHY, TES). *Atmospheric Chemistry and Physics*, 10(3):855–876.

Krewski, D., Jerrett, M., Burnett, R. T., Ma, R., Hughes, E., Shi, Y., Turner, M. C., Pope, C. A., Thurston, G., Calle, E. E., Thun, M. J., Beckerman, B., DeLuca, P., Finkelstein, N., Ito, K., Moore, D. K., Newbold, K. B., Ramsay, T., Ross, Z., Shin, H., and Tempalski, B. (2009). Extended follow-up and spatial analysis of the American Cancer Society study linking particulate air pollution and mortality. *Research Report (Health Effects Institute)*, 140:5–114.

Kurpius, M. R. and Goldstein, A. H. (2003). Gas-phase chemistry dominates O3 loss to a forest, implying a source of aerosols and hydroxyl radicals to the atmosphere. *Geophysical Research Letters*, 30(7):1371.

Lamarque, J.-F., Bond, T. C., Eyring, V., Granier, C., Heil, A., Klimont, Z., Lee, D., Liousse, C., Mieville, A., Owen, B., Schultz, M. G., Shindell, D., Smith, S. J., Stehfest, E., Van Aardenne, J., Cooper, O. R., Kainuma, M., Mahowald, N., McConnell, J. R., Naik, V., Riahi, K., and van Vuuren, D. P. (2010). Historical (1850–2000) gridded anthropogenic and biomass burning emissions of reactive gases and aerosols: methodology and application. *Atmospheric Chemistry and Physics*, 10(15):7017–7039.

Lamarque, J.-F., Emmons, L. K., Hess, P. G., Kinnison, D. E., Tilmes, S., Vitt, F., Heald, C. L., Holland, E. A., Lauritzen, P. H., Neu, J., Orlando, J. J., Rasch, P. J., and Tyndall, G. K. (2012). CAM-chem: description and evaluation of interactive atmospheric chemistry in the Community Earth System Model. *Geoscientific Model Development*, 5(2):369–411.

Lamarque, J.-F., Hess, P., Emmons, L., Buja, L., Washington, W., and Granier, C. (2005). Tropospheric ozone evolution between 1890 and 1990. *Journal of Geophysical Research: Atmospheres*, 110:D08304.

Lamarque, J.-F., Shindell, D. T., Josse, B., Young, P. J., Cionni, I., Eyring, V., Bergmann, D., Cameron-Smith, P., Collins, W. J., Doherty, R., Dalsoren, S., Faluvegi, G., Folberth, G., Ghan, S. J., Horowitz, L. W., Lee, Y. H., MacKenzie, I. A., Nagashima, T., Naik, V., Plummer, D., Righi, M., Rumbold, S. T., Schulz, M., Skeie, R. B., Stevenson, D. S., Strode, S., Sudo, K., Szopa, S., Voulgarakis, A., and Zeng, G. (2013). The Atmospheric Chemistry and Climate Model Intercomparison Project (ACCMIP): overview and description of models, simulations and climate diagnostics. *Geoscientific Model Development*, 6(1):179–206.

Lambert, G. and Schmidt, S. (1993). Reevaluation of the oceanic flux of methane: Uncertainties and long term variations. *Chemosphere*, 26(1-4):579–589.

Lamsal, L. N., Duncan, B. N., Yoshida, Y., Krotkov, N. A., Pickering, K. E., Streets, D. G., and Lu, Z. (2015). U.S. NO2 trends (2005–2013): EPA Air Quality System (AQS) data versus improved observations from the Ozone Monitoring Instrument (OMI). *Atmospheric Environment*, 110:130–143.

Lamsal, L. N., Martin, R. V., Padmanabhan, A., van Donkelaar, A., Zhang, Q., Sioris, C. E., Chance, K., Kurosu, T. P., and Newchurch, M. J. (2011). Application of satellite observations for timely updates to global anthropogenic NOx emission inventories. *Geophysical Research Letters*, 38(5).

Lamsal, L. N., Martin, R. V., van Donkelaar, A., Celarier, E. A., Bucsela, E. J., Boersma, K. F., Dirksen, R., Luo, C., and Wang, Y. (2010). Indirect validation of tropospheric nitrogen dioxide retrieved from the OMI satellite instrument: Insight into the seasonal variation of nitrogen oxides at northern midlatitudes. *Journal of Geophysical Research: Atmospheres*, 115:D05302.

Lamsal, L. N., Martin, R. V., van Donkelaar, A., Steinbacher, M., Celarier, E. A., Bucsela, E., Dunlea, E. J., and Pinto, J. P. (2008). Ground-level nitrogen dioxide concentrations inferred from the satellite-borne Ozone Monitoring Instrument. *Journal of Geophysical Research: Atmospheres*, 113:D16308.

Lee, C., Martin, R. V., van Donkelaar, A., Hanlim Lee, I., Dickerson, R. R., Hains, J. C., Krotkov, N., Richter, A., Konstantine Vinnikov, S., Schwab, J. J., Martin, R. V., van Donkelaar, A., Lee, H., Dickerson, R. R., Hains, J. C., Krotkov, N., Richter, A., and Vinnikov, K. (2011). SO2 emissions and lifetimes: Estimates from inverse modeling using in situ and global, space-based (SCIAMACHY and OMI) observations. *Journal of Geophysical Research: Atmospheres*, 116:D06304.

Lelieveld, J., Crutzen, P. J., and Dentener, F. J. (1998). Changing concentration, lifetime and climate forcing of atmospheric methane. *Tellus B*, 50(2):128–150.

Lelieveld, J., Peters, W., Dentener, F. J., and Krol, M. C. (2002). Stability of tropospheric hydroxyl chemistry. *Journal of Geophysical Research: Atmospheres*, 107(D23):ACH 17–1–ACH 17–11.

Levy, H. (1971). Normal atmosphere: large radical and formaldehyde concentrations predicted. *Science*, 173(3992):141–143.

Li, M., Zhang, Q., Kurokawa, J., Woo, J.-H., He, K. B., Lu, Z., Ohara, T., Song, Y., Streets, D. G., Carmichael, G. R., Cheng, Y. F., Hong, C. P., Huo, H., Jiang, X. J., Kang, S. C., Liu, F., Su, H., and Zheng, B. (2015). MIX: a mosaic Asian anthropogenic emission inventory for the MICS-Asia and the HTAP projects. *Atmospheric Chemistry and Physics Discussions*, 15(23):34813–34869.

Li, X., Rohrer, F., Hofzumahaus, A., Brauers, T., Häseler, R., Bohn, B., Broch, S., Fuchs, H., Gomm, S., Holland, F., Jäger, J., Kaiser, J., Keutsch, F. N., Lohse, I., Lu, K., Tillmann, R., Wegener, R., Wolfe, G. M., Mentel, T. F., Kiendler-Scharr, A., and Wahner, A. (2014). Missing gas-phase source of HONO inferred from Zeppelin measurements in the troposphere. *Science*, 344(6181):292–296.

Liang, J. and Jacobson, M. Z. (2000). Effects of subgrid segregation on ozone production efficiency in a chemical model. *Atmospheric Environment*, 34(18):2975–2982.

Lim, S. S., Vos, T., Flaxman, A. D., Danaei, G., Shibuya, K., Adair-Rohani, H., AlMazroa, M. A., Amann, M., Anderson, H. R., Andrews, K. G., Aryee, M., Atkinson, C., Bacchus, L. J., Bahalim, A. N., Balakrishnan, K., Balmes, J., Barker-Collo, S., Baxter, A., Bell, M. L., Blore, J. D., Blyth, F., Bonner, C., Borges, G., Bourne, R., Boussinesq, M., Brauer, M., Brooks, P., Bruce, N. G., Brunekreef, B., Bryan-Hancock, C., Bucello, C., Buchbinder, R., Bull, F., Burnett, R. T., Byers, T. E., Calabria, B., Carapetis, J., Carnahan, E., Chafe, Z., Charlson, F., Chen, H., Chen, J. S., Cheng, A. T.-A., Child, J. C., Cohen, A., Colson, K. E., Cowie, B. C., Darby, S., Darling, S., Davis, A., Degenhardt, L., Dentener, F., Des Jarlais, D. C., Devries, K., Dherani, M., Ding, E. L., Dorsey, E. R., Driscoll, T., Edmond, K., Ali, S. E., Engell, R. E., Erwin, P. J., Fahimi, S., Falder, G., Farzadfar, F., Ferrari, A., Finucane, M. M., Flaxman, S., Fowkes, F. G. R., Freedman, G., Freeman, M. K., Gakidou, E., Ghosh, S., Giovannucci, E., Gmel, G., Graham, K., Grainger, R., Grant, B., Gunnell, D., Gutierrez, H. R., Hall, W., Hoek, H. W., Hogan, A., Hosgood, H. D., Hoy, D., Hu, H., Hubbell, B. J., Hutchings, S. J., Ibeanusi, S. E., Jacklyn, G. L., Jasrasaria, R., Jonas, J. B., Kan, H., Kanis, J. A., Kassebaum, N., Kawakami, N., Khang, Y.-H., Khatibzadeh, S., Khoo, J.-P., Kok, C., Laden, F., Lalloo, R., Lan, Q., Lathlean, T., Leasher, J. L., Leigh, J., Li, Y., Lin, J. K., Lipshultz, S. E., London, S., Lozano, R., Lu, Y., Mak, J., Malekzadeh, R., Mallinger, L., Marcenes, W., March, L., Marks, R., Martin, R., McGale, P., McGrath, J., Mehta, S., Memish, Z. A., Mensah, G. A., Merriman, T. R., Micha, R., Michaud, C., Mishra, V., Hanafiah, K. M., Mokdad, A. A., Morawska, L., Mozaffarian, D., Murphy, T., Naghavi, M., Neal, B., Nelson, P. K., Nolla, J. M., Norman, R., Olives, C., Omer, S. B., Orchard, J., Osborne, R., Ostro, B., Page, A., Pandey, K. D., Parry, C. D., Passmore, E., Patra, J., Pearce, N., Pelizzari, P. M., Petzold, M., Phillips, M. R., Pope, D., Pope, C. A., Powles, J., Rao, M., Razavi, H., Rehfuess, E. A., Rehm, J. T., Ritz, B., Rivara, F. P., Roberts, T., Robinson, C., Rodriguez-Portales, J. A., Romieu, I., Room, R., Rosenfeld, L. C., Roy,

A., Rushton, L., Salomon, J. A., Sampson, U., Sanchez-Riera, L., Sanman, E., Sapkota, A., Seedat, S., Shi, P., Shield, K., Shivakoti, R., Singh, G. M., Sleet, D. A., Smith, E., Smith, K. R., Stapelberg, N. J., Steenland, K., Stöckl, H., Stovner, L. J., Straif, K., Straney, L., Thurston, G. D., Tran, J. H., Van Dingenen, R., van Donkelaar, A., Veerman, J. L., Vijayakumar, L., Weintraub, R., Weissman, M. M., White, R. A., Whiteford, H., Wiersma, S. T., Wilkinson, J. D., Williams, H. C., Williams, W., Wilson, N., Woolf, A. D., Yip, P., Zielinski, J. M., Lopez, A. D., Murray, C. J., and Ezzati, M. (2012). A comparative risk assessment of burden of disease and injury attributable to 67 risk factors and risk factor clusters in 21 regions, 1990-2010: a systematic analysis for the Global Burden of Disease Study 2010. *Lancet*, 380(9859):2224–2260.

Lin, J.-T. and McElroy, M. B. (2010). Impacts of boundary layer mixing on pollutant vertical profiles in the lower troposphere: Implications to satellite remote sensing. *Atmospheric Environment*, 44(14):1726–1739.

Lin, J.-T., Youn, D., Liang, X., and Wuebbles, D. (2008). Global model simulation of summertime U.S. ozone diurnal cycle and its sensitivity to PBL mixing, spatial resolution, and emissions. *Atmospheric Environment*, 42(36):8470–8483.

Lin, M., Fiore, A. M., Cooper, O. R., Horowitz, L. W., Langford, A. O., Levy, H., Johnson, B. J., Naik, V., Oltmans, S. J., and Senff, C. J. (2012). Springtime high surface ozone events over the western United States: Quantifying the role of stratospheric intrusions. *Journal of Geophysical Research: Atmospheres*, 117(D21):D00V22.

Lin, M., Holloway, T., Oki, T., Streets, D. G., and Richter, A. (2009). Multi-scale model analysis of boundary layer ozone over East Asia. *Atmospheric Chemistry and Physics*, 9(10):3277–3301.

Lin, S.-J., Rood, R. B., Lin, S.-J., and Rood, R. B. (1996). Multidimensional Flux-Form Semi-Lagrangian Transport Schemes. *Monthly Weather Review*, 124(9):2046–2070.

Logan, J. A. (1985). Tropospheric ozone: Seasonal behavior, trends, and anthropogenic influence. *Journal of Geophysical Research: Atmospheres*, 90(D6):10463–10482.

Logan, J. A., Prather, M. J., Wofsy, S. C., and McElroy, M. B. (1981). Tropospheric chemistry: A global perspective. *Journal of Geophysical Research: Oceans*, 86(C8):7210.

Logan, J. A., Staehelin, J., Megretskaia, I. A., Cammas, J.-P., Thouret, V., Claude, H., De Backer, H., Steinbacher, M., Scheel, H.-E., Stübi, R., Fröhlich, M., and Derwent, R. (2012). Changes in ozone over Europe: Analysis of ozone measurements from sondes, regular aircraft (MOZAIC) and alpine surface sites. *Journal of Geophysical Research: Atmospheres*, 117:D09301.

Lomb, N. R. (1976). Least-squares frequency-analysis of unequally spaced data. *Astrophysics and Space Science*, 39(2):447–462.

Louis, J., Tiedtke, M., and Geleyn, J. (1982). A short history of the PBL parameterization at ECMWF. In *Workshop on Planetary Boundary Layer parameterization*, Reading. ECMWF.

Loulergue, L., Schilt, A., Spahni, R., Masson-Delmotte, V., Blunier, T., Lemieux, B., Barnola, J.-M., Raynaud, D., Stocker, T. F., and Chappellaz, J. (2008). Orbital and millennial-scale features of atmospheric CH4 over the past 800,000 years. *Nature*, 453(7193):383–386.

Lovejoy, S. and Schertzer, D. (2013a). Low-Frequency Weather and the Emergence of the Climate. In *Extreme Events and Natural Hazards: The Complexity Perspective*, pages 231–254. American Geophysical Union.

Lovejoy, S. and Schertzer, D. (2013b). *The Weather and Climate: Emergent Laws and Multifractal Cascades*. Cambridge University Press, Cambridge, U.K.

Loveland, T. R., Reed, B. C., Brown, J. F., Ohlen, D. O., Zhu, Z., Yang, L., and Merchant, J. W. (2000). Development of a global land cover characteristics database and IGBP DISCover from 1 km AVHRR data. *International Journal of Remote Sensing*, 21(6-7):1303–1330.

Lu, Z., Streets, D. G., de Foy, B., Lamsal, L. N., Duncan, B. N., and Xing, J. (2015). Emissions of nitrogen oxides from US urban areas: estimation from Ozone Monitoring Instrument retrievals for 2005–2014. *Atmospheric Chemistry and Physics*, 15(18):10367–10383.

Mahajan, A. S., Plane, J. M. C., Oetjen, H., Mendes, L., Saunders, R. W., Saiz-Lopez, A., Jones, C. E., Carpenter, L. J., and McFiggans, G. B. (2010). Measurement and modelling of tropospheric reactive halogen species over the tropical Atlantic Ocean. *Atmospheric Chemistry and Physics*, 10(10):4611–4624.

Mao, J., Jacob, D. J., Evans, M. J., Olson, J. R., Ren, X., Brune, W. H., Clair, J. M. S., Crounse, J. D., Spencer, K. M., Beaver, M. R., Wennberg, P. O., Cubison, M. J., Jimenez, J. L., Fried, A., Weibring, P., Walega, J. G., Hall, S. R., Weinheimer, A. J., Cohen, R. C., Chen, G., Crawford, J. H., McNaughton, C., Clarke, A. D., Jaeglé, L., Fisher, J. A., Yantosca, R. M., Le Sager, P., and Carouge, C. (2010). Chemistry of hydrogen oxide radicals (HOx) in the Arctic troposphere in spring. *Atmospheric Chemistry and Physics*, 10(13):5823–5838.

Mao, J., Paulot, F., Jacob, D. J., Cohen, R. C., Crounse, J. D., Wennberg, P. O., Keller, C. A., Hudman, R. C., Barkley, M. P., and Horowitz, L. W. (2013). Ozone and organic nitrates over the eastern United States: Sensitivity to isoprene chemistry. *Journal of Geophysical Research: Atmospheres*, 118(19):11256–11268.

Mao, J., Ren, X., Zhang, L., Van Duin, D. M., Cohen, R. C., Park, J.-H., Goldstein, A. H., Paulot, F., Beaver, M. R., Crounse, J. D., Wennberg, P. O., DiGangi, J. P., Henry, S. B., Keutsch, F. N., Park, C., Schade, G. W., Wolfe, G. M., Thornton, J. A., and Brune, W. H. (2012). Insights into hydroxyl measurements and atmospheric oxidation in a California forest. *Atmospheric Chemistry and Physics*, 12(17):8009–8020.

Marais, E. A., Jacob, D. J., Jimenez, J. L., Campuzano-Jost, P., Day, D. A., Hu, W., Krechmer, J., Zhu, L., Kim, P. S., Miller, C. C., Fisher, J. A., Travis, K., Yu, K., Hanisco, T. F., Wolfe, G. M., Arkinson, H. L., Pye, H. O. T., Froyd, K. D., Liao, J., and McNeill, V. F. (2016). Aqueous-phase mechanism for secondary organic aerosol formation from isoprene: application to the southeast United States and co-benefit of SO2 emission controls. *Atmospheric Chemistry and Physics*, 16(3):1603–1618.

Marr, L. C. and Harley, R. A. (2002). Spectral analysis of weekday–weekend differences in ambient ozone, nitrogen oxide, and non-methane hydrocarbon time series in California. *Atmospheric Environment*, 36(14):2327–2335.

Matyssek, R., Karnosky, D., Wieser, G., Percy, K., Oksanen, E., Grams, T., Kubiske, M., Hanke, D., and Pretzsch, H. (2010). Advances in understanding ozone impact on forest trees: Messages from novel phytotron and free-air fumigation studies. *Environmental Pollution*, 158(6):1990–2006.

Matyssek, R., Sandermann, H., Wieser, G., Booker, F., Cieslik, S., Musselman, R., and Ernst, D. (2008). The challenge of making ozone risk assessment for forest trees more mechanistic. *Environmental Pollution*, 156(3):567–582.

McLinden, C. A., Olsen, S. C., Hannegan, B., Wild, O., Prather, M. J., and Sundet, J. (2000). Stratospheric ozone in 3-D models: A simple chemistry and the cross-tropopause flux. *Journal of Geophysical Research: Atmospheres*, 105(D11):14653–14665.

Melton, J. R., Wania, R., Hodson, E. L., Poulter, B., Ringeval, B., Spahni, R., Bohn, T., Avis, C. A., Beerling, D. J., Chen, G., Eliseev, A. V., Denisov, S. N., Hopcroft, P. O., Lettenmaier, D. P., Riley, W. J., Singarayer, J. S., Subin, Z. M., Tian, H., Zürcher, S., Brovkin, V., van Bodegom, P. M., Kleinen, T., Yu, Z. C., and Kaplan, J. O. (2013). Present state of global wetland extent and wetland methane modelling: conclusions from a model inter-comparison project (WETCHIMP). *Biogeosciences*, 10(2):753–788.

Miller, R. L., Schmidt, G. A., Nazarenko, L. S., Tausnev, N., Bauer, S. E., DelGenio, A. D., Kelley, M., Lo, K. K., Ruedy, R., Shindell, D. T., Aleinov, I., Bauer, M., Bleck, R., Canuto, V., Chen, Y., Cheng, Y., Clune, T. L., Faluvegi, G., Hansen, J. E., Healy, R. J., Kiang, N. Y., Koch, D., Lacis, A. A., LeGrande, A. N., Lerner, J., Menon, S., Oinas, V., Pérez García-Pando, C., Perlwitz, J. P., Puma, M. J., Rind, D., Romanou, A., Russell, G. L., Sato, M., Sun, S., Tsigaridis, K., Unger, N., Voulgarakis, A., Yao, M.-S., and Zhang, J. (2014). CMIP5 historical simulations (1850-2012) with GISS ModelE2. *Journal of Advances in Modeling Earth Systems*, 6(2):441–477.

Millet, D. B., Jacob, D. J., Boersma, K. F., Fu, T.-M., Kurosu, T. P., Chance, K., Heald, C. L., and Guenther, A. (2008). Spatial distribution of isoprene emissions from North America derived from formaldehyde column measurements by the OMI satellite sensor. *Journal of Geophysical Research: Atmospheres*, 113:D02307.

Mills, G., Buse, A., Gimeno, B., Bermejo, V., Holland, M., Emberson, L., and Pleijel, H. (2007). A synthesis of AOT40-based response functions and critical levels of ozone for agricultural and horticultural crops. *Atmospheric Environment*, 41(12):2630–2643.

Miyazaki, K., Eskes, H. J., and Sudo, K. (2012). Global NOx emission estimates derived from an assimilation of OMI tropospheric NO2 columns. *Atmospheric Chemistry and Physics*, 12(5):2263–2288.

Monks, P. S. (2000). A review of the observations and origins of the spring ozone maximum. *Atmospheric Environment*, 34(21):3545–3561.

Monks, P. S., Salisbury, G., Holland, G., Penkett, S. A., and Ayers, G. P. (2000). A seasonal comparison of ozone photochemistry in the remote marine boundary layer. *Atmospheric Environment*, 34(16):2547–2561.

Müller, G., Artz, R., Baltensperger, U., Carmichael, G., Dlugokencky, E., Penkett, S., Stähelin, J., Webb, A., Hov, Ø., Klausen, J., Sturges, B., Barrie, L., Braathen, G., Jalkanen, L., and Nickovic, S. (2007). WMO Global Atmosphere Watch (GAW) Strategic Plan: 2008–2015. Technical Report GAW Report No. 197, World Meteorological Organization.

Müller, J.-F. and Brasseur, G. (1995). IMAGES: A three-dimensional chemical transport model of the global troposphere. *Journal of Geophysical Research: Atmospheres*, 100(D8):16445.

Murazaki, K. and Hess, P. (2006). How does climate change contribute to surface ozone change over the United States? *Journal of Geophysical Research*, 111:D05301.

Murray, L. T., Jacob, D. J., Logan, J. A., Hudman, R. C., and Koshak, W. J. (2012). Optimized regional and interannual variability of lightning in a global chemical transport model constrained by LIS/OTD satellite data. *Journal of Geophysical Research: Atmospheres*, 117:D20307.

Musial, J. P., Verstraete, M. M., and Gobron, N. (2011). Technical Note: Comparing the effectiveness of recent algorithms to fill and smooth incomplete and noisy time series. *Atmospheric Chemistry and Physics*, 11(15):7905–7923.

Myhre, G., Shindell, D., Bréon, F.-M., Collins, W., Fuglestvedt, J., Huang, J., Koch, D., Lamarque, J.-F., Lee, D., Mendoza, B., Nakajima, T., Robock, A., Stephens, G., Takemura, T., and Zhang, H. (2013). Anthropogenic and Natural Radiative Forcing. In Stocker, T., Qin, D., Plattner, G.-K., Tignor, M., Allen, S., Boschung, J., Nauels, A., Xia, Y., Bex, V., and Midgley, P., editors, *Climate Change 2013: The Physical Science Basis. Contribution of Working Group I to the Fifth Assessment Report of the Intergovernmental Panel on Climate Change*. Cambridge University Press, Cambridge, UK.

Newell, R. E. (1963). Transfer through the tropopause and within the stratosphere. *Quarterly Journal of the Royal Meteorological Society*, 89(380):167–204.

Nguyen, T. B., Crounse, J. D., Teng, A. P., St Clair, J. M., Paulot, F., Wolfe, G. M., and Wennberg, P. O. (2015). Rapid deposition of oxidized biogenic compounds to a temperate forest. *Proceedings of the National Academy of Sciences of the United States of America*, 112(5):E392–401.

Niyogi, D., Alapaty, K., Raman, S., and Chen, F. (2009). Development and Evaluation of a Coupled Photosynthesis-Based Gas Exchange Evapotranspiration Model (GEM) for Mesoscale Weather Forecasting Applications. *Journal of Applied Meteorology and Climatology*, 48(2):349–368.

Novelli, P. C. (1999). CO in the atmosphere: measurement techniques and related issues. *Chemosphere - Global Change Science*, 1(1):115–126.

Novelli, P. C., Connors, V. S., Reichle, H. G., Anderson, B. E., Brenninkmeijer, C. A. M., Brunke, E. G., Doddridge, E. G., Kirchhoff, V. W. J. H., Lam, K. S., Masarie, K. A., Matsuo, T., Parrish, D. D., Scheel, H. E., and Steele, L. P. (1998). An internally consistent set of globally distributed atmospheric carbon monoxide mixing ratios developed using results from an intercomparison of measurements. *Journal of Geophysical Research: Atmospheres*, 103(D15):19285–19293.

Novelli, P. C., Elkins, J. W., and Steele, L. P. (1991). The development and evaluation of a gravimetric reference scale for measurements of atmospheric carbon monoxide. *Journal of Geophysical Research: Atmospheres*, 96(D7):13109.

Novelli, P. C., Steele, L. P., and Tans, P. P. (1992). Mixing ratios of carbon monoxide in the troposphere. *Journal of Geophysical Research: Atmospheres*, 97(D18):20731.

O'Connor, F. M., Johnson, C. E., Morgenstern, O., Abraham, N. L., Braesicke, P., Dalvi, M., Folberth, G. A., Sanderson, M. G., Telford, P. J., Voulgarakis, A., Young, P. J., Zeng, G., Collins, W. J., and Pyle, J. A. (2014). Evaluation of the new UKCA climate-composition model – Part 2: The Troposphere. *Geoscientific Model Development*, 7(1):41–91.

OECD (2012). *OECD Environmental Outlook to 2050*. OECD Publishing.

Olivier, J., Aardenne, J.A, Dentener, F., Ganzeveld, L., and Peters, J. (2005). Recent trends in global greenhouse gas emissions: regional trends and spatial distribution of key sources. *Environmetal Sciences*, 2(2-3):81–99.

Olson, J. S. (1994). Global ecosystem framework-definitions. Technical report, USGS EROS, Sioux Falls, South Dakota, USA.

Oltmans, S. J., Lefohn, A. S., Harris, J. M., Galbally, I., Scheel, H. E., Bodeker, G., Brunke, E., Claude, H., Tarasick, D., Johnson, B. J., Simmonds, P., Shadwick, D., Anlauf, K., Hayden, K., Schmidlin, F., Fujimoto, T., Akagi, K., Meyer, C., Nichol, S., Davies, J., Redondas, A., and Cuevas, E. (2006). Long-term changes in tropospheric ozone. *Atmospheric Environment*, 40(17):3156–3173.

Oltmans, S. J., Lefohn, A. S., Shadwick, D., Harris, J. M., Scheel, H. E., Galbally, I., Tarasick, D. W., Johnson, B. J., Brunke, E. G., Claude, H., Zeng, G., Nichol, S., Schmidlin, F., Davies, J., Cuevas, E., Redondas, A., Naoe, H., Nakano, T., and Kawasato, T. (2013). Recent tropospheric ozone changes - A pattern dominated by slow or no growth. *Atmospheric Environment*, 67:331–351.

Ordóñez, C., Brunner, D., Staehelin, J., Hadjinicolaou, P., Pyle, J. A., Jonas, M., Wernli, H., and Prévôt, A. S. H. (2007). Strong influence of lowermost stratospheric ozone on lower tropospheric background ozone changes over Europe. *Geophysical Research Letters*, 34(7):L07805.

Orlando, J. J. and Tyndall, G. S. (2012). Laboratory studies of organic peroxy radical chemistry: an overview with emphasis on recent issues of atmospheric significance. *Chemical Society Reviews*, 41(19):6294.

Padro, J. (1996). Summary of ozone dry deposition velocity measurements and model estimates over vineyard, cotton, grass and deciduous forest in summer. *Atmospheric Environment*, 30(13):2363–2369.

Palmer, P. I. (2003). Mapping isoprene emissions over North America using formaldehyde column observations from space. *Journal of Geophysical Research: Atmospheres*, 108(D6):4180.

Parrish, D. D., Galbally, I. E., Lamarque, J.-F., Naik, V., Horowitz, L., Shindell, D. T., Oltmans, S. J., Derwent, R., Tanimoto, H., Labuschagne, C., and Cupeiro, M. (2016). Seasonal cycles of O3 in the marine boundary layer: Observation and model simulation comparisons. *Journal of Geophysical Research: Atmospheres*, 121(1):538–557.

Parrish, D. D., Holloway, J. S., and Fehsenfeld, F. C. (1994). Routine, continuous measurement of carbon monoxide with parts per billion precision. *Environmental Science & Technology*, 28(9):1615–1618.

Parrish, D. D., Lamarque, J.-F., Naik, V., Horowitz, L., Shindell, D. T., Staehelin, J., Derwent, R., Cooper, O. R., Tanimoto, H., Volz-Thomas, A., Gilge, S., Scheel, H.-E., Steinbacher, M., and Fröhlich, M. (2014). Long-term changes in lower tropospheric baseline ozone concentrations: Comparing chemistry-climate models and observations at northern midlatitudes. *Journal of Geophysical Research: Atmospheres*, 119(9):5719–5736.

Parrish, D. D., Law, K. S., Staehelin, J., Derwent, R., Cooper, O. R., Tanimoto, H., Volz-Thomas, A., Gilge, S., Scheel, H. E., Steinbacher, M., and Chan, E. (2013). Lower tropospheric ozone at northern midlatitudes: Changing seasonal cycle. *Geophysical Research Letters*, 40(8):1631–1636.

Paulot, F., Crounse, J. D., Kjaergaard, H. G., Kroll, J. H., Seinfeld, J. H., and Wennberg, P. O. (2009a). Isoprene photooxidation: new insights into the production of acids and organic nitrates. *Atmospheric Chemistry and Physics*, 9(4):1479–1501.

Paulot, F., Crounse, J. D., Kjaergaard, H. G., Kürten, A., St. Clair, J. M., Seinfeld, J. H., and Wennberg, P. O. (2009b). Unexpected epoxide formation in the gas-phase photooxidation of isoprene. *Science*, 325(5941):730–733.

Paulot, F., Henze, D. K., and Wennberg, P. O. (2012). Impact of the isoprene photochemical cascade on tropical ozone. *Atmospheric Chemistry and Physics*, 12(3):1307–1325.

Peeters, J. and Müller, J.-F. (2010). HOx radical regeneration in isoprene oxidation via peroxy radical isomerisations. II: experimental evidence and global impact. *Physical Chemistry Chemical Physics*, 12(42):14227.

Peeters, J., Nguyen, T. L., and Vereecken, L. (2009). HOx radical regeneration in the oxidation of isoprene. *Physical Chemistry Chemical Physics*, 11(28):5935.

Penkett, S., Gilge, S., Plass-Duelmer, C., and Galbally, I. (2011). A WMO/GAW Expert Workshop on Global Long-term Measurements of Nitrogen Oxides and Recommendations for GAW Nitrogen Oxides Network. Technical Report GAW Report No. 195, World Meteorological Organization, Hohenpeissenberg.

Platt, U., Perner, D., and Pätz, H. W. (1979). Simultaneous measurement of atmospheric CH2O, O3, and NO2 by differential optical absorption. *Journal of Geophysical Research: Oceans*, 84(C10):6329.

Prather, M., Ehhalt, D., Dentener, F., Derwent, R. G., Dlugokencky, E., Holland, E., Isaksen, I. S. A., Katima, J., Kirchhoff, V., Matson, P., Midgley, P. M., and Wang, M. (2001). Atmospheric Chemistry and Greenhouse Gases. In Houghton, J., Ding, Y., Griggs, D., Noguer, M., van der Linden, P., Dai, X., Maskell, K., and Johnson, C., editors, *Climate Change 2001: The Scientific Basis. Contribution of Working Group I to the Third Assessment Report of the Intergovernmental Panel on Climate Change*, pages 239–289. Cambridge University Press, New York.

Prather, M. J. (1996). Time scales in atmospheric chemistry: Theory, GWPs for CH4 and CO, and runaway growth. *Geophysical Research Letters*, 23(19):2597–2600.

Press, W. H. and Rybicki, G. B. (1989). Fast algorithm for spectral-analysis of unevenly sampled data. *Astrophysical Journal*, 338(1):277–280.

Press, W. H., Teukolsky, S. A., Vetterling, W. T., and Flannery, B. P. (1992). *Numerical Recipes in Fortran 77 - The Art Of Scientific Computing - Volume I*, volume 1. Cambridge University Press.

Price, C. and Rind, D. (1992). A simple lightning parameterization for calculating global lightning distributions. *Journal of Geophysical Research: Atmospheres*, 97(D9):9919–9933.

Rasmussen, D., Fiore, A., Naik, V., Horowitz, L., McGinnis, S., and Schultz, M. (2012). Surface ozone-temperature relationships in the eastern US: A monthly climatology for evaluating chemistry-climate models. *Atmospheric Environment*, 47:142–153.

Rasmussen, R. A. and Khalil, M. A. K. (1981). Atmospheric methane (CH4): Trends and seasonal cycles. *Journal of Geophysical Research: Oceans*, 86(C10):9826.

Read, K. A., Mahajan, A. S., Carpenter, L. J., Evans, M. J., Faria, B. V. E., Heard, D. E., Hopkins, J. R., Lee, J. D., Moller, S. J., Lewis, A. C., Mendes, L., McQuaid, J. B., Oetjen, H., Saiz-Lopez, A., Pilling, M. J., and Plane, J. M. C. (2008). Extensive halogen-mediated ozone destruction over the tropical Atlantic Ocean. *Nature*, 453(7199):1232–1235.

Rehfeld, K., Marwan, N., Heitzig, J., and Kurths, J. (2011). Comparison of correlation analysis techniques for irregularly sampled time series. *Nonlinear Processes in Geophysics*, 18(3):389–404.

Reidmiller, D. R., Fiore, A. M., Jaffe, D. A., Bergmann, D., Cuvelier, C., Dentener, F. J., Duncan, B. N., Folberth, G., Gauss, M., Gong, S., Hess, P., Jonson, J. E., Keating, T., Lupu, A., Marmer, E., Park, R., Schultz, M. G., Shindell, D. T., Szopa, S., Vivanco, M. G., Wild, O., and Zuber, A. (2009). The influence of foreign vs. North American emissions on surface ozone in the US. *Atmospheric Chemistry and Physics*, 9(14):5027–5042.

Reis, S., Blank, P., Friedrich, R., Smiatek, G., José, R. S., Peña, J. I., Pérez, J. L., González, R. M., Lewyckyj, N., Colles, A., Janssen, L., Mensink, C., Reis, S., Blank, P., Wickert, B., Friedrich, R., Müezzinoğlu, A., Elbir, T., Dinçer, F., Bayram, A., Odabasi, M., Cetin, E., and Seyfioglu, R. (2004). Emission Models and Tools. In *Emissions of Air Pollutants*, pages 279–335. Springer, Berlin, Heidelberg.

Richardson, S. J., Miles, N. L., Davis, K. J., Crosson, E. R., Rella, C. W., and Andrews, A. E. (2012). Field Testing of Cavity Ring-Down Spectroscopy Analyzers Measuring Carbon Dioxide and Water Vapor. *Journal of Atmospheric and Oceanic Technology*, 29(3):397–406.

Ridgwell, A. J., Marshall, S. J., and Gregson, K. (1999). Consumption of atmospheric methane by soils: A process-based model. *Global Biogeochemical Cycles*, 13(1):59–70.

Ridley, B. A. and Howlett, L. C. (1974). An instrument for nitric oxide measurements in the stratosphere. *Review of Scientific Instruments*, 45(6):742.

Rohrer, F., Bohn, B., Brauers, T., Brüning, D., Johnen, F.-J., Wahner, A., and Kleffmann, J. (2005). Characterisation of the photolytic HONO-source in the atmosphere simulation chamber SAPHIR. *Atmospheric Chemistry and Physics*, 5(8):2189–2201.

Rollins, A. W., Kiendler-Scharr, A., Fry, J. L., Brauers, T., Brown, S. S., Dorn, H.-P., Dubé, W. P., Fuchs, H., Mensah, A., Mentel, T. F., Rohrer, F., Tillmann, R., Wegener, R., Wooldridge, P. J., and Cohen, R. C. (2009). Isoprene oxidation by nitrate radical: alkyl nitrate and secondary organic aerosol yields. *Atmospheric Chemistry and Physics*, 9(18):6685–6703.

Rondón, A., Johansson, C., and Granat, L. (1993). Dry deposition of nitrogen dioxide and ozone to coniferous forests. *Journal of Geophysical Research: Atmospheres*, 98(D3):5159.

Roof, C., Hansen, A., Fleming, G. G., Thrasher, T., Nguyen, A., Hall, C., Dinges, E., Bea, R., Grandi, F., Kim, B. Y., Hollingsworth, P., and S., U. (2007). Aviation Environmental Design Tool (AEDT) System Architecture. Technical report, Federal Aviation Administration Office of Environment and Energy.

Ryerson, T. B., Williams, E. J., and Fehsenfeld, F. C. (2000). An efficient photolysis system for fast-response NO2 measurements. *Journal of Geophysical Research: Atmospheres*, 105(D21):26447–26461.

Sadanaga, Y., Fukumori, Y., Kobashi, T., Nagata, M., Takenaka, N., and Bandow, H. (2010). Development of a Selective Light-Emitting Diode Photolytic NO2 Converter for Continuously Measuring NO2 in the Atmosphere. *Analytical Chemistry*, 82(22):9234–9239.

Sanhueza, E., Dong, Y., Lobert, J., and Crutzen, P. J. (1998). Carbon monoxide uptake by temperate forest soils: the effects of leaves and humus layers. *Tellus B*, 50(1):51–58.

Scargle, J. D. (1982). Studies in astronomical time-series analysis. ll. Statistical aspects of spectral-analysis of unevenly spaced data. *Astrophysical Journal*, 263(2):835–853.

Schaap, M., Cuvelier, C., Hendriks, C., Bessagnet, B., Baldasano, J., Colette, A., Thunis, P., Karam, D., Fagerli, H., Graff, A., Kranenburg, R., Nyiri, A., Pay, M., Rouïl, L., Schulz, M., Simpson, D., Stern, R., Terrenoire, E., and Wind, P. (2015). Performance of European chemistry transport models as function of horizontal resolution. *Atmospheric Environment*, 112:90–105.

Schneider, P., Lahoz, W. A., and van der A, R. (2015). Recent satellite-based trends of tropospheric nitrogen dioxide over large urban agglomerations worldwide. *Atmospheric Chemistry and Physics*, 15(3):1205–1220.

Schnell, J. L., Prather, M. J., Josse, B., Naik, V., Horowitz, L. W., Cameron-Smith, P., Bergmann, D., Zeng, G., Plummer, D. A., Sudo, K., Nagashima, T., Shindell, D. T., Faluvegi, G., and Strode, S. A. (2015). Use of North American and European air quality networks to evaluate global chemistry–climate modeling of surface ozone. *Atmospheric Chemistry and Physics*, 15(18):10581–10596.

Schöpp, W., Klimont, Z., Suutari, R., and Cofala, J. (2005). Uncertainty analysis of emission estimates in the RAINS integrated assessment model. *Environmental Science & Policy*, 8(6):601–613.

Schultz, M. G., Akimoto, H., Bottenheim, J., Buchmann, B., Galbally, I. E., Gilge, S., Helmig, D., Koide, H., Lewis, A. C., Novelli, P. C., Plass-Dülmer, C., Ryerson, T. B., Steinbacher, M., Steinbrecher, R., Tarasova, O., Tørseth, K., Thouret, V., and Zellweger, C. (2015). The Global Atmosphere Watch reactive gases measurement network. *Elementa: Science of the Anthropocene*, 3(1):000067.

Schultz, M. G., Backman, L., Balkanski, Y., Bjoerndalsaeter, S., Brand, R., Burrows, J. P., Dalsoeren, S., de Vasconcelos, M. Grodtmann, B., Hauglustaine, D., Heil, A., Hoelzemann, J. J., Isaksen, I. S. A., Kaurola, J., Knorr, W., Ladstaetter-Weißenm, A., Mota, B., Oom, D., Pacyna, J., Panasiuk, D., Pereira, J. M. C., Pulles, T., Pyle, J., Rast, S., Richter, A., Savage, N., Schnadt, C., Schulz, M., Spessa, A., Staehelin, J., Sundet, J. K., Szopa, S., Thonicke, K., van het Bolscher, M., van Noije, T., van Velthoven, P., Vik, A. F., and Wittrock, F. (2007). Re-analysis of the tropospheric chemical composition over the past 40 years (RETRO) – A long-term global modeling study of tropospheric chemistry. Technical report, Max Planck Institute for Meteorology, Hamburg.

Schulz, M. and Mudelsee, M. (2002). REDFIT: estimating red-noise spectra directly from unevenly spaced paleoclimatic time series. *Computers & Geosciences*, 28(3):421–426.

Schulz, M. and Stattegger, K. (1997). SPECTRUM: Spectral analysis of unevenly spaced paleoclimatic time series. *Computers & Geosciences*, 23(9):929–945.

Schumann, U. and Huntrieser, H. (2007). The global lightning-induced nitrogen oxides source. *Atmospheric Chemistry and Physics*, 7(14):3823–3907.

Schuur, E. A. G. and Abbott, B. (2011). Climate change: High risk of permafrost thaw. *Nature*, 480(7375):32–33.

Schwede, D., Zhang, L., Vet, R., and Lear, G. (2011). An intercomparison of the deposition models used in the CASTNET and CAPMoN networks. *Atmospheric Environment*, 45(6):1337–1346.

Shannon, J. D. and Sisterson, D. L. (1992). Estimation of S and NOx-N deposition budgets for the United States and Canada. *Water, Air, & Soil Pollution*, 63(3-4):211–235.

Sherwen, T., Evans, M. J., Carpenter, L. J., Andrews, S. J., Lidster, R. T., Dix, B., Koenig, T. K., Sinreich, R., Ortega, I., Volkamer, R., Saiz-Lopez, A., Prados-Roman, C., Mahajan, A. S., and Ordóñez, C. (2016). Iodine's impact on tropospheric oxidants: a global model study in GEOS-Chem. *Atmospheric Chemistry and Physics*, 16(2):1161–1186.

Shindell, D. T., Faluvegi, G., Stevenson, D. S., Krol, M. C., Emmons, L. K., Lamarque, J.-F., Pétron, G., Dentener, F. J., Ellingsen, K., Schultz, M. G., Wild, O., Amann, M., Atherton, C. S., Bergmann, D. J., Bey, I., Butler, T., Cofala, J., Collins, W. J., Derwent, R. G., Doherty, R. M., Drevet, J., Eskes, H. J., Fiore, A. M., Gauss, M., Hauglustaine, D. A., Horowitz, L. W., Isaksen, I. S. A., Lawrence, M. G., Montanaro, V., Müller, J.-F., Pitari, G., Prather, M. J., Pyle, J. A., Rast, S., Rodriguez, J. M., Sanderson, M. G., Savage, N. H., Strahan, S. E., Sudo, K., Szopa, S., Unger, N., van Noije, T. P. C., and Zeng, G. (2006). Multimodel simulations of carbon monoxide: Comparison with observations and projected near-future changes. *Journal of Geophysical Research: Atmospheres*, 111:D19306.

Silva, R. A., West, J. J., Zhang, Y., Anenberg, S. C., Lamarque, J.-F., Shindell, D. T., Collins, W. J., Dalsoren, S., Faluvegi, G., Folberth, G., Horowitz, L. W., Nagashima, T., Naik, V., Rumbold, S., Skeie, R., Sudo, K., Takemura, T., Bergmann, D., Cameron-Smith, P., Cionni, I., Doherty, R. M., Eyring, V., Josse, B., MacKenzie, I. A., Plummer, D., Righi, M., Stevenson, D. S., Strode, S., Szopa, S., and Zeng, G. (2013). Global premature mortality due to anthropogenic outdoor air pollution and the contribution of past climate change. *Environmental Research Letters*, 8(3):034005.

Simone, N. W. (2013). *Development of a Rapid Global Aircraft Emissions Estimation Tool with Uncertainty Quantification*. PhD thesis, Massachusetts Institute of Technology.

Sindelarova, K., Granier, C., Bouarar, I., Guenther, A., Tilmes, S., Stavrakou, T., Müller, J.-F., Kuhn, U., Stefani, P., and Knorr, W. (2014). Global data set of biogenic VOC emissions calculated by the MEGAN model over the last 30 years. *Atmospheric Chemistry and Physics*, 14(17):9317–9341.

Singh, H. B. and Hanst, P. L. (1981). Peroxyacetyl nitrate (PAN) in the unpolluted atmosphere: An important reservoir for nitrogen oxides. *Geophysical Research Letters*, 8(8):941–944.

Sitch, S., Cox, P. M., Collins, W. J., and Huntingford, C. (2007). Indirect radiative forcing of climate change through ozone effects on the land-carbon sink. *Nature*, 448(7155):791–794.

Sofen, E. D., Bowdalo, D. R., Evans, M. J., Apadula, F., Bonasoni, P., Cupeiro, M., Ellul, R., Galbally, I. E., Girgzdiene, R., Luppo, S., Mimouni, M., Nahas, A. C., Saliba, M., and Tørseth, K. (2016). Gridded global surface ozone metrics for atmospheric chemistry model evaluation. *Earth System Science Data*, 8(1):41–59.

Solazzo, E. and Galmarini, S. (2015). Comparing apples with apples: Using spatially distributed time series of monitoring data for model evaluation. *Atmospheric Environment*, 112:234–245.

Sommariva, R., Haggerstone, A.-L., Carpenter, L. J., Carslaw, N., Creasey, D. J., Heard, D. E., Lee, J. D., Lewis, A. C., Pilling, M. J., and Zádor, J. (2004). OH and HO2 chemistry in clean marine air during SOAPEX-2. *Atmospheric Chemistry and Physics*, 4(3):839–856.

Sparks, J. P., Walker, J., Turnipseed, A., and Guenther, A. (2007). Dry nitrogen deposition estimates over a forest experiencing free air CO2 enrichment. *Global Change Biology*, 14(4):768–781.

Squire, O. J., Archibald, A. T., Griffiths, P. T., Jenkin, M. E., Smith, D., and Pyle, J. A. (2015). Influence of isoprene chemical mechanism on modelled changes in tropospheric ozone due to climate and land use over the 21st century. *Atmospheric Chemistry and Physics*, 15(9):5123–5143.

Stefan, S., Necula, C., and Georgescu, F. (2010). Analysis of long-range transport of particulate matters in connection with air circulation over Central and Eastern part of Europe. *Physics and Chemistry of the Earth, Parts A/B/C*, 35(9-12):523–529.

Stein, O., Schultz, M. G., Bouarar, I., Clark, H., Huijnen, V., Gaudel, A., George, M., and Clerbaux, C. (2014). On the wintertime low bias of Northern Hemisphere carbon monoxide found in global model simulations. *Atmospheric Chemistry and Physics*, 14(17):9295–9316.

Steinbacher, M., Zellweger, C., Schwarzenbach, B., Bugmann, S., Buchmann, B., Ordóñez, C., Prevot, A. S. H., and Hueglin, C. (2007). Nitrogen oxide measurements at rural sites in Switzerland: Bias of conventional measurement techniques. *Journal of Geophysical Research: Atmospheres*, 112:D11307.

Stettler, M., Eastham, S., and Barrett, S. (2011). Air quality and public health impacts of UK airports. Part I: Emissions. *Atmospheric Environment*, 45(31):5415–5424.

Stevenson, D. S., Dentener, F. J., Schultz, M. G., Ellingsen, K., van Noije, T. P. C., Wild, O., Zeng, G., Amann, M., Atherton, C. S., Bell, N., Bergmann, D. J., Bey, I., Butler, T., Cofala, J., Collins, W. J., Derwent, R. G., Doherty, R. M., Drevet, J., Eskes, H. J., Fiore, A. M., Gauss, M., Hauglustaine, D. A., Horowitz, L. W., Isaksen, I. S. A., Krol, M. C., Lamarque, J.-F., Lawrence, M. G., Montanaro, V., Müller, J.-F., Pitari, G., Prather, M. J., Pyle, J. A., Rast, S., Rodriguez, J. M., Sanderson, M. G., Savage, N. H., Shindell, D. T., Strahan, S. E., Sudo, K., and Szopa, S. (2006). Multimodel ensemble simulations of present-day and near-future tropospheric ozone. *Journal of Geophysical Research: Atmospheres*, 111:D08301.

Stevenson, D. S., Young, P. J., Naik, V., Lamarque, J.-F., Shindell, D. T., Voulgarakis, A., Skeie, R. B., Dalsoren, S. B., Myhre, G., Berntsen, T. K., Folberth, G. A., Rumbold, S. T., Collins, W. J., MacKenzie, I. A., Doherty, R. M., Zeng, G., van Noije, T. P. C., Strunk, A., Bergmann, D., Cameron-Smith, P., Plummer, D. A., Strode, S. A., Horowitz, L., Lee, Y. H., Szopa, S., Sudo, K., Nagashima, T., Josse, B., Cionni, I., Righi, M., Eyring, V., Conley, A., Bowman, K. W., Wild, O., and Archibald, A. (2013). Tropospheric ozone changes, radiative forcing and attribution to emissions in the Atmospheric Chemistry and Climate Model Intercomparison Project (ACCMIP). *Atmospheric Chemistry and Physics*, 13(6):3063–3085.

Stone, D., Evans, M. J., Commane, R., Ingham, T., Floquet, C. F. A., McQuaid, J. B., Brookes, D. M., Monks, P. S., Purvis, R., Hamilton, J. F., Hopkins, J., Lee, J., Lewis, A. C., Stewart, D., Murphy, J. G., Mills, G., Oram, D., Reeves, C. E., and Heard, D. E. (2010). HOx observations over West Africa during AMMA: impact of isoprene and NOx. *Atmospheric Chemistry and Physics*, 10(19):9415–9429.

Streets, D. G., Bond, T. C., Carmichael, G. R., Fernandes, S. D., Fu, Q., He, D., Klimont, Z., Nelson, S. M., Tsai, N. Y., Wang, M. Q., Woo, J.-H., and Yarber, K. F. (2003). An inventory of gaseous and primary aerosol emissions in Asia in the year 2000. *Journal of Geophysical Research: Atmospheres*, 108(D21):8819.

Strode, S. A., Duncan, B. N., Yegorova, E. A., Kouatchou, J., Ziemke, J. R., and Douglass, A. R. (2015). Implications of carbon monoxide bias for methane lifetime and atmospheric composition in chemistry climate models. *Atmospheric Chemistry and Physics*, 15(20):11789–11805.

Strode, S. A., Worden, H. M., Damon, M., Douglass, A. R., Duncan, B. N., Emmons, L. K., Lamarque, J.-F., Manyin, M., Oman, L. D., Rodriguez, J. M., Strahan, S. E., and Tilmes, S. (2016). Interpreting space-based trends in carbon monoxide with multiple models. *Atmospheric Chemistry and Physics*, 16(11):7285–7294.

Tan, D., Faloona, I., Simpas, J. B., Brune, W., Shepson, P. B., Couch, T. L., Sumner, A. L., Carroll, M. A., Thornberry, T., Apel, E., Riemer, D., and Stockwell, W. (2001). HOx budgets in a deciduous forest: Results from the PROPHET summer 1998 campaign. *Journal of Geophysical Research: Atmospheres*, 106(D20):24407–24427.

Tang, Q., Prather, M. J., and Hsu, J. (2011). Stratosphere-troposphere exchange ozone flux related to deep convection. *Geophysical Research Letters*, 38(3).

Tang, Y. S., Cape, J. N., and Sutton, M. A. (2001). Development and types of passive samplers for monitoring atmospheric NO2 and NH3 concentrations. *Scientific World Journal*, 1:513–29.

Tanimoto, H. (2002). Seasonal cycles of ozone and oxidized nitrogen species in northeast Asia 2. A model analysis of the roles of chemistry and transport. *Journal of Geophysical Research: Atmospheres*, 107(D23):4706.

Tanimoto, H., Ohara, T., and Uno, I. (2009). Asian anthropogenic emissions and decadal trends in springtime tropospheric ozone over Japan: 1998–2007. *Geophysical Research Letters*, 36(23):L23802.

Tanimoto, H., Sawa, Y., Matsueda, H., Uno, I., Ohara, T., Yamaji, K., Kurokawa, J., and Yonemura, S. (2005). Significant latitudinal gradient in the surface ozone spring maximum over East Asia. *Geophysical Research Letters*, 32(21):L21805.

Theo, H., Anne, F.-M., Eddy, G., Markus, H., Ulrich, P., Hervé, P., Franco, D. S., Kevin, S., Wendy, S., Sim, T., Jaume, T., and Michel, G. (2009). *Review of the Application of Diffusive Samplers for the Measurement of Nitrogen Dioxide in Ambient Air in the European Union*. Publications Office of the European Union, Brussels.

Thornton, J. A., Wooldridge, P. J., Cohen, R. C., Williams, E. J., Hereid, D., Fehsenfeld, F. C., Stutz, J., and Alicke, B. (2003). Comparisons of in situ and long path measurements of NO2 in urban plumes. *Journal of Geophysical Research: Atmospheres*, 108(D16):4496.

Tørseth, K., Aas, W., Breivik, K., Fjæraa, A. M., Fiebig, M., Hjellbrekke, A. G., Lund Myhre, C., Solberg, S., and Yttri, K. E. (2012). Introduction to the European Monitoring and Evaluation Programme (EMEP) and observed atmospheric composition change during 1972–2009. *Atmospheric Chemistry and Physics*, 12(12):5447–5481.

Townsend, A. R. and Howarth, R. W. (2010). Fixing the Global Nitrogen Problem. *Scientific American*, 302(2):64–71.

Travis, K. R., Jacob, D. J., Fisher, J. A., Kim, P. S., Marais, E. A., Zhu, L., Yu, K., Miller, C. C., Yantosca, R. M., Sulprizio, M. P., Thompson, A. M., Wennberg, P. O., Crounse, J. D., St. Clair, J. M., Cohen, R. C., Laugher, J. L., Dibb, J. E., Hall, S. R., Ullmann, K., Wolfe, G. M., Pollack, I. B., Peischl, J., Neuman, J. A., and Zhou, X. (2016). NOx emissions, isoprene oxidation pathways, vertical mixing, and implications for surface ozone in the Southeast United States. *Atmospheric Chemistry and Physics Discussions*.

U.S. Environmental Protection Agency (2016). U.S. Code of Federal Regulations (CFR). Title 40: Protection of Environment. Technical report, U.S Government Publishing Office, Washington DC.

Val Martin, M., Heald, C. L., and Arnold, S. R. (2014). Coupling dry deposition to vegetation phenology in the Community Earth System Model: Implications for the simulation of surface O3. *Geophysical Research Letters*, 41(8):2988–2996.

Valenzuela, J. and Pontt, J. (2009). Real-Time Interharmonics Detection and Measurement Based on FFT Algorithm. In *Proceedings of Applied Electronics*, pages 259–264, Pilsen. Institute of Electrical and Electronics Engineers (IEEE).

van der Werf, G. R., Randerson, J. T., Giglio, L., Collatz, G. J., Kasibhatla, P. S., and Arellano, A. F. (2006). Interannual variability in global biomass burning emissions from 1997 to 2004. *Atmospheric Chemistry and Physics*, 6(11):3423–3441.

van der Werf, G. R., Randerson, J. T., Giglio, L., Collatz, G. J., Mu, M., Kasibhatla, P. S., Morton, D. C., DeFries, R. S., Jin, Y., and van Leeuwen, T. T. (2010). Global fire emissions and the contribution of deforestation, savanna, forest, agricultural, and peat fires (1997–2009). *Atmospheric Chemistry and Physics*, 10(23):11707–11735.

van Donkelaar, A., Martin, R. V., Leaitch, W. R., Macdonald, A. M., Walker, T. W., Streets, D. G., Zhang, Q., Dunlea, E. J., Jimenez, J. L., Dibb, J. E., Huey, L. G., Weber, R., and Andreae, M. O. (2008). Analysis of aircraft and satellite measurements from the Intercontinental Chemical Transport Experiment (INTEX-B) to quantify long-range transport of East Asian sulfur to Canada. *Atmospheric Chemistry and Physics*, 8(11):2999–3014.

van Donkelaar, A., Martin, R. V., Park, R. J., Heald, C. L., Fu, T.-M., Liao, H., and Guenther, A. (2007). Model evidence for a significant source of secondary organic aerosol from isoprene. *Atmospheric Environment*, 41(6):1267–1274.

Vestreng, V., Ntziachristos, L., Semb, A., Reis, S., Isaksen, I. S. A., and Tarrasón, L. (2009). Evolution of NOx emissions in Europe with focus on road transport control measures. *Atmospheric Chemistry and Physics*, 9(4):1503–1520.

Villena, G., Bejan, I., Kurtenbach, R., Wiesen, P., and Kleffmann, J. (2011). Development of a new Long Path Absorption Photometer (LOPAP) instrument for the sensitive detection of NO2 in the atmosphere. *Atmospheric Measurement Techniques*, 4(8):1663–1676.

Vinken, G. C. M., Boersma, K. F., Jacob, D. J., and Meijer, E. W. (2011). Accounting for non-linear chemistry of ship plumes in the GEOS-Chem global chemistry transport model. *Atmospheric Chemistry and Physics*, 11(22):11707–11722.

Vinken, G. C. M., Boersma, K. F., Maasakkers, J. D., Adon, M., and Martin, R. V. (2014). Worldwide biogenic soil NOx emissions inferred from OMI NO2 observations. *Atmospheric Chemistry and Physics*, 14(18):10363–10381.

Von Kuhlmann, R., Lawrence, M. G., Pöschl, U., and Crutzen, P. J. (2004). Sensitivities in global scale modeling of isoprene. *Atmospheric Chemistry and Physics*, 4(1):1–17.

Voulgarakis, A., Savage, N. H., Wild, O., Braesicke, P., Young, P. J., Carver, G. D., and Pyle, J. A. (2010). Interannual variability of tropospheric composition: the influence of changes in emissions, meteorology and clouds. *Atmospheric Chemistry and Physics*, 10(5):2491–2506.

Walker, T. W. (2014). *Applications of Adjoint Modeling in Chemical Composition: Studies of Tropospheric Ozone at Middle and High Northern Latitudes*. PhD thesis, University of Toronto.

Wang, Y., Jacob, D. J., and Logan, J. A. (1998). Global simulation of tropospheric O3-NOx-hydrocarbon chemistry: 1. Model formulation. *Journal of Geophysical Research: Atmospheres*, 103(D9):10713–10725.

Warneke, C., de Gouw, J. A., Del Negro, L., Brioude, J., McKeen, S., Stark, H., Kuster, W. C., Goldan, P. D., Trainer, M., Fehsenfeld, F. C., Wiedinmyer, C., Guenther, A. B., Hansel, A., Wisthaler, A., Atlas, E., Holloway, J. S., Ryerson, T. B., Peischl, J., Huey, L. G., and Case Hanks, A. T. (2010). Biogenic emission measurement and inventories determination of biogenic emissions in the eastern United States and Texas and comparison with biogenic emission inventories. *Journal of Geophysical Research: Atmospheres*, 115(D7):D00F18.

Warner, J., Carminati, F., Wei, Z., Lahoz, W., and Attié, J.-L. (2013). Tropospheric carbon monoxide variability from AIRS under clear and cloudy conditions. *Atmospheric Chemistry and Physics*, 13(24):12469–12479.

Wesely, M. (1989). Parameterization of surface resistances to gaseous dry deposition in regional-scale numerical models. *Atmospheric Environment (1967)*, 23(6):1293–1304.

Wesely, M. and Hicks, B. (2000). A review of the current status of knowledge on dry deposition. *Atmospheric Environment*, 34(12):2261–2282.

Whalley, L. K., Edwards, P. M., Furneaux, K. L., Goddard, A., Ingham, T., Evans, M. J., Stone, D., Hopkins, J. R., Jones, C. E., Karunaharan, A., Lee, J. D., Lewis, A. C., Monks, P. S., Moller, S. J., and Heard, D. E. (2011). Quantifying the magnitude of a missing hydroxyl radical source in a tropical rainforest. *Atmospheric Chemistry and Physics*, 11(14):7223–7233.

Whalley, L. K., Furneaux, K. L., Goddard, A., Lee, J. D., Mahajan, A., Oetjen, H., Read, K. A., Kaaden, N., Carpenter, L. J., Lewis, A. C., Plane, J. M. C., Saltzman, E. S., Wiedensohler, A., and Heard, D. E. (2010). The chemistry of OH and HO2 radicals in the boundary layer over the tropical Atlantic Ocean. *Atmospheric Chemistry and Physics*, 10(4):1555–1576.

WHO (2005). *Air quality guidelines for particulate matter, ozone, nitrogen dioxide and sulfur dioxide: Global update 2005*. World Health Organization, Regional Office for Europe, Copenhagen.

Wielgosz, R. I., Esler, M., Viallon, J., Moussay, P., Oh, S. H., Kim, B. M., Botha, A., Tshilongo, J., Mokgoro, I. S., Maruyama, M., Mace, T., Sutour, C., Stovcík, V., Valková, M., Musil, S., Castorena, A. P., Caballero, V. S., Murillo, F. R., Konopelko, L. A., Kustikov, Y. A., Pankratov, V. V., Gromova, E. V., Thorn, W. J., Guenther, F. R., Smeulders, D., Baptista, G., Dias, F., Wessel, R. M., Nieuwenkamp, G., and van der Veen, A. M. H. (2008). Final report on CCQM-P73: International comparison of nitrogen monoxide in nitrogen gas standards (30–70) µmol/mol. *Metrologia*, 45(1A):08002.

Wild, O. and Prather, M. J. (2006). Global tropospheric ozone modeling: Quantifying errors due to grid resolution. *Journal of Geophysical Research: Atmospheres*, 111:D11305.

Wilkinson, S. and Davies, W. J. (2010). Drought, ozone, ABA and ethylene: new insights from cell to plant to community. *Plant, Cell & Environment*, 33(4):510–525.

Williams, J. E., van Velthoven, P. F. J., and Brenninkmeijer, C. A. M. (2013). Quantifying the uncertainty in simulating global tropospheric composition due to the variability in global emission estimates of Biogenic Volatile Organic Compounds. *Atmospheric Chemistry and Physics*, 13(5):2857–2891.

Winer, A. M., Peters, J. W., Smith, J. P., and Pitts, J. N. (1974). Response of commercial chemiluminescent nitric oxide-nitrogen dioxide analyzers to other nitrogen-containing compounds. *Environmental Science & Technology*, 8(13):1118–1121.

WMO/GAW (2007). A WMO/GAW Expert Workshop on Global Long-term Measurements of Volatile Organic Compounds. Technical Report GAW Report No. 171, World Meteorological Organization, Geneva.

WMO/GAW (2010). Guidelines for the Measurement of Atmospheric Carbon Monoxide. Technical Report GAW Report No. 192, World Meteorological Organization.

Wolfe, G. M., Crounse, J. D., Parrish, J. D., St Clair, J. M., Beaver, M. R., Paulot, F., Yoon, T. P., Wennberg, P. O., and Keutsch, F. N. (2012). Photolysis, OH reactivity and ozone reactivity of a proxy for isoprene-derived hydroperoxyenals (HPALDs). *Physical Chemistry Chemical Physics*, 14(20):7276–86.

Wu, S., Mickley, L. J., Jacob, D. J., Logan, J. A., Yantosca, R. M., and Rind, D. (2007). Why are there large differences between models in global budgets of tropospheric ozone? *Journal of Geophysical Research: Atmospheres*, 112:D05302.

Wu, S., Mickley, L. J., Jacob, D. J., Rind, D., and Streets, D. G. (2008). Effects of 2000–2050 changes in climate and emissions on global tropospheric ozone and the policy-relevant background surface ozone in the United States. *Journal of Geophysical Research: Atmospheres*, 113:D18312.

Wu, Z., Wang, X., Chen, F., Turnipseed, A. A., Guenther, A. B., Niyogi, D., Charusombat, U., Xia, B., William Munger, J., and Alapaty, K. (2011). Evaluating the calculated dry deposition velocities of reactive nitrogen oxides and ozone from two community models over a temperate deciduous forest. *Atmospheric Environment*, 45(16):2663–2674.

Xiao, Y., Logan, J. A., Jacob, D. J., Hudman, R. C., Yantosca, R., and Blake, D. R. (2008). Global budget of ethane and regional constraints on U.S. sources. *Journal of Geophysical Research: Atmospheres*, 113:D21306.

Xie, Y., Paulot, F., Carter, W. P. L., Nolte, C. G., Luecken, D. J., Hutzell, W. T., Wennberg, P. O., Cohen, R. C., and Pinder, R. W. (2013). Understanding the impact of recent advances in isoprene photooxidation on simulations of regional air quality. *Atmospheric Chemistry and Physics*, 13(16):8439–8455.

Yevich, R. and Logan, J. A. (2003). An assessment of biofuel use and burning of agricultural waste in the developing world. *Global Biogeochemical Cycles*, 17(4):1095.

Yienger, J. J. and Levy, H. (1995). Empirical model of global soil-biogenic NOx emissions. *Journal of Geophysical Research: Atmospheres*, 100(D6):11447.

Yoon, J. and Pozzer, A. (2014). Model-simulated trend of surface carbon monoxide for the 2001–2010 decade. *Atmospheric Chemistry and Physics*, 14(19):10465–10482.

Young, P. J., Archibald, A. T., Bowman, K. W., Lamarque, J.-F., Naik, V., Stevenson, D. S., Tilmes, S., Voulgarakis, A., Wild, O., Bergmann, D., Cameron-Smith, P., Cionni, I., Collins, W. J., Dalsøren, S. B., Doherty, R. M., Eyring, V., Faluvegi, G., Horowitz, L. W., Josse, B., Lee, Y. H., MacKenzie, I. A., Nagashima, T., Plummer, D. A., Righi, M., Rumbold, S. T., Skeie, R. B., Shindell, D. T., Strode, S. A., Sudo, K., Szopa, S., and Zeng, G. (2013). Pre-industrial to end 21st century projections of tropospheric ozone from the Atmospheric Chemistry and Climate Model Intercomparison Project (ACCMIP). *Atmospheric Chemistry and Physics*, 13(4):2063–2090.

Zellweger, C., Hüglin, C., Klausen, J., Steinbacher, M., Vollmer, M., and Buchmann, B. (2009). Inter-comparison of four different carbon monoxide measurement techniques and evaluation of the long-term carbon monoxide time series of Jungfraujoch. *Atmospheric Chemistry and Physics*, 9(11):3491–3503.

Zhang, L., Brook, J. R., and Vet, R. (2002). On ozone dry deposition—with emphasis on non-stomatal uptake and wet canopies. *Atmospheric Environment*, 36(30):4787–4799.

Zhang, L., Jacob, D. J., Knipping, E. M., Kumar, N., Munger, J. W., Carouge, C. C., van Donkelaar, A., Wang, Y. X., and Chen, D. (2012). Nitrogen deposition to the United States: distribution, sources, and processes. *Atmospheric Chemistry and Physics*, 12(10):4539–4554.

Zhang, Q., Streets, D. G., Carmichael, G. R., He, K. B., Huo, H., Kannari, A., Klimont, Z., Park, I. S., Reddy, S., Fu, J. S., Chen, D., Duan, L., Lei, Y., Wang, L. T., and Yao, Z. L. (2009). Asian emissions in 2006 for the NASA INTEX-B mission. *Atmospheric Chemistry and Physics*, 9(14):5131–5153.

Zhang, Q., Streets, D. G., He, K., Wang, Y., Richter, A., Burrows, J. P., Uno, I., Jang, C. J., Chen, D., Yao, Z., and Lei, Y. (2007). NOx emission trends for China, 1995–2004: The view from the ground and the view from space. *Journal of Geophysical Research: Atmospheres*, 112:D22306.

Zhao, Y., Nielsen, C. P., Lei, Y., Mcelroy, M. B., and Hao, J. (2011). Quantifying the uncertainties of a bottom-up emission inventory of anthropogenic atmospheric pollutants in China. *Atmospheric Chemistry and Physics*, 11(5):2295–2308.

Zhu, L., Jacob, D. J., Kim, P. S., Fisher, J. A., Yu, K., Travis, K. R., Mickley, L. J., Yantosca, R. M., Sulprizio, M. P., De Smedt, I., Gonzalez Abad, G., Chance, K., Li, C., Ferrare, R., Fried, A., Hair, J. W., Hanisco, T. F., Richter, D., Scarino, A. J., Walega, J., Weibring, P., and Wolfe, G. M. (2016). Observing atmospheric formaldehyde (HCHO) from space: validation and intercomparison of six retrievals from four satellites (OMI, GOME2A, GOME2B, OMPS) with SEAC4RS aircraft observations over the Southeast US. *Atmospheric Chemistry and Physics Discussions*.

Ziemke, J. R., Douglass, A. R., Oman, L. D., Strahan, S. E., and Duncan, B. N. (2015). Tropospheric ozone variability in the tropics from ENSO to MJO and shorter timescales. *Atmospheric Chemistry and Physics*, 15(14):8037–8049.